University of Wollongong

Research Online

University of Wollongong Thesis Collection 1954-2016

University of Wollongong Thesis Collections

2004

The influence of microalloying elements on the hot ductility of thin slab cast steel

Kristin R. Carpenter

Follow this and additional works at: https://ro.uow.edu.au/theses

University of Wollongong

Copyright Warning

You may print or download ONE copy of this document for the purpose of your own research or study. The University does not authorise you to copy, communicate or otherwise make available electronically to any other person any copyright material contained on this site.

You are reminded of the following: This work is copyright. Apart from any use permitted under the Copyright Act 1968, no part of this work may be reproduced by any process, nor may any other exclusive right be exercised, without the permission of the author. Copyright owners are entitled to take legal action against persons who infringe their copyright. A reproduction of material that is protected by copyright may be a copyright infringement. A court may impose penalties and award damages in relation to offences and infringements relating to copyright material. Higher penalties may apply, and higher damages may be awarded, for offences and infringements involving the conversion of material into digital or electronic form.

Unless otherwise indicated, the views expressed in this thesis are those of the author and do not necessarily represent the views of the University of Wollongong.

Recommended Citation

Carpenter, Kristin, The influence of microalloying elements on the hot ductility of thin slab cast steel, PhD thesis, Department of Materials Engineering, University of Wollongong, 2004. http://ro.uow.edu.com.au/theses/161

Research Online is the open access institutional repository for the University of Wollongong. For further information contact the UOW Library: research-pubs@uow.edu.au

The Influence of Microalloying Elements on the Hot Ductility of Thin Slab Cast Steel

A thesis submitted in fulfilment of the requirements for the award of the degree

of

DOCTOR OF PHILOSOPHY

From

THE UNIVERSITY OF WOLLONGONG

By

KRISTIN CARPENTER

B.E (MATL)

DEPARTMENT OF MATERIALS ENGINEERING

2004

CANDIDATE'S CERTIFICATE

This is to certify that the work presented in this thesis is original and was carried out by the candidate in the Department of Materials Engineering, the University of Wollongong and has not been submitted to any other university or institution for a higher degree.

…….

Kristin Carpenter

Table of Contents

Table of Contents I

List of Figures VII

List of Tables XIV

Synopsis XV

Acknowledgements XVIII

CHAPTER 1: LITERATURE REVIEW: THIN SLAB CASTING TECHNOLOGY 1

1.1 Introduction: Thin Slab Casting Technology 1

1.2 Benefits of Thin Slab Casting 2

1.3 Metallurgical Considerations of Thin Slab Casting 4

1.3.1 Liquid Steel Quality 4

1.3.2 Caster Design 5

1.3.3 Metallurgical Aspects 6

1.3.4 Thin Slab Casting with Liquid Core Reduction (LCR) 7

1.4 Rolling Aspects of Thin Slab Casting 10

1.4.1 Tunnel/Holding Furnace 10

1.4.2 Metallurgical Considerations During Rolling of Thin Cast Slabs 10

1.5 Thin Slab Casting and Hot Direct Rolling Processes 12

1.5.1 CSP- Compact Strip Production 12

1.5.2 ISP- In-line Strip Production 15

1.5.3 "Danieli" Thin Slab Caster 16

1.5.4 TSP- Tippins-Samsung Process 18

1.5.5 Conroll (VAI) 19

1.5.6 QSP- Quality Strip Production 20

1.6 Concluding Remarks 22

CHAPTER 2: LITERATURE REVIEW: HOT DUCTILITY **23**

2.1 Introduction **23**

2.2 Origin of Transverse Cracks During Continuous Casting **25**

2.2.1 Role of Oscillation Marks in the Formation of Transverse Cracks 25

2.2.2 Effects of Chemical Composition on Oscillation Marks and Transverse Cracks 28

2.2.3 Influence of Carbon on Transverse Cracking 29

2.3 Relevance of the Hot Tensile Test to the Problem of Transverse Cracking **31**

2.4 The Hot Ductility Curve **34**

2.4.1 Intergranular Failure: Role of Ferrite films 35

2.4.2 Intergranular Failure: Precipitation Free Zones (PFZ) 37

2.4.3 Intergranular Failure: Grain Boundary Sliding 37

2.5 Effects of Microstructural Variables on Hot Ductility **39**

2.5.1 Grain Size 39

2.5.2 Precipitation 40

2.6 Effect of Composition on Hot Ductility **42**

2.6.1 Influence of Carbon on Hot Ductility 42

2.6.2 Effects of Sulphur on Hot Ductility 43

2.6.3 C-Mn-Al – Influence of AlN on Hot Ductility 46

2.6.4 C-Mn-Al-Nb - Influence of Nb on Hot Ductility 48

2.6.5 C-Mn-Al-Ti- Influence of Ti on Hot Ductility 50

2.6.6 Influence of Ti on Nb Microalloyed Steels 53

2.6.7 Role of Inclusions/Residuals on Hot Ductility 54

2.7 Effect of Test Variables on Hot Ductility **56**

2.7.1 Cooling Rate 56

2.7.2 Strain Rate 57

2.7.3 Test Direction 57

2.7.4 Thermal History 58

2.8 Dynamic Recrystallisation and Deformation Induced Ferrite 61
2.8.1 Deformation Induced Ferrite 61
2.8.2 Dynamic Recrystallisation Verses Deformation Induced Ferrite 62
2.8.3 Modelling of Dynamic Recrystallisation 63
2.8.4 Commercial Implications on the Formation of Deformation Induced Ferrite and Dynamic Recrystallisation 64

2.9 Concluding Remarks 65

CHAPTER 3: EXPERIMENTAL 67

3.1 Introduction 67

3.2 Materials and Compositions 67

3.3 Tensile Testing: Gleeble Thermomechanical Simulator 69
3.3.1 Solution Treatment Procedure 71
3.3.2 Melting and Solidification Procedure (Direct Casting) 72
3.3.3 Simulation of Thermal Oscillations During Direct Cast Gleeble Tests 74
3.3.4 Determination of Reduction of Area (RA) 77
3.3.5 Radial Temperature Gradient Measurements 78

3.4 Metallography 80
3.4.1 Determination of Dendritic Segregation 82
3.4.2 Determination of Homogenisation Time 83

3.5 Scanning Electron Microscope (SEM) 84

3.6 Transmission Electron Microscope (TEM) 84

3.7 Dilatometry 86

3.8 Determination of Young's Modulus and Yield Stress 87

CHAPTER 4: RESULTS 90

4.1 Hot Ductility Curves 90

4.1.1 C-Mn-Al (Base Composition) 90
4.1.2 C-Mn-Al-Nb (Nb steel) 91
4.1.3 C-Mn-Al-Ti (Ti Steel) 92
4.1.4 C-Mn-Al-Nb-Ti (Nb-Ti Steel) 93
4.1.5 Summary of Hot Ductility Data 94
4.1.6 Hot Ductility Results from Cyclic Thermal History Tests 95
4.1.7 Comparisons of Hot Ductility Curves Under Solution Treatment Conditions 96
4.1.8 Comparisons of Hot Ductility Curves Under Direct Cast Conditions 97

4.2 Stress Strain Curves 98
4.2.1 Stress-Strain Curves- Occurrence of Dynamic Recrystallisation 100

4.3 Austenite Grain Size 102

4.4 Segregation Pattern and Determination of Secondary Dendrite Arm Spacings (SDAS) 103
4.4.1 Homogenisation Time 105

4.5 Metallographic Examination of Fracture Surfaces 106
4.5.1 C-Mn-Al 110
4.5.2 C-Mn-Al-Nb 110
4.5.3 C-Mn-Al-Ti 110
4.5.4 C-Mn-Al-Nb-Ti 111
4.5.5 Cyclic Temperature Oscillation Tests 111

4.6 SEM 112
4.6.1 SEM- Cyclic Temperature Oscillation Tests 116

4.7 TEM Results 118
4.7.1 C-Mn-Al 118
4.7.2 C-Mn-Al-Ti 120
4.7.3 C-Mn-Al-Nb 125
4.7.4 C-Mn-Al-Nb-Ti 128
4.7.5 TEM Particle Size Distribution Histograms 135
4.7.6 Influence of Particle Size on Hot Ductility 144

4.7.7 Influence of Interparticle Spacing on Hot Ductility 145

4.8 Dilatometry and Transformation Temperatures 146

4.9 Young's Modulus and Yield Stress 148

5.0 DISCUSSION 150

5.1 Influence of Precipitation on Hot Ductility 151

5.1.1 Influence of Precipitate Size on Reduction of Area (RA) 151

5.1.2 Influence of Volume Fraction of Precipitation 153

5.1.3 Influence of Location of Precipitation 153

5.2 Influence of Alloying Additions 154

5.2.1 Base Composition- C-Mn-Al 155

5.2.2 Influence of Niobium (Nb) 158

5.2.3 Influence of Titanium (Ti) 161

5.2.3.1 Influence of Dynamic Recrystallisation on the Ti Steel Under Solution Treatment Conditions 162

5.2.4 Influence of Niobium-Titanium (Nb-Ti) 166

5.2.5 Comparisons of Hot Ductility Under Solution Treatment Conditions 167

5.2.6 Comparisons of Hot Ductility Under Direct Cast Conditions (as-cast) 168

5.3 Influence of Cooling Rate 170

5.3.1 C-Mn-Al 170

5.3.2 C-Mn-Al-Nb 173

5.3.3 C-Mn-Al-Ti 173

5.3.4 C-Mn-Al-Nb-Ti 174

5.4 Influence of Temperature 177

5.4.1 Influence of Cyclic Thermal Oscillations on Hot Ductility of Nb-Ti Steels 179

5.5 Limitations of Solution Treatment and Direct Cast Laboratory Hot Tensile Tests 182

5.5.1 Influence of Segregation and Homogenisation Time 184

6.0 CONCLUSIONS 186

6.1 Recommendations and Suggestions for Future Work 189

6.2 Publications 191

7.0 REFERENCES 192

APPENDIX A: INTERPRETING ABNORMAL DATA POINTS AND EXPERIMENTAL SCATTER 206

APPENDIX B: HISTOGRAMS- PARTICLE SIZE DISTRIBUTION 210

List of Figures

Figure 1.1: Comparison of the layout for conventional and thin slab, direct rolling processing routes. 2

Figure 1.2: Thermal histories of conventional (thick) and thin cast slabs during casting. 6

Figure 1.3: Comparison of SDAS for conventional, 230mm thick slab and thin slab, 50mm thick [2]. 7

Figure 1.4: Infinitely variable segment adjustment via position-controlled hydraulic cylinders for LCR at Thyssen Krupp Stahl. 8

Figure 1.5: Nucor's initial CSP plant layout. 13

Figure 1.6: Layout of CSP plant with twin strand casting at Thyssen Krupp Stahl's integrated works at Duisburg. 15

Figure 1.7: Layout of the ISP plant in Arvedi, Cermona. 15

Figure 1.8: Basic layout of the Tippins-Samsung Process (TSP). 18

Figure 1.9: Process configuration of Trico's medium thickness slab caster and compact hot strip mill. 21

Figure 2.1: Schematic diagram of a typical continuous casting machine and its inherent stresses [47]. 24

Figure 2.2: Three main mechanisms for the formation of oscillation marks, A) Overflow, B) Overfow and remelting and C) Meniscus bent back.. 26

Figure 2.3: Effect of heal time on oscillation mark depth. 28

Figure 2.4: The formation of thin sections in the shell wall in the mould for a) fine grain and b) Coarse grain steel. 30

Figure 2.5: Effect of carbon content on the depth of oscillation marks. 31

Figure 2.6: Schematic diagram showing the three characteristic ductility regions on a hot ductility curve. Reproduced from Ref [47]. 34

Figure 2.7: Intergranular thin films of ferrite formed in C-Mn-Al-Nb steel when tensile tested at 800°C. Note the intergranular cracking along the ferrite films. 35

Figure 2.8: Intergranular microvoid coalescence of low alloy steels by deformation in low temperature γ region a-c, and α/γ duplex phase region, d-f. Where; a, d dynamic precipitation and strain concentration

within soft layers along γ grain boundaries in initial stages of deformation; b, e microvoid formation by decohesion of precipitate/matrix interfaces; c, f coalescence of microvoids, resulting in ductile intergranular fracture of austenite. 36

Figure 2.9: Schematic models showing three scenarios that can lead to the formation of wedge cracks by grain boundary sliding; arrows indicate sliding boundary and sense of translation. 38

Figure 2.10: Hot ductility curves for 0.65%C steel showing effect of grain size. 40

Figure 2.11: Influence of particle size on reduction of area values for Nb, Ti and Nb-Ti steels in single-phase austenite (reproduced from Comineli [73]). 41

Figure 2.12: Change of activation energy for dynamic recrystallisation with carbon content, reproduced from Crowther et al. [75]. 43

Figure 2.13: Effect of sulphur content on the minimum reduction of area for two cooling rates of 1°C/s and 4°C/s. 44

Figure 2.14: Hot ductility curves for high and low S, C-Mn-Al steels. The solution treatment temperature was 1430°C. 46

Figure 2.15: The precipitation-time-temperature (PTT) diagram for undeformed austenite (static precipitation), 5% pre-strain and dynamic precipitation for 0.05%C, 0.035% Nb steel. 49

Figure 2.16: Representative diagram depicting the general thermal histories simulated in references [61, 62, 103, 104]. 61

Figure 2.17: Schematic diagrams showing (a) how the width of the ductility trough could be controlled by dynamic recrystallisation (DRX) and (b) how increasing the strain rate can reduce the depth and width of the trough. 64

Figure 3.1: Position of steel block samples taken from 230mm as-cast slab, prior to hot rolling. 68

Figure 3.2: Specimen set-up for tensile testing in the Gleeble machine. 70

Figure 3.3: Schematic representation of placement of thermocouples on tensile specimens. 71

Figure 3.4: Schematic diagram showing two cycles employed during the tensile tests (a) Solution treatment and (b) Direct casting. 72

Figure 3.5: Schematic diagram showing the thermal cycle used to simulate the thermal pattern experienced near the surface a thin slab during continuous casting, where Cycle 1 had an average cooling rate of 200K/min with oscillations of ±50°C, Cycle 2 had an average cooling rate of 200K/min with oscillations of ±100°C and Cycle 3 had an average cooling rate of 100K/min with oscillations of ±50°C 75

Figure 3.6: Plant data (F.E.M) of temperature profiles for a continuously cast slab, taken from the NS/BHP medium thickness caster. Slab dimensions were 90mm x 950mm and caster speed was 5.0M/min. 76

Figure 3.6: Temperature profile of surface and centre temperature measurements without Nextel sleeving. 79

Figure 3.7: Temperature profile of surface and centre temperature measurements with Nextel sleeving. 80

Figure 3.8: Thermo-cycle used to find $\gamma \rightarrow \alpha$ and $\alpha \rightarrow \gamma$ transformation temperatures by dilatometry. 87

Figure 4.1: Hot ductility curves generated for C-Mn-Al steel from solution treatment (Sol) and direct cast (Melt) conditions at cooling rates of 100K/min and 200K/min. 91

Figure 4.2: Hot ductility curves generated from the Nb steel for solution treatment (Sol) and direct cast (Melt) conditions at cooling rates of 100K/min and 200K/min. 92

Figure 4.3: Hot ductility curves generated from the Ti Steel for solution treatment (Sol) and direct cast (Melt) conditions at cooling rates of 100K/min and 200K/min. 93

Figure 4.4: Hot ductility curves generated from the Nb-Ti Steel for solution treatment (Sol) and direct cast (Melt) conditions at cooling rates of 100K/min and 200K/min. Included in Fig 4.4 are the RA points for the three cyclic thermal patterns, Cycles 1-3, generated at 900°C for the Nb-Ti Steel. 94

Figure 4.5: Comparison of reduction of area (RA) values at 900°C for different test conditions for the Nb-Ti steel 96

Figure 4.6: Hot ductility curves for solution treatment conditions for all four steels at cooling rates of 100K/min and 200K/min. 97

Figure 4.7: Hot ductility curves for direct cast conditions for all four steels at cooling rates of 100K/min and 200K/min. 98
Figure 4.8: Stress-strain curves as a function of temperature for the Ti steel at 100K/min under solution treatment conditions. 99
Figure 4.9: Stress-strain curves as a function of temperature for the Ti steel at 100K/min under direct cast conditions. 99
Figure 4.10: Stress-strain curves at 1000°C for indicated composition under solution treatment conditions and direct cast conditions. 101
Figure 4.12: Dendritic pattern after normalising where a) solution treatment conditions (Nb Steel), b) direct cast conditions (Nb-Ti Steel) and c) transition zone at edge of hot zone (Nb-Ti Steel). 104
Figure 4.13: Representative microstructures of fracture surfaces a) predominately ferrite (700°C), b-c) intergranular cracking along ferrite films at 750°C and 800°C, 107
Figure 4.13: (cont.) d) 850°C, showing ferrite films, e) 850°C, no ferrite films, f) Intergranular cracking in martensite (transformed from parent austenite) at 900°C 108
Figure 4.13: (Cont.) Intergranular cracking in martensite (transformed from parent Austenite) at (g) 950°C and (h) 1000°C, i) Voiding in martensite (transformed from parent austenite) at 1000°C. 109
Figure 4.14: Typical fracture surface, in the longitudinal direction, displaying sharp intergranular cracks, region A and large open cracks, region B. 111
Figure 4.15: Representative SEM photos of the fracture surface, where; a) Intergranular with ductile voiding at 700°C (Nb-Ti Sol), b) Intergranular failure via microvoid coalescence 750°C (Ti Melt), c) Higher mag of (b). 113
Figure 4.15: (Cont.) d-e) Intergranular failure via decohesion 800°C (Nb Melt), f) Mixed mode- intergranular failure and ductile voiding 900°C (Nb-Ti Melt). 114
Figure 4.15: (Cont.) g) Mixed failure mode where ductile mode is predominant 900°C (Ti Sol) and h) High temperature, high ductile fracture displaying deep voids 900°C (Al Sol). 115

Figure 4.16: SEM image of fracture surfaces for a) Nb-Ti direct cast conditions at 900°C and b) Nb-Ti direct cast- cyclic temperature oscillation test at 900°C 117

Figure 4.17: Typical morphology of rectangular precipitates (note rounding of corners) found under solution treatment conditions at temperatures 950°C and above, for Ti steel. 121

Figure 4.18: Typical morphology of fine circular precipitates found at 900°C and 850°C under solution treatment conditions for Ti steel, photo taken at 900°C at cooling rate of 200K/min. 121

Figure 4.19: Typical morphology of Fine TiN precipitates found under direct cast conditions, for Ti steel at 900°C. Precipitate size <30nm. 123

Figure 4.20: Typical morphology of fine circular Nb precipitates found at 850°C under direct cast conditions, for Ti steel. Precipitate size <15nm. 123

Figure 4.21: Typical morphology of fine Nb precipitates, formed in a row, taken at 900°C under direct cast conditions for Nb steel. 126

Figure 4.22: Typical morphology of rectangular and circular precipitates found under solution treatment conditions, taken at temperature 1000°C for Nb-Ti steel. 129

Figure 4.23: Typical morphology of star shaped (crucifix) precipitates found at 1000°C under solution treatment conditions for Nb-Ti Steel. 129

Figure 4.24: Typical morphology of fine precipitates found between 950°C and 850°C under solution treatment conditions, Nb-Ti Steel. (Photo taken at 950°C) 130

Figure 4.25: Typical morphology of fine precipitates found between 950°C and 850°C under direct cast conditions, Nb-Ti Steel. (Photo taken at 900°C) 130

Figure 4.26: Precipitate displaying caps (possibly higher in Nb than the core) on each corner of a larger rectangular precipitate, taken at 850°C under solution treatment conditions, Nb-Ti Steel. 131

Figure 4.27: Histograms displaying the number of particles per unit area as a function of size distribution for Nb-Ti, direct cast conditions (900°C), where a) 100K/min and b) 200K/min. 136

Figure 4.28: Histograms displaying the number of particles per unit area as a function of size distribution for Nb-Ti, thermal temperature oscillations, where a) cycle 1, b) cycle 2 and c) cylce 3. 137

Figure 4.29: Histograms displaying the number of particles per unit area as a function of size distribution for Nb-Ti, thermal temperature oscillations, where a) quenched at 900°C (T_{min}) and b) quenched at 1100°C (T_{max}). 139

Figure 4.30: Histograms displaying the number of particles per unit area as a function of size distribution for Nb-Ti, solution treatment conditions 100K/min, where a) 950°C, b) 900°C and c) 850°C. 141

Figure 4.31: Histograms displaying the number of particles per unit area as a function of size distribution for Nb-Ti, solution treatment conditions 200K/min, where a) 950°C, b) 900°C and c) 850°C. 143

Figure 4.32: Reduction of area (RA) as a function of average particle size (nm) for precipitates in Nb and Nb-Ti specimens in the single-phase austenite region for direct cast specimens. Included in the figure is the influence of precipitation in the two-phase region, 750-800°C, on RA. 145

Figure 4.33: Reduction of area as a function of interparticle spacing (1/IP) for the Nb-Ti steel, under direct cast conditions. 146

Figure 4.34: Yield stress as a function of test temperature for the Nb-Ti steel for all thermomechanical conditions. 149

Figure 5.1: Reduction of area as a function of average particle size (nm) for precipitation (at a test temperature of ≥ 850°C) in Nb and Nb-Ti specimens. 151

Figure 5.2: Precipitation arranged in a row, probably indicating the former position of an austenite grain boundary. (Nb-Ti steel, direct cast 975°C, 200K/min). 154

Figure 5.2: Differences in the stress-strain curves between solution treatment and direct cast conditions for C-Mn-Al specimens at 700, 800 and 900ºC, where the arrows indicate the differences in stress of the curves at the same temperature. 157

Figure 5.3: Stress-strain curves for Ti specimens under solution treatment conditions at 900°C, where two curves, corresponding to specimens with high ductility, displayed evidence of dynamic recrystallisation (marked with arrows). 163

Figure 5.4a: Grain delineation at the edge of the 'hot zone' in a Ti specimen tested at 900°C, 100K/min, with low hot ductility. Note the large grain size. 164

Figure 5.4b: Grain delineation at the edge of the 'hot zone' in a Ti specimen tested at 900°C, 100K/min, with high hot ductility. Note the fine grain size. 164

Figure 5.5: Interparticle spacing as a function of temperature with the corresponding RA values plotted on the secondary Y-axis. Values were obtained from the Nb-Ti steel under direct casting conditions. 167

Figure 5.5a: Microvoid coalescence, typical of a C-Mn-Al specimen tested at 850°C at 200K/min (100x). 172

Figure 5.5b: Discrete voids, typical of a C-Mn-Al specimen tested at 850°C at 100K/min (50x). 172

Figure 5.6: Stress-strain curves for the Nb-Ti steel showing the changes in the stress-strain behaviour between 100K/min and 200K/min at 800°C, 900°C and 1000°C. 174

Figure 5.7: Interparticle spacing as a function of temperature for the cooling rates of 100K/min and 200K/min for the Nb-Ti steel under solution treatment conditions. 176

Figure 5.8: Typical example of clustering seen in Nb-Ti specimens (900°C) tested under solution treatment conditions, 200K/min. 176

Figure A: Hot ductility curves for the Nb-Ti steel showing experimental scatter and two abnormal data points. 206

Figure B: Stress-strain curves for 1000°C and 985°C, Nb-Ti steel 200K/min direct cast conditions, for normal and abnormal tensile tests. 207

List of Tables

Table 3.1: Chemical compositions of alloys. 69

Table 3.2: Transformation temperatures calculated from the chemistry of the respective steels. 73

Table 4.1: Summary of the hot ductility data taken from the reduction in area as a function of temperature curves 95

Table 4.2: Average austenite grain size measured as equivalent diameter. 102

Table 4.3: Measured and calculated Secondary Dendrite Arm Spacings (SDAS) 105

Table 4.4: Diffusion data for solutes in austenite, the diffusion coefficients of these elements at 1330°C in austenite and the homogenisation times. 105

Table 4.5: Summary of the mean particle size and particle number density of selected steels and thermomechanical treatments. 119

Table 4.7.2a: TEM results, C-Mn-Al-Ti 100K/min- Solution Treatment 122

Table 4.7.2b: TEM results, C-Mn-Al-Ti 200K/min- Solution Treatment 122

Table 4.7.2c: TEM results, C-Mn-Al-Ti 100K/min- Direct Cast 124

Table 4.7.2d: TEM results, C-Mn-Al-Ti 200K/min- Direct Cast 124

Table 4.7.3a: Nb Steel 100K/min- Direct cast 127

Table 4.7.3b: Nb Steel 200K/min- Direct cast 127

Table 4.7.4a: Nb-Ti 100K/min- Solution Treatment 132

Table 4.7.4b: Nb-Ti 200K/min- Solution Treatment 132

Table 4.7.4c: Nb-Ti 100K/min- Direct cast 133

Table 4.7.4d: Nb-Ti 200K/min- Direct Cast 134

Table 4.7: Interparticle spacing for the microalloyed steels at 900°C and 950°C, for direct cast conditions. 146

Table 4.8: Summary of Transformation Temperatures. 147

Table 4.9: Young's modulus values for all steels determined theoretically. 148

Synopsis

Experiments were performed on a Gleeble 3500 Thermomechanical Simulator to study the hot ductility behaviour of C-Mn-Al steel and the influence of Nb, Ti and Nb-Ti additions. The simple hot tensile test has been shown to correlate well to the problem of transverse cracking. Therefore, the principle aim of this research is to gain a greater understanding of transverse cracking during the straightening of continuously cast slabs. In particular, attention was paid to thin slab casting conditions.

Hot tensile test specimens were either solution treated or melted *in-situ* (direct cast) and cooled to the deformation temperature. Solution treatment tests simulated conventional casting, where slabs are cooled to room temperature then reheated prior to rolling. Direct cast tests simulated hot direct rolling conditions, where slabs are rolled directly after casting without being cooled below the austenite to ferrite transformation. Specimens were cooled to the deformation temperature at two cooling rates, 100K/min and 200K/min. The cooling rate of 100K/min corresponds to the average cooling rate experienced for a conventionally cast slab, 250mm in thickness. The cooling rate of 200K/min corresponds to the average cooling rate for thin-cast slabs, 50mm in thickness.

The development of the combination of thin slab casting with hot direct rolling requires hot ductility work to be performed under direct cast conditions and at higher cooling rates. Surface quality is of the utmost importance in thin slab casting so the elimination of transverse cracking is of prime economic importance. There are significant differences between as-cast (direct cast) and reheated (solution treatment) microstructures. In particular, changes in precipitate behaviour, austenite grain size, and the relationship between segregation and the position of austenite grain boundaries was investigated. An attempt has been made to determine what influence these differences in microstructure have on hot ductility.

Niobium bearing steels were selected for the reason that there are still problems with Nb steels regarding transverse cracking. Furthermore, there have been contradictory reports on the effects of Ti additions on the transverse cracking behaviour of Nb steels. There is

evidence from commercial practice that indicates that small additions of Ti improve the transverse cracking susceptibility of Nb steels. However, laboratory results generally show Ti additions have little influence or even a detrimental effect on hot ductility. Disparities in the thermal history simulated in laboratory tests to actual conditions near the surface of a continuously cast slab is the most likely reason for this discrepancy. Therefore, the influence of more closely simulating the thermal history conditions near the surface of a continuously cast slab was evaluated for the Nb-Ti steel.

Experimental work involved metallographic and scanning electron microscopy examination of the fracture surface. Transmission electron microscopy was used to determine precipitation characteristics. Tensile tests were conducted to determine mechanical properties, where reduction in area (RA) was used as a measure of ductility. The dendritic structure for direct cast and solution treatment specimens was revealed using a heat treatment procedure (normalising). Particle size was correlated to reduction of area for precipitates in the single-phase austenite temperature region. It was shown that particles below 15nm were detrimental to hot ductility. The relationship between interparticle spacing and reduction of area was also determined.

Microalloying additions to C-Mn-Al steels significantly widen the ductility trough but the depth remains similar. Low ductility was found at higher temperatures in the microalloyed steels due to intergranular failure as a result of grain boundary sliding in the austenite. Grain boundary sliding was favoured by the slow strain rate and was enhanced by fine microalloyed nitrides and/or carbides. Fine particles can pin austenite grain boundaries, allowing sufficient time for cracks to link together, ultimately causing intergranular fracture. Increasing the cooling rate generally lowered ductility further by promoting finer precipitation. The trough depth is similar in all steels as the formation of thin ferrite films controls ductility at the minimum trough position. The formation of thin films of ferrite allowed strain to concentrate in the softer ferrite phase and intergranular failure occurred due to microvoid coalescence.

Direct cast conditions always led to lower ductility compared to solution treatment conditions. This is explained in terms of differences in the microstructure, namely, grain size, segregation and precipitation. It is recommended that direct cast conditions should

be used to determine hot ductility behaviour as it more accurately simulates continuous casting conditions.

It was found that simulating the thermal history near the surface of a continuously cast slab, as opposed to cooling directly to the deformation temperature, improved ductility of the Nb-Ti steel. This improvement in ductility was attributed to the thermal history providing favourable conditions for coarsening of NbTi(C,N).

Acknowledgements

The research work reported in this thesis was carried out under the supervision of Professor Brendon Parker and Mr Chris Killmore, who was the associate supervisor. I express my appreciation for their guidance, encouragement and constant support during the course of this work.

I acknowledge the support of Professor Rian Dippanaar who assisted with supervision of my work during 2002-03 when Professor Parker relocated to the University of New South Wales in January 2002.

I thank Mr. Chris Killmore, Mr. Paul Kelly and Mr. Les Moore (BHP, Central Research Laboratories, Product Development Group) for their guidance. Their assistance in interpreting the data was of great help and their input in to the experimental program retained the projects industrial relevance. I also acknowledge Mr. Stuart Laird (BHP, Central Research Laboratories, Product Development Group) for his assistance in providing me with steel slab samples

I express my gratitude to the Australian Research Council and BHP Steel, Port Kembla for providing financial support. I also thank BHP Steel for providing me with the steel and the analysis of the chemical composition.

I thank Mr. Greg Tillman for his assistance in metallographic preparation and optical microscopy, Mr. Nick Mackie for his help in electron microscopy, Mr. Bob DeJong and Dr. Priya Manohar for their help with the Gleeble 3500 Thermomechanical simulator and their assistance in developing the experimental program. I also thank Dr. Priya Manohar for his help in reviewing my work. I thank Professor Paul Munroe (University of NSW, Australia) for his assistance in electron microscopy at the University of New South Wales.

Finally, I thank my parents, Mr. Trevor Carpenter and Mrs. Susan Carpenter for their loving support and encouragement during the progression of my thesis.

Chapter 1:

Literature Review: Thin Slab Casting Technology

Chapter 1: Literature review: Thin Slab Casting Technology

1.1 Introduction: Thin Slab Casting Technology

Thin Slab Casting (TSC) technology was first introduced in 1986 when Nucor Steel developed the "Compact Strip Production" (CSP) process. Nucor's first CSP plant was commissioned in Crawfordsville, Indiana, USA, 1989 [1]. The new CSP technology featured casting of 50mm thick slabs, considerably thinner than conventional Cold Cast Rolled (CCR) slab, typically 200-250mm in thickness. The concept of the CSP mini-mill was to enable the casting of near-net-shape thin slabs that could be Hot Direct Rolled (HDR) into finished strip in a single step.

The total length of the Nucor plant was approximately 260m, hence the name, 'Compact strip production'. In comparison, a conventional plant can be over 900m in length or for a conventional production line, which incorporates direct or hot charging, around 500m in length. Figure 1.1 compares the plant layout for conventional thick slab casting (CCR) to thin slab casting (TSC) with hot direct rolling (HDR) [2]. This compact design allows for comparatively small mini-mills to be developed at a much lower capital cost.

Since the establishment of CSP technology, many new designs of TSC units have been developed. The most widely incorporated TSC units include, In-line Strip Production (ISP), Tippins-Samsung Process (TSP), Conroll, Quality Strip Production (QSP) and the Danieli thin slab caster. All processes mentioned above are discussed further in following sections. Several of these "thin slab" caster designs have diverged away from the 50mm slab thickness set by Nucor steel and have produced slabs in the 70-125mm thickness range. This led to a new classification for thin slab casters termed 'intermediate' or 'medium' thickness slab casters.

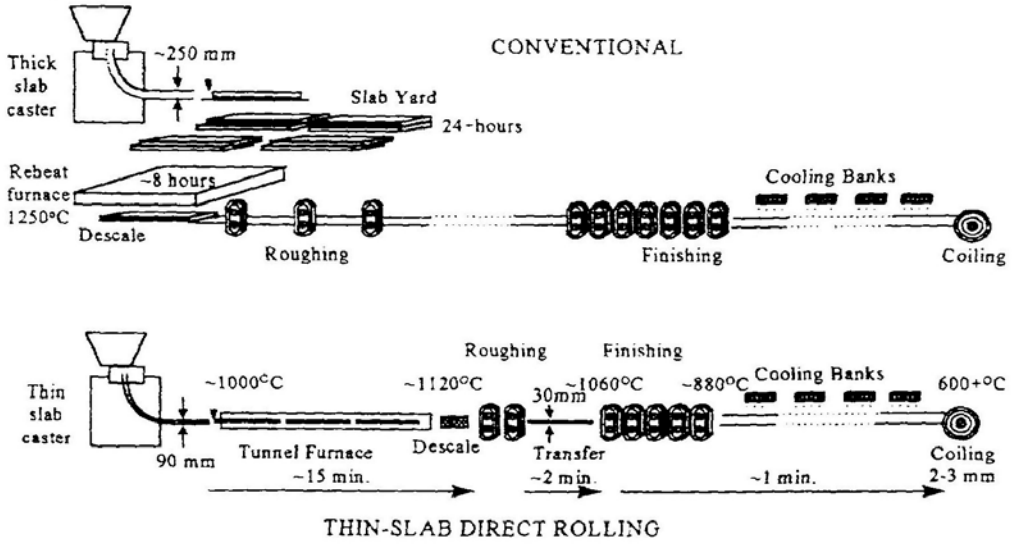

Figure 1.1: Comparison of the layout for conventional and thin slab, direct rolling processing routes.

1.2 Benefits of Thin Slab Casting

The development of TSC technology has lead to a boom in the number of Mini-mills featuring TSC. The economic advantages of TSC mini-mills make them considerably more attractive to build than large, capital intensive, integrated conventional steelworks. Conventional fully integrated steel plants need to produce at least 4-5 million tones per annum to be cost competitive [4]. This requires both a large capital investment and major entry in to the market place, while a TSC based plant allows a less intensive entrance to the market place, with considerably less risk. The continued improvement of casting, rolling technology and quality control has enabled the production of an increasingly wider range of final products with mechanical properties as good as, if not better, than most conventionally rolled products. Economical and environmental advantages of TSC over CCR are listed below.

Economic advantages:

- Lower capital costs,
    - Short length, less height and less space required for casting and rolling equipment,

    - Thin-slab rolling mills generally have lower capital costs, especially if the roughing stage is eliminated [3].

- Energy savings,
    - No re-heating stage and shorter production times,

- Thin slab casters can be economically viable at relatively low capacities, 0.5-2 Mt/year, compared to integrated works that must operate above 2 Mt/year [4], where 4-5 Mt/year is preferable,

- Faster and more flexible than CCR, therefore product changes are easier and quicker for TSC.

Environmental advantages:

- TSC is often supplied by electric arc furnace steel that has the environmental advantages of using scrap as a major raw material,

- CCR integrated plants rely on ore and coal, thus, have great difficulty satisfying environmental regulations [4],

- Reduced energy consumption [3].

One of the most striking advantages of TSC combined with hot direct rolling (HDR) is its speed and flexibility. Hot direct rolling is the process of rolling a cast slab with out allowing the slab to cool below the austenite to ferrite transformation temperature. Coiled products can be removed from the mill within 20 minutes of the slab leaving the caster [1], [2], [5]. For CCR, slabs can be held for more than 24 hours before being reheated and reheating itself takes around 8 hours. It is clear that TSC mini-mills can produce a finished produce in considerable less time then that for CCR plants. The flexibility of TSC based steel mills is an advantage for meeting the demand of customers. Demand for small batches of high-grade steel at competitive prices, variable specifications and short delivery times are difficult to meet for conventional integrated

steelworks. Thin slab based mini-mills have the flexibility to meet these demands economically [4].

1.3 Metallurgical Considerations of Thin Slab Casting

There are many metallurgical differences between TSC and CCR that can have a profound effect on the mechanical properties and quality of the final product. Understanding the metallurgical aspects of TSC with HDR is a vital step towards improving the production and processing technology involved with TSC and thus, improving the quality and mechanical properties of the final product. The following section will deal with the metallurgical aspects of TSC from the supply of liquid steel to the coiling of the final product.

1.3.1 Liquid Steel Quality

The majority of TSC plants are supplied liquid steel via an electric arc furnace. Steel from an electric arc furnace is regarded as having high N contents and high levels of residual (tramp) elements, such as Cu, Sn, Sb, Ni, Cr [4], [6-8]. Concentrations of residual elements can be minimised by careful scrap selection and diluting the amount of scrap by charging pre-reduced iron. High levels of residual elements, particularly Cu and Sn, can lead to intergranular cracking problems, hot shortness and slab quality problems. Nitrogen adversely affects formability, especially in plain-C steels [8], reduces toughness and has been linked to slab cracking. High N levels are normally regarded as a disadvantage in steelmaking but can have some advantages if N is carefully utilised in some high strength steels (i.e. HSLA) through precipitation strengthening by nitrides and carbonitrides [4, 6-8]. High N promotes the formation of microalloying nitrides rather than carbides, which is favourable in vanadium microalloyed steels. Alloying costs may be reduced by taking advantage of high N levels by alloying strong nitride-formers, such as titanium and vanadium, to strengthen the steel by precipitation strengthening and allowing a leaner composition with out compromising strength.

Steel cleanliness and liquid steel temperature play an important role in casting high quality slabs. In CCR, liquid steel temperature has a profound influence on the cast structure, formation of internal cracks, severity of centre-line segregation and central porosity. High liquid steel temperatures promote columnar structures, as opposed to equiaxed, which leads to poor internal quality [9]. For TSC, due to the thickness of the slab and relatively rapid solidification, these problems are largely avoided. However, the liquid steel temperature is still important in TSC as it can cause the mould flux to melt leading to problems such as excessive roping, bridging between the mould wall and the SEN (Submerged entry nozzle) and sticking to the mould wall [9]. These problems are more difficult to control due to the small mould cavity. A small mould cavity and tundish results in short residence times so turbulence must be minimised to achieve required quality. Turbulence reduces steel quality by entraining slag residuals into the melt [8, 9].

The cleanliness of the steel (degree of solid inclusions) affects the SEN and may cause liquid steel flow problems (clogging). Submerged entry nozzles for TSC have very small diameters and in order to avoid problems with SEN clogging specialised deoxidisation practices are required [4, 9].

1.3.2 Caster Design

Thin slab production demands that the caster operates under strict control because high quality slabs are essential for HDR. A narrower mould then for conventional casters magnifies any casting problems and there is a need for strict control of casting parameters. The design of a thin slab caster must allow for the following [3]:

- Reliable control of casting speeds in excess of 3m/min, variable casting speeds and sequence casting,

- Excellent control of the liquid steel supply into a narrow mould,

- High surface and internal quality of thin-cast slabs is critical as the slabs are directly hot rolled, not allowing any remedial scarfing,

- Uniform temperature distribution over the cross-section of the slab before and after the re-heating/soaking furnace.

1.3.3 Metallurgical Aspects

A profound difference between TSC and CCR is the rapid solidification of thin cast slabs. The time for solidification of a conventional, 250mm thick, slab is approximately 22.5 minutes, for a thin slab of 80mm thickness it takes 2.5 minutes and for 50mm thick slabs, 1.5 minutes [2, 10]. This difference in solidification behaviour is illustrated in Figure 1.2 [2]. Faster solidification promotes a finer, more uniform structure due to a higher number of solidification nuclei in an under-cooled melt [3, 11, 12].

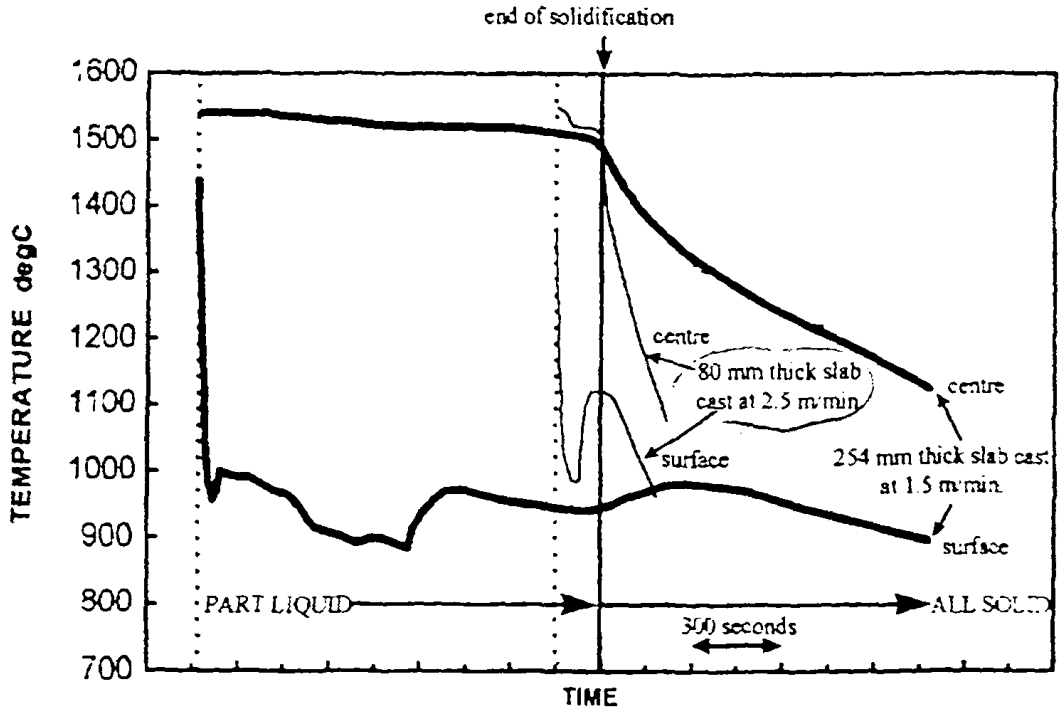

Figure 1.2: Thermal histories of conventional (thick) and thin cast slabs during casting.

Fine secondary dendrite arm spacing (SDAS), achieved due to rapid solidification in TSC, promotes a more homogeneous structure with less microsegregation than for

conventional slabs. Microsegregation is segregation between dendrite arms where the minimum solute concentration is at the centre of the dendrite arm and the maximum solute concentration is between the arms. In this respect, SDAS is a measure of heterogeneity in continuously cast slabs [2, 11]. A comparison of SDAS in conventional and TSC is shown in Figure 1.3 [2].

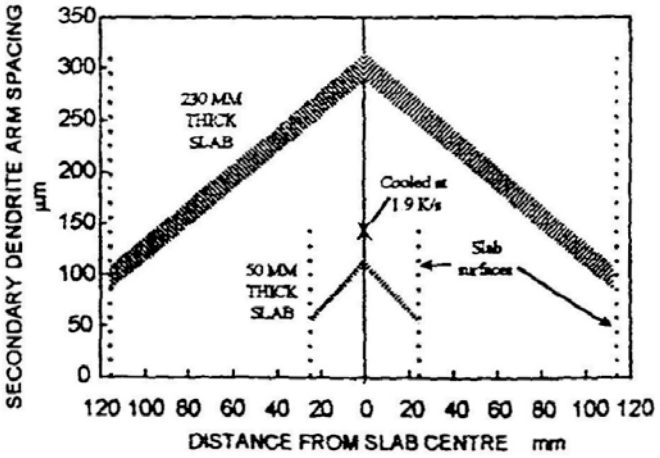

Figure 1.3: Comparison of SDAS for conventional, 230mm thick slab and thin slab, 50mm thick [2].

The absence of the re-heating stage, for HDR, removes the beneficial effects of the grain refining $\gamma \rightarrow \alpha$ and $\alpha \rightarrow \gamma$ transformations. The re-heated structure of CCR steel is quite different from the as-cast structure from thin cast steels. The typical austenite grain size after re-heating is in the range of 200µm, while the as-cast austenite grain size from thin cast slabs is 600µm to over 1000µm. This large as-cast austenite grain size leads to complications during rolling, as it is difficult to achieve fine, uniform final microstructures when the starting microstructure is large. Thus, a new approach to microstructural design must be developed to obtain the required final grain size and properties. This will be discussed in more detail in Section 1.4: “Rolling aspects of thin slab casting”.

1.3.4 Thin Slab Casting with Liquid Core Reduction (LCR)

A growing trend for thin slab casters is the utilisation of liquid core reduction (LCR), or soft reduction, technology. Liquid core reduction allows for the thickness of the strand below the mould to be reduced while the core is still in a liquid state. Usually, the first segment in the strand guidance system can be adjusted to obtain the desired reduction in thickness of the strand. Plant manufacturer SMS Schloemann-Siemag AG has developed two alternative designs for the use of liquid core reduction. In the first alternative, strand thickness is adjusted via hydraulic cylinders and stops. The second alternative utilises a more complex position-controlled hydraulic cylinder system that allows infinitely variable adjustment to the strand thickness [13]. Figure 1.4 displays an infinitely variable segment adjustment unit for LCR via position-controlled hydraulic cylinders at Thyssen Krupp Stahl [13]. Plant maker Danieli's LCR (soft-core reduction) system also allows the strand thickness to be adjusted at any time [14, 15].

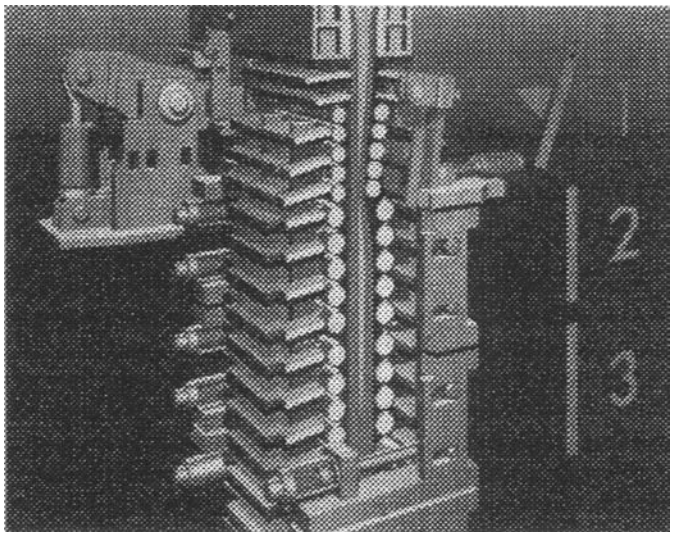

Figure 1.4: Infinitely variable segment adjustment via position-controlled hydraulic cylinders for LCR at Thyssen Krupp Stahl.

Liquid core reduction allows greater flexibility through tailoring the cast thickness to the required rolling thickness [13, 15]. Thin strip is more easily achieved when a thinner slab is cast because there is less reduction required. Liquid core reduction is believed to improve both the surface quality and internal quality of the strand [13-19].

Improvements in surface quality and internal quality are largely due to the greater mould dimensions (greater initial slab thickness) that can be used when using LCR.

Increased mould dimensions improve surface and internal quality due to; greater stability at the meniscus, less turbulence, longer mould lengths and lower flow velocities [14, 20]. Reduction during solidification improves the internal quality by promoting a finer solidification structure, a reduction in centreline porosity and segregation, breakage of columnar structures (for more favourable equiaxed structures) and finer grain dimensions [13, 14, 16-18]. The shorter solidification time for slabs subjected to LCR reduces the time available for precipitation elements to concentrate at the centre of the slab [13].

Essadiqi et al. [21] studied the metallurgical effects of LCR on simulated thin-cast 1020-carbon steel. Mean values of SDAS in the columnar zone of a 50mm thick plate with no reduction and a 50mm plate with 44% reduction were both found to vary between 50 to 150μm. Essadiqi et al. noted that the measurements suggested a slight refinement in SDAS may have occurred during reduction but due to the scatter of the results no firm conclusions could be drawn. The prior austenite structure for the through-thickness of as-cast slabs with LCR was also studied. It was found that LCR significantly refined the columnar zone but there was only a small improvement in the equiaxed grain size. The prior austenite grain size of the equiaxed zone was found to depend mainly on the final thickness of the slab and therefore on the reduction ratio [21]. The effects of LCR on segregation were not determined.

Yamanaka et al. [22] investigated the possibility of the formation of internal cracking due to LCR. A reduction of 40mm on a medium carbon steel of initial thickness 100mm and a reduction of 25mm on a high carbon steel of initial thickness 90mm yielded no evidence of internal cracking. Yamanaka et al. [22] also found that the slab must be reduced while the centre is still liquid in order to achieve the target reduction. Otherwise, an excessive force will be required for reduction if applied after complete solidification.

1.4 Rolling Aspects of Thin Slab Casting

1.4.1 Tunnel/Holding Furnace

The function of the tunnel furnace is to homogenise, or equalise, the slab temperature and heat the slab to the correct rolling temperature. Equalising the slab temperature before rolling is vital to ensure consistent rolling properties. The uniform slab temperature will be maintained down to finishing and coiling and is necessary to achieve consistent shape, gauge, microstructure and mechanical properties [8]. Scale formation in the tunnel furnace must be minimised by controlling the furnace temperature and atmosphere to avoid excessive yield losses via scaling [8, 23].

The short residence time in the tunnel furnace, 15-20 minutes, limits grain growth, dissolution of precipitates and scale formation. During conventional re-heating, the slab is soaked at ~1250°C for 2-3 hours, allowing time for extensive grain growth, dissolution of precipitates and a thick scale jacket to form. An advantage of the thick scale jacket however, is the removal of surface defects with the removal of the surface layer (scale jacket) [7]. Thin slabs do not have this advantage, surface defects must be carefully controlled and minimised to ensure that the cast slab is suitable for direct rolling. Some steel grades, such as peritectic carbon grades and Nb bearing steels, are prone to the formation of surface defects and this limits their production by the thin slab casting route. The reasons why peritectic grades and Nb bearing steels are difficult to cast, with respect to transverse cracking susceptibility, will be discussed in Chapter 2: Hot Ductility.

1.4.2 Metallurgical Considerations During Rolling of Thin Cast Slabs

Processing parameters during rolling are affected by the coarse, as-cast austenite grain size, the limited value of total strain available (limited reduction) and the behaviour of microalloying additions. The coarse, as-cast austenite grain size retards recrystallisation and increases the ‘recrystallisation stop temperature’ (Trs). The ‘recrystallisation stop

temperature' is the temperature below which austenite remains unrecrystallised after deformation. The 'recrystallisation stop temperature' (T_{rs}) is also referred to as the 'non-recrystallisation temperature', (T_{nr}). High T_{rs} may lead to partial recrystallisation in the second and even the first pass of the rolling schedule due to the T_{rs} being higher than the rolling temperature. Partial recrystallisation increases the heterogeneity of the mechanical properties due to the formation of a mixed grain size.

To achieve complete recrystallisation of coarse, as-cast austenite, heavy reduction (>50%) per rolling pass is required. The reductions in thin slab rolling mills can be twice [8] or even 2.5 [6] times greater than the reduction per pass in a conventional rolling mill. Consequently, it is possible to achieve fine uniform grain size comparable to conventionally rolled products. Unfortunately, heavy reduction has the disadvantage of higher roll wear [6, 8, 10, 23]. Thin slab rolling mills are characterised by slower rolling speeds, 0.25-0.6m/s, than for conventional mills, 0.8-1.6m/s. High reduction coupled with slower strain rates encourages dynamic recrystallisation during thin slab rolling [7]. In conventional mills, moderate reductions and high strain rates encourage static recrystallisation [7]. The occurrence of dynamic recrystallisation is however offset by the coarse initial grain size and may be suppressed.

Changes in behaviour of microalloying additions between as-cast and re-heated structures must also be taken into consideration when designing rolling schedules. In order to maintain a reasonable austenite grain size during re-heating (in CCR), the re-heating temperature is limited to 1250°C, leading to partial dissolution of alloying additions such as Ti, Nb, V and sulphides. Partial dissolution has the consequence of reducing the microalloying potential. For example, undissolved TiN precipitates reduce the amount of Ti available for austenite grain refining and final precipitation hardening [11, 12].

This can be illustrated by the observation that Ti additions can have little or no effect on steel properties after CCR but can have a significant effect if thin slab casting with HDR is utilised [24, 25]. In HDR steels, Ti remains in super-saturated solid solution during the soaking period and can precipitated during rolling as fine TiN particles which contribute to strengthening. In CCR, Ti is found as coarse TiN particles after the

soaking process and contribute little to strengthening [25]. . It has also been found that fine MnS precipitation can control ferrite grain growth and improve yield strength and tensile strength for low-C steels produced via thin slab casting. This fine MnS precipitation is believed to be due to delayed precipitation (decreased time for particle coarsening) because the high cooling rate keeps the S in solid-solution [24].

In order to produce the desired microstructure and mechanical properties, careful control of the cooling rate after rolling and control of the coiling temperature is required. Accelerated cooling contributes both to ferrite grain size refining, by promoting intensive ferrite nucleation via the under cooling of austenite, and to improving precipitation strengthening. Rapid cooling after rolling suppresses precipitation until the strip is coiled, allowing a fine dispersion of precipitates to evolve in the coil [6]. This technique can improve final mechanical properties by promoting precipitation hardening in ferrite. The correct cooling rate and coiling temperature must be tailored to suit the microalloying system and required mechanical properties.

1.5 Thin Slab Casting and Hot Direct Rolling Processes

1.5.1 CSP- Compact Strip Production

Nucor steel was the first to build a mini mill steel works, based on thin slab technology, in 1986. The new technology was termed “Compact Strip Production”, CSP, due to the compact design of the mini-mill. Commissioning of the plant occurred in 1989 at Crawfordsville, Indiana, USA. The CSP process was the first process capable of casting, rolling and finishing a strip in one heat [1]. A typical CSP thin slab casting process is shown in Figure 1.5 [4].

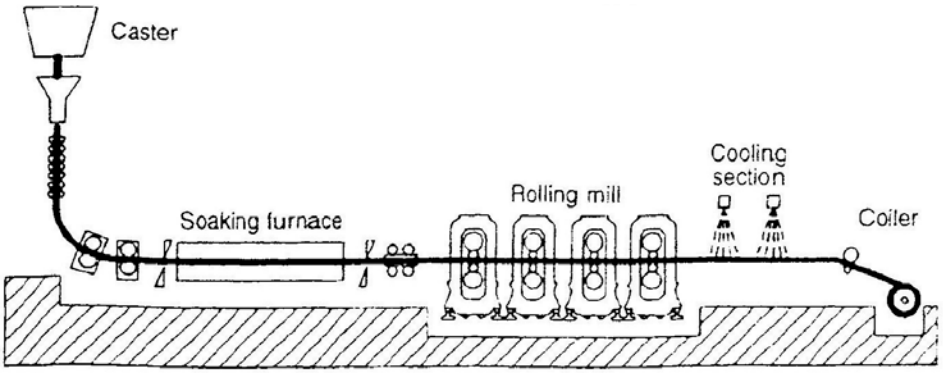

Figure 1.5: Nucor's initial CSP plant layout.

The CSP process is generally supplied hot metal via an Electric Arc Furnace (EAF). The caster produces slabs 50mm in thickness and widths in the range 1295 to 1560mm. High casting speeds of 6.0m/min for plain carbon grades and 3.5m/min for all other grades are achievable due to the thickness of the slab [8]. Due to the confinement of a relatively small mould cavity, it can be difficult to achieve high quality cast steel. To overcome this problem, the funnel mould and a specially designed submerged entry nozzle system was developed. A longer than usual (than for conventional casting) mould length of 1100mm was used to improve quality, while still maintaining caster speed. The casting machine is of vertical design with in-line bending [8, 9, 26, 27].

Thin slabs are fed directly into an in-line roller hearth furnace to prevent built-up of scale by minimising the time between casting and rolling. The hearth furnace also equalises the slab temperature and heats the slab to the correct rolling temperature. Scale build-up must be closely controlled, by controlling the furnace temperature and atmosphere, to prevent excessive yield losses due to the thinness of the slab [8]. The in-line tunnel furnace acts as a buffer between the caster and rolling mill.

The finishing mill at the Crawfordsville plant initially consisted of only four rolling stands but was quickly increased to six stands to allow for thinner and wider strips to be produced. A roughing mill was not required for the CSP process. Strip dimensions using six stands are between 1295-1560mm in width and 1.95-12.7mm in thickness. The rolling mill employs a high-pressure water de-scaler, laminar cooling and a down-coiler with step control [1, 8, 27].

The CSP process has been restricted to producing plain carbon steels, outside the peritectic range, due to excessive cracking problems, during casting and straightening, of peritectic steels. This problem initially restricted steel types to general structural steels and drawing grades. However, advances in technology and the opening of updated plants led to the successful casting of high carbon (>0.55%), high alloyed, HSLA and Stainless steels [8, 28, 29].

The CSP plant at ACME Steel [30] was the first CSP facility to supply its liquid steel from a Basic Oxygen Furnace (BOF). The plant produces; low carbon, structural, high carbon and HSLA steel grades. The CSP plant at Hylsa is capable of producing, “ultra light hot strip”, strip thinner than 1.5mm. The production of thin gauge strip has led to Hylsa concentrating on producing drawing grades, structural grades and galvanised products.

One of the more recent steelmakers to incorporate CSP technology was Thyssen Krupp Stahl in March 1999 [29]. A thin slab casting and rolling plant was fitted to the existing Duisburg-Bruckhausen works, in Germany, utilising clean steel delivered via a converter steelworks and ore-based blast furnace. Thyssen Krupp Stahl incorporates the first CSP casting machine with two strands, operating in parallel, that are both fed by the same tundish, as shown in Figure 1.6 [31]. Thyssen Krupp Stahl plans to produce ultra thin hot strip by improving the practical operation and integrated technology packages that are installed in the casting and rolling mills.

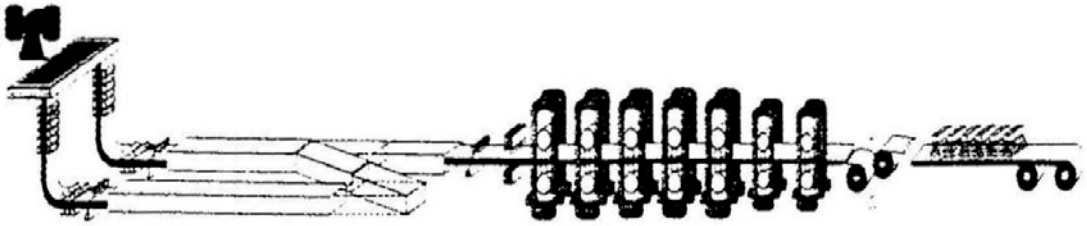

Figure 1.6: Layout of CSP plant with twin strand casting at Thyssen Krupp Stahl's integrated works at Duisburg.

1.5.2 ISP- In-line Strip Production

The ISP (In-line Strip production) process was jointly developed by German plant maker, Mannesmann Demag Huttentechnik (MDH) and the Italian pipe and tube producer, Arvedi. The first plant started production in 1993 in Arvedi, Cremona [17]. The layout for the Arvedi ISP plant is illustrated in Figure 1.7 [4].

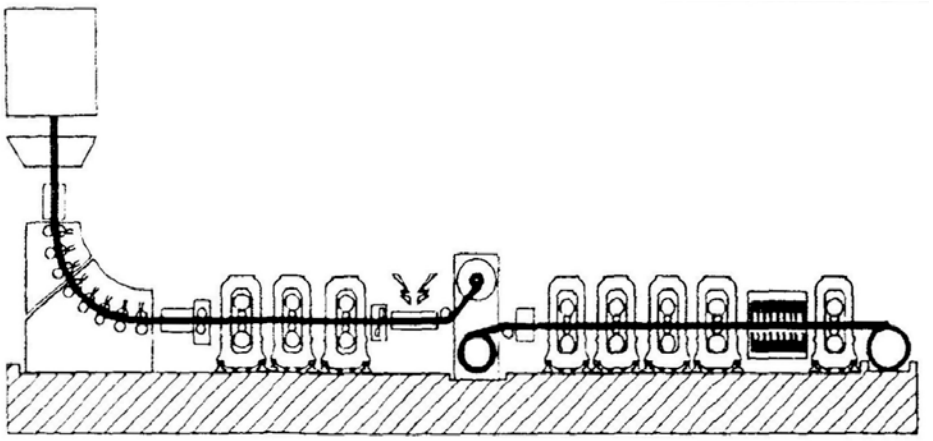

Figure 1.7: Layout of the ISP plant in Arvedi, Cermona.

The caster features soft reduction rolling technology capable of reducing the slab while the core is still molten. Cast slabs are "soft reduced" from 80mm to 60mm in thickness. After exiting the caster the slab enters a three-stand tandem mill, where it is reduced down to a suitable thickness (15-25mm) for coiling in the Cermona furnace. The strip is sheared then enters the reheating furnace, which acts as a buffer between the caster and final rolling mill. The reheated strip is then coiled in a twin coilbox furnace, named the "Cremona furnace". This furnace receives strip from the caster, while at the same time,

feeds out previously coiled strip to the finishing mill. The finishing mill is a four-stand hot finishing tandem mill capable of reducing strip thickness from 12mm to 1.5mm [5, 9, 17, 32].

One of the main features of Arvedi's ISP plant is the compact design. The Coilbox feature allows the plant to be compacted down to only 180m, compared to 260m for Nucor's CSP plant [5]. A short processing time of 15-30 minutes for the entire process is also a major advantage over conventional plants.

It is claimed that soft reduction (cast rolling) refines the grain size in the centre of the slab and also helps reduce segregation, particularly of Mn. Cast rolling suppresses segregation and improves grain refinement due to a combination of; deformation of the mushy zone, small casting thickness and short solidification times [5].

The casting machine has a vertical-bow type mould design with flat parallel sides, employs air-cooling and has a maximum strip width of 1300mm. The maximum casting speed for low carbon steel is 6m/min. Steel grades produced are deep drawing grades, unalloyed and alloyed structural steels, HSLA steels for pipelines and highly alloyed austenitic and ferritic stainless steels [9, 17].

1.5.3 "Danieli" Thin Slab Caster

Plant-maker Danieli developed their thin slab casting machine in Sabolarie, Italy and first operated the pilot plant in 1984. The pilot mill produced slabs between 28 to 50mm in thickness and 1000mm in width. Operational data from the pilot mill was used to develop a full-scale thin slab caster. The objective of the thin slab-casting project was to eliminate the requirement of a roughing mill and eliminate the reheating stage, that is, to enable HDR [33, 34].

The plant at Sabolarie consists of a Danieli thin slab casting machine, reheating/equalising furnace, de-scaler, four-high rolling stand and a cooling bed. The caster is a vertical curved type caster with a nominal radius of 5.5m. Slabs 50-90mm

thick and 800-2300mm wide are cast at speeds varying between 0.5-6m/min [9, 14, 35]. A lens-shaped curved mould of 1000mm in length was designed to help avoid depressions and surface cracks [14]. The caster is capable of LCR (soft reduction) and can reduce the slab to a final thickness in the range of 35-70mm. Soft reduction enables HDR and was claimed to produce a finer solidification structure, reduce centre-line segregation and porosity [14, 33, 34].

Cast slabs enter the induction furnace where they are heated to the correct rolling temperature. De-scaling of the slab is required before entry into the finishing mill. The speed of the rolling mill matches that of the caster to keep production running smoothly. The rolled plate is cut to length by a rotary shear method, engineered to minimise deflection caused by cutting [33, 34].

A Danieli thin slab caster was commissioned at Algoma Steel Corp. in Sault Ste. Marie, Ontario, Canada, in October 1997. Algoma steel was second behind ACME for producing thin slabs from BOF supplied steel. Algoma's "Direct Strip Production Complex" (DSPC), incorporates the Danieli flexible thin slab caster (fTSC), gas-fired tunnel furnace, roughing mill, heated transfer table and a six-stand finishing mill. A soft reduction system reduces 90mm thick slabs down to 70mm. Slab widths are between 800-1600mm and the caster is capable of operating at speeds between 2.8 to 5.5m/min. A roughing mill reduces 70mm thick slabs into 30-45mm thick transfer bars. A heated transfer table provides the link between the roughing mill and the finishing mill. The finishing mill can reduce the transfer bar down to 1.7mm strip. The run-out table and the down-coiler have been set-up to handle ultra-thin gauge strip [16, 36, 37].

The product mix at Algoma includes; low carbon, peritectic, medium carbon, high carbon and HSLA steel grades [16, 36, 37]. Algoma have one of the first thin slab casters capable of successfully casting peritectic grade steels. Peritectic grades (0.09 to 0.16% C) are the most difficult to cast as they are extremely sensitive to forming defects, especially longitudinal and transverse cracks.

1.5.4 TSP- Tippins-Samsung Process

The TSP (Tippins-Samsung Process) combines an intermediate slab caster (100-125mm thick slabs) with a single stand Steckel hot strip mill. The basic layout of TSP is shown in Figure 1.8 [38]. Tippins Incorporated (American) teamed up with caster builder Samsung Heavy Industries (SHI) of South Korea to develop the TSP technology for TSC and HDR of steels. The process is suitable for low carbon to high carbon grades of steels, stainless, HSLA, Silicon, API (American Petroleum Institute) and drawing quality steels. One of the strengths of the mill is its versatility; it can produce coiled or discrete plates, enabling a wide range of widths and gauges to be produced [39].

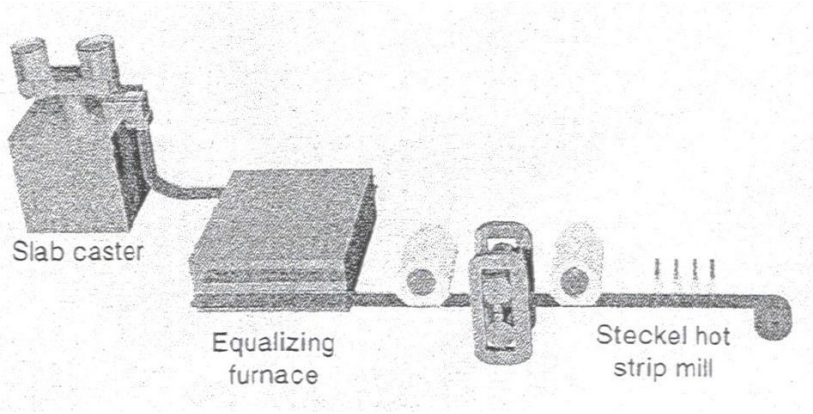

Figure 1.8: Basic layout of the Tippins-Samsung Process (TSP).

The TSP continuous caster employs a low head single strand slab caster to cast intermediate, 100 to 125mm, thick slabs. The general slab width is between 500 and 2500mm but it is possible to achieve up to 3000mm. A straight mould of conventional design, with flat broad and narrow faces, is used to achieve good liquid steel quality. The mould features width and taper adjustment and is capable of soft reduction to improve internal soundness [38, 39].

The casting of intermediate thickness slabs has several advantages. The slab is thin enough to eliminate the need for a separate roughing mill (in this case) and thick enough to maintain good surface quality. The intermediate thickness allows for greater slab width, reduced reheating time (due to better heat retention) and hence, reduced scale formation compared to 50mm thin slabs.

After casting, slabs are sent directly to the reheating furnace to equalise the slab to the correct rolling temperature. The typical holding time to heat a slab to 1250°C is 12-13 minutes. A single stand four-high reversing Steckel-type rolling mill conducts both the roughing and finishing operations in reversing passes. Once the strip has been reduced to 20 to 25mm, it is coiled in the coiling furnaces to retain strip temperature. The strip is then reversed back and forth through the rolling mill. A total of three flat roughing passes and six coiling finishing passes are generally required to reduce a slab to finish gauges as thin as 1.5mm. A vertical edger controls slab width and laminar flow cooling banks control cooling rates, coiling and finish temperatures [38, 39].

1.5.5 Conroll (VAI)

The thin slab casting and hot direct rolling technology coined “Conroll” was developed by Voest-Alpine Industrieanlagendau (VAI). The Conroll process produces 70-80mm thick slabs through a straight mould with parallel sides but does not perform strand thickness reductions (soft reduction). The caster is designed for easy change of the tundish and submerged entry nozzle to maximize steel cleanliness. High casting speeds of 2-4m/min and widths of 800 to 1600mm are possible [9, 40].

The caster is connected to the rolling mill via a roller hearth-reheating furnace that equalises slab temperature to approximately 1120°C. The rolling mill can include four, five or six finishing stands, depending on the product mix and required finishing gauge. The rolling mill includes a hydraulic shear mechanism, high-pressure water descaler, edger, laminar strip cooling system and a downcoiler. Final strip thickness is between 1.8 and 20mm [9, 40].

The Conroll technology was installed at Armco’s Mansfield operations in April 1995. Armco adopted the Conroll technology because it was designed specifically for stainless steels. Steel grades produced include carbon steels, 409 and 430 grade stainless steels as well as a small percentage of HSLA, high alloyed and silicon steels. Armco aims to

produce unstabilised high chrome grades, such as 434 and 436 for automotive trims, and also stainless grades such as 410, 420 and 440 martensitic stainless steels [41, 42].

1.5.6 QSP- Quality Strip Production

A medium thickness high-speed slab caster, termed QSP (Quality Strip Production), was jointly developed by Sumitomo Metal Industries Ltd. and Sumitomo Heavy Industry. The technology was first developed at Kashima steelworks before being implemented at North Star/BHP Steel and Trico Steel in the USA.

The QSP continuous casting machine is of the vertical bending type and casts 90mm thick slabs. The mould is of the plane parallel-sided design (parallel faces) with Electro-Magnetic Brake (EMBr) and high frequency mould oscillation installed. Good surface quality is one of the attractive features of a parallel mould. Low carbon steel can be cast at 5.0m/min and other steel grades, namely peritectic, medium carbon, high carbon and HSLA steels are cast at 3.5m/min [43].

In 1994, North Star Steel and BHP Steel formed a joint venture to build a QSP based mini mill. The medium thickness continuous caster was designed and supplied by SHI. It is a single strand design with a 950mm long vertical mould, a top zone and has eleven segments. The casting machine was not fitted with soft reduction technology. Slab dimensions are 90mm in thickness and 900mm to 1565mm in width [43, 44].

The hot strip mill consists of a rotary descaler, Bricmont roller hearth tunnel furnace, two roughing mills, heated transfer bar table and a finishing mill. Non-reversing roughing stands reduce 90mm cast slabs to 35mm transfer bars. The transfer bar table heats the bar to the correct rolling temperature. The thin transfer bar enables high speed rolling, which reduces scale generation and promotes excellent surface quality [43]. Coils are produced in the thickness range 1.4 to 9.5mm and 900 to 1500mm in width [44].

Trico Steel has also implemented a medium thickness slab caster from Sumitomo but has included several changes from the caster supplied to BHP/NS. Trico's caster utilises a rectangular mould to produce slabs 90mm thick and can "soft reduce" slabs to 70mm with a Liquid Core Reduction (LCR) system. The casting machine has seven segments, the first of which carries out LCR using guide rolls with adjustable gaps and sensors fitted to control the slab thickness [43, 45, 46]. Trico adopted the 90mm slab size due to improved surface and internal quality over 50mm slabs. Figure 1.9 shows the process configuration of Trico's medium thickness slab caster and compact hot strip mill [43].

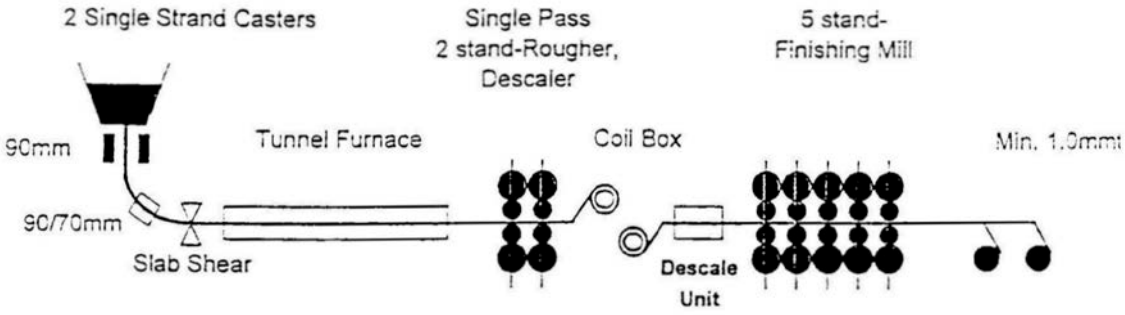

Figure 1.9: Process configuration of Trico's medium thickness slab caster and compact hot strip mill.

Trico use two roughing mills to reduce the slab thickness down to 17 or 18mm. The first roughing mill is a two-high non-reversing mill and the second is a four-high variable speed mill. A coil box replaces a run-out table, considerably reducing the overall length of the mini mill. The coil box equalises slab temperature, dislodges scale and coils at a maximum speed of 230mpm. The workable slab dimensions for the coil box are 17-30mm in thickness and 900-1100mm in width [45]. The transfer bar is uncoiled and fed into a four-high, five-stand, tandem mill. Final strip thickness is between 1.4 to 15.0mm [43, 45].

1.6 Concluding Remarks

From the previous sections, it is clear that there are numerous metallurgical differences between TSC and CCR, which in turn can influence the mechanical properties and quality of the final product. In order to improve production and technology associated with TSC, it is vital to understanding the metallurgical aspects of TSC with HDR. This will improve the quality and mechanical properties of the final product.

Rapid solidification, compared to that for conventional casting, is characteristic of TSC and will significantly alter the microstructure formed on solidification. Rapid solidification promotes a finer, more homogeneous microstructure, as measured by SDAS. Therefore, the affect of a finer solidification structure on mechanical properties, such as tensile strength and yield strength, will be investigated. Mechanical properties will be tested using the Gleeble Thermomechanical simulator and by controlling the solidification rate of the tensile specimen, the size of the solidification structure can be varied.

The absence of the re-heating stage, for HDR, removes the beneficial effects of the grain refining $\gamma \rightarrow \alpha$ and $\alpha \rightarrow \gamma$ transformations; therefore, re-heated structures are quite different from as-cast structures. The influence of re-heated structures compared to as-cast (direct cast) structures on hot ductility will be determined under simulated conventional casting and thin slab casting conditions.

Casting of peritectic grades are generally avoided at the majority of TSC plants due to severe problems with the occurrence of transverse cracking in these grades. Thus, the composition of the steels investigated had carbon levels close to the peritectic composition.

Chapter 2 will discuss the relationships between hot ductility tests and transverse cracking, where the influence of re-heated and as-cast structures on hot ductility and the mechanisms of transverse cracking, particularly for peritectic grades, will be examined in greater depth.

Chapter 2:

Literature review: Hot Ductility

Chapter 2: Literature review: Hot Ductility

2.1 Introduction

The problem of transverse cracking of continuously cast steel slabs has been extensively investigated over the last 20 years. This research has led to alloying and process modifications that have reduced the problem of transverse cracking to a large degree but difficulties are still encountered for microalloyed steels. The advent of thin slab casting (TSC) with hot direct rolling (HDR) requires new research tailored to suit conditions of these emerging processes. Surface inspection prior to HDR is not possible so good surface quality and the elimination of transverse cracks are of the utmost importance if defect-free rolling is to be obtained. A defect free slab surface has now become a prime requirement for the economic production of HDR steel [47-49].

The continuous casting operation and its inherent stresses are shown schematically in Figure 2.1 [47]. Molten steel is poured from a tundish into an oscillating, water-cooled copper mould at the start of the continuous casting machine. Mould oscillation is necessary to prevent sticking but it is responsible for producing transverse ripples, or oscillation marks, on the surface of the strand. Under certain conditions, cracks may form along the oscillation marks on the top surfaces and edges of the strand. When the vertically cast strand is straightened, the top surface and edges are put under tension and transverse crack propagation can take place [47].

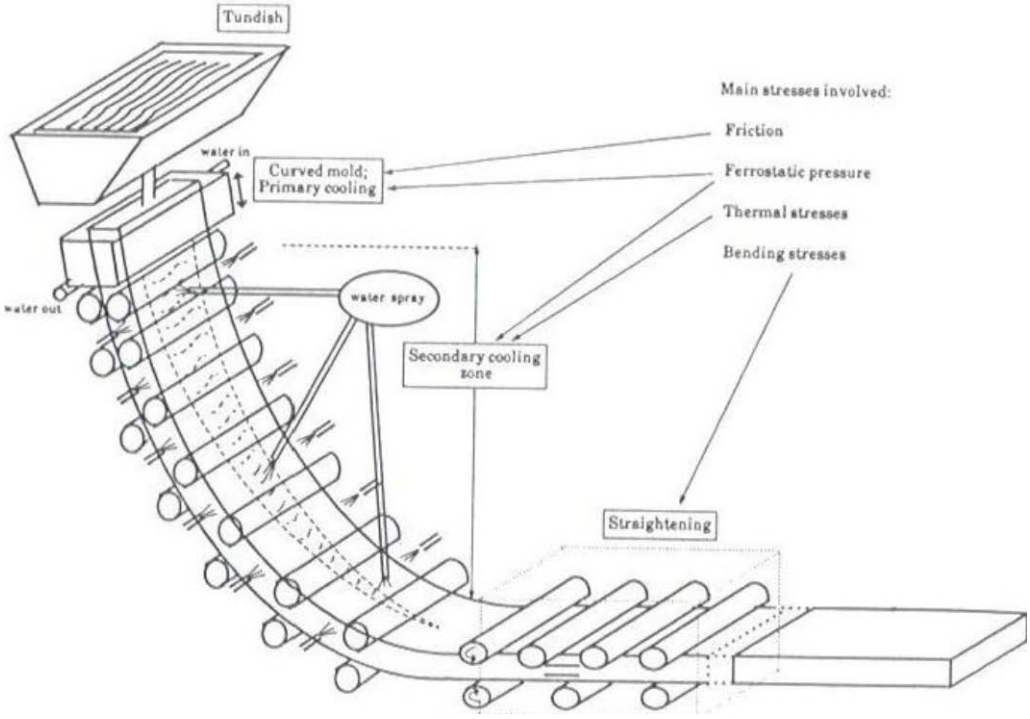

Figure 2.1: Schematic diagram of a typical continuous casting machine and its inherent stresses [47].

The straightening operation is carried out in the temperature range of 1100-700°C at a low strain rate deformation of 10^{-3} to 10^{-4} s^{-1} with a degree of straining of only 1-2%. The temperature range of 1100 to 700°C coincides with the interval in which steel exhibits a ductility trough in laboratory hot tensile tests. This apparent correlation between transverse cracking and tensile hot ductility has led to extensive research, which has alleviated the problem of transverse cracking considerably. However, there are still casting problems for the most difficult grades of steel and it is not uncommon to roll wide and trim the edges of the strand adding considerably to scrap losses. Peritectic steels (0.08 – 0.16%C) and microalloyed steels containing niobium give the most trouble; therefore, considerable research in these areas is still on going. With the increasing use of thin slab casting (TSC) and hot direct rolling (HDR) operations, research on hot ductility under these new conditions is increasingly necessary. It is essential to tailor laboratory hot tensile testing to closely simulate TSC and HDR conditions to gain a greater understanding of the occurrence of transverse cracking for peritectic, microalloyed steels.

2.2 Origin of Transverse Cracks During Continuous Casting

Transverse cracks occur on the top surface of a cast strand normal to the axis of the product. Transverse corner cracks occur at the edges of the slab. Factors that influence transverse cracking, including chemical, process and engineering, have been listed by Irving [50] and these are:

- Mould powder,
- Sensitive chemical compositions,
- Mould taper too large,
- Poor oscillation conditions,
- Low surface temperature at straightening,
- Non uniform cooling,
- Abrupt speed changes.

It is commonly found that transverse cracks are initiated in valleys of deep oscillation marks.

2.2.1 Role of Oscillation Marks in the Formation of Transverse Cracks

Mould oscillation is an important aspect of continuous casting as it prevents the strand shell from sticking to the mould wall. Mould oscillation operates in a sinusoidal cycle, where the downward velocity exceeds the casting speed for at least part of the cycle. During this time, termed the ‘negative strip’ or ‘heal time’, sticking between the mould and the strand shell is overcome. Oscillation marks are also formed during this period [50, 51].

There have been several proposed mechanisms for the formation of oscillation marks but the exact mechanism is not completely clear. There are three main mechanisms proposed for the formation of oscillation marks as shown in Figure 2.2 [50]. All three mechanisms involve the infiltration of molten or solid slag between the mould wall and the shell to force the meniscus into the melt. There are three propositions for the driving force behind slag infiltration [52].

1) The periodical inflow of liquid slag during negative strip time of mould oscillation,

2) The periodical inflow of liquid slag during positive strip time of mould oscillation,

3) The periodical inflow of the solid slag rim during negative strip time of mould oscillation.

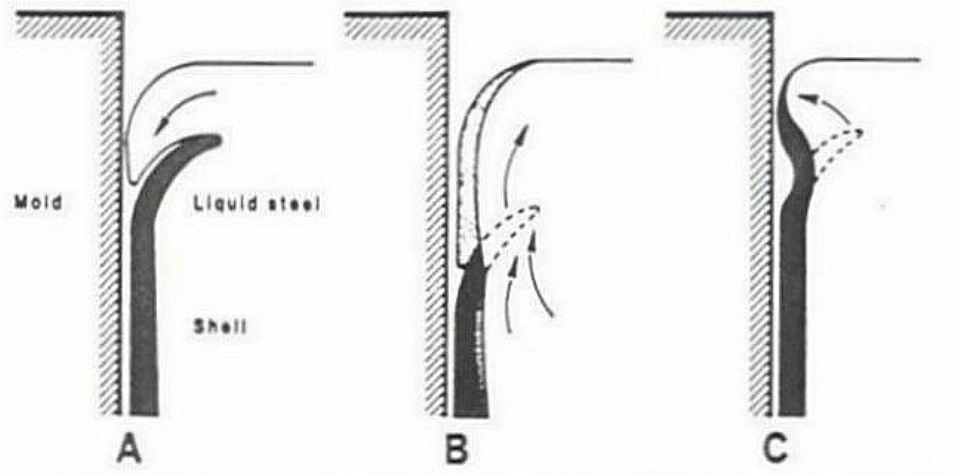

Figure 2.2: Three main mechanisms for the formation of oscillation marks, A) Overflow, B) Overfow and remelting and C) Meniscus bent back..

Once the driving force that pushed the meniscus shell into the melt recedes, ferrostatic pressure either causes the molten steel to overflow the partially solidified meniscus (A & B in Figure 2.2) or the meniscus is pushed back towards the mould wall (C in Figure 2.2). If molten steel overflows the partially formed, or bent, meniscus, the bent meniscus either remains (Figure 2.2- A) or remelts (Figure 2.2- B). All mechanisms are based on the solidification of the curved section or bent section of the meniscus against the mould wall and are influenced by mould conditions [50-56].

Regardless of which mechanism forms the oscillation mark, there is an influx of impurity-enriched interdendritic liquid, “dirty liquid”, at the valley of the oscillation mark [51, 52, 56]. Harada [51] has proposed two mechanisms for the influx of dirty segregated liquid during the formation of oscillation marks. The first involves the squeezing out of segregated liquid between dendrite arms due to the deformation of the partially solidified shell. The second is due to segregated liquid between dendrite arms being pumped out to the surface, in order to maintain the balance of pressure of the liquid steel. The second mechanism is related to the overflow of the bulk liquid onto the tip of the shell (this causes the imbalance in pressure). This localised “dirty” segregation is believed to be the origin of cracks when the strand is subjected to any stresses below the mould. Segregation of solute elements results in increased precipitation of nitrides and carbonitrides reducing the ductility of the strand at elevated temperatures [56]. Segregation also reduces the solidus temperature and the semi-solid shell can easily fracture along segregated regions [52].

The degree of segregation depends largely on the depth of the oscillation mark. Thus, severe transverse cracks are associated with deep oscillation marks. Deep oscillation marks can be avoided or minimised by the following factors [50, 51, 56]:

- Minimising fluctuations in mould liquid level,
- Increasing the frequency of mould oscillation and decrease length of stroke (decreases the negative strip time),
- Using mould flux with low surface tension, good lubricating and heat transfer properties,
- Optimising taper on narrow face of mould,
- Maintaining uniform temperature in the liquid pool in the mould,
- Avoiding peritectic carbon levels, 0.08 – 0.16%C

Care must be taken however, when adjusting mould oscillation conditions to be favourable for shallow oscillation marks. If the negative strip time is too short breakouts can occur due to the sticking of the strand to the mould wall. Figure 2.3 correlates heal time with oscillation mark depth [50]. It is clear from Figure 2.3, that increasing the heal

time increases the oscillation-mark depth. However, Figure 2.3 gives no information on the minimum heal time required to prevent breakouts.

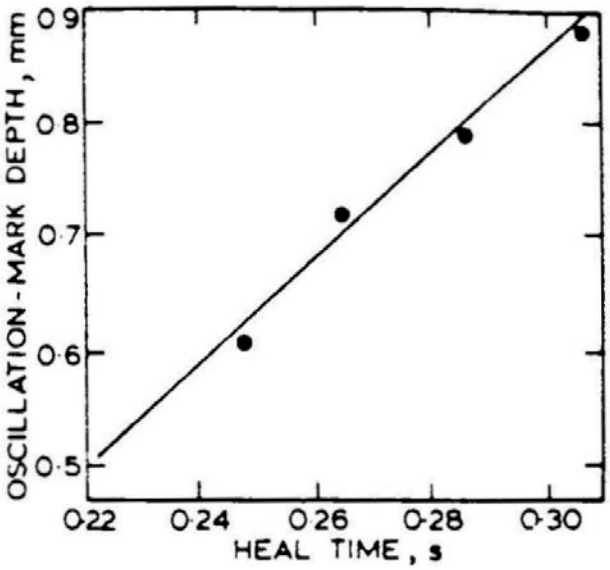

Figure 2.3: Effect of heal time on oscillation mark depth.

2.2.2 Effects of Chemical Composition on Oscillation Marks and Transverse Cracks

Deep oscillation marks may encourage the formation of transverse cracks, but they are not always a prerequisite for transverse cracking to occur. Transverse cracks can readily form in shallow oscillation marks if the steel has a sensitive chemical composition. Steels containing Al, Nb, V which have greater than 1% Mn are particularly susceptible to cracking, especially if the carbon content is in the peritectic range [50, 51, 53, 54].

Steel grades that are sensitive to transverse cracking display a region of low ductility between approximately 700-1000°C. Transverse cracks are encouraged if the surface temperature of the strand is in the low ductility region during straightening. Large tensile stresses develop in the top surface of the strand during straightening, if the inherent strength of the steel is below that of the stresses generated, then cracks can propagate into the bulk. To avoid cracking during straightening, the surface temperature of the strand should be kept either below or above the low ductility temperature region.

In the case of HDR, the surface temperature of the strand must be kept above the low ductility temperature region. Therefore, it is vital to control secondary spray cooling to maintain a uniform slab temperature above the low ductility region. It is also important to minimise temperature cycling during secondary spray cooling as this encourages precipitation [53, 54]. The influence of precipitation on transverse cracking will be discussed in following sections of this Chapter.

2.2.3 Influence of Carbon on Transverse Cracking

The hot cracking susceptibility of low alloy steels during continuous casting is usually a strong function of the carbon content. Maximum cracking susceptibility is attained in the peritectic region, 0.08 to 0.16%C [57]. Hot tensile tests on reheated specimens fail to show this effect, which suggests that the carbon content dependence is due to microstructural change during solidification [49, 57]. In hot tensile tests, intergranular failure in austenite is a dominant failure mode, so the hot ductility of direct cast specimens will have a strong dependence on the austenite grain size [49, 71, 72]. The high austenite transformation temperature in the peritectic region results in large austenite grains due to rapid grain growth. Grain growth at carbon levels lower then the peritectic is restricted by the delta phase formation, while at higher carbon levels growth is restricted by liquid phase formation with increasing temperature. The austenite grain size generally reaches a maximum in the peritectic carbon range [57].

The volume change associated with the peritectic reaction results in uneven surface solidification in the mould and can lead to the formation of thinner shell walls that can lose contact with the mould wall. This results in a localised delay in cooling (in the thinner section) due to a reduction of heat extraction via the mould wall. The delay in cooling promotes an even coarser austenite structure, which is more susceptible to intergranular cracking. This process is schematically illustrated in Figure 2.4 for (a) fine grain size and (b) coarse grain size. The gap between the meniscus and the mould wall gives rise to irregular heat transfer, non-uniform skin formation and deep oscillation marks. [49]

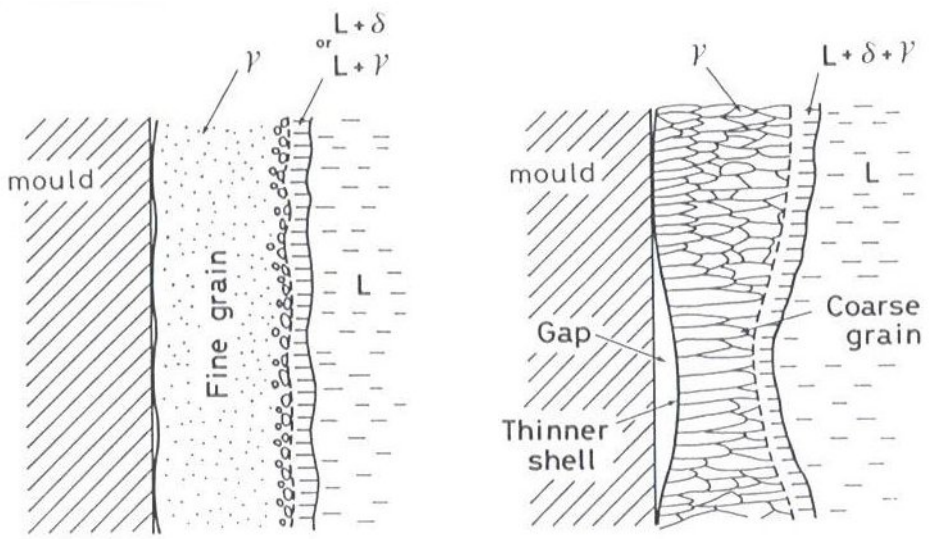

a) b)

Figure 2.4: The formation of thin sections in the shell wall in the mould for a) fine grain and b) Coarse grain steel.

The influence of carbon content on the depth of oscillation marks is illustrated in Figure 2.5 [50]. It is clear from Figure 2.5 that the peritectic composition has a strong influence on the oscillation mark depth. As discussed previously, deep oscillation marks have been associated with transverse cracking but are not always a prerequisite for transverse cracking. Nevertheless, the above results suggest that alloys in close proximity to the peritectic composition may be susceptible to the formation of transverse cracking. The addition of alloying elements will vary the peritectic composition; therefore, the 'Carbon equivalence' instead of carbon content may be a more useful parameter for assessing an alloys susceptibility to transverse cracking [49].

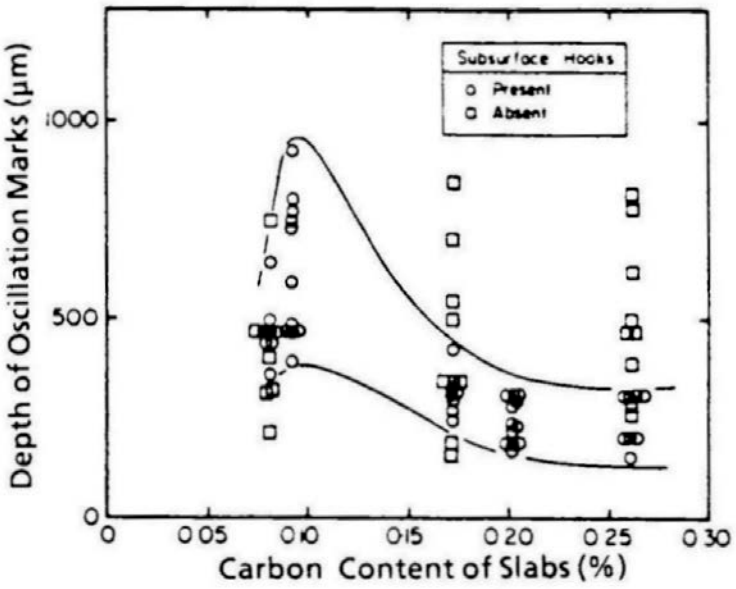

Figure 2.5: Effect of carbon content on the depth of oscillation marks.

2.3 Relevance of the Hot Tensile Test to the Problem of Transverse Cracking

There are several test methods for simulating the unbending operation during continuous casting; they include the hot bend test, hot compression test (including SICO- Secondary Induced Crack Opening), torsion testing and hot tensile testing. The hot bend test most closely simulates the unbending operation but it is difficult to quantify the severity of surface cracking from these tests. The hot compression test is carried out on flanged samples, where the hoop strain corresponding to the first appearance of a crack is taken as a measure of hot ductility. Torsion testing produces large strains and the difficulties in interpreting the fracture appearance after failure makes the test unsuitable. The most popular test for studying the problems of transverse cracking is the simple hot tensile test. [47]

Conditions chosen for the hot tensile test should be as close as possible to the conditions related to the straightening operation during continuous casting. Samples are solution treated (1200-1400°C) to dissolve the majority of the microalloying additions and to produce a large austenite grain size. More sophisticated methods involve casting (melting) the sample *in-situ* to improve the accuracy in attaining a microstructure

similar to that of a continuously cast strand [47, 48]. Samples are melted, either by induction or electrical resistance, depending on the type of tensile testing equipment. The molten zone, normally in the centre of the sample, is contained and supported by a quartz crucible. The sample is cooled, at a rate chosen to correspond to the average cooling rate near the surface of a continuous cast strand, down to the tensile testing temperature. For conventional continuous casting (200-250mm thick slabs) the cooling rate is approximately 60K/min and for thin slab casting (50mm thick slabs) the cooling rate is approximately 200K/min. Samples are usually tested to failure in the temperature range of 1100 to 700°C. This temperature range corresponds to the ductility trough experienced in steels, a region of relatively low ductility below 1100ºC. A strain rate is chosen to simulate that which is experienced during the straightening operation, 10^{-3} to 10^{-4} s^{-1}. [47, 48]

Simulation of the complex cooling patterns that are experienced in the secondary cooling zones before straightening improves the accuracy of the test with respect to continuous casting conditions. Research shows [47, 58-62] that the complex cooling patterns experienced during continuous casting affects hot ductility results. Unfortunately, research investigating the influence of complex thermal histories on hot ductility has seldom been done or only a simple pattern was simulated. Research is still required in order to gain a greater understanding in this area.

The majority of researchers have used reduction of area, RA, for measuring ductility after fracture. The RA value required to prevent transverse cracking from occurring is dependent on the exact test conditions. Reported critical values of RA to prevent transverse cracking vary between 30% [56] and 60%. Mintz [48] suggests that for a basic hot tensile test, solution treated at 1330°C and tested at a strain rate of 3×10^{-3} s^{-1}, a RA value of 40% would be required to prevent cracking.

Simple ‘solution treatment’ tensile tests readily show the detrimental effects of Nb and Al on hot ductility but can be misleading when elements that are not dissolved at the solution temperature, such as Ti and S, are involved. If elements are not dissolved at the solution treatment temperature then their behaviour will not be representative of the casting process and the tensile tests can be misleading. Many of the drawbacks of

solution treatment tests are overcome by casting tensile samples *in-situ*. This ensures complete resolution of TiN particles, MnS inclusions and allows segregation to interdendritic boundaries. Precipitate sizes and distributions in direct cast tensile samples approach those found near the surface of continuously cast slabs [48].

There are still many limitations of tensile testing that must be taken into account when interpreting results. Due to the small size of the tensile sample the segregation patterns and columnar grain structure found near the surface of a strand cannot be reproduced and these are the structures most relevant to transverse cracking. The effect of mould oscillation conditions on segregation patterns cannot be simulated [63]. Impurity-enriched segregation entrapped between solidifying dendrites can be introduced by mould oscillations. This can lead to weak boundary regions, particularly if phosphorous segregates, giving rise to deep cracks at the slab surface and transverse cracking problems [52, 63]. Equiaxed grains are usually formed in tensile samples as opposed to a columnar structure, which is found near the surface of a strand [64].

The cooling history of a continuous cast strand is very complex and is difficult to accurately reproduce in the laboratory. Thermal history affects precipitation and the microstructure, especially if the temperature in localised regions falls to low enough temperatures, such as 900°C, encouraging precipitation. Tensile samples are normally well protected from oxidation, while a strand is exposed to severe oxidising conditions. Coarse Nb(C,N) particles are often present in direct cast tensile samples but are not observed at the surface of cast strands [64]. Consequently, there is more Nb available for precipitation in the strand so a more severe influence on cracking is expected [64]. All these factors may well cause deterioration in the ductility of a continuous cast strand and care must be taken when assessing the steels likelihood to develop transverse cracking based on information obtained from tensile tests.

Steels with a carbon content close to the peritectic can be particularly susceptible to transverse cracking. Little information can be given on the influence of the peritectic transformation on transverse cracking from hot ductility tests [48]. The δ-γ phase transformation results in a contraction of the solidifying shell, away from the mould wall, thus reducing the heat extracted by the mould. An uneven shell is formed and can

be more easily broken in the thinner sections. The hot tensile test can give little information on this phenomenon [48].

2.4 The Hot Ductility Curve

A typical hot ductility curve for steel is shown schematically in Figure 2.6 [47]. The curve contains three general regions, as described by Mintz [47]:

i) High ductility, low temperature region
ii) Ductility trough, or region of embrittlement
iii) High ductility, high temperature region

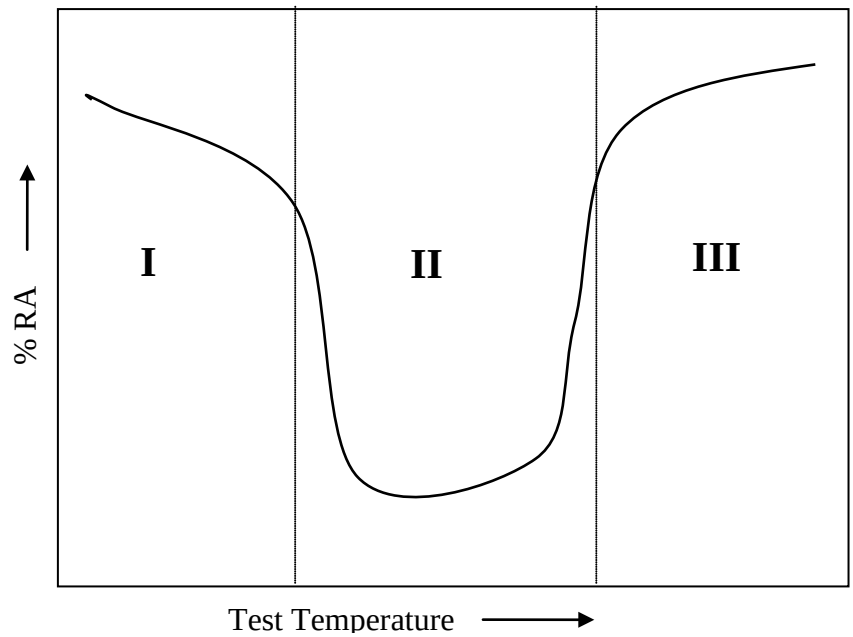

Figure 2.6: Schematic diagram showing the three characteristic ductility regions on a hot ductility curve. Reproduced from Ref [47].

The region of embrittlement (II) is of most interest and is invariably associated with intergranular fracture at austenite grain boundaries [47, 48]. Intergranular failure in the austenite can be caused via two mechanisms, grain boundary sliding in single phase austenite or transformation controlled intergranular failure. The latter is usually associated with intergranular microvoid coalescence in thin films of ferrite at prior austenite grain boundaries. The higher the temperature of the region of embrittlement,

the more likely it will be for straightening to be carried out in this region, leading to a greater susceptibility of transverse cracking problems.

2.4.1 Intergranular Failure: Role of Ferrite films

Transformation controlled intergranular failure is due to the formation of thin films of ferrite (~5-20μm) surrounding the austenite grain boundary. A typical microstructure depicting thin films of ferrite is shown in Figure 2.7. Ferrite is softer than austenite at elevated temperatures, due to a higher dynamic recovery rate, than austenite. This allows strain to concentrate in the ferrite film, encouraging voiding around precipitates and/or inclusions situated at the boundaries. These voids link up to give failure by microvoid coalescence. The fracture process for transformation controlled, intergranular microvoid coalescence is shown schematically in Figure 2.8, (d-f) [49].

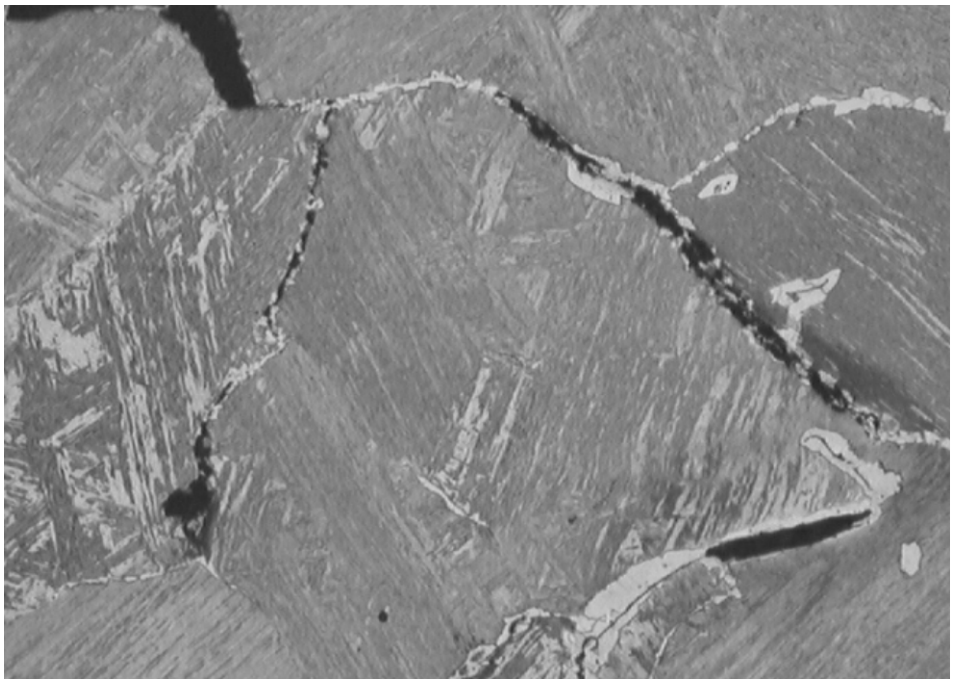

Figure 2.7: Intergranular thin films of ferrite formed in C-Mn-Al-Nb steel when tensile tested at 800°C. Note the intergranular cracking along the ferrite films.

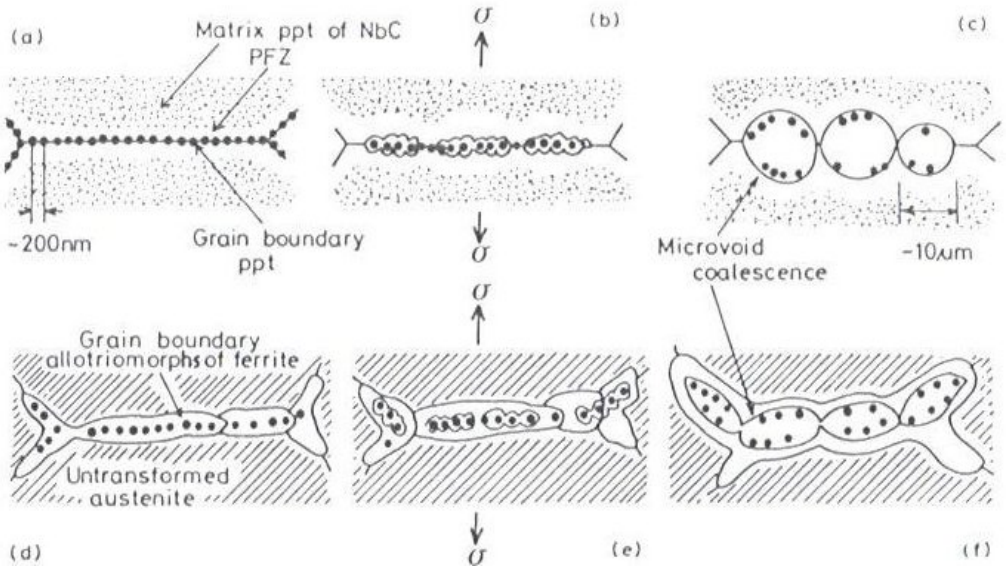

Figure 2.8: Intergranular microvoid coalescence of low alloy steels by deformation in low temperature γ region a-c, and α/γ duplex phase region, d-f. Where; a, d dynamic precipitation and strain concentration within soft layers along γ grain boundaries in initial stages of deformation; b, e microvoid formation by decohesion of precipitate/matrix interfaces; c, f coalescence of microvoids, resulting in ductile intergranular fracture of austenite.

Due to the excellent ductility of ferrite, ductility will recover at low temperatures when a sufficient amount of ferrite has formed and the strain concentration is eliminated. Ductility normally recovers at 20-30K below the Ar_3 when ~45-50% ferrite is present. Thin films of ferrite are normally deformation induced and can readily form at temperatures up to the Ae_3 transformation temperature [47, 65, 66]. Thus, the ductility trough extends from the Ae_3 temperature to 20-30K below the Ar_3 temperature if transformation controlled failure is the only failure mechanism. It is often observed that the ductility trough for C-Mn-Al steels stretches from the Ae_3 to 20-30K below the Ar_3 (undeformed) temperatures [47, 48, 65, 66].

Narrow troughs can occur if conditions favour the formation of large quantities of deformation induced ferrite just below the Ae_3, eliminating the stress concentration [48]. Higher strain rates and fine-grained steels favour the above mechanism. A higher strain rate increases the rate of formation of deformation induced ferrite and work-hardens the ferrite film [67, 68]. Work hardening of the ferrite film enables the film to thicken, distributing the strain across a larger area and reducing the susceptibility of the

steel to the occurrence of intergranular cracking. Fine-grained steels have a high number of nucleation sites (high grain boundary area and a high number of triple points) and large quantities of ferrite will form rapidly [67, 68].

2.4.2 Intergranular Failure: Precipitation Free Zones (PFZ)

In Nb containing steels, intergranular microvoid coalescence is enhanced due to the formation of precipitate free zones (PFZ) adjacent to austenite grain boundaries. During deformation in austenite, precipitation of Nb(C,N) can occur on the grain boundaries as well as in the matrix and is frequently accompanied by the formation of PFZ on both sides of the boundaries. Precipitation free zones are narrow bands without any precipitation adjacent to austenite grain boundaries. Very fine matrix precipitation (high volume fraction) produces significant matrix strengthening, which leads to the formation of a soft band (PFZ) surrounding the austenite boundary. Strain will concentrate in the weaker PFZ and a similar situation develops to that which occurs in soft ferrite films at the prior austenite boundaries. Microvoids form around grain boundary precipitates, such as Nb(C,N) or AlN, leading to fracture via the microvoid coalescence mechanism [47-49, 69]. This fracture process is shown schematically in Figure 2.8a-c.

2.4.3 Intergranular Failure: Grain Boundary Sliding

Low ductility in single phase austenite, where ductility is no longer transformation controlled, is generally due to intergranular failure via grain boundary sliding. Due to the limited dynamic recovery of austenite, grain boundary sliding can readily cause intergranular cracking. Limited dynamic recovery promotes work hardening, allowing high stresses to build up at triple points or grain boundary particles, leading to intergranular failure via the nucleation of grain boundary cracks. Schematic models showing the formation of wedge cracks by grain boundary sliding are illustrated in Figure 2.9 [47]. The presence of particles at grain boundaries will initiate cracks during grain boundary sliding and accelerate intergranular failure [47, 48].

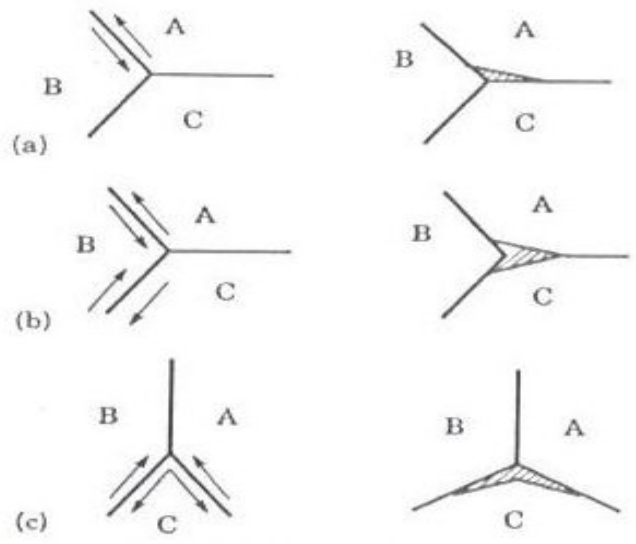

Figure 2.9: Schematic models showing three scenarios that can lead to the formation of wedge cracks by grain boundary sliding; arrows indicate sliding boundary and sense of translation.

At the high temperature end of the trough (region iii), dramatic ductility improvement has been associated with dynamic recrystallisation [47]. Any cracks that have formed as a result of grain boundary sliding, or stress concentration due to PFZ, are halted as a consequence of the grain boundary moving away from the crack. Isolated cracks can grow into large voids and failure ultimately takes place along the ridges separating the voids. Grain boundaries can move away from cracks (isolating them) via grain boundary migration [47]. Ductility also improves at higher temperatures because dynamic recovery becomes more active and flow stress is reduced. The absence of precipitation at higher temperatures promotes dynamic recrystallisation and hence, excellent ductility.

It is important, however, to note that dynamic recrystallisation will not occur during continuous casting due to the low strains during straightening (~2%) and the coarse grain size [48, 65, 66, 70]. The strains in TSC can be greater than in conventional casting but the strain is still low enough and the grain size still coarse enough to prevent dynamic recrystallisation [48]. Therefore, care must be taken when evaluating the susceptibility of steel to transverse cracking with the data obtained from the high temperature-high ductility region of the ductility curve.

2.5 Effects of Microstructural Variables on Hot Ductility

2.5.1 Grain Size

Generally, hot ductility improves with decreasing grain size. Finer grain size improves ductility for a number of reasons [47, 64, 71]:

1) It is more difficult to propagate small cracks formed by grain boundary sliding through triple points,

2) The crack aspect ratio, which controls the stress concentration at the crack tip, is reduced, discouraging crack propagation,

3) The specific grain boundary area for a given volume fraction of precipitate is reduced, resulting in a decrease in the precipitation density on the grain boundary,

4) The increase in grain boundary nucleation sites reduces the critical strain for dynamic recrystallisation. This can improve the ductility via grain boundary migration.

The effect of grain size on hot ductility for 0.65%C steel is shown in Figure 2.10 [47]. It can be seen from Figure 2.10 that ductility deteriorates considerably as the grain size was increased.

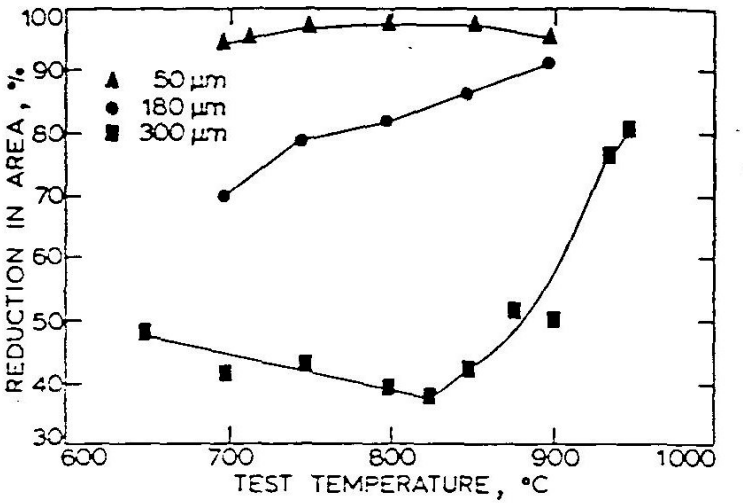

Figure 2.10: Hot ductility curves for 0.65%C steel showing effect of grain size.

While refining the grain size may improve ductility, it is generally noted that the grain size needs to be below 200-300µm to have any significant effect on ductility [47, 71, 72]. Figure 2.10 shows that good ductility still remains at a grain size of 180µm, but not for 300µm. It is generally not possible to achieve such a fine grain size in continuous casting. One should also consider that the detrimental effects of the precipitation of AlN and/or Nb(C, N) override the influence of grain size in microalloyed steels [47].

2.5.2 Precipitation

Precipitation has a major influence on determining hot ductility behaviour of an alloy. Generally, grain boundary precipitation has the greatest influence and the finer the precipitation the lower the ductility [47, 49]. Grain boundary precipitates are detrimental to ductility because they encourage void formation in ferrite films at lower temperatures, while at higher temperatures; they encourage voiding during grain boundary sliding. Failure via microvoid coalescence is encouraged by an increase in precipitation (higher volume fraction) or inclusion density due to the influence of precipitation on void formation. In the case of grain boundary sliding in the austenite, fine precipitates are more effective in pinning boundaries, allowing time for cracks to link-up causing failure. Strain induced precipitation is always finer and more

detrimental to ductility than precipitation that is present before straining for the above reason.

Figure 2.11 shows the influence of particle size in austenite on reduction in area (RA), which was reproduced from data by Comineli for Nb, Ti and Nb-Ti steels [73]. From Figure 2.11 it can be seen that RA values fall sharply when the particle size is below approximately 15nm. While Figure 2.11 displays the influence of particle size on RA, it fails to indicate the influence of volume fraction, or more importantly, interparticle spacing on hot ductility. The interaction of dislocations with precipitates, which determines mechanical properties, is strongly influenced by interparticle spacing. The scatter of RA values with similar particle size (in Fig 2.11) may well be related to changes in volume fraction (and interparticle spacing) for the different steels.

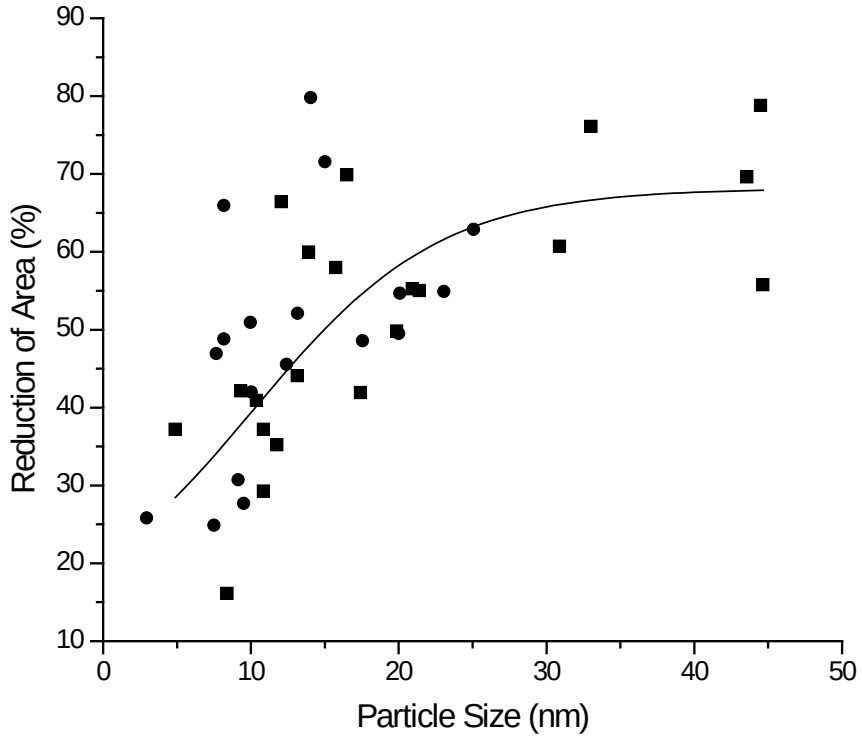

Figure 2.11: Influence of particle size on reduction of area values for Nb, Ti and Nb-Ti steels in single-phase austenite (reproduced from Comineli [73]).

The effect of precipitates on hot ductility depends strongly on their size, distribution (interparticle spacing) and location [73]. Steel composition and thermomechanical history of the ductility test controls these characteristics. Therefore, it is important to understand the influence of composition and test variables on precipitation and hence, transverse cracking.

2.6 Effect of Composition on Hot Ductility

2.6.1 Influence of Carbon on Hot Ductility

The carbon content has a distinct effect on the position of the ductility trough, especially in plain C-Mn steels [66, 74, 75]. As the carbon content increases, the ductility trough shifts to lower temperatures due to the corresponding decrease in the $\gamma \rightarrow \alpha$ phase transformation temperature. This is due to ductility being controlled by the formation of thin films of ferrite at low temperatures, which in turn is controlled by the Ae_3 and Ar_3 transformation temperatures. Recovery of ductility at the low temperature side of the trough (region i) will occur when a sufficient volume fraction of ferrite forms. Recovery of ductility at higher temperatures (region iii) transpires when ferrite films no longer form and dynamic recrystallisation becomes possible.

However, for steels with carbon contents greater than ~0.28%, a distinct change in fracture mode is evident and the trough position shifts approximately 100K higher [74, 75]. Intergranular failure now occurs in the austenite as a result of grain boundary sliding rather than in thin films of ferrite at the prior austenite grain boundaries. The cause of this change in fracture mode was believed to be due to the increasing carbon content raising the activation energy for dynamic recrystallisation and hence, the critical strain for dynamic recrystallisation [75]. Figure 2.12 displays the change of activation energy with carbon content for dynamic recrystallisation as plotted by Crowther [75], along with data generated by Sellars and Sankar (in ref. [75]). Agreement of the data was good. It was believed [75] that this increase in the critical strain for dynamic

recrystallisation produced intergranular failure by enhancing the tendency for grain boundary sliding in austenite.

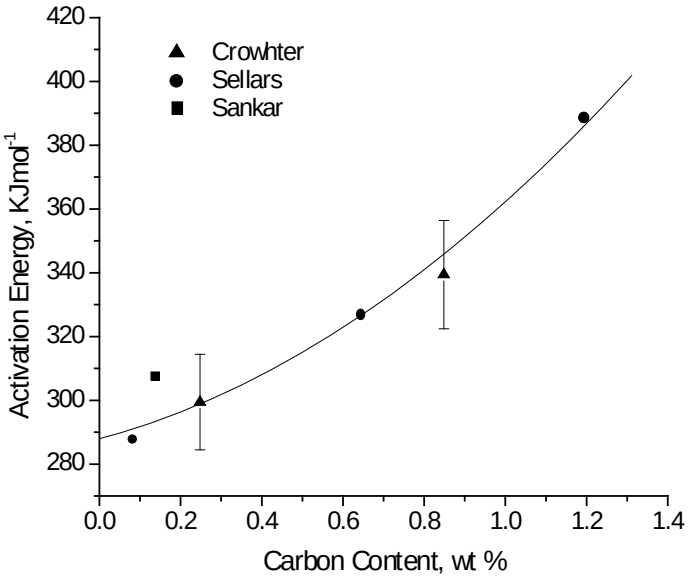

Figure 2.12: Change of activation energy for dynamic recrystallisation with carbon content, reproduced from Crowther et al. [75].

2.6.2 Effects of Sulphur on Hot Ductility

The effect of sulphur (S) content on hot ductility behaviour depends largely on the test conditions. For specimens that are solution treated at 1330°C, it is the amount of S that goes into solution, and subsequently re-precipitates as fine sulphides, which is important for controlling the ductility [47, 49, 64, 69, 76]. Dissolution of sulphides allows S to segregate to grain boundary precipitate/matrix interfaces as well as austenite grain boundaries. This leads to enhanced nucleation of microvoids and a loss in ductility [77]. The amount of S that redissolves depends on the Mn content of the specimen and the purity of the sulphides [64]. Using the solubility data of Turkdogan [51], for a steel containing 1.4%Mn at 1330°C, the amount of S redissolved is ~ 0.001%. Accordingly, once the S content becomes high enough to reach the maximum dissolvable amount at the solution treatment temperature, increasing the S content further will show no change in the hot ductility behaviour.

For direct cast conditions, it is the total S level that is important for controlling hot ductility [47, 49, 64]. Figure 2.13 illustrates the effect of sulphur on RA at two cooling rates, 1°C/s and 4°C/s, where RA decreased as S content increased (from 40ppm to 90ppm) [98]. Abushosha [78] found that increasing the S level caused lower ductility for C-Mn-Al steels and C-Mn-Al-Nb steels under direct cast conditions. Increasing the S level increases the volume fraction of sulphides formed on solidification, reducing ductility. The reduction in ductility is related to the increase in the volume fraction of sulphides at the interdendritic boundaries. The interdendritic boundaries later form the austenite grain boundaries; as a consequence sulphide particles are located at austenite grain boundaries. These sulphide inclusions enhance intergranular failure in austenite by preventing either austenite grain boundaries from migrating or encourage voiding during grain boundary sliding [47, 64, 69]. Sulphide inclusions are also instrumental in accelerating intergranular failure in thin, deformation induced, ferrite films formed at lower temperatures.

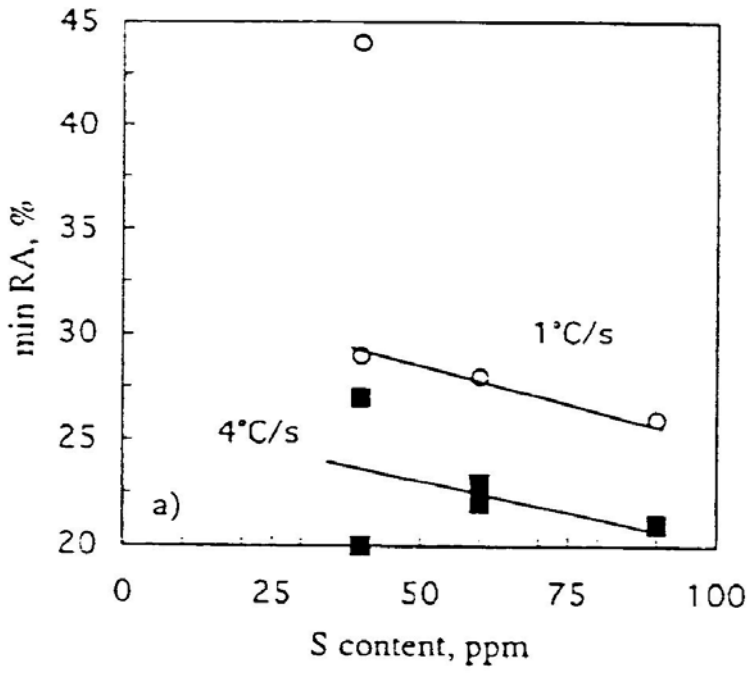

Figure 2.13: Effect of sulphur content on the minimum reduction of area for two cooling rates of 1°C/s and 4°C/s.

In direct cast steels that have been reheated, segregation that occurs during solidification will influence the amount of S that can redissolve at the holding temperature. The regions surrounding the sulphides are depleted in Mn, so a higher volume fraction of S can be redissolved at grain boundaries on reheating [64]. Hence, if specimens are as cast and reheated prior to testing, they may have a lower ductility than if the specimen were reheated to the solution treatment temperature.

Sulphur can impair hot ductility by forming PFZ, allowing strain to concentrate in the weaker regions (where there are no precipitates) in the vicinity of austenite boundaries. In specimens exhibiting poor ductility, PFZ have been found responsible for encouraging intergranular failure. Dense precipitation at the prior austenite grain boundaries and an extremely fine dispersion of sulphides in the matrix are observed in these steels [47, 49]. The influence of S on hot ductility for C-Mn-Al steels that were solution treated at 1430°C are displayed in Figure 2.14 [76]. It can be observed from Figure 2.14 that S can have a significant influence on hot ductility for C-Mn-Al steels subjected to a solution treatment temperature of 1430°C. Sulphur can also weaken austenite boundaries by segregating to the boundary and forming sulphides that encourage the formation of void cavities or by forming low melting point Fe-S compounds [47, 78, 79].

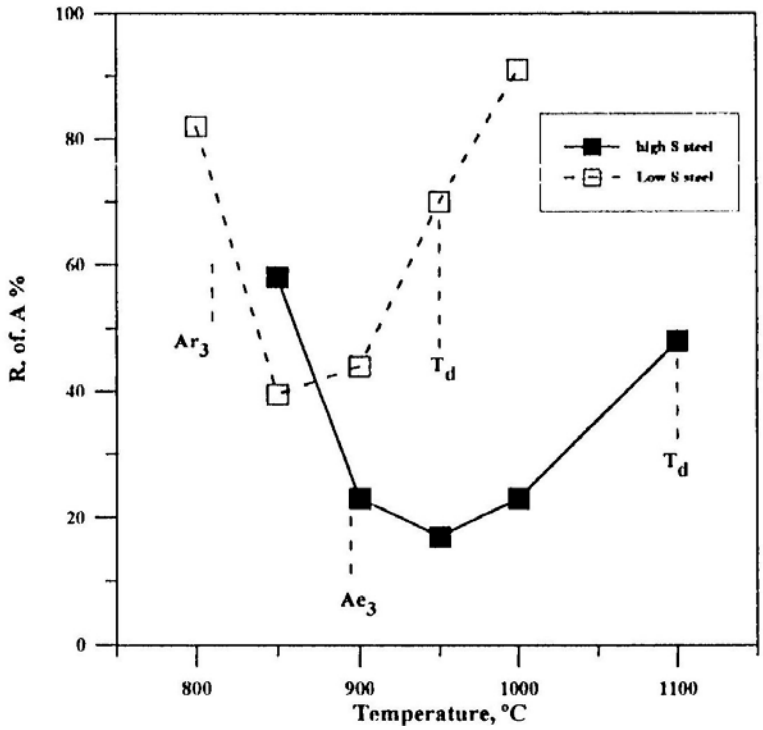

Figure 2.14: Hot ductility curves for high and low S, C-Mn-Al steels. The solution treatment temperature was 1430°C.

It is generally recommended that S levels be kept to a minimum to avoid transverse cracking. Reducing S levels reduces the volume fraction of sulphides available for precipitation on solidification. Calcium treatment has been shown to be beneficial for improving hot ductility by modifying the sulphides. These modified sulphides show little ability to redissolve at 1330°C, thus reducing the amount of S available for precipitation. Calcium additions will also reduce the total amount of S available in the steel (important for direct cast specimens) and reduce precipitation in this way [47, 78, 80].

2.6.3 C-Mn-Al – Influence of AlN on Hot Ductility

Tensile tests generally show that increasing either the Al or N levels leads to deterioration in the ductility, affecting both the width and the depth of the trough. However, in solution treatment tests, at low levels of Al and N (0.02-0.04% Al and 0.005% N), it is often difficult to find any influence of Al or N on the hot ductility, as

precipitation of AlN is very sluggish in austenite [47, 48, 81]. The solubility product, [Al] x [N], was reported to be important in controlling ductility [48]. For high Mn steels (1.4% Mn), the solubility product of [Al] x [N] had to approach 2 x 10^{-4} for precipitation to occur in samples solution treated and cooled to the test temperature, eg. 0.04% Al and 0.005% N.

The precipitation behaviour of AlN in specimens that have been solution treated (1200-1350°C) may not lead to the expected results. For example, AlN precipitation has been observed in low [Al] x [N] steels ([Al] x [N] = 1 x 10^{-4}), where precipitation would not be expected, when temperature oscillations have been introduced [47, 48]. Similar behaviour in direct cast C-Mn-Al steels with low [Al] x [N] levels has been noted, presumably due to marked segregation of Al to the boundaries during solidification [48, 69, 76, 82, 83]. Turkdogan [51] has calculated that the concentration of Al can increase by a factor of 6, due to segregation of Al to the boundaries.

In C-Mn-Al-Nb steels, increasing the Al or the N level generally causes the ductility to deteriorate. The explanation for this phenomenon is not universally agreed upon. Many researchers [47] believe the precipitation of AlN at the austenite grain boundaries in addition to that of Nb(C,N) cause the poor ductility. However, several researchers [47, 48, 78] have found no evidence of AlN precipitation in hot tensile test specimens. There was some evidence to suggest that the deterioration in ductility due to the addition of Al was caused by the presence of Al producing a finer precipitation of Nb(C,N) [84]. It was believed that Al might be increasing the driving force for Nb(C,N) precipitation resulting in closely spaced Nb(C,N) [84]. This idea has not been substantiated.

It should be noted that the detection of AlN is often difficult so precipitation of AlN, especially in high Al or N steels, should not be ruled out as a possible influence on hot ductility. Clearly, for both C-Mn-Al and C-Mn-Al-Nb steels, the Al and N levels should be kept to a minimum to avoid problems with transverse cracking.

2.6.4 C-Mn-Al-Nb - Influence of Nb on Hot Ductility

Precipitation of Nb(C,N) is particularly effective in deepening and widening the hot ductility trough for the following reasons [47, 48, 69, 78, 85]:

1) Very fine matrix precipitation of Nb(C,N) strengthens the matrix and increases the stress in the grain boundary regions,

2) The presence of PFZ, which often occur in Nb containing steels, concentrates strain to the relatively weaker, precipitate free, grain boundary regions,

3) Extensive grain boundary precipitation encourages voiding and the extension of cracks formed by grain boundary sliding. Consequently, Nb precipitates enhance grain boundary sliding,

4) Niobium delays the onset of dynamic recrystallisation to higher temperatures and delays the recovery of ductility to higher temperatures.

Niobium is particularly detrimental to hot ductility, compared to other microalloying elements, because Nb(C,N) precipitates out very rapidly during deformation at a temperature corresponding to that of the low ductility region. The temperature for the maximum rate of precipitation of Nb(C,N) for undeformed austenite (static precipitation) is approximately 950°C, as shown in the Precipitation-Time-Temperature (PTT) diagram by Weiss and Jonas [86] in Figure 2.15. The composition of the steel used to develop the PTT curves was 0.05%C and 0.035%Nb. Figure 2.15 also displays the PTT curves for 5% pre-strain and dynamic precipitation conditions. The application of a 5% pre-strain accelerates the rate of static precipitation by about one order of magnitude and decreases the nose temperature, while dynamic precipitation is more than an order of magnitude faster than that of static precipitation following a 5% pre-strain [86]. Due to the low strain rate, most, if not all, of the Nb is expected to precipitate out during the test, even for static precipitation, with no deformation [86].

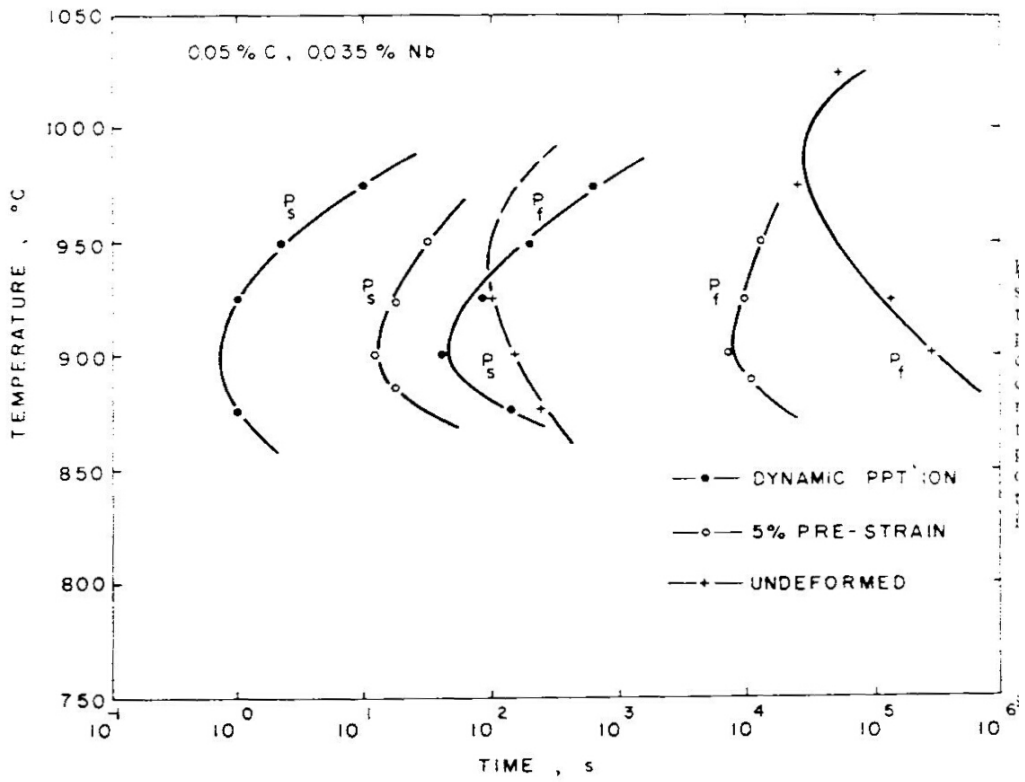

Figure 2.15: The precipitation-time-temperature (PTT) diagram for undeformed austenite (static precipitation), 5% pre-strain and dynamic precipitation for 0.05%C, 0.035% Nb steel.

The ductility of the sample depends largely on the amount of static or dynamic Nb(C,N) precipitation that occurs during straining. Increasing the amount of static precipitation favours ductility. Dynamic precipitates are much finer than static precipitates and finer precipitates are more detrimental to ductility. Precipitates that form after prestraining will also be finer than static precipitates (in undeformed austenite) due to the higher dislocation density [86]. Dynamic precipitation will precipitate-out at a much faster rate than that for static precipitation (as shown in Figure 2.15). Conditions that favour static precipitation will favour improved ductility. Slow cooling has been shown to improve ductility by encouraging the formation of coarse static precipitates of Nb(C,N) and thus reducing the amount of fine strain induced precipitation [47, 49, 69]. Isothermal holding will yield a similar result. Consequently, the cooling rate of the strand should be carefully controlled to improve ductility. For thin slab casting, the increased cooling rate during solidification would be expected to result in a deterioration of ductility.

Grain boundary sliding in the austenite is the accepted mechanism of intergranular failure in Nb steels after the disappearance of ferrite films at prior austenite grain boundaries [47, 72, 78, 81, 87]. As stated earlier, extensive grain boundary precipitation of Nb enhances failure via grain boundary sliding.

Many researchers [47, 69, 78, 88] have shown that the ductility of Nb microalloyed steels that were direct cast and cooled to the test temperature were better when compared to solution treatment samples. This can be readily explained by the influence of solidification on precipitation. Segregation of Nb was believed to be responsible for the formation of coarse Nb(C,N) at interdendritic boundaries and as a result the amount of Nb available for fine strain-induced Nb(C,N) precipitation was reduced. As fine particles are detrimental to hot ductility, reducing the amount of fine particles would be expected to improve ductility. However, other authors have found that ductility was reduced for in-situ melting tests, over that for reheated tests for C-Mn-Al-Nb steels [79, 89]. In these experiments, coarse, interdendritic Nb(C,N) was not observed. In the absence of coarse, interdendritic Nb(C,N) precipitation, precipitation of fine Nb(C,N) is unrestricted and inferior ductility under direct casting conditions would be expected.

In steels containing both Al and Nb it has been shown that Al can deepen and widen the ductility trough, even in small amounts [47]. This is supported commercially where it has been observed that increasing Al and, in particular, N will increase the likelihood of transverse cracking in Nb containing steels [47]. The influence of AlN on Nb steels was discussed in more detail in the previous section on C-Mn-Al Steels.

2.6.5 C-Mn-Al-Ti- Influence of Ti on Hot Ductility

The addition of Ti can result in a significant improvement in hot ductility for steels tested under solution treatment conditions. This is due to TiN and Ti-rich precipitates not completely re-dissolving at the solution treatment temperature so they are able to pin the austenite grain boundaries and prevent rapid grain growth [47, 48, 87, 90]. Therefore, large improvements in ductility observed for solution treatment samples are largely due to grain refinement rather than compositional effects. However, Ti can also

improve ductility from its ability to combine preferentially with nitrogen. This will reduce the amount of N available for precipitation as either AlN or Nb(C,N), both of which will reduce ductility.

For direct cast tensile specimens, Ti has little influence on the grain size and a coarse solidified structure is formed. Hence, the benefit of Ti on hot ductility via grain refinement is lost. Previous work [47] has shown that the benefit of Ti to the ductility for direct cast conditions is either small or it may be detrimental. Controlling the size and form of Ti precipitation is the key to controlling the influence of titanium on hot ductility. If Ti additions are to benefit ductility, then Ti precipitates must be sufficiently coarse so as not to be detrimental to ductility. Conversely, if fine particles are formed then ductility is expected to deteriorate.

Coarse TiN particles are favoured if they are formed at high temperatures and there is sufficient Ti in solution to allow coarsening of these particles during cooling [48]. The Ti:N ratio will indicate how much Ti is in solution and is an important parameter for controlling ductility. When the stoichiometric composition for Ti:N is reached, 3.4:1, the maximum volume fraction of precipitates can be formed at the lowest temperature. This produces extensive fine precipitation (<10nm) so such a composition would be expected to give the worst ductility [48]. If Ti:N is at the stoichiometric composition, then low ductility may only be avoided if the Ti level is sufficiently low (<0.01%) to limit the volume fraction of precipitation.

When excess Ti is in solution, there is a greater driving force for precipitation at higher temperatures and subsequent coarsening can occur during cooling. To obtain an excess of Ti, either the Ti addition must increase or the N level must decrease. Raising the Ti level can cause problems with the impact behaviour of plate steel due to excessive numbers of coarse Ti rich particles [48]. Raising the Ti level will also increase the cost of the alloy. For the above reason, lowering N is generally preferred to raising titanium. For low N steels (~0.004%N), either low levels (0.01%Ti) or high levels (0.04%Ti) of Ti are recommended [48] (to avoid stoichiometric ratio) to give optimum ductility. Low levels of Ti will reduce the amount of precipitation while high levels, such as Ti:N ratios of 4-5:1, will promote precipitation at high temperature and the excess Ti will

promote coarsening. However, low N levels are not always possible, particularly for mini-mills based on TSC that are predominantly fed by electric arc furnace steel, where N levels >0.008% are typical. High Ti:N ratios can improve ductility in these conditions but the precipitate fraction of coarse particles will be high, resulting in poor impact properties [48].

The cooling rate is a significant factor in controlling morphology of the precipitates, which in turn, will have a significant effect on hot ductility. Slow cooling favours the formation of coarse TiN particles and promotes good ductility [48, 90, 91]. Increasing the cooling rate will result in deteriorating ductility. Higher cooling rates typical of TSC can lead to finer precipitation and a corresponding deterioration of ductility. The high straightening temperatures, 950-1000ºC, for TSC are favourable for ductility and are expected to offset the influence of the higher cooling rate [48]. Higher straightening temperatures can benefit ductility by promoting coarsening of precipitates [48]. Unfortunately for Ti steels, previous research [48, 90, 91] has shown that the cooling rate must be in the order of 25K/min to have any real impact on ductility. Such a cooling rate is impracticable for continuous casting of most grades of steels.

Commercial data on the influence of Ti additions on the problem of transverse cracking indicate that small Ti additions have a beneficial effect [48, 90, 91]. This suggests that laboratory conditions do not indicate the true behaviour of Ti on the problem of transverse cracking. This discrepancy is most likely explained by the influence of temperature oscillations on the precipitation of Ti during continuous casting. The cyclic rise and fall of surface temperature is known to encourage precipitation so it can improve ductility by promoting the formation of Ti particles at higher temperatures [47, 58, 61, 62]. The influence of thermal history on hot ductility is dealt with in more detail in Section 2.7.4: “Thermal History”.

Care must be taken when interpreting hot ductility data on Ti containing steels. Furthermore, conditions in the small tensile samples are very different from those experienced at the surface of a slab, as was discussed in Section 2.3. The behaviour of Ti in tensile specimens is likely to be different from that in a continuously cast strand.

2.6.6 Influence of Ti on Nb Microalloyed Steels

The influence of Ti on C-Mn-Al-Nb steels follows the same trends as was discussed for the influence of Ti on hot ductility in the previous section. The important aspects will again be briefly reported. Hot ductility is generally controlled by the precipitate size and the volume fraction (or the level of microalloying elements added to the steel). Adding Ti to Nb steels generally results in coarser particles but can lead to an increase in volume fraction [93]. As a result, if Ti is to be beneficial, particles must be sufficiently coarse to counter-act the increase in volume fraction. Conditions that favour coarse precipitation are; low Ti/N ratios, high-test temperatures and slow cooling rates.

Slow cooling rates (~25K/min) are impractical for the continuous casting of microalloyed steel grades, thus little benefit from manipulating the cooling rate can be obtained. A low Ti/N ratio (low Ti and high N) encourages coarse precipitation at high temperatures and reduces fine strain-induced precipitation [92, 93]. Comineli [93] found that high Ti/N ratios, 8:1 can also encourage coarse precipitation and hence, improved ductility. The composition of the steel in question had a high Ti level of 0.045%. Considering 0.01%Ti is the optimum Ti addition for HAZ toughness improvement [48], this approach to improving ductility is not ideal.

Commercially, small additions of Ti have been found to reduce the occurrence of transverse cracking for Nb bearing steels [48, 63, 90, 92-94]. It has been suggested [51] that for Nb steels with Ti additions, coarse TiN particles formed on solidification act as preferential precipitation sites for niobium. Niobium precipitates at higher temperatures than normal on these Ti particles, coarsens on cooling and consequently become too coarse to influence transverse cracking during straightening. As a secondary benefit, there will be less Nb left in solution to form detrimental strain-induced precipitation.

Laboratory work generally fails to show any benefit from adding Ti to Nb steels, unless the cooling rate is slow (25K/min) [63, 90, 92, 93]. Slow cooling allows time for particles to coarsen sufficiently to give good ductility. Abushosha [63] and Suzuki [95] both found that Ti additions to Nb steels improved hot ductility at slow cooling rates, as

precipitates had sufficient time to coarsen and their influence on hot ductility was reduced. Recent work by Comineli reported that Ti additions lowered the ductility of C-Mn-Al-Nb steels [93] as well as for C-Mn-Al steels [73], where the cooling rate was 100K/min or higher. It has been suggested by Mintz [48] that the benefit of Ti cannot be seen due to the difficulty in accurately simulating the complex cooling patterns before straightening.

However, recent work by Luo [92] found low ductility in Nb-Ti steels, regardless of the prior thermal history. It should be noted however, that the prior thermal history was only a simple simulation, where undercooling by 100°C before reheating to the test temperature was performed. A cyclic cooling pattern was not simulated, and as discussed earlier, cyclic temperature oscillations experienced by a continuously cast slab prior to straightening, may determine the influence of Ti on transverse cracking.

Luo [92] concluded that small additions of Ti might only be considered advantageous to the hot ductility of electric arc furnace steels, due to their high N contents (0.008%N). However, commercial data suggests that Ti can be beneficial at much lower N levels than 0.008%N. For example, for steels with 0.0045%N, additions of Ti in the range of 0.015-0.02% [51], 0.02-0.04%Ti and 0.015-0.04%Ti [90] have been shown to have improved transverse cracking behaviour. In fact, Luo [92] found that additions of 0.015-0.04%Ti to a 0.1%C-0.03%Nb-0.005%N steel lowered ductility. It is clear that the influence of Ti on C-Mn-Al-Nb steels is not fully understood and requires further research.

2.6.7 Role of Inclusions/Residuals on Hot Ductility

Residual elements, particularly Cu and Sn, can be detrimental to slab surface quality and encourage transverse cracking by the phenomenon known as “hot shortness”. Residual elements more noble than iron, such as Cu, Sn, Ni, As and Sb, cannot be preferentially oxidised during the solidification of the steel in air. Under oxidising conditions, Fe is oxidised from the surface layer and residual elements progressively enrich in the sub-scale layer. Once a residual enriches to a level exceeding its solubility

limit in austenite, it will precipitate out as a low melting point phase and seriously impair ductility [48].

Copper is the major cause of hot shortness, it has a solubility limit of 9% and such enrichment is quite possible under severe oxidising conditions. The Cu rich phase that forms is molten (melting point of 1080°C) and tends to penetrate the austenite grain boundaries, weakening them and leading to surface cracking during subsequent processing. Nickel can prevent hot shortness by stabilising austenite and increasing the solubility of Cu in the austenite. Increasing the solubility of Cu in austenite may prevent precipitation of low melting point Cu rich phases. The Ni:Cu ratio must be in the range 1.5 to 2.0 to avoid hot shortness [48, 96].

Hot ductility tests performed under laboratory conditions have generally shown that Cu has had little influence on the ductility trough. This is because most testing is performed under a controlled atmosphere, not oxidising conditions. Mintz [96] has studied the effects of oxidising conditions for steels containing up to 5% Cu with or without Ni additions. Results revealed that an oxidising atmosphere had little influence on solution treatment samples but was detrimental for direct cast tensile samples. Nickel proved to be effective in preventing the detrimental effect of Cu on hot ductility behaviour under oxidising conditions. Hot shortness was ruled out as the explanation for the decrease in ductility as no evidence of Cu rich films penetrating the austenite grain boundaries were found. Fine copper sulphides formed at austenite boundaries during cooling were believed to have been responsible for the reduced ductility.

2.7 Effect of Test Variables on Hot Ductility

2.7.1 Cooling Rate

The influence of cooling rate on hot ductility for a wide range of steels has been studied over the range of 25 to 240K/min. Generally, increasing the cooling rate results in lower ductility for most types of steel. In most cases, the decrease in ductility with increasing cooling rate is ascribed to either the formation of a finer particle size or finer inclusion distribution.

For C-Mn steels, a finer MnS distribution in the ferrite film surrounding the austenite grains, as well as a reduction in thickness of the ferrite film, can led to the deterioration in ductility at increased cooling rates [69]. In the case of C-Mn-Al steels, the deterioration in ductility is due to finer AlN precipitation and/or a finer sulphide distribution [69, 82]. For C-Mn-Al-Nb steels, an increase in cooling rate can lead to a greater amount of Nb being held in solution, resulting in an increase in finer, more detrimental, strain-induced Nb(C,N) precipitation [82].

The addition of Ti to Nb containing steels under solution treatment conditions can significantly improve ductility at low cooling rates (25K/min) but little or no improvement is shown at higher cooling rates (60-200K/min). At slow cooling rates, the Nb can precipitate out at high temperatures on TiN precipitates, allowing precipitates to coarsen before testing [49, 82, 90]. For solution treatment conditions, TiN precipitates can restrict grain growth in the steel, resulting in finer grain size and a large improvement in ductility. For direct cast C-Mn-Al and C-Mn-Al-Nb steels, the influence of TiN particles on grain size is lost and accordingly, Ti additions are observed to have little influence at any cooling rate [49, 90]. The addition of Ti may improve ductility by reducing the N available for AlN and Nb(C,N) precipitation. Ductility is improved due to the reduced volume fraction of precipitation [49, 78, 90, 91].

2.7.2 Strain Rate

The typical strain rates applicable to straightening during continuous casting are between 10^{-3} and 10^{-4} s^{-1}. Invariably, increasing the strain rate improves the hot ductility and a narrower trough is observed [47, 49, 69, 97-99]. It is usually found that an increase in strain rate will raise the minimum reduction of area value but will not influence the position of the minimum value. Higher strain rates improves hot ductility for the following reasons [47, 69]:

1) Reduced time for strain induced precipitation,

2) Grain boundary sliding is reduced,

3) There is insufficient time for the formation and growth of voids at the grain boundaries,

4) Increasing the strain rate work hardens the ferrite film, thus reducing the stress concentration in the ferrite.

Unfortunately, it is not possible to vary the strain rate of the continuous caster enough to have any significant affect on hot ductility [47, 48]. In thin slab casting the strain rate can be greater by a factor of approximately five compared to conventional casting and this can lead to improved hot ductility [48].

2.7.3 Test Direction

Test direction can influence hot ductility, particularly for steels with high S levels [100]. Specimens tested in the short transverse direction have the lowest ductility while samples tested in the longitudinal direction have the greatest ductility. This scenario is also true for room temperature tensile tests. The anisotropy of the hot ductility is intensified by lower strain rates (3×10^{-4} s^{-1}) and high S levels, but is improved for Ca modified steel [100]. Calcium improves hot ductility by modifying the sulphide inclusions from elongated inclusions to spherical [80, 100]. Calcium rich sulphides

compared with MnS have a much lower solubility at 1330ºC. This reduces the amount of S available for subsequent precipitation as fine sulphides at the γ-grain boundaries for solution treatment tests [80].

The influence of test direction on hot ductility is closely related to the shape and position of MnS inclusions. Elongated inclusions act as regions of weakness and stress concentrators, in the same way as a notch or a crack [100]. The strain concentration associated with elongated inclusions is considered to be proportional to the ratio of the axis normal and parallel to the strain axis [101]. Hence, when a sample is hot tensile tested under solution treatment conditions in the rolling direction, the stress concentration from the elongated inclusions will be much lower compared to the transverse direction. As a result hot ductility is better in the longitudinal direction.

2.7.4 Thermal History

The thermal cycling pattern experienced at the surface of a slab is very complex and difficult to simulate in a laboratory tensile test. Temperature oscillations are produced at the slab surface from the alternate impingement of the water sprays and contact with the guide rolls [50, 54, 102]. Simulations of the thermal history have been carried out [47, 58, 61, 62, 95, 103, 104] and generally show that the thermal history does affect hot ductility.

Specimens that have been subjected to thermal history simulations display hot ductility that is almost always lower than that predicted by simple hot ductility tests. The simplest technique for investigating the influence of thermal history on hot ductility is to undercool the specimen below the test temperature. The minimum drop in temperature (undercooling) has a significant influence on ductility. A drop in temperature allows an increased volume fraction of finer precipitates to be present at the start of testing and consequently, the ductility is reduced [47, 59, 60]. This has been shown to apply to C-Mn-Al, C-Mn-Al-Nb and C-Mn-Al-Nb-Ti steels. Introducing cyclic temperature variations for solution treatment specimens will also cause the ductility trough to deepen and widen [59].

Luo [92] investigated the effects of 'prechilling' (undercooling) on hot ductility of C-Mn-Al-Nb and C-Mn-Al-Nb-Ti steels. Specimens were melted, then cooled at 4°C/s to 100°C below the deformation temperature, held for 1 minute, reheated at the same rate to the test temperature and deformed at 5×10^{-4} s^{-1}. Prechilling reduced ductility for both steels when tested at 800°C but there was practically no influence above 900°C.

The influence of undercooling by 100°C was also investigated by Cardoso [83], on C-Mn-Al steels that were solution treated at 1350°C. Undercooling by 100°C in the austenite region encouraged AlN precipitation, which increased the temperature for the onset of dynamic recrystallisation and a widening of the trough was observed. The undercooling also resulted in ferrite forming earlier, improving ductility at lower temperatures; consequently, troughs were raised by 50-100°C. Undercooling influenced the low Al steel (0.026%Al) more than the high Al steel (0.085%Al), because AlN precipitation was enhanced for the low Al steel but was already significant for the high Al steel. This suggests that thermal cycling, as found in continuous casting, can deteriorate the ductility of low Al steels and simple hot ductility tests may not reveal this effect, leading to misleading results.

Mintz [59] investigated the influence of two cyclic thermal patterns on the hot ductility of C-Mn-Al-Nb steels, solution treated at 1330°C. The average cooling rate to the test temperature was 60°C/min and two cyclic patterns were introduced at 1100°C, one with an amplitude of ±50°C the other ±100°C. Results showed that introducing the thermal cycles lowered hot ductility due to pre-precipitation of Nb(C,N) at the bottom of each cycle. Increasing the amplitude of the oscillation further widened the ductility troughs. Suzuki [95] performed similar work where cyclic temperature oscillations, up to amplitudes of 250°C, were simulated prior to solution treatment at 1330°C. Results indicated that hot ductility decreased as the temperature cycles increased in magnitude due to an increase in Nb precipitation. The above results suggest that water spray cooling, during continuous casting, should be carefully controlled to minimise thermal oscillations for Nb bearing steels.

Research by El-Wazri et al. [61, 103] and also by Akhlaghi et al. [62, 104] followed a similar thermal history to that reproduce in Figure 2.16. In general, specimens were melted, cooled at ~10°C/s to T_{min} (700-900°C), reheated to T_{max} (1100-1200°C) at a slower rate, ~100°C/min, and slow cooled to the unbending temperature T_u (~1000-1180°C). No cyclic thermal oscillations were introduced to simulate the thermal pattern due to water spray cooling. In general, the hot ductility of specimens subjected to thermal simulations were almost always lower than that predicted by isothermal tests.

Akhlaghi et al. [62, 104] also subjected specimens to three different deformation schedules, prior to the tensile test. The deformation schedules were; i) deformation close to the melting point, ii) deformation at intermediate temperatures and iii) deformation at low temperatures. Deformations close to the melting point dramatically improve ductility. Ductility improvement was attributed to a refinement in austenite grain size via a strain induced transformation of δ–ferrite to austenite and a decrease number of precipitates. Deformation at intermediate temperatures had no influence. Deformation at lower temperatures decreased ductility via an increase in precipitation due to strain induced precipitation.

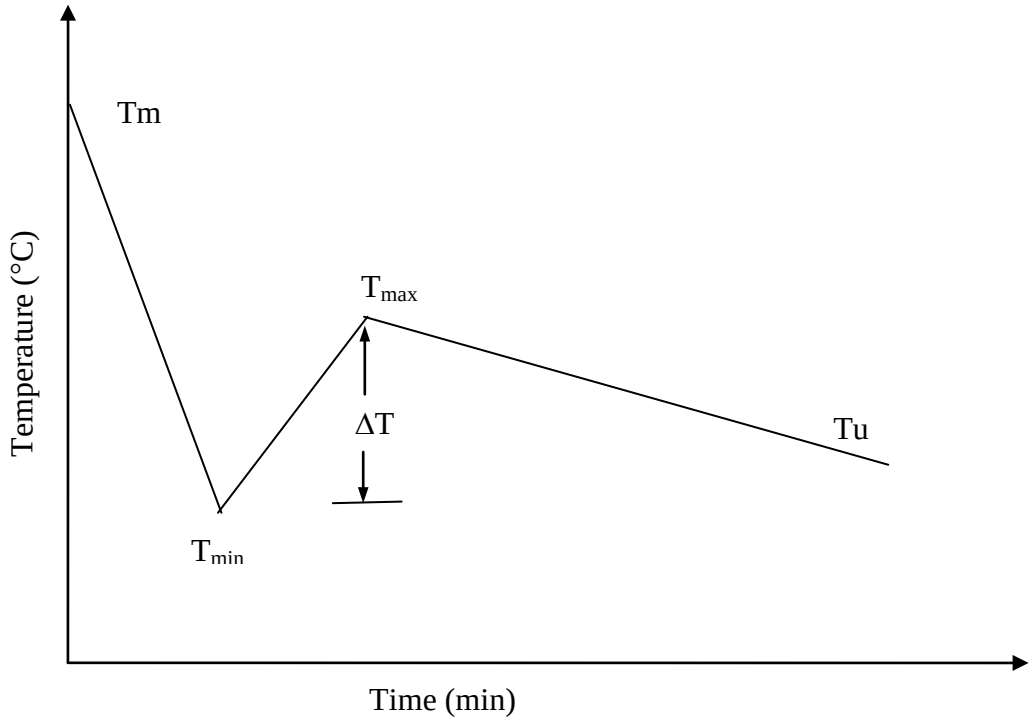

Figure 2.16: Representative diagram depicting the general thermal histories simulated in references [61, 62, 103, 104].

2.8 Dynamic Recrystallisation and Deformation Induced Ferrite

2.8.1 Deformation Induced Ferrite

Thin films of ferrite that form at the austenite boundaries are usually deformation induced and can occur over a wide temperature range from the undeformed Ar_3 to the Ae_3 [74, 105]. Deformation induced ferrite is influenced by the amount of strain, the strain rate and the austenite grain size. Very small strains are sufficient to induce thin films of ferrite and these films are readily formed in both fine grain and coarse grain steels [68]. At low strain rates, thin bands of ferrite are able to recover so they remain soft and the strain will remain concentrated at the boundary. Consequently, low strain rates result in particularly poor ductility [67, 68, 74]. Increasing the strain rate is believed to improve ductility by work hardening the ferrite boundaries and reducing the strength differential between austenite and ferrite. This allows an increase in deformation to occur in the austenite matrix, distributing the strain more uniformly. As

the strain rate increases further, the thickness of the deformation induced ferrite band increases and ductility improves [67, 68, 74].

The austenite grain size plays an important role in controlling the formation of deformation induced ferrite, which in turn controls ductility. For fine-grained austenite, deformation at low strain rates produces a large volume fraction and a more homogeneous distribution of ferrite. For coarse-grained austenite, only narrow bands of ferrite form, even at very low strain rates (~10^{-4} s^{-1}) [67, 68]. Consequently, hot ductility in fine-grained steels at low strain rates is superior to the ductility of coarse-grained steels.

2.8.2 Dynamic Recrystallisation Verses Deformation Induced Ferrite

At the high temperature end of the trough, the improvement in hot ductility is generally ascribed to two factors: the disappearance of deformation induced ferrite or, the occurrence of dynamic recrystallisation. It is difficult to separate the effect of these two parameters on the recovery of ductility. In plain C-Mn and C-Mn-Al steels, the Ae_3 temperature that marks the onset of good ductility, is generally high enough for dynamic recrystallisation to occur. Therefore, it is not possible to independently assess the influence of the removal of thin ferrite films from the occurrence of dynamic recrystallisation on the recovery of ductility. For C-Mn-Al-Nb steels, dynamic recrystallisation and the full recovery of ductility are not observed until temperatures well above the Ae_3. However, the independence of dynamic recrystallisation on the recovery of hot ductility is still difficult to assess due to the overriding influence of strain-induced precipitation [105].

In plain C-Mn and C-Mn-Al steels, it is often observed that dynamic recrystallisation first occurs at the temperature when ductility begins to recover. This correlation arises because deformation induced ferrite stifles dynamic recrystallisation and by the time deformation induced ferrite is removed the temperature is high enough for dynamic recrystallisation to readily take place [105]. The relative contributions of these two factors are difficult to separate. Plain C-Mn steels, high in C (>0.35%), have been

shown [75] to have a very wide ductility trough that extends into the single-phase austenite region, well above the Ae_3 temperature. In these steels, the removal of deformation induced ferrite did not lead to improved ductility as the failure mechanism was replaced by grain boundary sliding. Recovery of ductility can only occur during grain boundary sliding, when there is sufficient grain boundary migration, i.e.. Dynamic recrystallisation, to isolate the cracks and prevent them joining together [74]. Dynamic recrystallisation can play an important role in the recovery of ductility in plain, high carbon, C-Mn steels.

In coarse-grained microalloyed steels and high Al and N containing C-Mn-Al steels, it is often observed that the recovery of hot ductility at high temperature coincides with the occurrence of dynamic recrystallisation. However, dynamic recrystallisation is not the controlling factor, it is the removal of precipitates and/or inclusions that controls the recovery in hot ductility [105]. At low strain rates, 10^{-3} to 10^{-4} s^{-1}, grain boundary sliding is the chief mode of failure at high temperature. Precipitates and inclusions enhance failure during grain boundary sliding, so the removal of precipitates and inclusions will improve ductility. The apparent correlation observed between the recovery of ductility and the onset of dynamic recrystallisation can be explained by the influence of precipitation on dynamic recrystallisation. Particles at the austenite boundaries discourage dynamic recrystallisation so the temperature when dynamic recrystallisation can occur is related to the volume fraction of strain-induced precipitation [105]. If there is a large fraction of strain-induced precipitation, then ductility will only improve when the temperature is high enough to significantly coarsen the precipitates.

2.8.3 Modelling of Dynamic Recrystallisation

Attempts have been made to model the hot ductility curve based on dynamic recrystallisation being responsible for the recovery in hot ductility at the high temperature side of the trough. The model is shown in Figure 2.17a, [105], where ε'_c is the critical strain for dynamic recrystallisation and ε'_f is the total strain to failure in the absence of dynamic recrystallisation. The temperature at which dynamic

recrystallisation first occurs, T_D, can be found from the interception of ε'_f and ε'_c. This model can also explain the influence of strain rate and is illustrated Figure 2.17b. Raising the strain rate increases both ε'_f and ε'_c, resulting in a shallower and narrower trough. However, this model fails to take into account the influence of second phase particles and does not fully address the influence of grain boundary sliding on RA values [48].

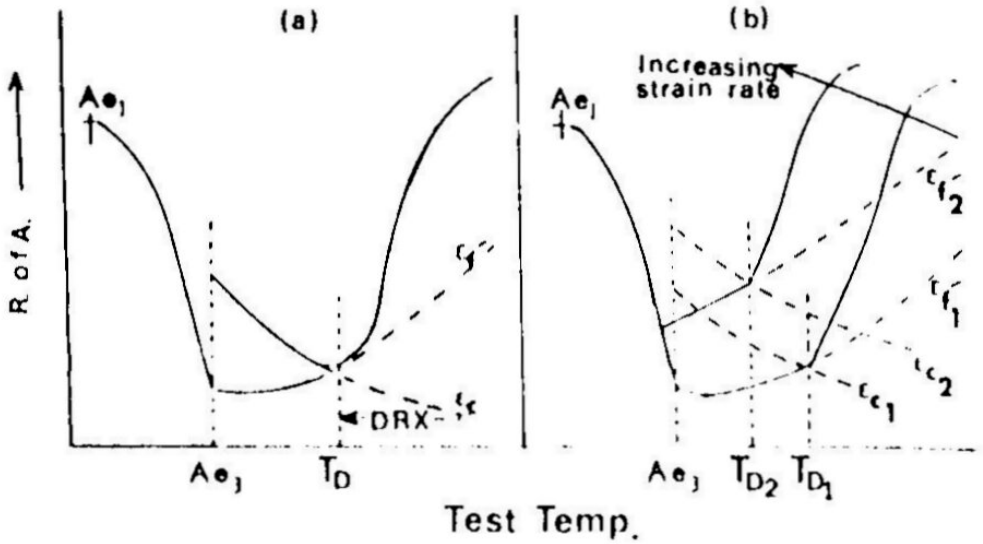

Figure 2.17: Schematic diagrams showing (a) how the width of the ductility trough could be controlled by dynamic recrystallisation (DRX) and (b) how increasing the strain rate can reduce the depth and width of the trough.

2.8.4 Commercial Implications on the Formation of Deformation Induced Ferrite and Dynamic Recrystallisation

In practice, the strain involved during straightening is too low (~2%) and the size of direct cast grains too large for dynamic recrystallisation to take place. This means that attention must be concentrated on factors that can decrease the depth of the ductility trough when coarse unrecrystallised austenite is present. Controlling the temperature during straightening is the most relevant method for reducing the occurrence of transverse cracking. Raising the temperature can improve the problem of transverse cracking by promoting the resolution and coarsening of precipitates. [74, 105]

Maintaining the temperature above the Ae_3 will prevent the formation of deformation induced ferrite. Deformation induced ferrite has been shown to occur at the low strain rate for straightening [74]. Straightening at low temperatures, where a large volume fraction of ferrite is present, should be beneficial for transverse cracking [74, 105]. However, straightening at low temperature is not practical for microalloyed steels because the microalloying additions must be kept in solution to maximize their benefit during further thermomechanical processing. Finally, the refinement of the austenite grain size due to rapid solidification during thin slab casting can also be beneficial for the hot ductility [74].

2.9 Concluding Remarks

There are still casting problems for difficult grades of steel, where peritectic (0.08 – 0.16%C) microalloyed steels containing niobium give the most trouble, therefore, research on these types of steels is still required. Furthermore, it is generally accepted that solution treatment hot ductility tests are adequate for revealing the hot ductility behaviour of Nb bearing microalloyed steels. However, it is important to simulate continuous casting conditions as accurately as possible. It has been seen over the course of the preceding two chapters that there are significant microstructural differences between re-heated structures (solution treatment) and as-cast (direct cast) structures. Therefore, it is important to test Nb-bearing steels under direct cast conditions to more closely simulate the microstructure of a continuously cast slab.

There has been little work done on the influence of TSC on the hot ductility of microalloyed steels. Studying TSC conditions requires ductility test to be preformed under direct cast conditions and cooling rates of approximately 200K/min (the average cooling rate near the surface of a thin cast slab). Thus, hot ductility experiments under TSC conditions were performed to improve the knowledge of this area.

The influence of the complex cooling patterns during continuous casting has been shown to influence hot ductility results. However, due to the difficulties in simulating the complex cooling patterns, research in this area has seldom been done and generally,

only simple cooling patterns have been investigated. A greater understanding of more complex cooling patterns on hot ductility tests is required, particularly for direct cast conditions.

There are still conflicting results on the claimed beneficial effects of small additions of Ti on improving transverse cracking, particularly for Nb-Ti steels, in hot ductility experiments. Furthermore, hot ductility experiments, particularly direct cast tests, generally fail to show any benefit of Ti additions despite the fact that there is substantial commercial evidence that Ti additions decrease the occurrence and severity of transverse cracking. Consequently, the influence of Ti on the hot ductility of Nb microalloyed steel was investigated.

Chapter 3:

Experimental

Chapter 3: Experimental

3.1 Introduction

Transverse cracking during straightening of microalloyed steels, particularly in the peritectic carbon range, is still a problem in industry, especially for thin slab casters. Therefore, microalloyed steels with carbon contents in the peritectic range were chosen for this investigation. Conditions for tensile tests were chosen to simulate both conventional casting (200-250mm thick slabs) and thin slab casting (50-100mm thick slabs) conditions. A Gleeble 3500 was used to perform laboratory tensile tests, which have been shown to correlate well with the problem of transverse cracking [47].

Niobium additions are well known to increase the likelihood of transverse cracking during continuous casting. The Nb level of 0.02% was chosen because similar levels are commonly found in industry. The C-Mn-Al-Nb steel (referred to as Nb Steel) was included to investigate what effects relatively low Nb additions have on transverse cracking properties. The C-Mn-Al-Nb-Ti steel (referred to as Nb-Ti Steel) was chosen to determine the effects of addition of Ti to Nb steels, as there have been contradictory reports on the effect of Ti on the transverse cracking properties of Nb bearing steels. The C-Mn-Al-Ti steel (referred to as Ti Steel) was chosen to observe the effect of Ti in the absence of niobium. The C-Mn-Al steel was used as a base composition for the microalloyed steels.

3.2 Materials and Compositions

Steel was supplied by BHP- Port Kembla, where blocks were cut from 230mm thick, conventionally cast slabs, in approximately the position shown in Figure 3.1. The blocks were taken from as-cast slabs, prior to the re-heating and rolling stage. Care was taken when cutting-out the blocks to avoid centreline segregation and the side edges of the as-cast slab. The heat-affected regions from the oxy-cuts were removed by machining before preparation of the tensile samples.

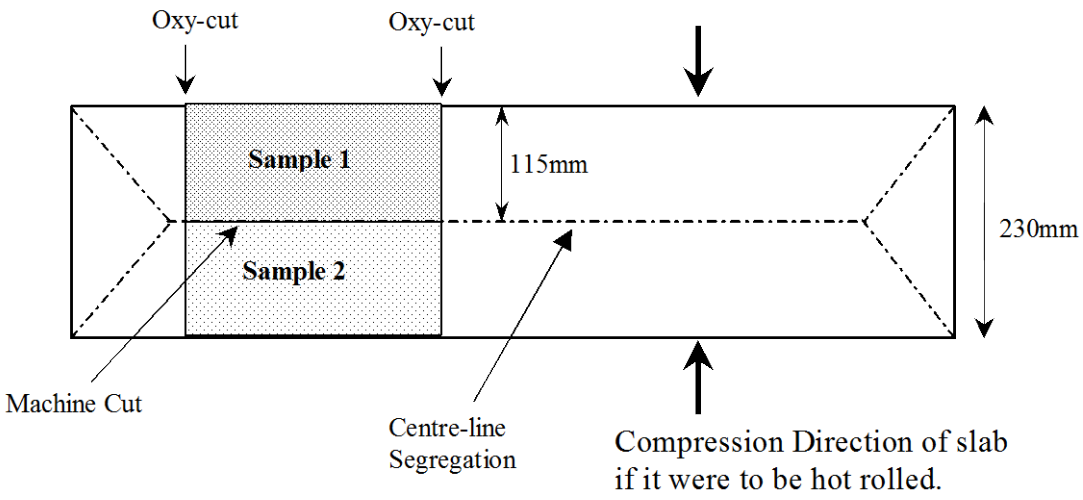

Figure 3.1: Position of steel block samples taken from 230mm as-cast slab, prior to hot rolling.

The chemical compositions of the steels studied are given in Table 3.1. The C-Mn-Al steel represents the base composition. This allowed comparisons to be made to determine the influence of Nb, Ti and Nb-Ti on C-Mn-Al steels. The Nb steel had slightly lower carbon than the C-Mn-Al steel, a similar Mn content, 0.022% Nb and there was no Silicon (Si) in this grade. The Nb-Ti steel had a higher Mn and Si content then the C-Mn-Al steel and contained 0.019% Nb and 0.015% Ti. The Ti steel was similar to the Nb-Ti steel but contained 0.018% Ti and no Niobium. All four steels had similar Al and N contents.

Table 3.1: Chemical compositions of alloys.

Element Wt.%	C-Mn-Al	Ti	Nb-Ti	Nb
C	0.165	0.165	0.160	0.155
P	0.023	0.015	0.016	0.008
Mn	0.63	1.11	1.23	0.73
Si	0.14	0.19	0.25	<0.005
S	0.012	0.012	0.017	0.013
Ni	0.02	0.018	0.017	0.021
Cr	0.019	0.015	0.021	0.019
Al (total)	0.031	0.033	0.027	0.036
Nb	<0.001	<0.001	0.019	0.022
Ti	<0.003	0.018	0.015	<0.003
N	0.0021	0.0027	0.0031	0.0033
Ti:N	N/A	6.67	4.84	N/A
[Ti][N]	N/A	4.86×10^{-5}	4.65×10^{-5}	N/A

3.3 Tensile Testing: Gleeble Thermomechanical Simulator

A Gleeble 3500 thermomechanical simulator was used to carry out all hot tensile tests. The Gleeble 3500 is a fully integrated, digital closed loop controlled, physical simulation and thermomechanical-testing machine. A series 3 digital control system enables either fully automatic, fully manual control or a combination of both. Control methods include, stroke, force, stress, strain and variables include stroke, force, engineering and true stress and strain, strain rate, temperature and time. The Gleeble mechanical system utilises a hydraulic servo system, capable of exerting 10 tons in tension and compression, at high strain rates. Direct resistance heating allows high speed heating (10,000°C/s) and holding grips with high thermal conductivity allows high cooling rates. Extremely high cooling rates can be achieved via air, gas or water quenching.

Tensile samples were machined with their axes parallel to the rolling direction. A good surface finish was attained to reduce the likelihood of machining marks acting as stress raisers. Sample dimensions were 115mm in length, 10mm in diameter and included a 10mm threaded portion at each end. The specimen set-up is shown in Figure 3.2. Copper grips hold the specimen in the jaws of the Gleeble to ensure precise, controlled and reliable resistive heating. C-shaped clamps are used to firmly hold the grips and the sample in position.

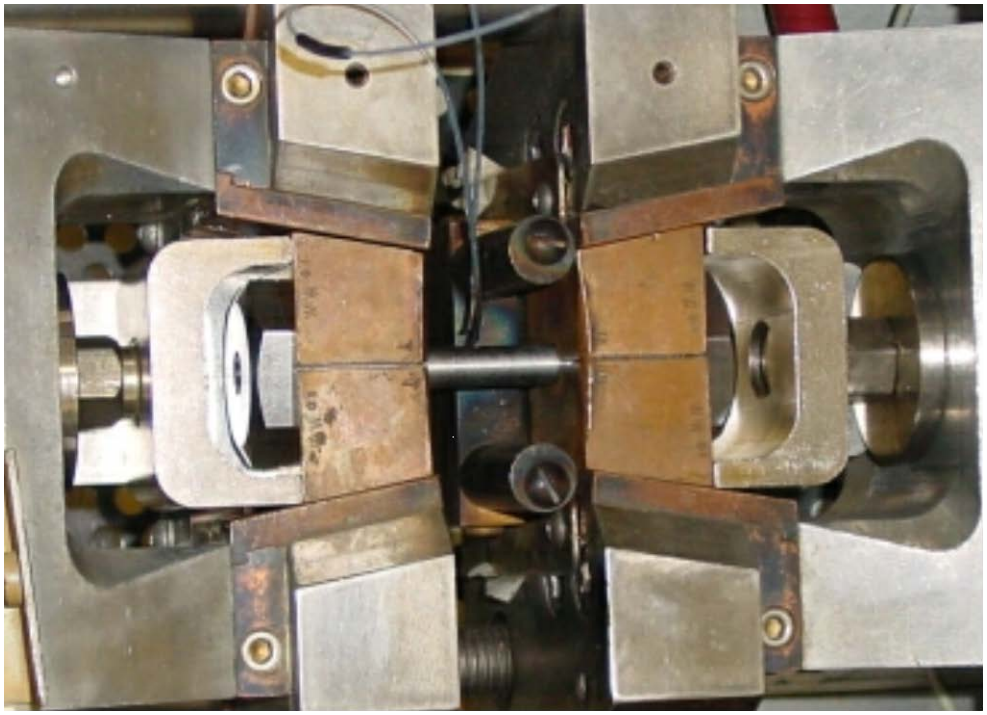

Figure 3.2: Specimen set-up for tensile testing in the Gleeble machine.

Thermocouples were spot-welded individually, in the same perpendicular plane, at the centre of the sample as illustrated in Figure 3.3. Type K, Ni-Cr – Ni-Al, thermocouples were used for solution treatment tests and type R, Pt - Pt/13% Rh thermocouples were used for all direct cast tests. Care was taken to ensure thermocouples were securely welded in position to ensure reliable temperature control.

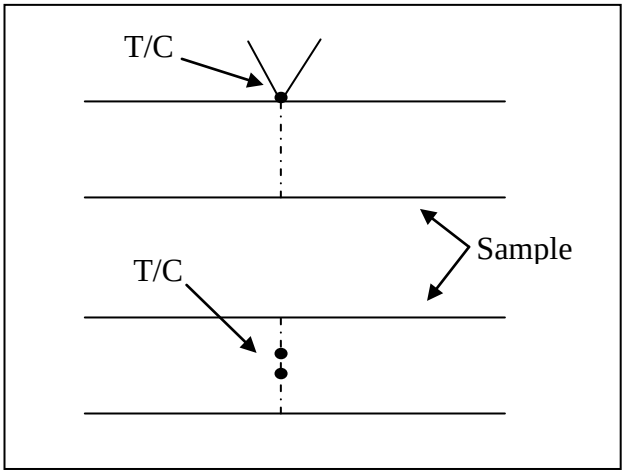

Figure 3.3: Schematic representation of placement of thermocouples on tensile specimens.

3.3.1 Solution Treatment Procedure

Figure 3.4a schematically shows the thermomechanical cycle used to simulate solution treatment conditions. This cycle is sometimes abbreviated to “Sol” in figures and tables. Samples were heated to a solution treatment temperature of 1330°C at 10°C/s and held for 1 minute. A solution treatment temperature of 1330ºC was used because it was the most commonly used temperature in the literature. Two cooling rates of 100K/min and 200K/min were used to cool specimens to the test temperatures. These cooling rates were chosen to simulate conventional casting, 100K/min (~250mm thick slabs), and thin slab casting, 200K/min (~50mm thick slabs). Test temperatures to determine hot ductility curves ranged between 1100°C-700°C. Samples were held at the test temperature for 1 minute then strained to failure at a strain rate of approximately 7.5 x 10^{-4} s^{-1}. The strain rate was chosen to simulate the approximate strain rate of the North Star/BHP thin slab caster (90mm think slabs). After failure, samples were immediately water quenched to retain the microstructure at failure. Tests were carried out in a vacuum of approximately 10^{-3} atm. The chamber was back-flushed with argon, once the specimen was close to failure, to allow quenching.

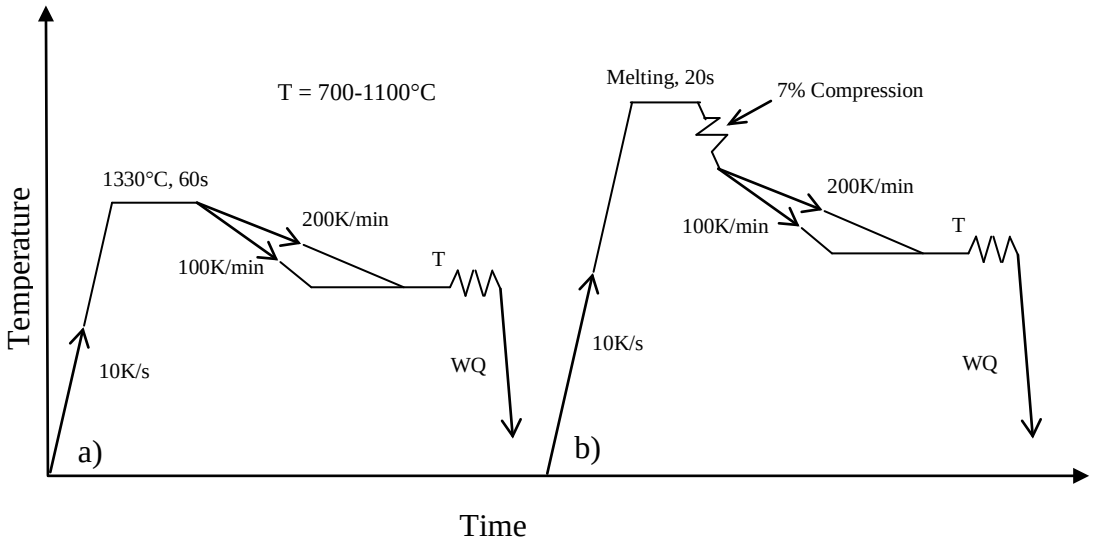

Figure 3.4: Schematic diagram showing two cycles employed during the tensile tests (a) Solution treatment and (b) Direct casting.

3.3.2 Melting and Solidification Procedure (Direct Casting)

Trials were conducted to determine the correct melting temperature and solidification procedure for *in-situ* melting in the Gleeble machine. Research by Suzuki [106] has shown that a thermal gradient of approximately 100°C between the surface and centre of a sample exists at temperatures above 1400°C. The temperature at the axis of the specimen was measured by drilling a 3mm diameter hole parallel to the axis of the specimen to the mid-centre of the sample. A Pt - Pt/13% Rh thermocouple was spot welded to the bottom of the hole and the temperature was measured simultaneously with a thermocouple welded at the surface.

Due to the radial temperature gradient, setting the surface temperature (thermocouple temperature) to the equilibrium melting temperature of the steel results in superheating the centre of the sample, leading to a turbulent molten zone. Experimental control is subsequently lost due to thermocouple detachment. Trials showed that a thermocouple temperature (surface temperature) of 1430°C was sufficient to melt Nb-Ti and Ti samples and 1440°C was sufficient for the Nb and C-Mn-Al samples.

When the melted specimen solidifies, significant shrinkage occurs. If the shrinkage is resisted cracking will occur because the steel has little or no ductility during solidification. A suitable solidification technique was required to eliminate cracking and to remove any shrinkage cavity formation. Applying a compressive strain during solidification of the specimen compensates for the shrinkage. A compressive strain was applied over the temperature range from the melting temperature down to approximately the solidus temperature. Applying compressive strain below the solidus or too high a compression, leads to bulging at the central portion of the specimen. A suitable compressive strain to accommodate shrinkage, without resulting in significant bulging, could only be determined by trial and error.

Trials showed that a compressive deformation of ~7% applied while the samples were cooled from the melting temperature down to 1370°C was sufficient to remove the shrinkage cavity without introducing significant bulging in the sample. The cooling rate during compression was 6K/s. For C-Mn-Al specimens, only 6% compression was required to alleviate shrinkage during solidification.

Transformation temperatures were calculated on the basis of chemical composition using Thermo-calc and are shown in Table 3.2. Deformation was stopped at 1370°C because it coincided closely with the solidus temperature, minus approximately 100°C to compensate for the radial temperature gradient. Compression below the solidus temperature has no impact on removing shrinkage porosity and will cause barrelling of the sample.

Table 3.2: Transformation temperatures calculated from the chemistry of the respective steels.

Temperature	Nb Steel	Nb-Ti Steel
Liquidus	1519.5°C	1512.8°C
Solidus	1469.6°C	1461.6°C
Peritectic	1484.6°C	1472.5°C

Quartz crucibles, Cylindrical in shape with a 2-3mm slot to allow attachment of the T/C, were used to contain the melted section (melt zone) of the specimen. The diametrical clearance between the specimen and the quartz crucible must be chosen carefully to ensure smooth control of melting and solidification. Too large a clearance allows the specimen to sink, causing a misalignment along the specimen axis, and also increases the tendency of T/C detachment. Too small a clearance and the crucible could break, prior to melting, due to expansion of the specimen. A diametrical clearance of 0.2mm was found to be suitable for containment of the molten zone.

Figure 3.4b illustrates the thermomechanical cycle used to simulate the melting and solidification procedure (direct cast). The melting and solidification procedure will be referred to as "Direct Cast" and will also be abbreviated to "Melt" for graphs and tables. Samples were melted at the indicated temperature of 1430°C or 1440°C and solidified using the above-mentioned procedure. Once 1370°C was reached, the same thermomechanical pattern used in the solution treatment cycle was followed.

3.3.3 Simulation of Thermal Oscillations During Direct Cast Gleeble Tests

Figure 3.5 details the thermal pattern designed to simulate the cooling conditions near the surface of a slab during thin slab casting. Specimens were direct cast (melted), held for 20 seconds, then cooled at a rate of 20K/s to 900°C (T_{min}). During cooling to 900°C, 7% compression was applied on solidification, as per the previous direct cast procedure. After cooling to 900°C, three different thermomechanical-cycles were employed, Cycles 1-3. In Cycle 1 and Cycle 2, the specimen was heated from T_{min} (900°C) to T_{max} (1100°C) at 200K/min, and then cooled to the test temperature of 900°C (T_{test}), at an average cooling rate of 200K/min. Temperature oscillations were introduced on cooling from 1100°C (T_{max}) down to the test temperature. The amplitude of oscillations was ±50°C with a period of 30 seconds for Cycle 1, or ±100°C with a period of 60 seconds, for Cycle 2. For Cycle 3, the same pattern for Cycle 1 was followed (oscillations of ±50°C) but with an average cooling rate of 100K/min from T_{min} to T_{test}. For all cycles, specimens were held at the test temperature for 1 minute then strained to failure at 7.5 x 10^{-4} s^{-1}. Samples were water quenched immediately after failure.

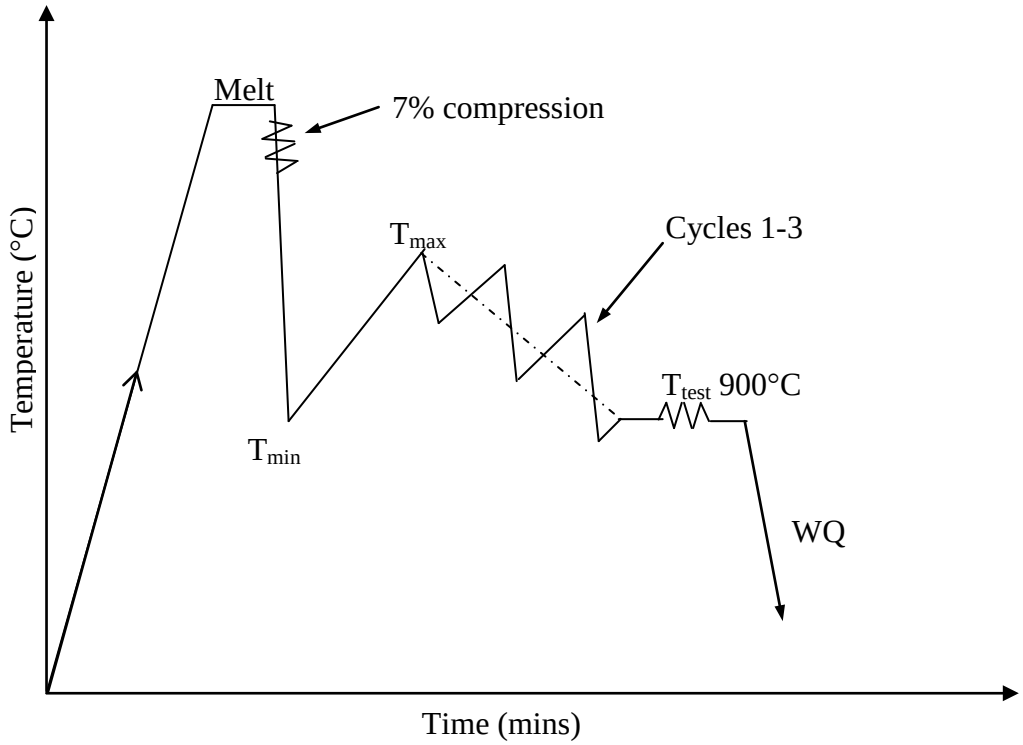

Figure 3.5: Schematic diagram showing the thermal cycle used to simulate the thermal pattern experienced near the surface a thin slab during continuous casting, where Cycle 1 had an average cooling rate of 200K/min with oscillations of ±50°C, Cycle 2 had an average cooling rate of 200K/min with oscillations of ±100°C and Cycle 3 had an average cooling rate of 100K/min with oscillations of ±50°C

The chosen thermal cycle pattern was generated from a combination of information from plant data and previous thermal history simulations in the literature. A plot of the plant data, showing the temperature profile of the centre, centre of wide surface, centre of narrow surface and corner of a continuously cast slab, is displayed in Figure 3.6. BHP Steel supplied the plant data of the North Star (NS)/BHP, medium thickness continuous caster. Literature on influence of thermal history on hot ductility was discussed in section 2.7.4 in Chapter 2.

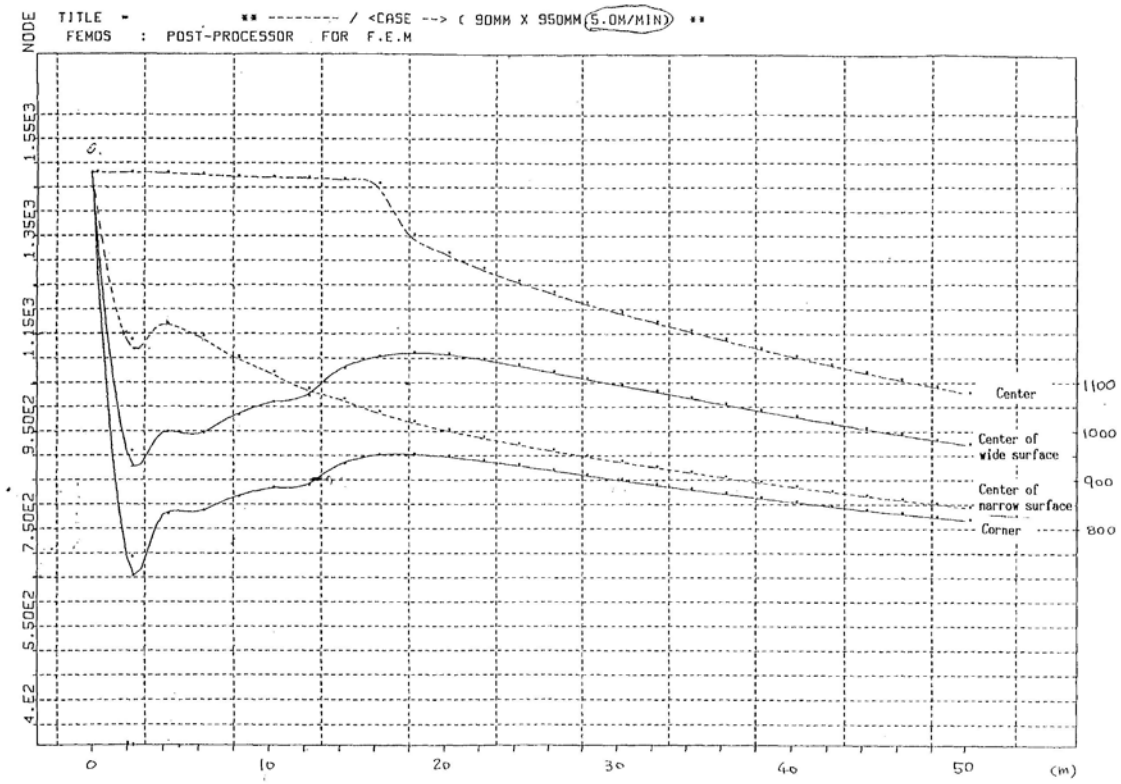

Figure 3.6: Plant data (F.E.M) of temperature profiles for a continuously cast slab, taken from the NS/BHP medium thickness caster. Slab dimensions were 90mm x 950mm and caster speed was 5.0M/min.

From Figure 3.6, the temperature profile for the centre of the wide surface was used as a guide to establishing the thermal history profile. The temperature profile for the centre of the wide surface displays a sharp temperature drop after exiting the mould, reheating to approximately 1150°C then slowly cooling thereafter. The minimum drop in temperature was 925°C at a cooling rate of approximately 23K/s. Similar values were adopted for the thermal history simulation tests.

The average cooling rates of 100K/min and 200K/min, taken after the minimum temperature was reached, were used to maintain consistency with the previous direct cast tests, without temperature oscillations. The thermal oscillations from 1100°C to the test temperature were modelled on similar work by Mintz et al. [59].

3.3.4 Determination of Reduction of Area (RA)

Reduction in area (RA) was calculated using the following formulae:

$$RA = 1 - \left(\frac{Af}{Ao}\right) \tag{3.1}$$

Where: A_f= final area = $\pi(D_f)^2/4$

A_0 = initial area = $\pi(D_o)^2/4$

D_f = final diameter

D_o = initial diameter

The final diameter was measured using vernier callipers. An average of five measurements were taken from each half of the fractured specimen at random locations to accommodate for any asymmetry in the fracture diameter. If the fracture had particularly poor symmetry, making it difficult to interpret the final diameter, tests were repeated. The variance of the reduction of area measurements was generally ±5% RA. Any unusual results not fitting the curve or any fractures outside the hot-zone (5mm either side of the thermocouple) were repeated. Occasionally, one or both of the thermocouples would detach and immediately re-weld to the specimen without complete signal loss (The Gleeble machine would automatically stop the test if the control T/C signal was lost). If this occurred, the temperature reading from the T/C was unreliable and the result would be discarded. A sharp spike in the temperature plot indicated if there was a T/C problem during the test. If a specimen displaying a significant difference in hot ductility did not have any of the problems discussed above, then a more detailed analysis on the sample was under taken, such an analysis is described in **Appendix A**. The scatter in the hot ductility values can also be viewed in **Appendix A**.

3.3.5 Radial Temperature Gradient Measurements

The Gleeble uses copper grips to allow resistive heating of specimens and also to cool the specimen via heat extraction along the length of the sample. When the specimen reaches a certain temperature, heat extraction along the length of the sample becomes inadequate and radiant heat loss from the surface becomes active. Once heat loss from the surface of the specimen becomes significant, a radial temperature gradient develops. The radial temperature gradient increases as the temperature rises and heat loss from the surface becomes more dominant.

A 3mm diameter hole was drilled along the axis of the specimen to the mid-point to allow a T/C to be attached at the centre of the sample to measure the difference between the centre and surface temperatures. A type R T/C was placed inside an alumina sheath, to insulate the wires from the sample, and was spot-welded to the centre of the sample at the end of the hole. A second T/C was spot welded to the surface of the sample, in the same plane as the T/C at the centre. The thermal program for direct cast tests was used for the radial temperature gradient tests. A total of three tests were performed to determine the radial temperature gradient.

To investigate the feasibility of using thermal sleeving to minimise the radial temperature gradient, Nextel tubing was placed over the quartz crucible and three more tests were performed. Nextel tubing, recommended by Dynamic Systems Inc. (DSI), was claimed to reduce the thermal gradient down to a difference of approximately 10°C. Dynamic Systems Inc. is the company that owns the Gleeble Thermomechanical Simulator machines.

Representative graphs of temperature as a function of time from the radial gradient simulation tests are shown in Figure 3.6 with no sleeving and Figure 3.7, with Nextel sleeving. The graphs show that the temperature recorded at the centre of the sample lags behind that for the surface of the sample, up until melting occurs. For resistive heating, the temperature at the centre of the sample cannot be lower than at the surface. This indicates that significant errors in the heating behaviour and/or temperature

measurement are introduced due to the influence of the 3mm hole drilled to the centre of the sample. Thus, the results were inconclusive as to whether or not the Nextel tubing reduced the expected radial thermal gradient so Nextel tubing was not used for any further testing.

The graphs showed a sudden jump in the temperature at the centre of the specimen, while the surface temperature stayed relatively constant, once the expected melting temperature was reached. The temperature jump in Figure 3.6 was 1478°C with a spike of 1503°C, and the temperature jump for Figure 3.7 was 1475°C with a spike of 1500°C. This sudden temperature jump indicated that localised melting at the centre of the sample occurred. Cross sectioning of specimens revealed solidified metal surrounding the internal thermocouple. This suggests that the predicted radial thermal gradient of approximately 100°C, by Suzuki [106], can occur in Gleeble specimens under these conditions.

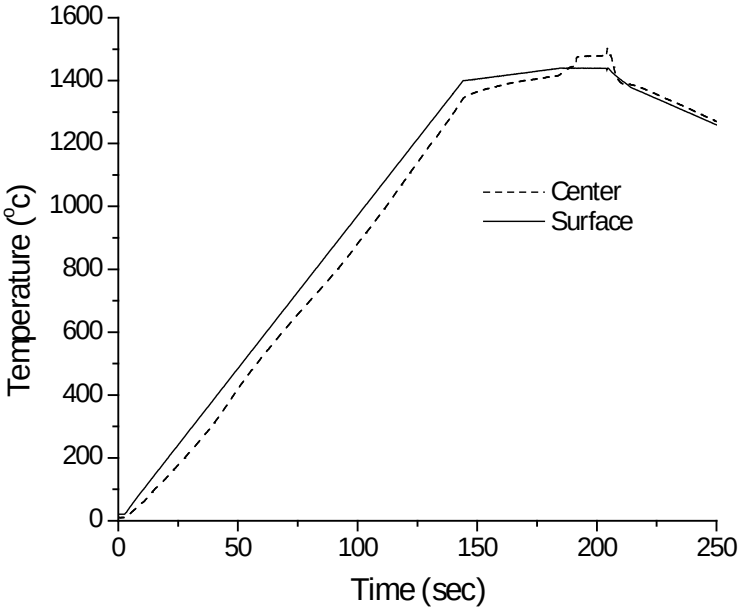

Figure 3.6: Temperature profile of surface and centre temperature measurements without Nextel sleeving.

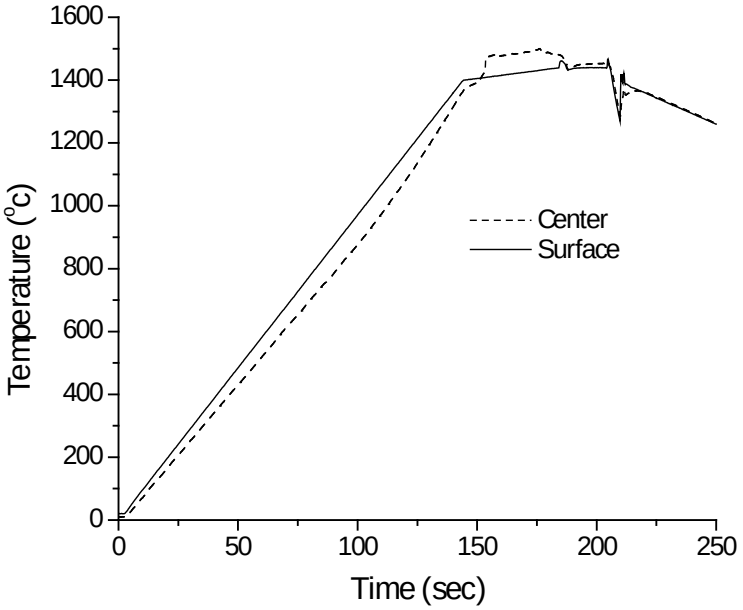

Figure 3.7: Temperature profile of surface and centre temperature measurements with Nextel sleeving.

3.4 Metallography

The fractured region was sectioned down the centre, in the longitudinal direction, by an Accutom precision cutting machine. Samples were mounted in Bakelite then ground and polished to a 1μm finish using standard metallographic techniques. Polished samples were immediately etched in 2.5% Nital.

Prior austenite grain boundaries were partially revealed using saturated picric acid mixed with HCl and a wetting agent, Teepol. To a base concentration of 100ml of sat. picric acid, additions of HCl was varied between 5-12 drops and additions of Teepol varied between 10-20 drops. Etching temperature was maintained between 60-65°C and etching times varied between 6 to 15 minutes.

Difficulties in delineating the prior austenite grain boundaries led to the used of an alternate etching technique described by Zhang and Guo [107]. The etchant contained 10g of chromium trioxide (CrO_3), 50g of sodium hydroxide (NaOH), 1.5g of picric acid and 100ml of distilled water. The solution was prepared by dissolving chromium

trioxide in the water, followed by the sodium hydroxide and then the picric acid. Care was taken to add the NaOH slowly to avoid splattering due to rapid heat evolution. The solution was heated to 120°C before immersing the polished specimen. Etching times varied between 30-45 minutes.

Satisfactory delineation of the prior austenite grain size using the above etchant could not be obtained. The etch depth varied markedly across the sample, resulting in some areas, presumably triple points, heavily etched, pitted and in other areas the etchant film was destroyed and no structure was revealed. In some areas, etching was very poor and delineation was not clear. It was believed that the large grain size contributed to the unsatisfactory delineation of the prior austenite grain boundaries due to difficulties in obtaining uniform etching.

The prior austenite grain size was finally determined by the ferrite delineation technique. In this technique, the sample is cooled from the austenite region (following the thermomechanical schedule used for hot ductility testing) down to a temperature low enough to allow a continuous film of ferrite to transform along the austenite grain boundaries. Samples were then quenched at this temperature, as a result delineating the prior austenite boundaries with ferrite.

Transformation temperatures, found by dilatometry, were used as a guide to find the correct quenching-out temperature for each composition. Trial and error was still required to find the optimum quenching temperature in order to obtain a continuous film of ferrite at the austenite boundaries without significant formation of matrix ferrite.

Due to the large grain size of samples, standard intercept techniques could not be used due to very low sampling (count) rates. Measuring each grain in the hot zone and then taking the average equivalent diameter as the grain size was used to determine average grain size. Measurements of the grains were performed using Video Pro 32 imaging software. Images were viewed using a Leica DMR microscope under the lowest magnification of x3.2 (objective lens) and captured via a digital video camera.

For the Ti-bearing steels, under solution treatment conditions, the grain size was sufficiently small to use the mean linear intercept technique. Approximately 50 intercepts (counts) per line were recorded per field of view. A total of five fields of view, chosen randomly, were used to find the average grain size. Both grain size determination techniques were used for the Ti bearing steels to allow comparisons between the two techniques.

3.4.1 Determination of Dendritic Segregation

An attempt was made to reveal the dendritic structure, or solidification structure, of the solution treatment and direct cast samples by etching with Brauner's reagent. Brauner's reagent is a saturated aqueous picric acid solution, containing Copper II Chloride ($CuCl_2$) and Teepol as a wetting agent, supplied by BHP Steel. Specimens were well polished to 1μm and care was taken to obtain a flat sample finish to improve etch quality. Etch times were between 30 seconds and 1 minute or until a dark film settled on the sample. Samples were immediately washed and the copper film was removed with ammonia and cotton wool. Care must be taken when cleaning the sample before etching to avoid staining during etching. Etching was repeated 2 or 3 times, depending on etching response, to improve delineation.

The etchant revealed the dendrites for the Nb-Ti alloy but poor results were obtained for the C-Mn-Al, Nb and Ti containing alloys. This suggests that Brauner's reagent is very sensitive to small changes in alloying additions. It is believed that the higher Mn level in the Nb-Ti alloy improved etch response [123]. The dendritic pattern in the Nb-Ti steel could be best seen under oblique lighting. It was difficult to resolve the dendrites under optical microscopes so accurate measurements of the secondary dendrite arm spacing (SDAS) could not be performed.

An alternative method was used to reveal the dendritic segregation pattern. Specimens were normalized in a furnace at 900°C, held for 15 minutes and then furnace cooled. Normalizing allowed pearlite to form preferentially at interdendritic segregation, thus revealing the dendritic structure. Samples were mounted in Bakelite, polished to 1μm

and lightly etched in 2.5% Nital. This procedure allowed clear resolution of the dendritic pattern under an optical microscope and the SDAS could be measured using digital imaging software.

The SDAS were also estimated using two separate equations, based on cooling rate and carbon composition, taken from Young-Mok Won [108], equation (3.2) and Weisgerber [109], equation (3.3). Equations (3.2) and (3.3) are shown below:

$$SDAS = 143.9 \times Cr^{-0.3616} \times Cc^{(0.5501-1.996Cc)} \quad (3.2)$$

$$SDAS = 64.8 \times Cr^{-0.36} \times \exp^{(2.12*Cc)} \quad (3.3)$$

Where: SDAS = Secondary dendrite arm spacing (μm)
Cr = Cooling rate (°C/s)
Cc = Carbon content (wt%)

3.4.2 Determination of Homogenisation Time

The secondary dendrite arm spacing (SDAS) can be used as a measure of the scale of microsegregation in solidified steel. Microsegregation is segregation between dendrite arms where the minimum solute concentration is at the centre of the dendrite arm and the maximum solute concentration is between the arms. To remove segregation, that is, to homogenise the steel, the segregated solute must diffuse across the dendrite arm spacing distance to obtain a uniform solute concentration. Accordingly, the time required for homogenisation, will be related to the dendrite arm spacing (d) and the diffusion coefficient (D) of the solute species in Fe at temperature (T). A simple equation (3.4) can be use to predict to homogenisation time (t) [110]:

$$t = d^2 / D \quad (3.4)$$

The SDAS (d) were determined by metallographic techniques, as discussed in the previous section. The diffusion coefficient, D, can be found at any given temperature by the well know equation:

$$D = D_o \exp(-Q/RT) \quad (3.5)$$

Where: Do = Constant

Q = Activation energy for diffusion

R = Gas constant (8.314 J $mole^{-1}$ K^{-1})

T = Temperature (K)

3.5 Scanning Electron Microscope (SEM)

SEM work was carried out on a Leica Stereoscan 440 Scanning Electron Microscope at the University of Wollongong. Fracture samples were cut to size and mounted on a standard aluminium SEM stud with double-sided conductive tape. Samples were initially cleaned in acetone in an ultrasonic cleaner to remove dust, debris and greases from the specimen. Samples were kept in airtight containers to keep the samples clean and dust free.

3.6 Transmission Electron Microscope (TEM)

TEM samples were prepared using a single stage carbon extraction replication technique. Samples were sectioned longitudinally to the fracture surface and mounted in Bakelite. Polished samples (1μm) were pre-etched in 2.5% nital for 8-12 seconds. Before carbon coating, samples were ultrasonically cleaned in acetone to remove any debris or particles exposed during pre-etching. Samples were immediately transferred to a Dynavac Evaporation unit for carbon deposition. Filter paper placed adjacent to the samples was used as a guide to the coating thickness. Carbon rods, one rod with a flat end and the other rod sharpened to a point, were used as the carbon source. Evaporation was conducted under a vacuum of at least 7.5 x 10^{-4} torr to ensure a good deposition. Rotation of the samples ensured an even carbon deposition.

After carbon coating, samples were scored into 3mm grids and stripped in 10% Hydrobromic acid (90% ethanol). Replicas were only taken from areas adjacent to the fracture face to ensure that only those precipitates involved in the fracture process were replicated. The replicas were picked up on 200 mesh copper grids, rinsed in two ethanol baths to ensure cleanliness of the replica and to remove any traces of the Hydrobromic acid. A final bath of 80% distilled water and 20% ethanol was use to un-curl the replicas by surface tension effects. Replicas were carefully dried on filter paper and stored in a TEM storage box.

Replicas were examined using a Phillips CM200, field emission TEM, located at the University of New South Wales. The microscope was fitted with an EDAX DX-4 energy dispersive spectrometry analyses system. Due to the large number of tests, extensive TEM work would be required to obtain good statistical results. Due to time constraints this could not be carried out. A minimum of three different replicas were studied at three separate grid locations for each replica, at each test temperature, to give an adequate overview and allow qualitative comparisons to be made.

Photos were taken of representative particles and energy dispersive X-ray (EDXS) was used to determine precipitate composition. To obtain a qualitative representation of precipitate density (volume fraction), fifteen randomly taken photos from three different replicas were taken at test temperatures that had sufficient particles. One should note however, that a true representation of particle volume fraction is difficult to determine by carbon extraction replicas due to complications in determining extraction efficiency [111, 112].

The initial representative precipitates (selected particles as opposed to randomly selected) were analysed to determine their morphology, composition and size range. Precipitates were measured manually, for rectangular precipitates the width and length was recorded, circular precipitates had their diameter recorded and rhombus shaped precipitates had the longest diagonal measured.

A more detailed analysis was performed to determine the mean particle size and particle distribution using the randomly taken TEM photographs. TEM negatives were scanned into a computer and were analysed using Video Pro 32, image analysis software. Precipitates were distinguished from the background via thresh-holding (pixels were distinguished according to their grey scale level). The computer could not distinguish precipitates if they were of a similar intensity to the background. When this was the case, precipitates had to be manually marked. Precipitates were counted and measured; the equivalent diameter was recorded to represent precipitate size. Histograms were prepared to determine the mean precipitate size and precipitate distribution.

The average interparticle spacing was calculated for selected test conditions using the 15 randomly taken TEM micrographs. The total area of the 15 micrographs was calculated and from this the number of particles per unit area (nm^2) was calculated. The interparticle spacing is simply the inverse of the number of particles per unit area. It is acknowledged that using the two-dimensional area, calculated from the micrographs, is not correct due to the depth of etching introducing a third dimension. The correct measurement should be the number of particle per unit volume. However, as the etching times were kept constant, it was assumed that the etch depth would not vary significantly. Therefore, etch depth was ignored for the purpose of this investigation.

The intention of calculating the interparticle spacing was to give an indication of the volume fraction of precipitates on a comparative bases. Specimens with different microalloying additions may have precipitates of similar size, but not a similar volume fraction (one alloy has a increased addition of microalloying elements). It was assumed that the interparticle spacing would be finer the greater the volume fraction, for a given particle size.

3.7 Dilatometry

Dilatometry was carried out on a “Theta Industries- Dialatronic Dilatometer”, located at the University of Wollongong, to find $\gamma \rightarrow \alpha$ and $\alpha \rightarrow \gamma$ transformation temperatures. Tubular samples 10mm in length were prepared with an outer diameter of 5mm and an inner diameter of 3.5mm. Type K thermocouples were carefully spot-welded to the mid-

centre of the sample. The thermo-cycle used for the dilatometer work is shown in Figure 3.8. Samples were heated at 10°C/s, held at 1050°C for 30 seconds, and then cooled at either 1.7°C/s (100K/min) or 3.33°C/s (200K/min) down to room temperature.

It is noted that the maximum working temperature for the dilatometry, 1050°C, will not be sufficient to dissolve all microalloying elements, particularly TiN particles. Nevertheless, some useful information can be gained on changes in transformation temperatures with composition and cooling rate.

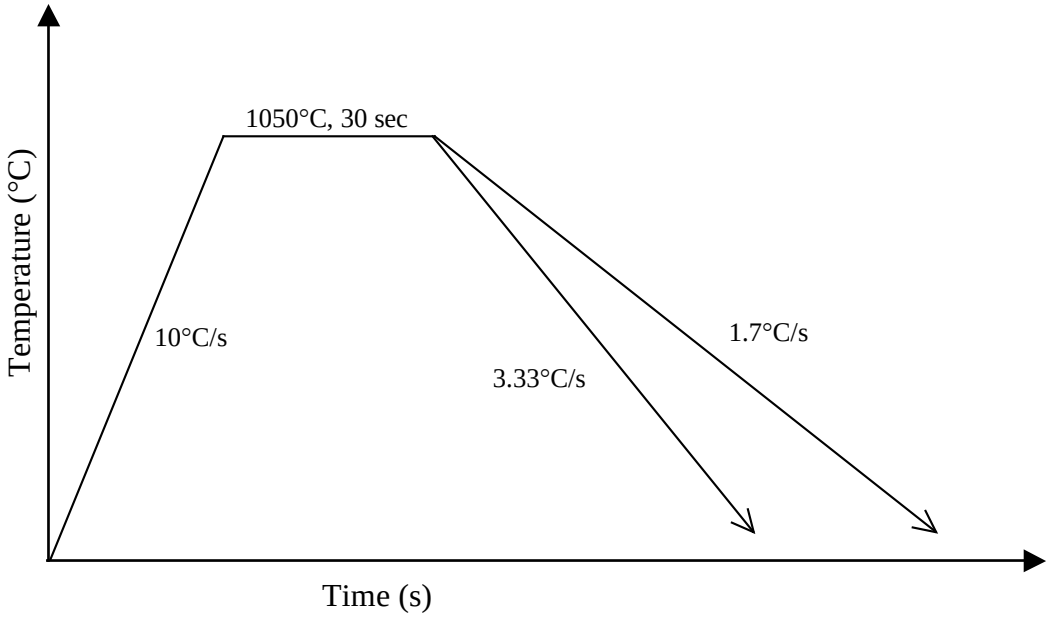

Figure 3.8: Thermo-cycle used to find $\gamma \rightarrow \alpha$ and $\alpha \rightarrow \gamma$ transformation temperatures by dilatometry.

3.8 Determination of Young's Modulus and Yield Stress

Young's modulus (E), or modulus of elasticity, is the slope of the stress-strain curve in the elastic region. The modulus of elasticity is a measure of the stiffness of the material. Yield stress is defined as the stress that will produce a small amount of permanent

(plastic) deformation [113, 114]. Plastic deformation begins when the elastic limit is exceeded. Due to the difficulty in determining the exact elastic limit and hence the yield point, an offset yield strength is measured. Offset yield strength is determined by the stress corresponding to the intersection of the stress-strain curve and a line parallel to the elastic section of the curve offset by a specified strain, usually 0.2 or 0.1 percent [114].

The Young's modulus was calculated theoretically following the principles set out by Frost and Ashby [115]. The temperature dependence of shear modulus, μ, was calculated from the following formulae:

$$\mu = \mu_o \, (1 + [(T-300)/T_m] \times [T_m d\mu/\mu_o dT]) \qquad (3.6)$$

Where: μ = Shear modulus (MN/m^2)

μ_o = Shear modulus at 300K

T = Temperature (K)

T_m = Melting temperature (K)

$T_m d\mu/\mu_o dT$ = Temperature dependence of modulus

The following values, taken from Frost and Ashby [115], were used to calculating the shear modulus; μ_o = 81,000 Mpa, $T_m d\mu/\mu_o dT$ = -0.91 and T_m was the melting temperature of the respective alloy. The Young's modulus (E) is approximated to the shear modulus (G) by the following relationship [115, 116]:

$$G = (3/8)E \qquad (3.7)$$

Young's modulus was calculated for each test temperature using the above approach. Using the Young's modulus, the initial elastic portion of the stress-strain curve could be plotted by assuming that the curve starts at (0,0) and goes through (σ^*, ε^*). Where σ^* is the stress required to give the calculated Young's modulus (E = initial slope) at a certain strain (ε^*). The strain used, for calculation purposes, was 0.02. Using the relationship, E = Initial slope, σ^* can be found as shown below:

Using:

$$E = (x_2 - x_1)/(y_2 - y_1) \quad (3.8)$$

When: $(x_1,y_1) = (0,0)$ (origin)

$(x_2,y_2) = (\sigma^*,0.02)$

E = Young's Modulus at Temperature (T)

Equation (3.8) becomes:

$$\sigma^* = 0.02/E \quad (3.9)$$

The line between (0,0) to (σ^*,0.02) has the correct slope of the Young's modulus and can be plotted on the stress-strain curve. The offset yield stress can than be calculated by drawing a parallel line at 0.02% strain. A proof stress at 0.02% strain was chosen due to the short elastic range displayed in the stress-strain curves at the elevated testing temperatures.

Chapter 4:

Results

Chapter 4: Results

4.1 Hot Ductility Curves

A Gleeble 3500 Thermomechanical Simulator was used to generate hot ductility curves, as a function of reduction in area (%RA) versus temperature. A total of four curves were generated for each steel type. Two curves were generated under solution treatment conditions, one at a cooling rate of 100K/min and the other at 200K/min. A further two curves were generated under direct cast conditions for each of the above cooling rates. The following sections will deal with each steel composition and the influence of thermomechanical processing on hot ductility in more detail.

It is pointed out to the reader that descriptions of the hot ductility curves will generally be considered from right to left (high temperature to low temperature). A trough may be regarded as a region of lower ductility relative to the highest ductility. For ease of comparison, across a range of steels with varying ductility, the ductility trough was defined as the temperature range in which the ductility fell below 60% RA, and the ductility had significantly improved (above 40%) with decreasing temperature.

4.1.1 C-Mn-Al (Base Composition)

Reduction in area (RA) curves as a function of temperature for the C-Mn-Al steel are shown in Figure 4.1. For the solution treatment tests, the ductility troughs were between 760-830°C for both cooling rates. The ductility troughs for direct cast specimens were between 750-840°C for 100K/min and 750-890°C for 200K/min. There was no effect from the cooling rate for solution treatment conditions. For direct cast specimens, increasing the cooling rate widened the trough by approximately 50°C but the depth of the trough remained the same.

Comparing ductility curves between the two thermomechanical cycles showed that both conditions had similar, narrow troughs, except that the RA values were approximately 10-20% lower for direct cast conditions. The minimum ductility, at 800°C, was

approximately 30% RA for solution treatment conditions, while for direct cast conditions the minimum was 10% RA, for both cooling rates.

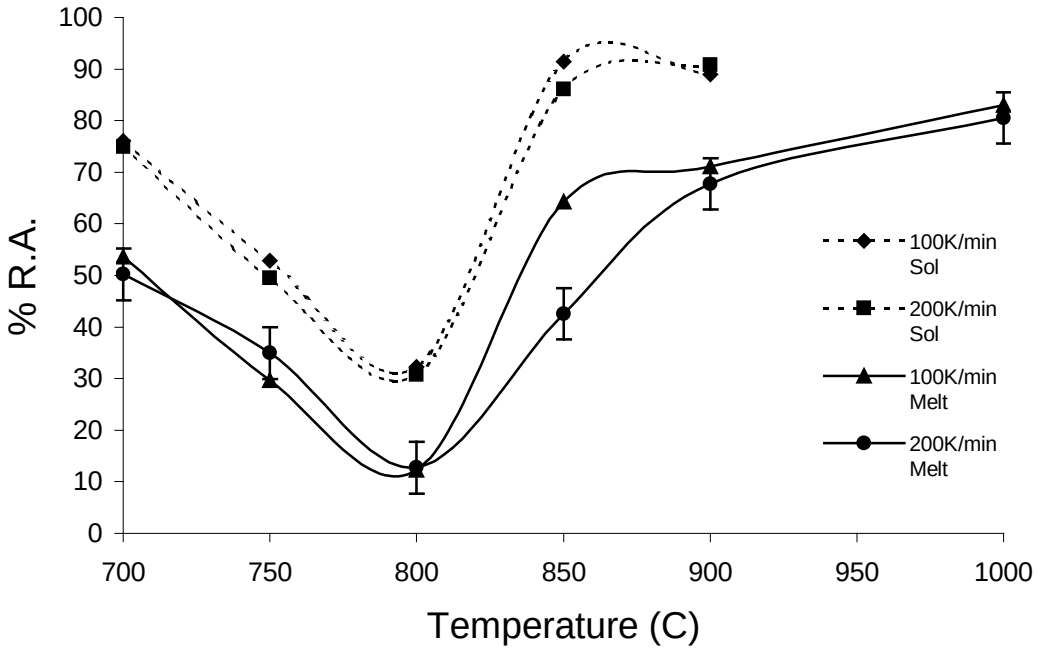

Figure 4.1: Hot ductility curves generated for C-Mn-Al steel from solution treatment (Sol) and direct cast (Melt) conditions at cooling rates of 100K/min and 200K/min.

4.1.2 C-Mn-Al-Nb (Nb steel)

Figure 4.2 displays the RA curves as a function of temperature for Nb steel. Under solution treatment conditions, the ductility troughs were 750-930°C for both cooling rates. For the direct cast samples, the troughs were 750-955°C and 750-970°C for 100K/min and 200K/min, respectively. Increasing the cooling rate had very little influence on either the solution treatment or direct cast ductility curves. The minimum ductility occurred at approximately 800°C for all conditions.

The direct cast curves followed similar trends to the solution treatment curves but displayed lower ductility (as was found for C-Mn-Al). The solution treatment curves had a sharp drop from 950°C to 900°C then continued with only a slight decrease in ductility down to 800°C. The direct cast curves dropped steadily from 1000°C down to

800°C. A deeper and wider trough then that for the solution treatment tests was generated for the direct cast tests.

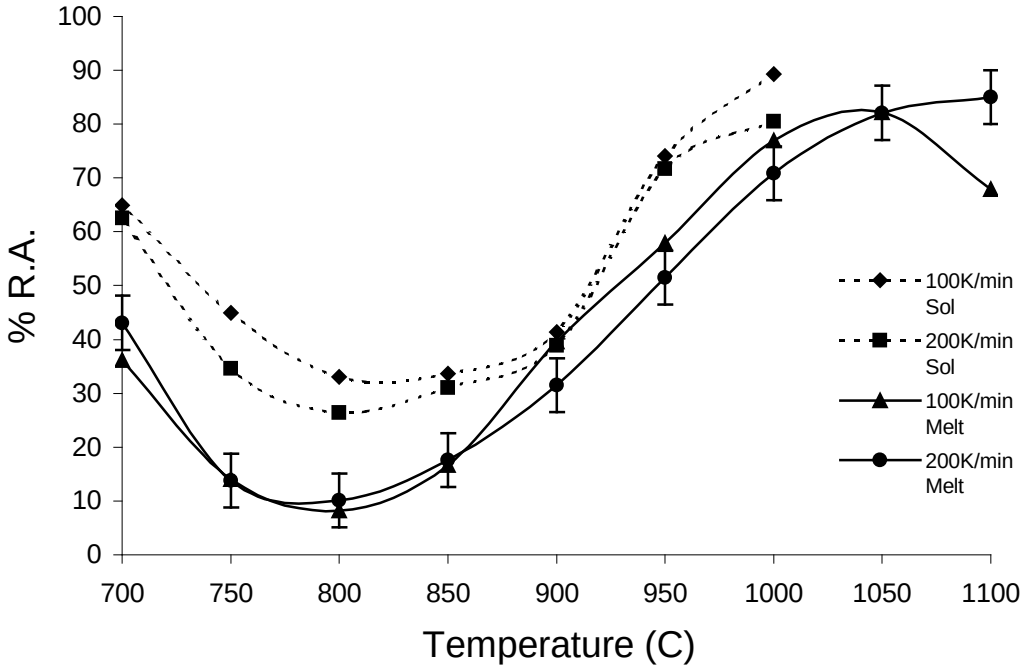

Figure 4.2: Hot ductility curves generated from the Nb steel for solution treatment (Sol) and direct cast (Melt) conditions at cooling rates of 100K/min and 200K/min.

4.1.3 C-Mn-Al-Ti (Ti Steel)

The RA curves as a function of temperature for the Ti steel are shown in Figure 4.3. It is clear from Figure 4.3 that there was a marked difference in ductility between the solution treatment and direct cast conditions. A significantly deeper and wider trough was obtained under direct cast conditions. The troughs for the solution treatment curves were between 750-885°C and 750-875°C for 100K/min and 200K/min, respectively. Ductility remained relatively good, close to 60%, down to 800°C, and then dropped to 40% by 750°C. The troughs for direct cast conditions were between 750- 975°C for both cooling rates and the ductility was well below that for solution treatment conditions.

Increasing the cooling rate had only a small influence on both solution treatment specimens and direct cast specimens. For the direct cast specimens, the higher cooling

rate resulted in a sharper drop between 1000°C and 950°C. Ductility also improved more sharply at 800°C at the lower cooling rate. This resulted in a change in the minimum ductility from 850°C for 100K/min to 800°C for 200K/min. For the solution

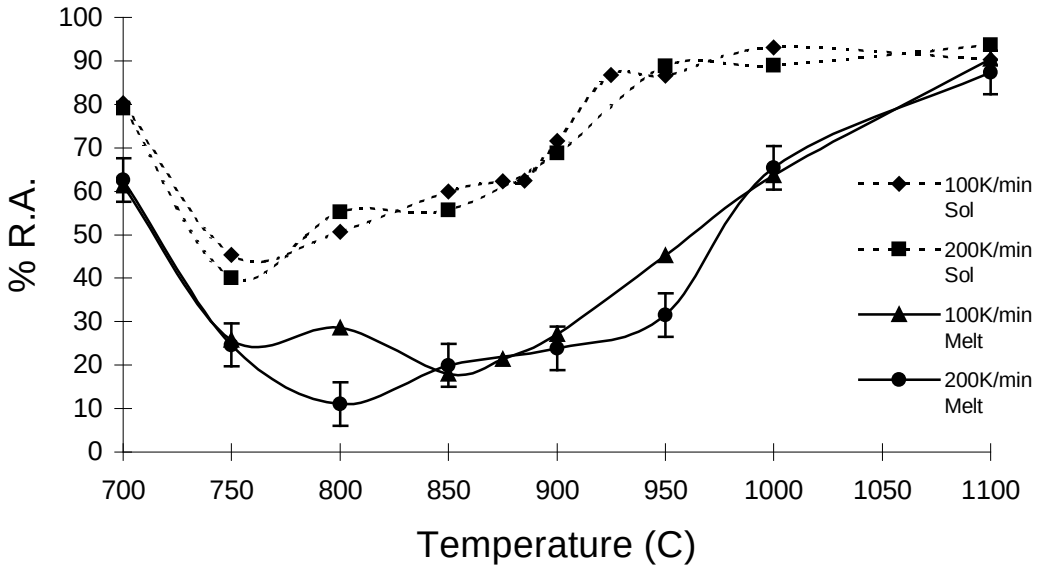

treatment curves, the minimum ductility occurred at a lower temperature of 750°C.

Figure 4.3: Hot ductility curves generated from the Ti Steel for solution treatment (Sol) and direct cast (Melt) conditions at cooling rates of 100K/min and 200K/min.

4.1.4 C-Mn-Al-Nb-Ti (Nb-Ti Steel)

The RA curves as a function of temperature for the Nb-Ti steel are shown in Figure 4.4. The ductility troughs for the solution treatment curves were 750-800°C and 750-930°C for the cooling rates of 100K/min and 200K/min, respectively. The direct cast specimens displayed troughs of 750-1000°C and 750-1010°C for cooling rates of 100K/min and 200K/min, respectively. Direct cast conditions produced significantly deeper and wider troughs compared to solution treatment conditions. All curves reached minimum ductility at 750°C.

Increasing the cooling rate reduced ductility for both solution treatment and direct cast conditions. The cooling rate had a much greater influence on the solution treatment curves for the Nb-Ti composition then for any other composition. Reduction in area

values were significantly lower at the higher cooling rate at all temperatures except 1100°C. Under direct cast conditions, increasing the cooling rate resulted in a sharper drop in ductility between 1000°C and 950°C.

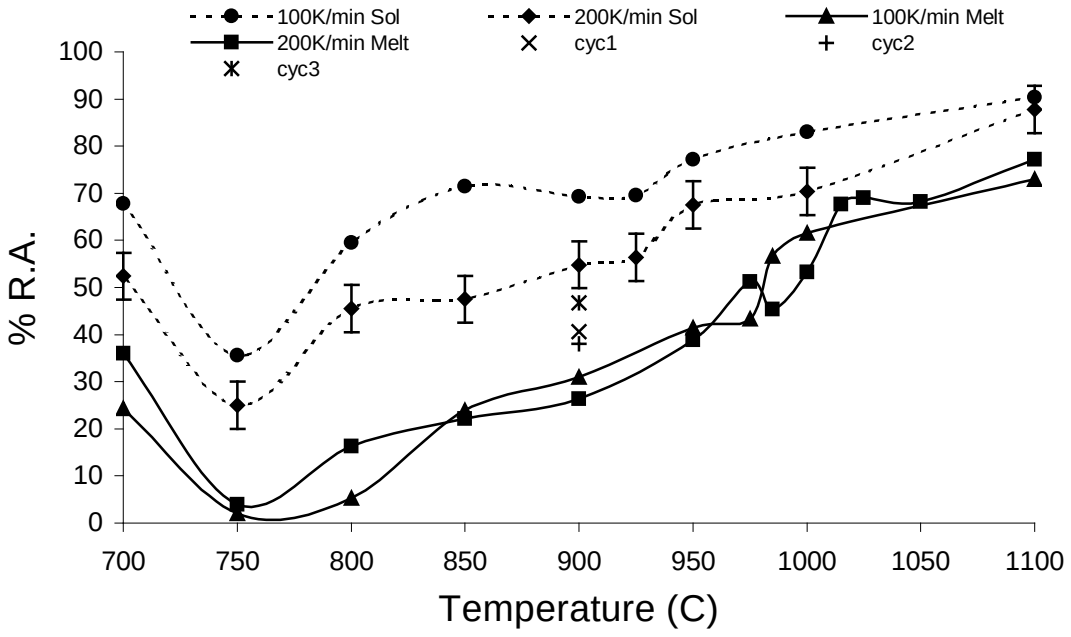

Figure 4.4: Hot ductility curves generated from the Nb-Ti Steel for solution treatment (Sol) and direct cast (Melt) conditions at cooling rates of 100K/min and 200K/min. Included in Fig 4.4 are the RA points for the three cyclic thermal patterns, Cycles 1-3, generated at 900°C for the Nb-Ti Steel.

4.1.5 Summary of Hot Ductility Data

The hot ductility results for each composition are summarized below in Table 4.1. The data was taken from the respective hot ductility curves. As defined earlier, the ductility trough was from 60% RA, until the temperature at which ductility had significantly improved, with decreasing temperature.

Table 4.1: Summary of the hot ductility data taken from the reduction in area as a function of temperature curves

Steel	Min R.A.		Trough <40% RA		Temp when R.A. >60%	
	Sol	Melt	Sol	Melt	Sol	Melt
C-Mn-Al 100K/min	31% at 800°C	10% at 800°C	760-820°C	750-825°C	830°C	840°C
200K/min	30% at 800°C	10% at 800°C	760-820°C	750-850°C	830°C	890°C
Nb 100K/min	33% at 800°C	10% at 800°C	760-900°C	700-900°C	930°C	955°C
200K/min	26% at 800°C	10% at 800°C	740-900°C	700-930°C	930°C	970°C
Ti 100K/min	45% at 750°C	15% at 850°C	~750°C	740-945°C	885°C	975°C
200K/min	40% at 750°C	11% at 800°C	~750°C	740-960°C	875°C	975°C
Nb-Ti 100K/min	35% at 750°C	2% at 750°C	~750°C	700-950°C	800°C	1000°C
200K/min	25% at 750°C	4% at 750°C	720-780°C	700-1000°C	930°C	1010°C

4.1.6 Hot Ductility Results from Cyclic Thermal History Tests

The RA values determined for each of the cyclic thermal histories (Cyc1, Cyc2 and Cyc3) have been graphed together with the RA values at 900°C for the Nb-Ti steel, without thermal oscillations, in Figure 4.5. It can be seen from Figure 4.5 that introducing thermal patterns under direct cast conditions improved the ductility at 900°C for Nb-Ti specimens. However, the ductility was not as good as that found under solution treatment conditions. The relative positions of the RA values for the thermal cycles, compared to the hot ductility curves of the Nb-Ti specimens, were included in Figure 4.4.

The highest ductility for the cyclic thermal patterns was obtained for Cycle 3, followed by Cycle 1 and Cycle 2. Cycle 3 was cooled at an average rate of 100K/min with

amplitude of oscillations of ±50°C, Cycle 1 was cooled at an average rate of 200K/min with amplitude of oscillations of ±50°C and Cycle 2 was cooled at an average rate of 200K/min with amplitude of oscillations of ±100°C.

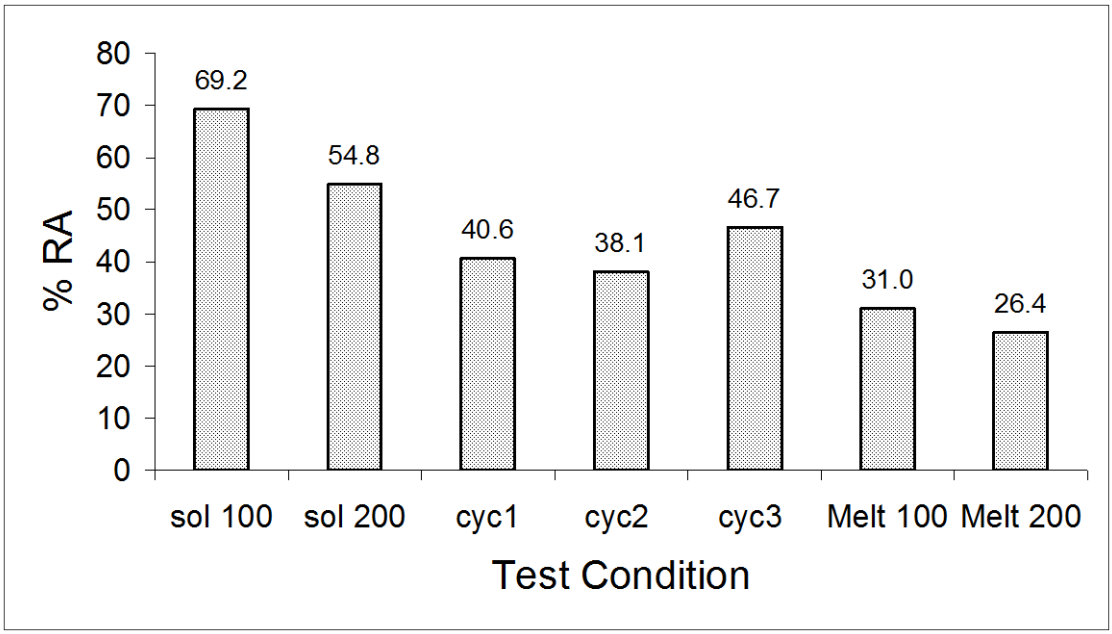

Figure 4.5: Comparison of reduction of area (RA) values at 900°C for different test conditions for the Nb-Ti steel

4.1.7 Comparisons of Hot Ductility Curves Under Solution Treatment Conditions

Figure 4.6 displays the solution treatment curves for all four compositions. Good ductility (above 60%) was obtained for all the microalloyed steels at 950°C and above under solution treatment conditions. Compared to the microalloyed steels, the C-Mn-Al steel had a much narrower trough and good ductility was reached above 830°C. All steels displayed a similar depth (minimum ductility), although the temperature for the minimum ductility varied between 750-800°C. Niobium steel had a significant proportion of the ductility curve below 40% RA (750-900°C), in comparison to the rest of the alloys. . Ductility began to recover at temperatures below 750°C for all steels. Nb-Ti was the only alloy to show any significant deterioration of ductility when the cooling rate was increased from 100K/min to 200k/min.

Nb steel had the deepest and widest trough compared to the other microalloyed steels. The addition of Ti (Nb-Ti Steel) improved ductility between 950°C and 800°C and in comparison to the Nb Steel; lower ductility was only displayed at 750°C. The ductility curve for the Ti steel (Nb free) was similar to the Nb-Ti steel below 900°C. Above 900°C the ductility for the Ti steel was better than both the Nb and Nb-Ti steels.

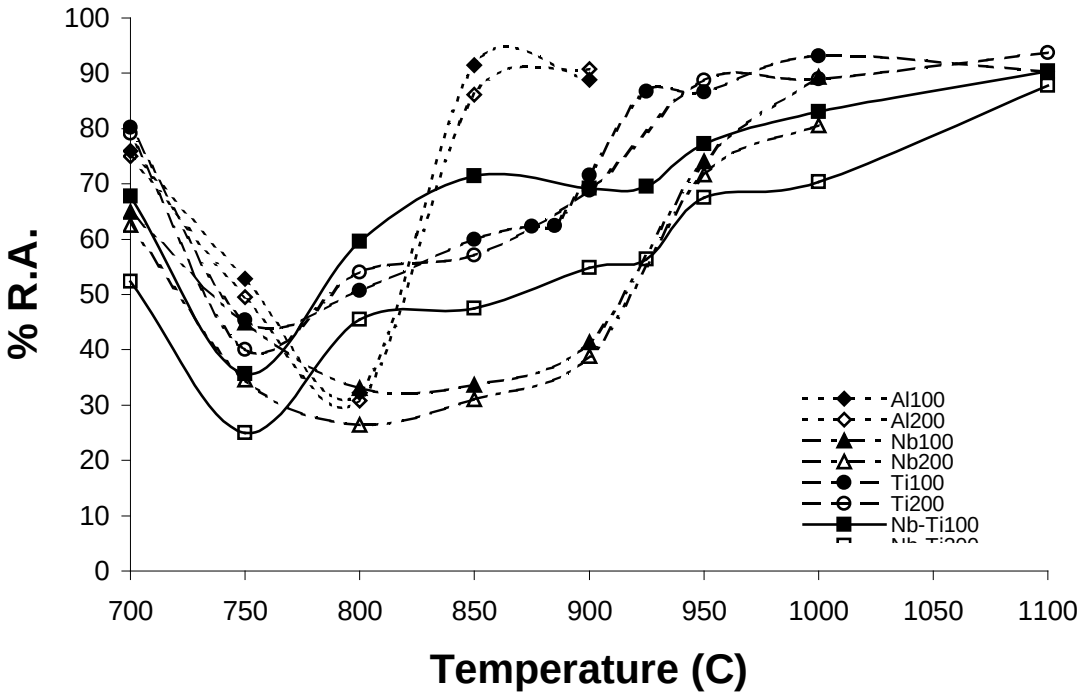

Figure 4.6: Hot ductility curves for solution treatment conditions for all four steels at cooling rates of 100K/min and 200K/min.

4.1.8 Comparisons of Hot Ductility Curves Under Direct Cast Conditions

Figure 4.7 displays the hot ductility curves under direct cast conditions for all compositions. The C-Mn-Al steel displayed a deep and narrow trough between approximately 750-850°C. Additions of microalloying elements (Nb, Ti and Nb-Ti) significantly widened the trough to higher and lower temperatures. In contrast to solution treatment conditions, the Nb steel displayed the better ductility above 900°C. The microalloyed steels displayed similar ductility between 800 and 900°C. Below

800°C, the ductility for Nb-Ti steel continued to fall, while ductility improved for both the Nb steel and Ti steel. Between the Nb and Ti steels, the Ti steel had better ductility.

The two Ti containing steels displayed lower ductility compared to the Nb steel at higher temperatures. The addition of Nb and Ti together resulted in a sharp drop in ductility between 950-1025°C, particularly for the higher cooling rate. This was not observed for any other composition.

Increasing the cooling rate generally reduced the ductility at the high temperature end of the trough, although the decrease in ductility was only moderate in most cases.

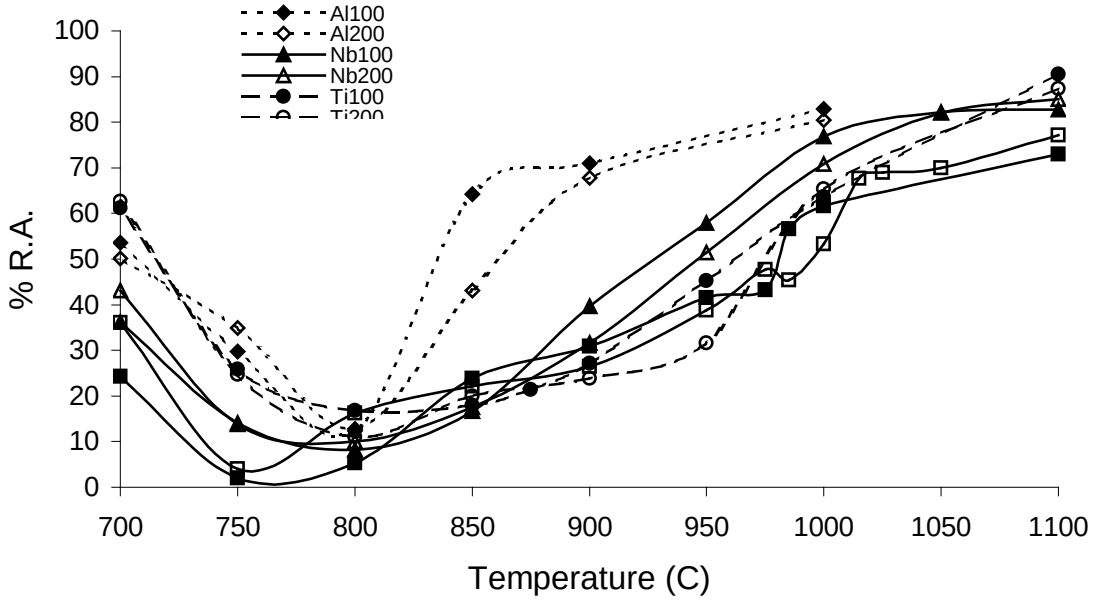

Figure 4.7: Hot ductility curves for direct cast conditions for all four steels at cooling rates of 100K/min and 200K/min.

4.2 Stress Strain Curves

Stress-strain curves for each composition displayed similar trends and therefore, will be represented by the curves generated for the C-Mn-Al-Ti steel at 100K/min. The stress-strain (σ-ε) curves as a function of temperature are shown in Figure 4.8 for solution treatment conditions and Figure 4.9 for the direct cast conditions.

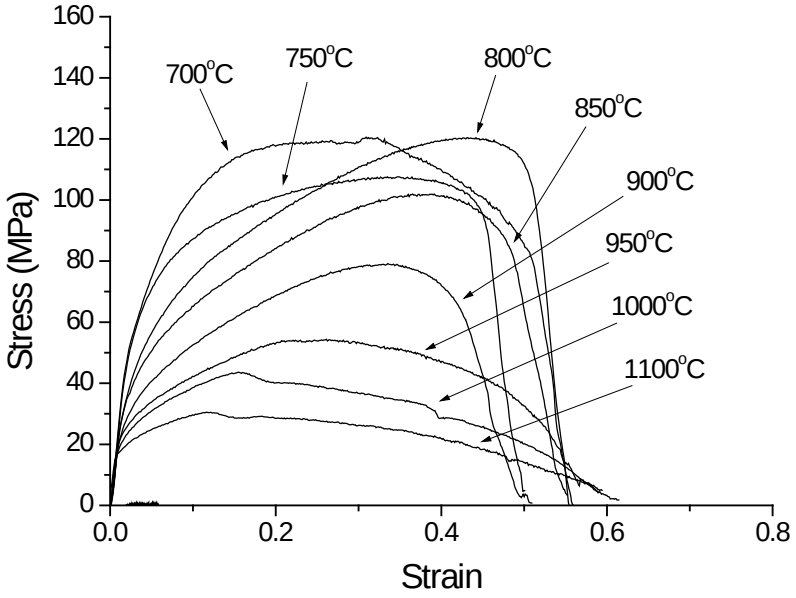

Figure 4.8: Stress-strain curves as a function of temperature for the Ti steel at 100K/min under solution treatment conditions.

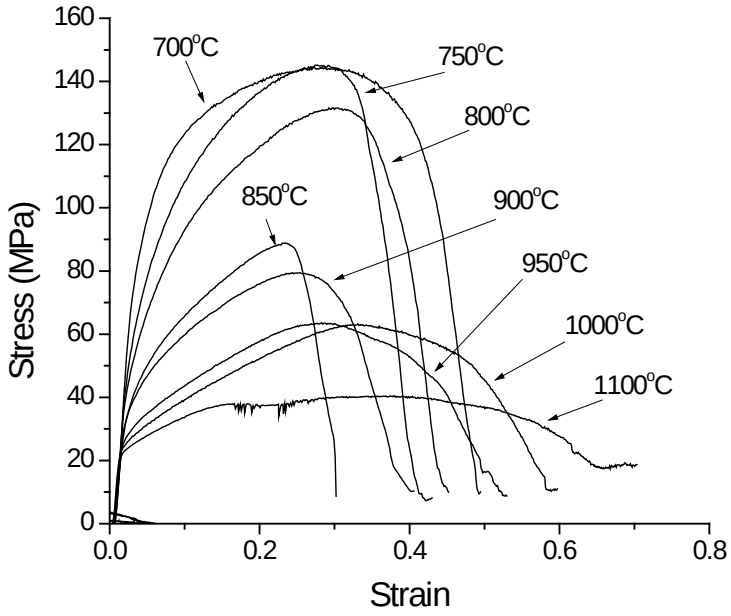

Figure 4.9: Stress-strain curves as a function of temperature for the Ti steel at 100K/min under direct cast conditions.

Figures 4.8 and 4.9 generally show that the maximum stress decreased with increasing temperature, as would be expected. Once the ultimate tensile strength was reached, the stress drops sharply to failure for curves between 750°C and 900°C. Above 900°C, the curves displayed increasing ductility, indicated by the lengthening of the stress-strain curve (larger plastic deformation). Comparing Figure 4.8 with Figure 4.9, it can be seen that the ultimate tensile strength under direct cast conditions was slightly higher compared to that for solution treatment conditions at corresponding temperatures.

4.2.1 Stress-Strain Curves- Occurrence of Dynamic Recrystallisation

The occurrence of dynamic recrystallisation during straining has been associated with excellent ductility. Dynamic recrystallisation is indicated by fluctuations in the stress-strain curve after yielding. In order to examine the occurrence of dynamic recrystallisation, stress-strain curves at 1000°C, Figure 4.10, and at 1100°C, Figure 4.11, were plotted for all compositions.

In Figure 4.10, dynamic recrystallisation was evident (at 1000°C) for the Nb, Ti and Nb-Ti steels under solution treatment conditions but not for direct cast conditions. In Figure 4.11, dynamic recrystallisation was evident for all steels at 1100°C.

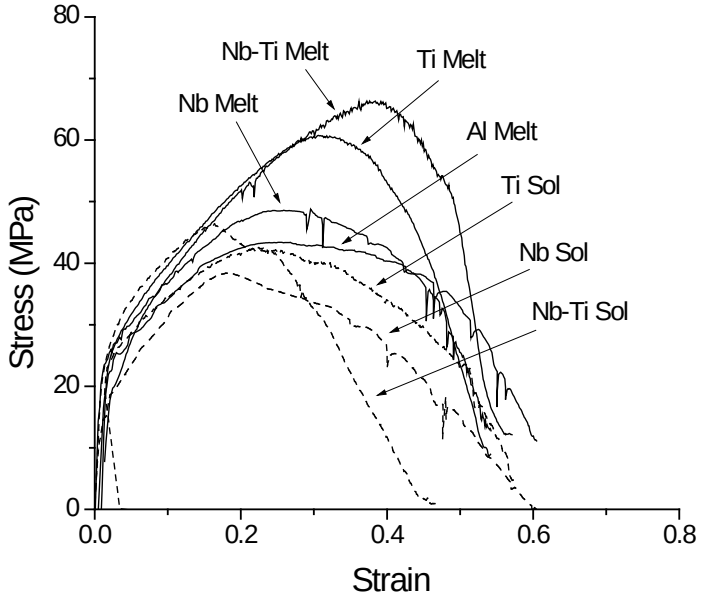

Figure 4.10: Stress-strain curves at 1000°C for indicated composition under solution treatment conditions and direct cast conditions.

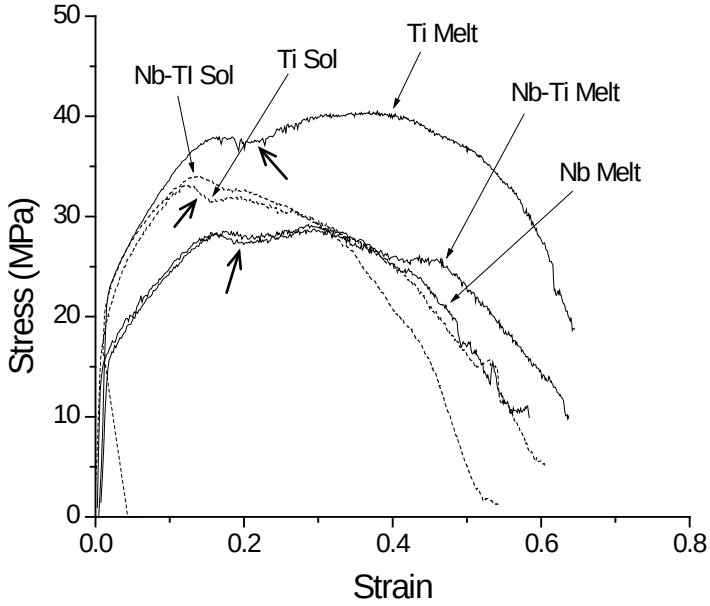

Figure 4.11: Stress-strain curves at 1100°C for indicated composition under solution treatment conditions and direct cast conditions. The arrows indicate dynamic recrystallisation.

4.3 Austenite Grain Size

The average austenite grain sizes (measured as equivalent diameter) for solution treatment and direct cast conditions for all steels are displayed in Table 4.2. For the Nb and C-Mn-Al steels, the grain size was large for both thermomechanical conditions, but was generally larger under direct cast conditions. For the Nb-Ti and Ti Steel, the grain size was much finer under solution treatment conditions compared to direct cast conditions. The direct cast grain size for Nb-Ti and Ti steel was slightly finer than those for the Nb and C-Mn-Al steels. Due to the significantly finer grain size for the Nb-Ti steel under solution treatment conditions, the linear intercept technique could be used to measure the average grain size with a satisfactory number of counts. The average grain size for the Nb-Ti steel using the linear intercept technique was 144.1μm and 144.6μm for 100K/min and 200K/min, respectively. This result compares well with the equivalent diameter method.

Table 4.2: Average austenite grain size measured as equivalent diameter.

Steel and Cooling Rate	Equivalent Diameter (μm)	
	Solution	Direct Cast
Al, 100K/min	677.9	700-1000
Al, 200K/min	502.7	700-1000
Nb, 100K/min	460.2	552.4
Nb, 200K/min	441.3	602.1
Nb-Ti, 100K/min	168.2	427.5
Nb-Ti, 200K/min	156.2	452.1
Ti, 100K/min	159.3	435.3
Ti, 200K/min	148.9	444.3

4.4 Segregation Pattern and Determination of Secondary Dendrite Arm Spacings (SDAS)

Selected solution treatment and direct cast specimens were normalized to reveal the dendritic (segregation) pattern. A macro image of a Nb specimen, representing the typical structure for solution treatment conditions is shown in Figure 4.12a. In Figure 4.12b, the typical structure for direct cast conditions was represented by a Nb-Ti specimen. It is apparent from Figure 4.12b that there was a distinct change in the segregation pattern and dendrite size in the hot zone, compared to the un-melted sections of the specimen. Figure 4.12c is a higher magnification of Figure 4.12b, featuring the transition zone. The transition zone is where there is a sharp gradient in temperature along the length of the sample, which marks the edges of the “hot zone”.

Table 4.3 displays the measured and calculated SDAS for direct cast and solution treatment conditions. SDAS were estimated from equations (3.2) and (3.3) (See Experimental Section), for the direct cast specimens. The above equations were not used for the solution treatment specimens because the cooling rate was unknown. For the solution treatment specimens, the cooling rate was equivalent to the solidification rate during casting but the exact value of this was not known. There was good agreement between the measured and calculated results for the direct cast specimens. From Table 4.3, it is clear that the SDAS for the direct cast specimens were significantly smaller than those measured for the solution treatment specimens.

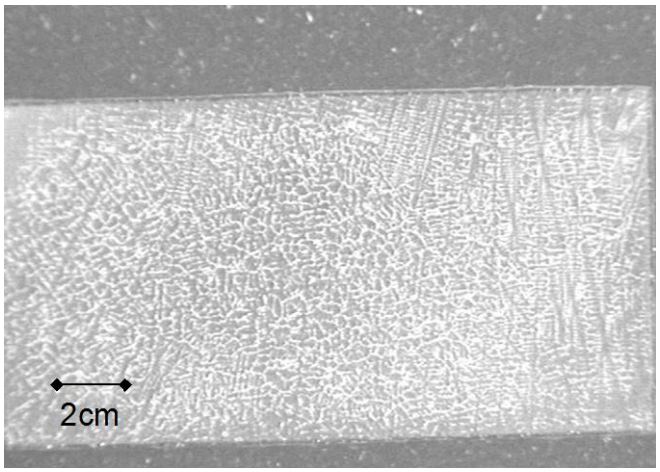

a)

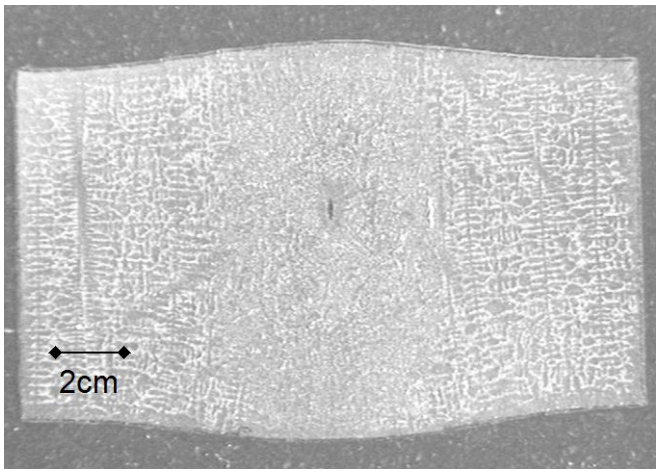

b)

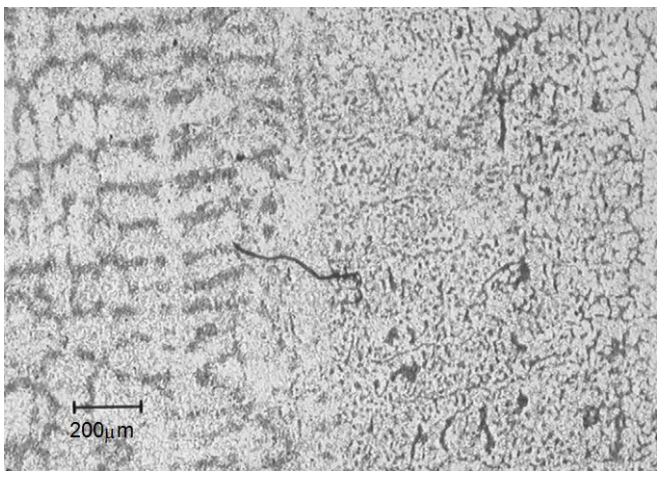

c)

Figure 4.12: Dendritic pattern after normalising where a) solution treatment conditions (Nb Steel), b) direct cast conditions (Nb-Ti Steel) and c) transition zone at edge of hot zone (Nb-Ti Steel).

Table 4.3: Measured and calculated Secondary Dendrite Arm Spacings (SDAS)

Steel	Condition & cooling rate	SDAS (μm)		
		Eqn (3.2)	Eqn (3.3)	Measured
C-Mn-Al	Melt- 6k/s	50.57	48.23	50.6
	Sol- ascast	-	-	137
Nb	Melt- 6k/s	47.22	48.06	54.9
	Sol- ascast	-	-	157.7
Nb-Ti	Melt- 6k/s	47.73	49.32	46.65
	Sol- ascast	-	-	163

4.4.1 Homogenisation Time

The diffusion data for the solutes of interest were calculated for diffusion in austenite and were taken from Smithell's Metals Reference Book [117]. The time for homogenisation for each solute element at a solution treatment temperature of 1330°C was calculated and values of D_o, Q and $D_{(1330°C)}$ are presented in Table 4.4. The homogenisation time was determined using Formula 3.4 in Experimental Section 3.4.2. The SDAS (d) was taken as 150μm, similar to that measured for solution treatment specimens, or 50μm, similar to that measured for direct cast conditions.

Table 4.4: Diffusion data for solutes in austenite, the diffusion coefficients of these elements at 1330°C in austenite and the homogenisation times.

Element	D_o (m^2s^{-1})	Q ($KJmol^{-1}$)	$D_{(1330°C)}$ (m^2s^{-1})	t (d=150μm)	t (d=50μm)
C	0.1×10^{-4}	135.7	3.78×10^{-10}	59.4 sec	6.6 sec
N	0.91×10^{-4}	168.6	2.92×10^{-10}	77.1 sec	8.5 sec
Fe	0.49×10^{-4}	284.1	2.71×10^{-14}	230 hrs	25.6 hrs
Ti	0.15×10^{-4}	251.2	9.78×10^{-14}	63.9 hrs	7.1 hrs
Nb	0.26×10^{-6}	344.6	1.53×10^{-16}	40,765 hrs	4,529 hrs
Mn	0.16×10^{-4}	261.7	4.74×10^{-14}	131.7 hrs	14.6 hrs
S	1.7×10^{-4}	221.9	9.99×10^{-12}	37.5 min	4.2 min

Table 4.4 shows that apart from the two interstitials, C and N, the homogenisation time at 1330°C for a dendrite arm spacing of 150μm would be extremely long. In this case, changes in the segregation pattern due to reheating (solution treatment) to 1330°C for 1 minute would be negligible. The time require for homogenisation for direct cast specimens, where d = 50μm (approximately), was much shorter than that for solution treatment specimens but was still considerably compared to the time spent at high temperatures during testing.

4.5 Metallographic Examination of Fracture Surfaces

The microstructures were similar for each composition; as a result of this only representative micrographs displaying important features will be shown. Individual descriptions of the fracture surface for each steel type will be dealt with in the following sections. The representative structures are shown in Figures 4.13a-i. All steels showed a predominately ferritic microstructure at 700°C, see Figure 4.13a. A predominately ferritic microstructure corresponded with good ductility. Between 750-800°C (Figures 4.13b-c), thin films of ferrite were observed at the prior austenite boundaries and intergranular cracking was observed along these ferrite films. At 850°C (Figures 4.13d-e), microstructures were generally fully martensitic, transformed from the parent austenite phase, but very thin films of ferrite at the prior austenite boundaries were occasionally detected. All steels showed evidence of intergranular cracking at 850°C, especially the microalloyed steels. At 900°C and above, Figures 4.13f-i, the microstructures were completely martensitic, transformed from the parent austenite phase. Intergranular cracking was observed up to 1000°C in some steels, but above 1000°C, no intergranular cracking was observed. When intergranular cracking did not occur, voiding was seen, as shown in Figure 4.13i.

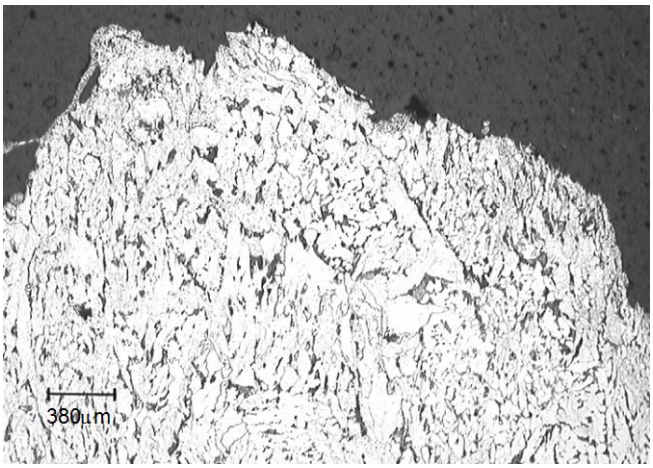

a) 700°C (Nb 200K/min Melt) x32

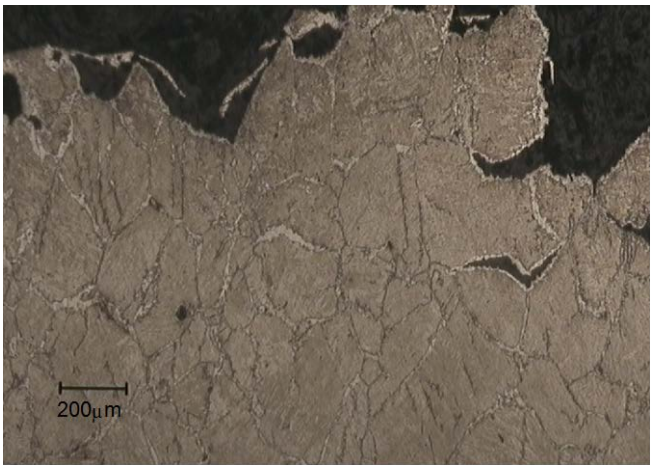

b) 750°C (Nb-Ti 100K/min Solution) x50

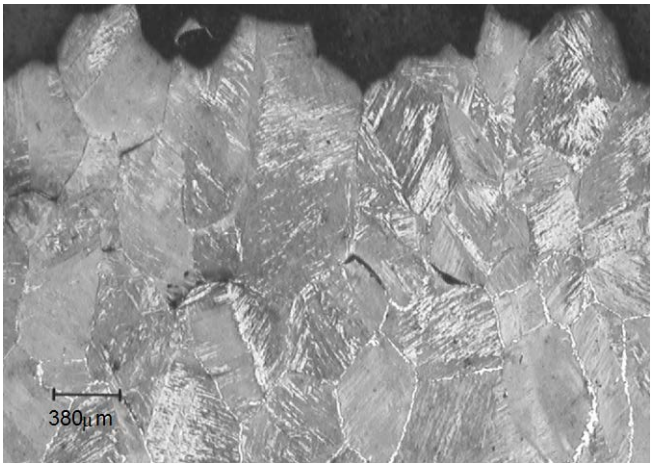

c) 800°C (Nb 200K/min Solution) x32

Figure 4.13: Representative microstructures of fracture surfaces a) predominately ferrite (700°C), b-c) intergranular cracking along ferrite films at 750°C and 800°C,

Continued over page.

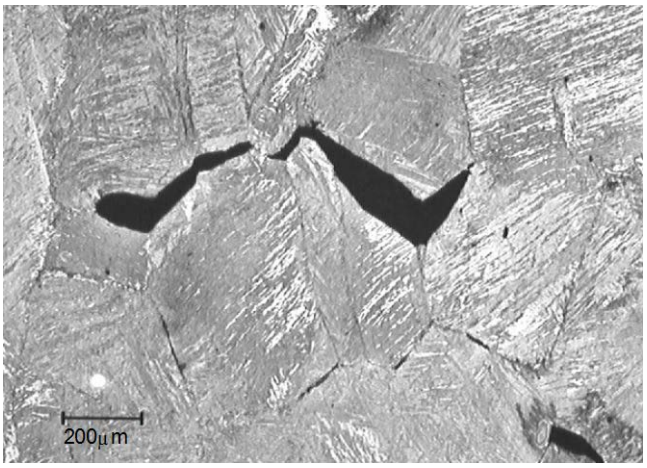

d) 850°C (Nb 200K/min solution) x50

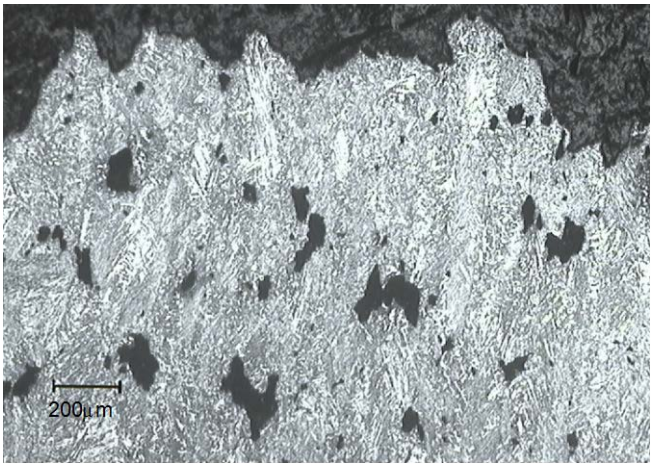

e) 850°C (Nb-Ti 100k.min solution) x50

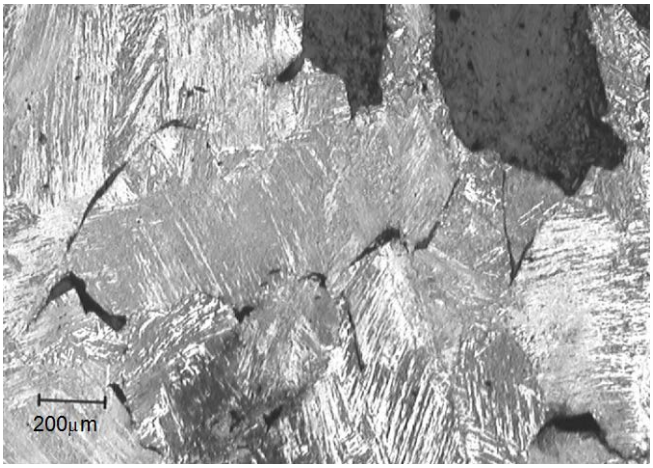

f) 900°C (Nb 200K/min Melt) x50

Figure 4.13: (cont.) d) 850°C, showing ferrite films, e) 850°C, no ferrite films, f) Intergranular cracking in martensite (transformed from parent austenite) at 900°C

Continued over page

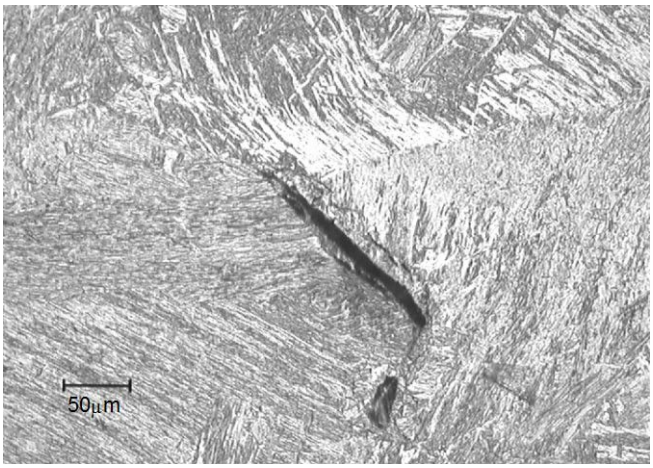

g) 950°C (Nb-Ti 100K/min melt) x200

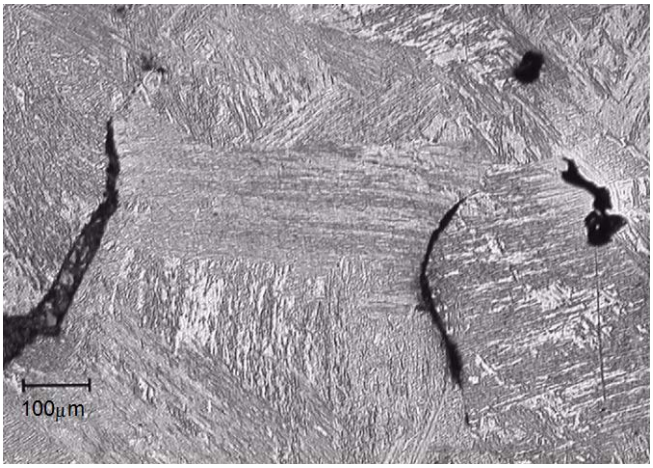

h) 1000°C (Nb-Ti 200K/min melt) x100

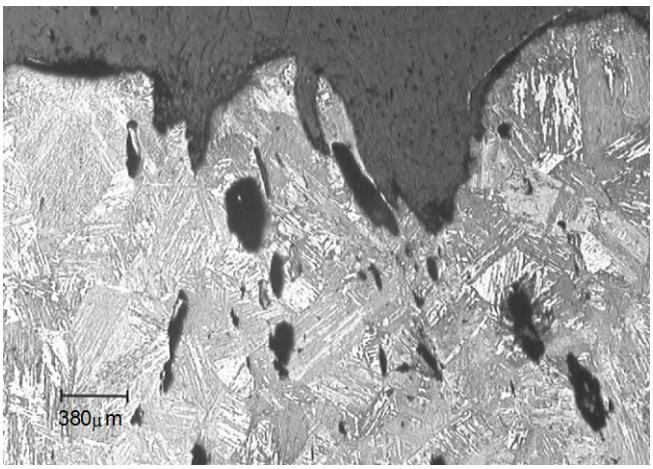

i) 1000°C (Nb 200K/min Solution) x32

Figure 4.13: (Cont.) Intergranular cracking in martensite (transformed from parent Austenite) at (g) 950°C and (h) 1000°C, i) Voiding in martensite (transformed from parent austenite) at 1000°C.

4.5.1 C-Mn-Al

Details of the microstructures for C-Mn-Al specimens are described below. At 700°C the microstructure is predominately ferrite and no intergranular cracking was observed for any of the test conditions. Intergranular cracking along ferrite films at the prior austenite grain boundaries was evident at temperatures from 750-800°C under solution treatment and direct cast conditions. At 850°C, there was some evidence of intergranular cracking in austenite and this was more prevalent under direct cast conditions. Above 850°C, the structure had transformed completely to martensite and there was no evidence of intergranular cracking, voids were present and ductility was good.

4.5.2 C-Mn-Al-Nb

At 700°C the microstructure was predominately ferrite with some martensite still remaining after quenching. At 750°C, the matrix was predominately martensitic with relatively coarse grain boundary ferrite, some matrix ferrite and intergranular cracking was observed at ferrite films at prior austenite grain boundaries. At 800°C and 850°C, intergranular cracking along thin films of grain boundary ferrite was evident. The microstructures observed at 900°C and above had transformed completely to martensite. Evidence of intergranular cracking was found at 900°C for both thermomechanical conditions. At 950°C and above, deep voids, characteristic of good ductility, were observed.

4.5.3 C-Mn-Al-Ti

At 700°C the microstructure was predominately ferrite and no intergranular cracking was observed. Intergranular cracking along ferrite films at the prior austenite grain boundaries was evident at temperatures from 750-800°C under both thermomechanical conditions. Ferrite films were occasionally detected at 850°C. Intergranular cracking in prior austenite was detected up to 900°C for solution treatment samples and 1000°C for direct cast samples.

4.5.4 C-Mn-Al-Nb-Ti

Once again the microstructure was mainly ferrite at 700°C. The presence of grain boundary ferrite was observed only at 750°C for solution treatment conditions and up to 800°C under direct cast conditions. Intergranular cracking, in a fully transformed, martensitic microstructure, was evident up to 950°C for both thermomechanical conditions but was also observed at 1000°C at 200K/min (see Figure 4.13h) under direct cast conditions.

4.5.5 Cyclic Temperature Oscillation Tests

A typical fracture surface, in the longitudinal direction, is shown in Figure 4.14 for a cyclic thermal history specimen. The microstructure was fully austenitic, before quenching, no ferrite was detected in any of the cyclic test specimens. In Figure 4.14, sharp intergranular cracking at grain boundaries can be observed at region A, and large, open cracks, region B (voids), were also present. This mixture of sharp, intergranular cracks, presumably at grain boundaries and large open cracks was seen for all three cyclic patterns (not shown here).

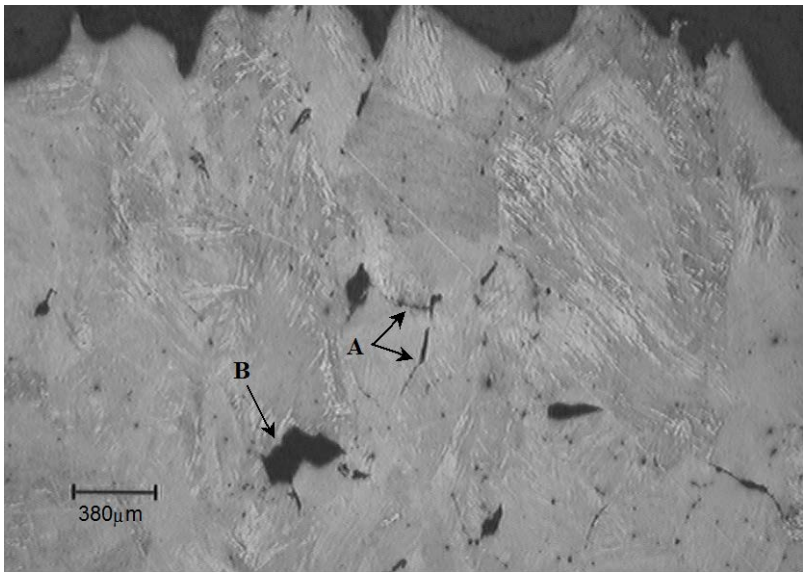

Figure 4.14: Typical fracture surface, in the longitudinal direction, displaying sharp intergranular cracks, region A and large open cracks, region B.

4.6 SEM

Fracture surfaces were examined using an SEM. Representative SEM photos, which characterize changes in fracture behaviour, are displayed in Figures 4.15a-h.

At 700°C, ductility had recovered for all steels and the typical fracture surface is represented by Figure 4.15a. The fracture was intergranular but displayed ductile features, indicated by the shallow network of voids covering the majority of the fracture surface, especially along ridges. Ductility at 700°C showed a large variation between 30-80% RA over the different thermomechanical conditions and steel types. As the ductility of specimens increased, voiding became increasingly deeper and more extensive. Specimens tested under solution treatment conditions generally had better ductility than that for direct cast conditions and correspondingly, displayed larger and more extensive void networks.

Figure 4.15b, displays intergranular failure typical of microvoid coalescence, indicated by the ductile dimples (cavities), covering the fracture surface [47, 49, 77, 78]. These dimples are shown at higher magnification in Figure 4.15c. This style of fracture occurred for all steels at 750°C, while at 800°C dimples were detected under solution treatment conditions for all steels, but only for C-Mn-Al steels, under direct cast conditions.

Figure 4.15d shows intergranular fracture with relatively smooth facets (surfaces), indicating that intergranular decohesion had occurred, typifying failure due to grain boundary sliding in austenite [47, 49, 77, 78]. The smoothness of the fracture facet can be seen more clearly at higher magnification, as seen in Figure 4.15e. This style of fracture occurred at 800°C and 850°C for all microalloyed steels.

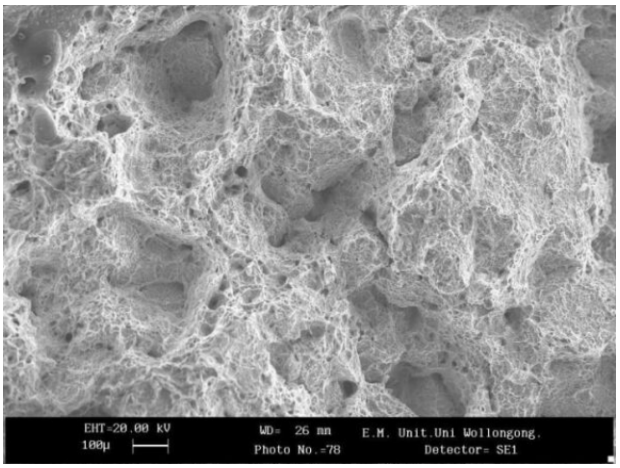

a)

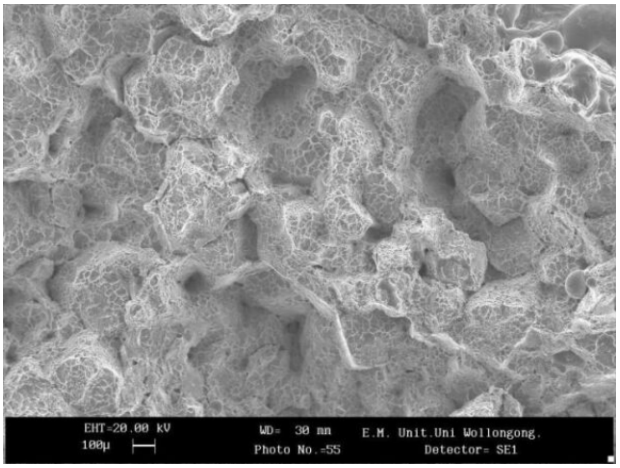

b)

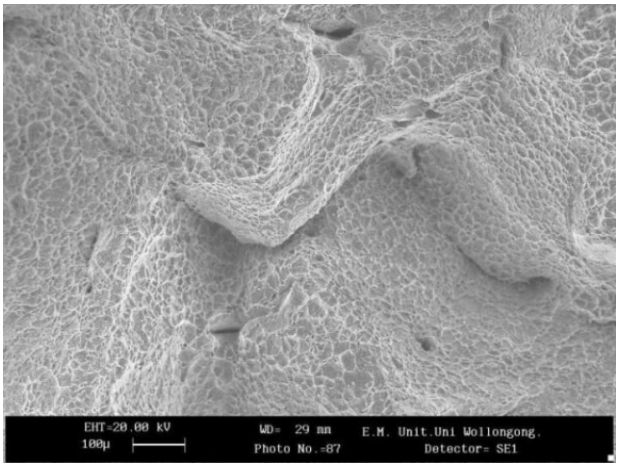

c)

Figure 4.15: Representative SEM photos of the fracture surface, where; a) Intergranular with ductile voiding at 700°C (Nb-Ti Sol), b) Intergranular failure via microvoid coalescence 750°C (Ti Melt), c) Higher mag of (b).

Continued over page

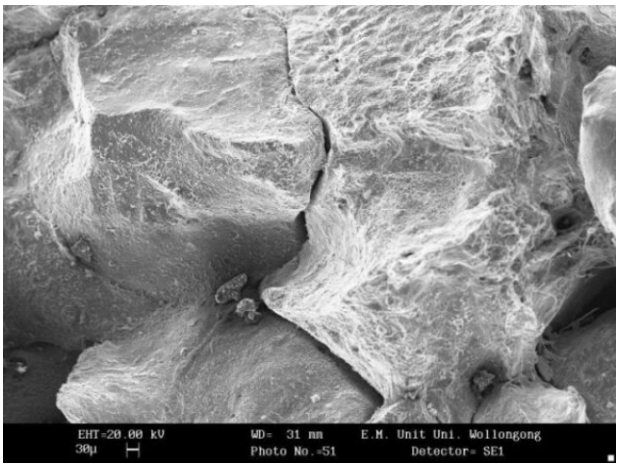

d)

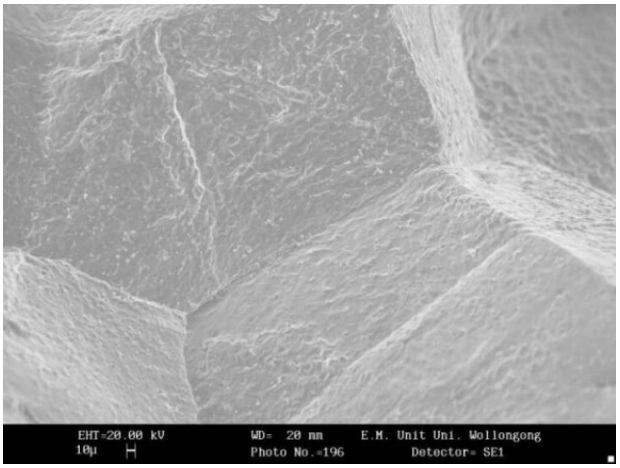

e)

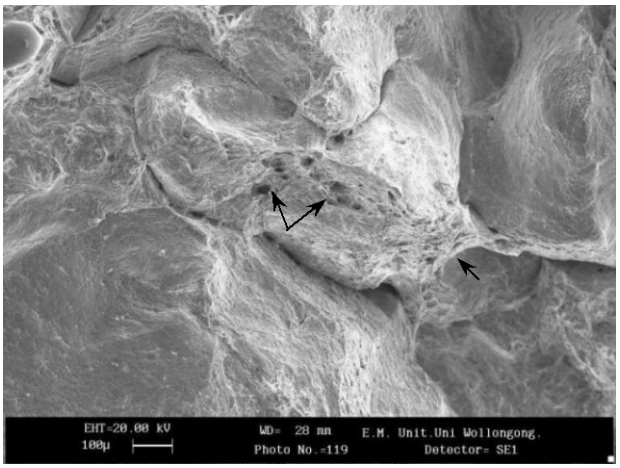

f)

Figure 4.15: (Cont.) d-e) Intergranular failure via decohesion 800°C (Nb Melt), f) Mixed mode- intergranular failure and ductile voiding 900°C (Nb-Ti Melt).

Continued over page

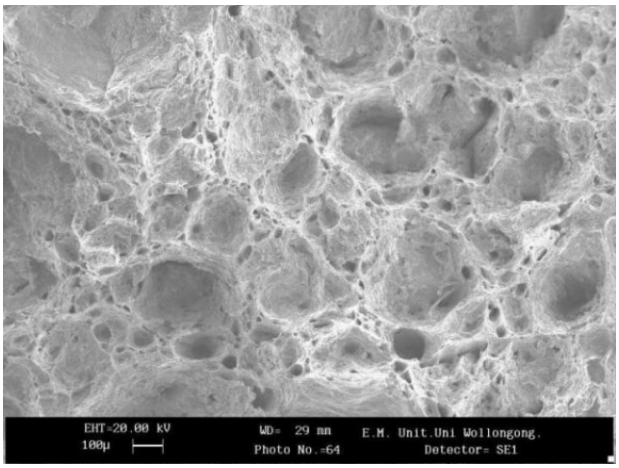

g)

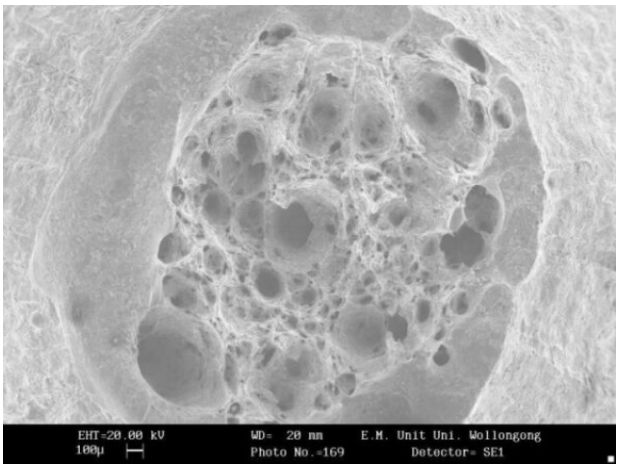

h)

Figure 4.15: (Cont.) g) Mixed failure mode where ductile mode is predominant 900°C (Ti Sol) and h) High temperature, high ductile fracture displaying deep voids 900°C (Al Sol).

Figure 4.15f displays a typical example of mixed fracture modes, where intergranular fracture was predominating and small regions of ductile voiding (indicated by the arrows) were evident. This style of fracture was displayed at 900°C for all direct cast microalloyed steels, while under solution treatment conditions, only for the Nb steel. Nb-Ti displayed this fracture mode up to 1000°C and the Ti steel displayed this fracture mode up to 950°C, under direct cast conditions. Ductility was generally below 40% if the mixed fracture mode was predominately intergranular.

Figure 4.15g shows the typical appearance of mixed fracture modes when the ductile fraction is predominating. Note the extensive network of heavily voided ridges. This style of fracture was typically observed for samples displaying moderate ductility, around 50%. The Nb-Ti and Ti steels displayed this behaviour at 900°C under solution treatment conditions, while the Nb steel displayed this fracture behaviour at 950°C under solution treatment conditions. Under direct cast conditions, microalloyed steels exhibited this mode of failure at 950°C and the Nb-Ti steel also showed this failure mode up to 1000°C. At temperatures higher than those described above for the respective steel types, the fracture surface exhibited large deep voids (craters) typical of high ductility (RA >60%). A representative SEM picture displaying high ductility is shown in Figure 4.15h. The C-Mn-Al specimens exhibited this behaviour at 850°C and above, under both thermomechanical conditions.

4.6.1 SEM- Cyclic Temperature Oscillation Tests

SEM images of the fracture surface for all three patterns for the cyclic temperature oscillation tests displayed a mixed style of fracture mode, where an extensive network of small voids was dominant. Figure 4.16 compares SEM images, of Nb-Ti specimens, tested at 900°C, where, a) direct cast conditions and b) cyclic temperature oscillations conditions. The fracture surface in Figure 4.16a shows much less voiding compared to the fracture surface in Figure 4.16b. Therefore, when temperature oscillations are introduced for the Nb-Ti steel, a more ductile fracture surface was observed, as indicated by an increased network of ductile voiding.

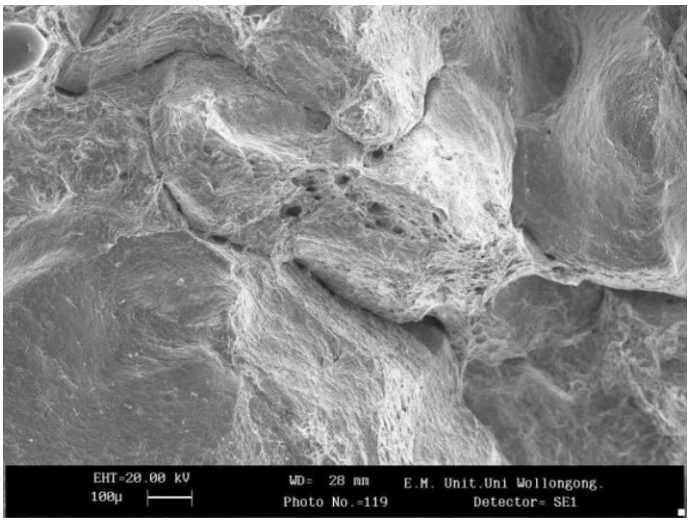

a)

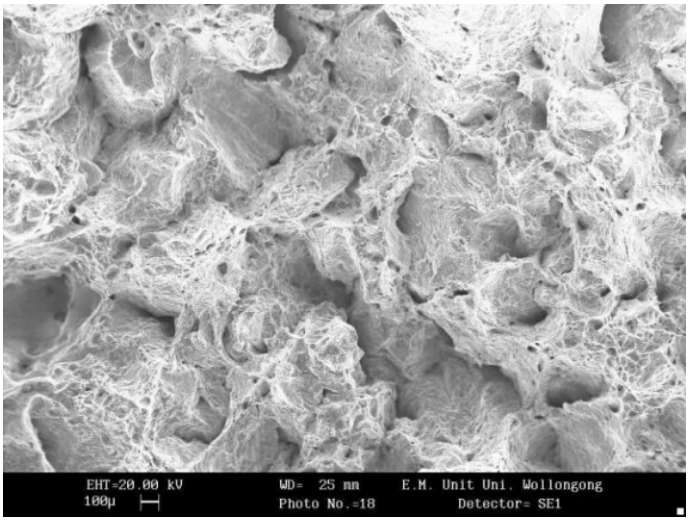

b)

Figure 4.16: SEM image of fracture surfaces for a) Nb-Ti direct cast conditions at 900°C and b) Nb-Ti direct cast- cyclic temperature oscillation test at 900°C

4.7 TEM Results

TEM work was conducted on a Phillips CM200, field emission transmission electron microscope, located at the University of New South Wales. Precipitates were identified by EDXS, using a thin window detector. Unfortunately, due to using a carbon replica, C and N could not be identified. As a result, precipitates are generally referred to as Ti precipitates in the Ti steel; Nb precipitates in the Nb steel or NbTi(C,N) in the Nb-Ti steel. It was assumed that mixed precipitates were nearly always complex NbTi(C,N).

The mean particle size and particle number density for selected steels and conditions are summarised in Table 4.5. The particle size was measured using the equivalent diameter to account for different morphologies.

4.7.1 C-Mn-Al

Investigation of carbon extraction replicas for C-Mn-Al specimens under direct cast conditions yielded very few precipitates at any temperature. A few sparse Al containing precipitates were found at 750°C and below, while no precipitates were found at higher temperatures. Precipitate analysis was not preformed on solution treatment specimens, as precipitation was not expected.

Table 4.5: Summary of the mean particle size and particle number density of selected steels and thermomechanical treatments.

Steel	Thermomechanical Condition	Temp (°C)	Mean (nm) and Count	
Nb-Ti	Melt 100K/min	1000	42.8	22
		985	26.4	100
		950	11.4	60
		900	5.2	840
		850	4.7	100
Nb-Ti	Melt 200K/min	1000	23.6	273
		975	29.0	48
		950	12.2	199
		900	5.8	332
		850	4.1	245
Nb-Ti	Solution 100K/min	950	16.0	90
		925	11.0	85
		900	11.4	32
		850	5.1	95
Nb-Ti	Solution 200K/min	950	7.4	228
		925	7.4	103
		900	6.3	495
		850	4.0	689
C-Mn-Al-Nb	Melt 100K/min	950	27.2	20
		900	13.4	107
		850	4.9	111
C-Mn-Al-Nb	Melt 200K/min	950	7.7	96
		900	6.4	90
		850	6.2	47
C-Mn-Al-Ti	Melt 100K/min	Precipitation insufficient for analysis		
C-Mn-Al-Ti	Melt 200K/min	950	10.6	78
		900	4.6	184
		850	5.1	74

4.7.2 C-Mn-Al-Ti

Results of the TEM analysis for solution treatment conditions for Ti specimens are displayed in Table 4.7.2a for 100K/min and Table 4.7.2b for 200K/min. Large precipitates were generally rectangular, as shown in Figure 4.17, and were predominant at temperatures of 950°C and above. At 950°C and below, fine (<20nm) circular precipitates evolved, the finest of which were at 900 and 850°C. Figure 4.18 shows the typical morphology of fine precipitates found at 900 and 850°C. All precipitates were Ti-bearing, presumable TiN.

The results for direct casting conditions are detailed in Table 4.7.2c for 100K/min and Table 4.7.2d for 200K/min. Precipitates found on carbon extraction replicas were analysed using energy dispersive X-rays. Detailed analysis of precipitates were performed for temperatures between 950 and 850°C, only for the higher cooling rate, as there were insufficient precipitates for analysis at 100K/min. For all other temperatures, the average precipitate size was measured manually, directly from the TEM negative.

Large Ti precipitates were found at all temperatures except 700°C and were mainly cubic or rectangular in shape and a few were oval shaped. The larger precipitates were similar to those found under solution treatment conditions (Figure 4.17). Finer Ti precipitates, <30nm, were generally circular in morphology. An example of fine Ti precipitates at 900°C is displayed in Figure 4.19. At 850°C and 750°C, fine (<15nm) Nb precipitates with a circular morphology were evident, as shown in Figure 4.20. The appearance of fine Nb precipitates in the Ti steel will be expanded on in the discussion.

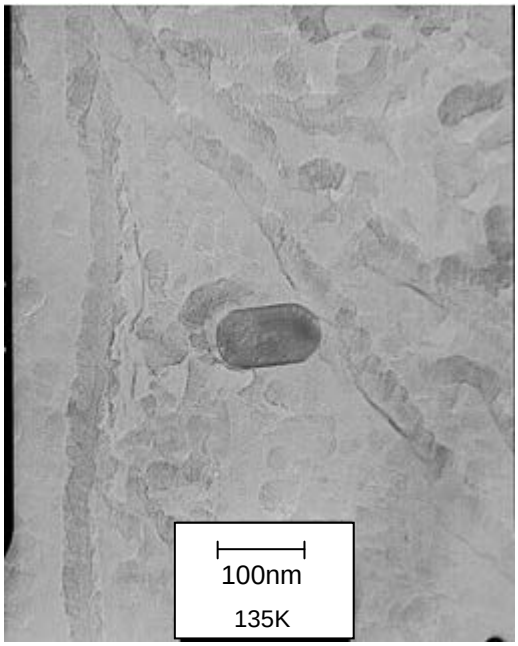

Figure 4.17: Typical morphology of rectangular precipitates (note rounding of corners) found under solution treatment conditions at temperatures 950°C and above, for Ti steel.

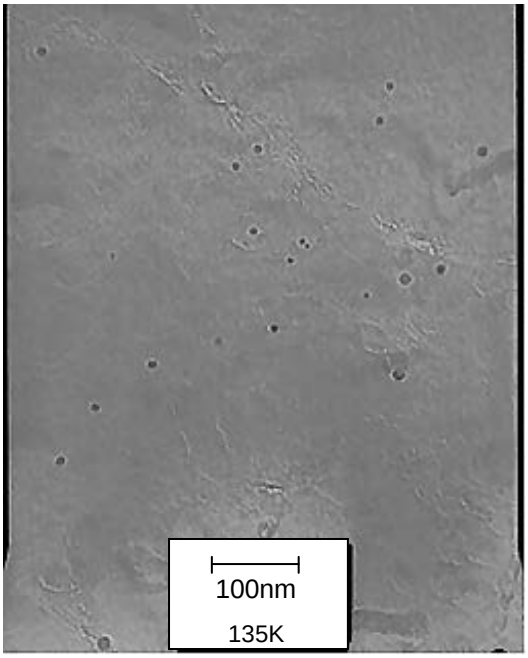

Figure 4.18: Typical morphology of fine circular precipitates found at 900°C and 850°C under solution treatment conditions for Ti steel, photo taken at 900°C at cooling rate of 200K/min.

Table 4.7.2a: TEM results, C-Mn-Al-Ti 100K/min- Solution Treatment

Temp (°C)	Atomic ratio (%)	Description & Observations
1100	NA	
1000	100% Ti	100+ nm Rectangular few
950	100% Ti	40-80nm Rectangular
		15-25nm Circular
900	100% Ti	20-80nm Rectangular
		6-12nm circular
850	100% Ti	14-40nm circular, some 40+ nm rectangular
800	100% Ti	30-100nm Rectangular, square
		3-12nm Circular
750	100% Ti	70-120nm rectangular
		4-12nm Circular, few
700	N/A	

Table 4.7.2b: TEM results, C-Mn-Al-Ti 200K/min- Solution Treatment

Temp (°C)	Atomic ratio (%)	Description & Observations
1100	100% Ti	50-130nm Rectangular with rounded corners
1000	100% Ti	40-80nm Rectangular with rounded corners and Ovals
950	100% Ti	30-80nm Rectangular
		15-25nm Circular
900	100% Ti	20-60nm Rectangular
		6-15nm circular
850	100% Ti	4-8nm circular
800	100% Ti	30-80nm Rectangular
		5-12nm Circular, small clusters
750	100% Ti	4-12nm Circular, 50-120nm rectangular
700	N/A	

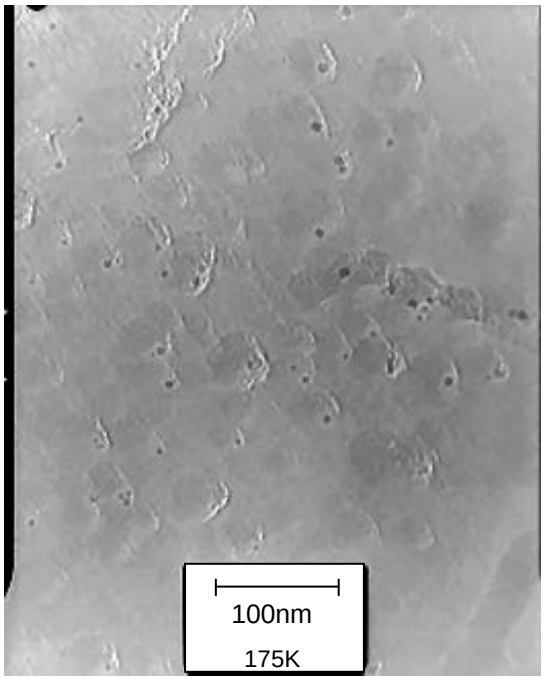

Figure 4.19: Typical morphology of Fine TiN precipitates found under direct cast conditions, for Ti steel at 900°C. Precipitate size <30nm.

Figure 4.20: Typical morphology of fine circular Nb precipitates found at 850°C under direct cast conditions, for Ti steel. Precipitate size <15nm.

Table 4.7.2c: TEM results, C-Mn-Al-Ti 100K/min- Direct Cast

Temp (°C)	Atomic ratio (%)		Description & Observations
	Ti (%)	Nb (%)	
1000	100	0	20-40nm Circular and rounded Cubic
950	0	100	25-40nm Rectangular and a few Oval (uneven)
900	0	100	15-20nm Oval, some elongated
875	0	100	6-20nm Circular
800	100	0	5-15nm Circular & Cubic, Sparse
750	100	0	4-12nm Circular & Oval, some 20-30nm
700	100	0	5-20nm Circular & Oval

Table 4.7.2d: TEM results, C-Mn-Al-Ti 200K/min- Direct Cast

Temp (°C)	Atomic ratio (%)		Description & Observations
	Ti (%)	Nb (%)	
1100	100	0	50-275nm Rectangular
1000	100	0	120-250nm Rectangular, Oval & 20-30nm Circular
950	100	0	300-750nm Square, Rect. & 10-20nm Circular
900	100	0	50-180nm Square & 3-10nm Circular
850	100	0	80-160nm Rhombus, Oval
	0	100	3-15nm Circular **Note** Nb!
800	100	0	120-230nm Oval or Rounded
	0	100	4-15nm Circular **Note** Nb!
750	100	0	100-140nm Rounded
	0	100	3-10nm Circular, Sparse
700	100	0	3-20nm Circular

4.7.3 C-Mn-Al-Nb

Under solution treatment conditions, precipitation was found at 900°C and 850°C, while at all other temperatures precipitation was sparse. The typical size of precipitates at 900°C was 5-12nm with a few larger precipitates up to 30nm in size. The typical size of precipitates at 850°C was 4-8nm and there were no larger precipitates. Precipitates generally had a circular morphology.

Details of the analysis of precipitation found under direct cast conditions for the Nb Steel are shown in Tables 4.7.3a-b. Extracted precipitates were Nb bearing and were circular or oval in morphology. Many of the larger Nb precipitates found above 900°C had traces of up to 3% Ti (atomic). Between 800-700°C, precipitates were sparse and several MnS precipitates were detected. At 700°C, Al was found to be associated with several of the Nb precipitates. The typical morphology of fine Nb precipitates is shown in Figure 4.21, taken at 900°C, under direct cast conditions.

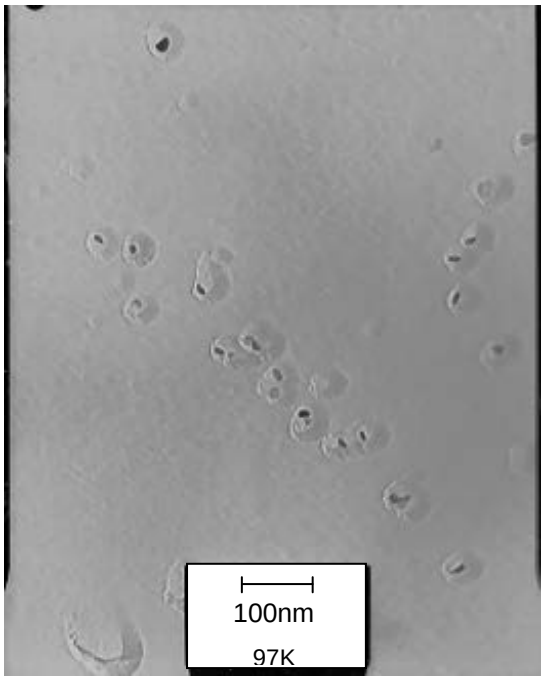

Figure 4.21: Typical morphology of fine Nb precipitates, formed in a row, taken at 900°C under direct cast conditions for Nb steel.

Table 4.7.3a: Nb Steel 100K/min- Direct cast

Temp (°C)	Atomic ratio (%)	Description & Observations
1050	-	Nothing
1000	100% Nb, ~2-3% Ti	20-40nm, Uneven or kidney shaped
	100% Nb, ~2-3% Ti	60-80nm Rectangular
950	100% Nb, ~2-3% Ti	20-30nm Circular
900	100% Nb	12-40nm Circular (uneven)
	~90% Al, 10% S	Al & S 40-90nm odd shaped, sparse
850	100% Nb	10-15nm Circular, few up to 30nm
800	-	Nothing
750	45% Mn, 55% S	MnS very few found
700	100% Nb	5-15nm Rounded
	85-75% Nb, 15-25% Al	10-20nm Circular, Darker spot at centre
	40-50% Mn, 50-60% S	MnS 50-150nm Oval

Table 4.7.3b: Nb Steel 200K/min- Direct cast

Temp (°C)	Atomic ratio (%)	Description & Observations
1100	-	Nothing
1050	100% Nb	200nm very few
1000	100% Nb, ~2-3% Ti	70-120nm Circular
950	100%Nb, ~2-3% Ti	30-50nm Rounded squares, 20-40nm Slits
	100% Nb, ~2-3% Ti	60-100nm Oval
900	100% Nb, ~2-3% Ti	10-15nm Oval, round
	100% Nb	4-10nm Circular, few groups
850	100% Nb	5-14nm Circular
800	5-30% Nb, Bal Si	4-5nm Circular, Sparse & associated with Si
750	100% Nb	15-20nm Circular, Sparse
700	100% Nb	5-15nm Circular
	~85% Nb, 15% Al	10-15nm, Circular (uneven), Dot at centre

4.7.4 C-Mn-Al-Nb-Ti

Precipitates for the Nb-Ti steel at all temperatures were almost always mixed NbTi(C,N). Larger precipitates, under both thermomechanical conditions, showed several precipitate morphologies including: rectangular, cubic (rhombus), oval and star shaped (crucifix precipitates). Figure 4.22 displays typical rectangular and oval morphologies (At 1000°C, solution treatment conditions), while Figure 4.23 displays the typical crucifix morphology (At 1000°C, solution treatment conditions). Fine precipitates, <15nm, were mainly circular in appearance. Figure 4.24 represents fine precipitates under solution treatment conditions, while Figure 4.25 represents fine precipitates under direct cast conditions (also shows a crucifix shaped precipitate). In Figure 4.26, an example of the growth of caps, presumable Nb, on a rectangular precipitate, possibly TiN but more likely to be a complex NbTi(C,N), was observed at 850°C under solution treatment conditions. EDXS failed to pick-up any variation in the Nb:Ti ratio, so it was not clear if the caps were high in Nb. Work by Craven at el [118] found similar capped precipitates, where the core was TiN and the caps were NbC based. Tables' 4.7.4a-d details the precipitation results for the Nb-Ti steel.

Figure 4.22: Typical morphology of rectangular and circular precipitates found under solution treatment conditions, taken at temperature 1000°C for Nb-Ti steel.

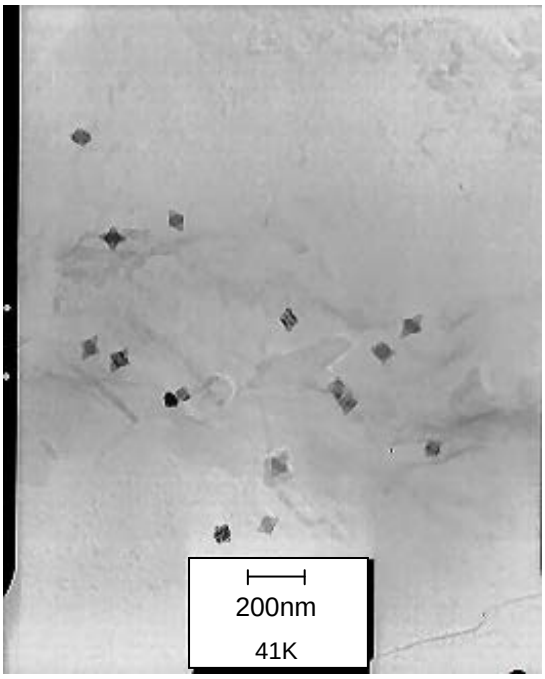

Figure 4.23: Typical morphology of star shaped (crucifix) precipitates found at 1000°C under solution treatment conditions for Nb-Ti Steel.

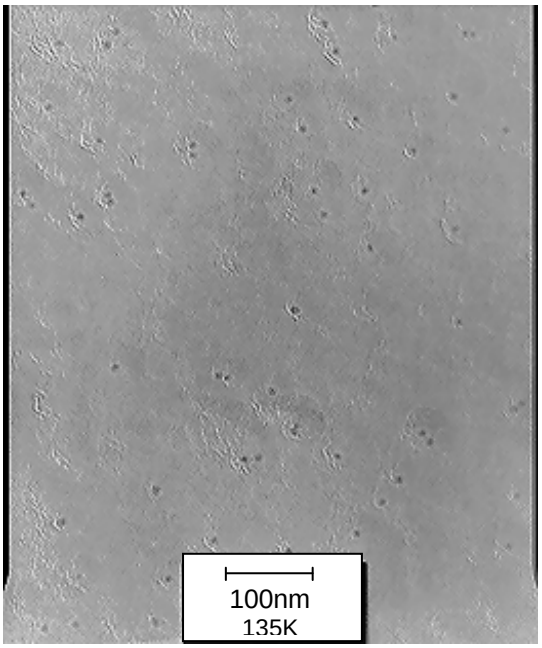

Figure 4.24: Typical morphology of fine precipitates found between 950°C and 850°C under solution treatment conditions, Nb-Ti Steel. (Photo taken at 950°C)

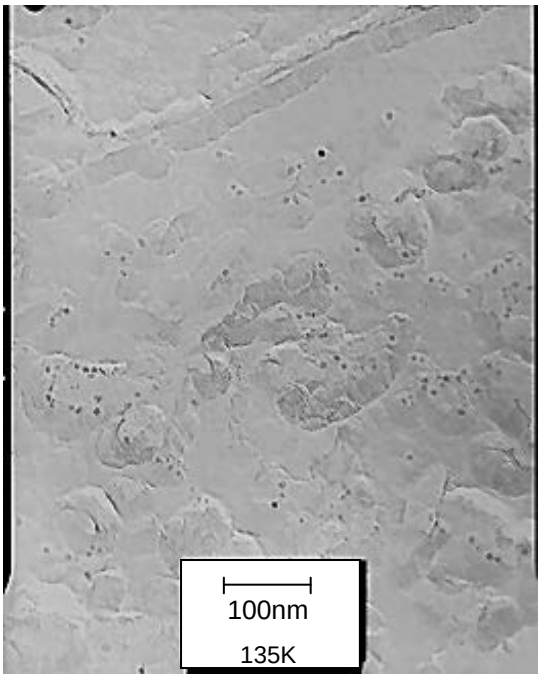

Figure 4.25: Typical morphology of fine precipitates found between 950°C and 850°C under direct cast conditions, Nb-Ti Steel. (Photo taken at 900°C)

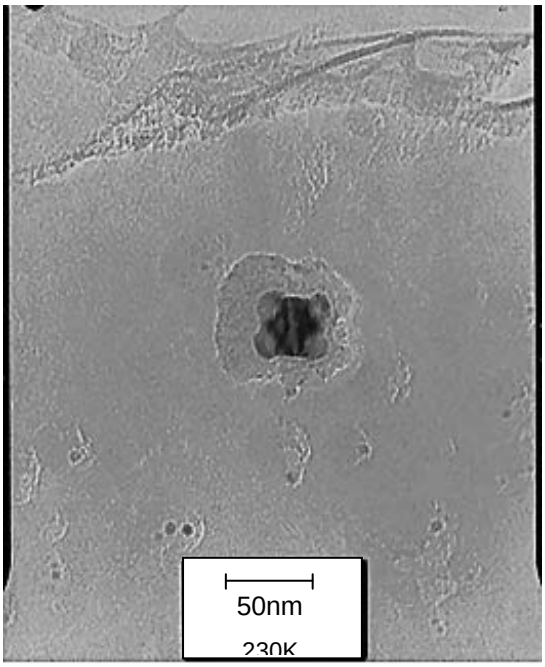

Figure 4.26: Precipitate displaying caps (possibly higher in Nb than the core) on each corner of a larger rectangular precipitate, taken at 850°C under solution treatment conditions, Nb-Ti Steel.

Table 4.7.4a: Nb-Ti 100K/min- Solution Treatment

Temp (°C)	Atomic ratio (%)		Description & Observations
	Ti (%)	Nb (%)	
1100	70-80	30-20	40-200nm Rectangular, 60-80nm Oval
	60-80	40-20	30-40nm Square
1000	100	0	Rectangular, 40-120nm, 40-220nm & Oval, 60-80nm
950	45-50	50-55	10-20nm Circular, few Rhombus ~30-40nm
925	55	45	12-40nm Rounded Squares
	75	25	20-50nm Rhombus & Rectangular
900	100	0	100-250nm Rectangular
	100	0	6-12nm Circular
850	70-85	30-25	30-80 Rectangular, Rhombus
	10-15	90-85	3-10nm Circular
800	70-90	30-10	40nm Rhombus, 300-800nm Rectangular
	10	90	80-300nm Ovals, sparse
750	100	0	50-200nm Rectangular and a few Fine ~2-3nm
700	40-20	60-80	4-12nm Circular
	85	15	100+ nm Rectangular

Table 4.7.4b: Nb-Ti 200K/min- Solution Treatment

Temp (°C)	Atomic ratio (%)		Description & Observations
	Ti (%)	Nb (%)	
1100	70-85	30-15	40-140nm Rhombus (some rounded) & Rectangular
1000	80-90	20-10	50-250nm Rectangular
	30	70	40-100nm Rhombus
	50-55	50-45	50-90nm Oval & Star shaped
950	65	35	Larger ppt, >30nm
	15	85	20-25nm rhombus
925	74	26	40-50nm rhombus
	28	72	10-15nm circular
900	75-85	25-15	40-100nm Rectangular
	35-45	65-45	8-10nm Circular, Rhombus
850	85	15	150+nm rectangular & rounded
	N/A	N/A	~5nm circular, Atomic ratio not clear at this stage
800	85-91	15-9	40-170nm Rectangular
	32-42	68-58	3-5nm Circular
750	70-95	30-5	50-350nm Rectangular, Larger the higher Ti%
	15-20	85-80	5-10nm Circular
700	30-50	50-70	3-12nm Circular
	90	10	70-150nm Rectangular, Sparse

Table 4.7.4c: Nb-Ti 100K/min- Direct cast

Temp (°C)	Atomic ratio (%)		Description & Observations
	Ti (%)	Nb (%)	
1100	60	40	40-80nm Square to Star shaped
	70	30	120-400nm (larger)
1000	80	20	20-35nm Rhombus
	96	4	80-100nm Rectangular
985	55	45	15-40nm Rectangular
975	60-40	40-60	10-20nm Rhombus & Circular and some at 50nm
950	55	45	20-30nm Rhombus & Circular
	100	0	60-100nm Circular
900	50	50	5-15nm circular
850	50	50	5-10nm circular
	100	0	50-150nm Circular
800	50-60	40-50	10-20nm Rhombus or rounded
750	48-58	52-42	8-20nm Rhombus & Circular
	100	0	150-400nm Rhombus
700	35-55	65-45	3-10nm Circular
	40	60	10-15nm Rhombus

Table 4.7.4d: Nb-Ti 200K/min- Direct Cast

Temp (°C)	Atomic ratio (%)		Description & Observations
	Ti (%)	Nb (%)	
1100	85	15	Large rectangular, 100-200nm
1050	35	65	Av. Size 100nm, Star shaped
	64	36	Larger Star ppt, 150+ nm
	60	40	Fine ppt, 5nm
1025	40-50	50-60	40-80nm circular, Oval
	65	35	100+nm Oval and Star shaped
1015	55-65	45-35	30-70nm Rhombus and occasional Star
1000	60	40	10-50nm rhombus
985	65	35	30-50nm rhombus
975	55	45	40-70nm Rhombus & ovals
	70	30	100nm+ oval shaped
950	54	46	10-30nm rhombus
900	50-56	44-50	5-15nm Rhombus & circular
850	52	48	8-15nm circular
	70	30	10-15nm circular, less common
800	30-40	70-60	10-30nm Rhombus, 50-100nm Star shaped
750	56	44	5-15nm Rhombus & circular
700	40	60	3-5nm Circular
	60	40	15-20 Circular

4.7.5 TEM Particle Size Distribution Histograms

Histograms displaying the particle size distributions are detailed in **Appendix B**. Here, the most relevant histograms in relation to the discussion have been included. The following histograms have been converted to display the number of particles per unit area to permit more accurate comparisons of the particle density. Equivalent diameter was used as the measure of the particle size.

Figure 4.27 includes histograms for Nb-Ti specimens, tested under direct cast conditions, taken at 900°C. The particles per unit area as a function of size distribution are shown for 100K/min in Figure 4.27a and for 200K/min in Figure 4.27b. The two figures show similar distributions but there were a higher number of particles per unit area for the cooling rate of 200K/min.

The number of particles per unit area as a function of size distribution of the Nb-Ti specimens tested under the thermal temperature oscillation conditions are shown in Figure 4.28, where a) Cycle 1, b) Cycle 2 and c) Cycle 3. It can be observed that Cycle 2 had a significantly higher number of fine particles than Cycles 1 and 3.

Figure 4.29 displays the histograms for Nb-Ti specimens that have been quenched at key temperatures during the thermal temperature oscillation program. In Figure 4.29a, the specimen was quenched at the minimum temperature drop (T_{min}), 900°C and in Figure 4.29b, the specimen was quenched at the maximum reheating temperature (T_{max}), 1100°C, prior to the introduction of the thermal oscillations. (Refer to Figure 3.5 in the experimental section). For the specimen quenched at 900°C (Figure 4.29a), only a few fine precipitates were found. For the specimen quenched at 1100°C (Figure 4.29b), a relatively large number of fine, <10nm, precipitates (compared to specimens quenched at 900ºC) were found and a lower amount of coarser, >10nm, precipitates were found.

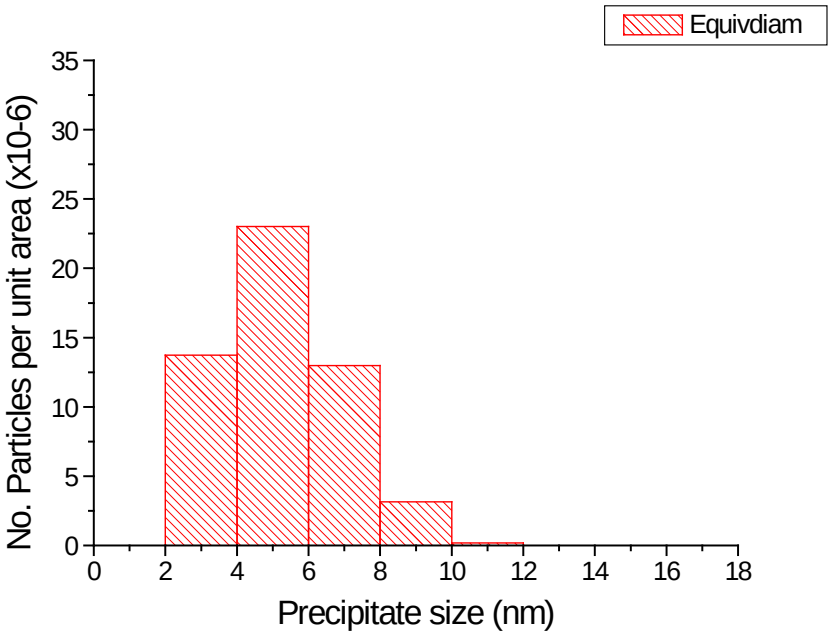

a)

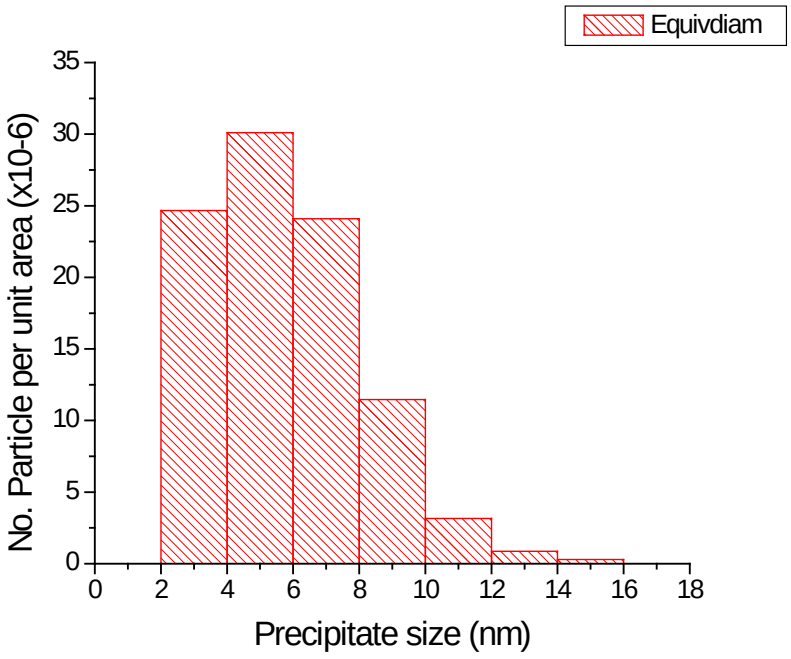

b)

Figure 4.27: Histograms displaying the number of particles per unit area as a function of size distribution for Nb-Ti, direct cast conditions (900°C), where a) 100K/min and b) 200K/min.

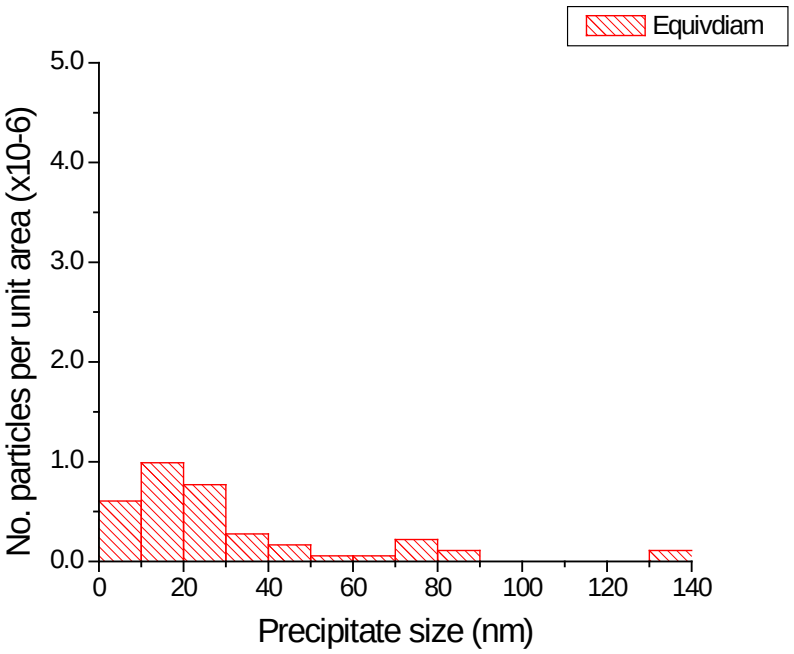

a)

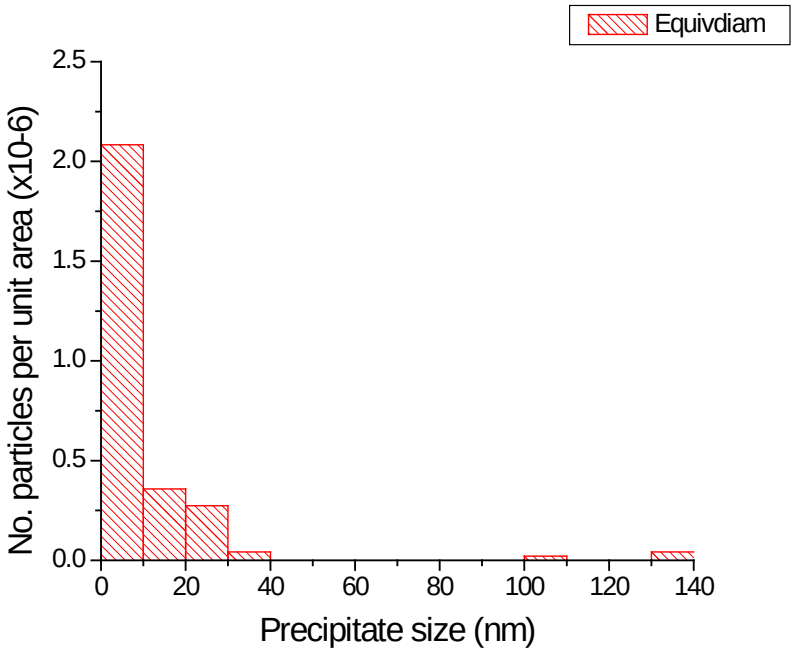

b)

Figure 4.28: Histograms displaying the number of particles per unit area as a function of size distribution for Nb-Ti, thermal temperature oscillations, where a) cycle 1, b) cycle 2 and c) cylce 3.

(Continued over page)

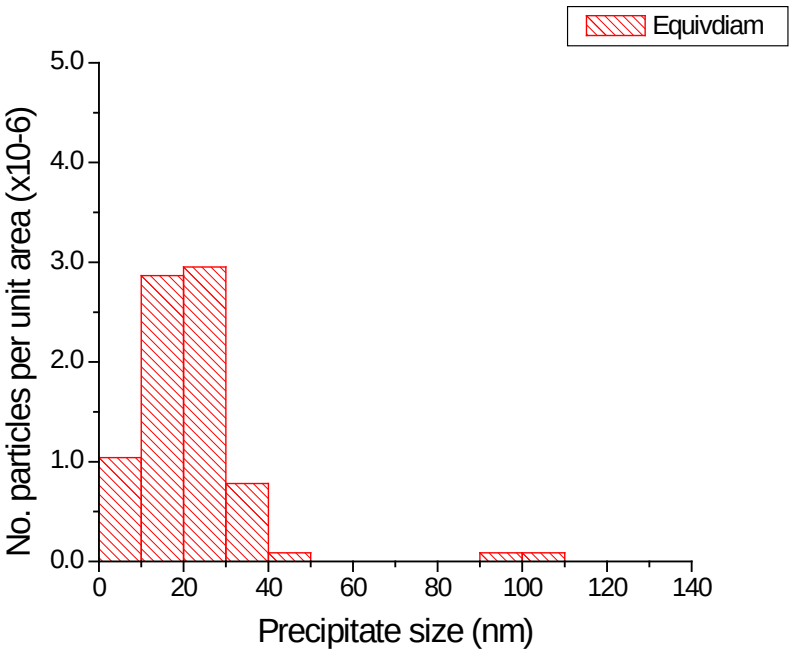
Equivdiam
No. particles per unit area (x10-6)
5.0
4.0
3.0
2.0
1.0
0.0
0
20
40
60
80
100
120
140
Precipitate size (nm)

c)

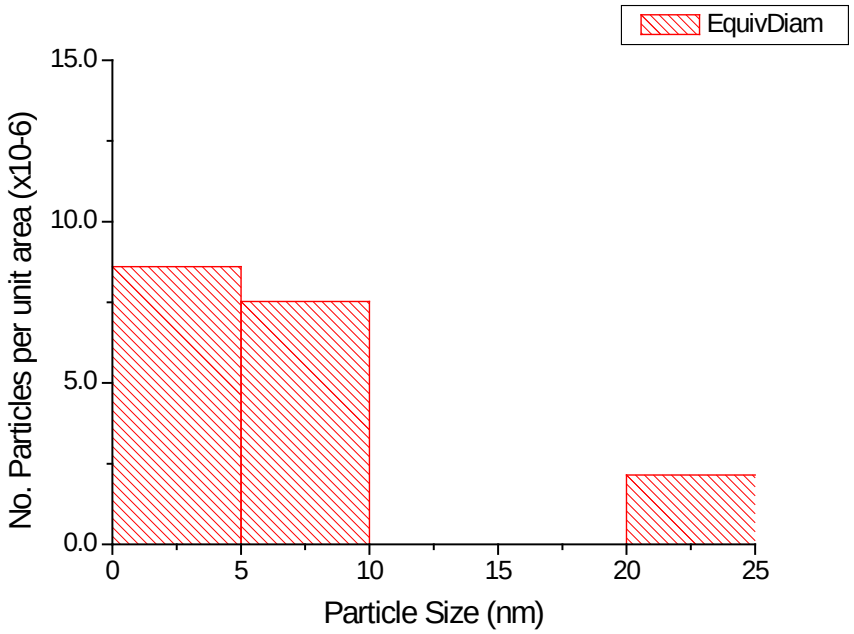

a)

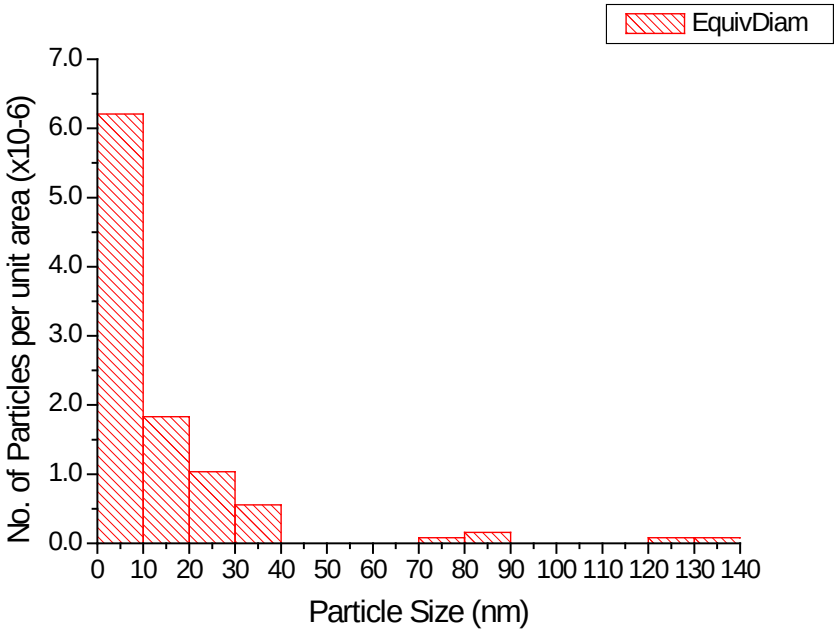

b)

Figure 4.29: Histograms displaying the number of particles per unit area as a function of size distribution for Nb-Ti, thermal temperature oscillations, where a) quenched at 900°C (T_{min}) and b) quenched at 1100°C (T_{max}).

Figures 4.30a-c and 4.31a-c display histograms for the number of particles per unit area as a function of particle size distribution for Nb-Ti specimens tested under solution treatment conditions. Figure 4.30 contains the histograms for temperatures 950°C, 900°C and 850°C for 100K/min, while Figure 4.31 contains histograms for the same temperatures but at 200K/min. The scale is the same for corresponding temperatures, for the two cooling rates.

From comparing the histograms, it can be seen that there was a much greater volume fraction of finer particles at all temperatures shown for the higher cooling rate. The particle size distributions were much broader at the lower cooling rate, for corresponding temperatures, than those seen at the higher cooling rate. Both conditions had the highest density of fine particles at 850°C.

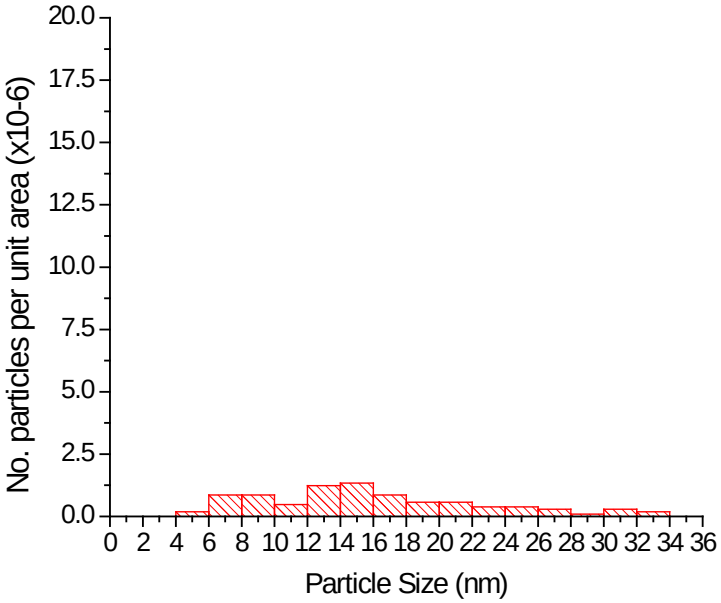

a)

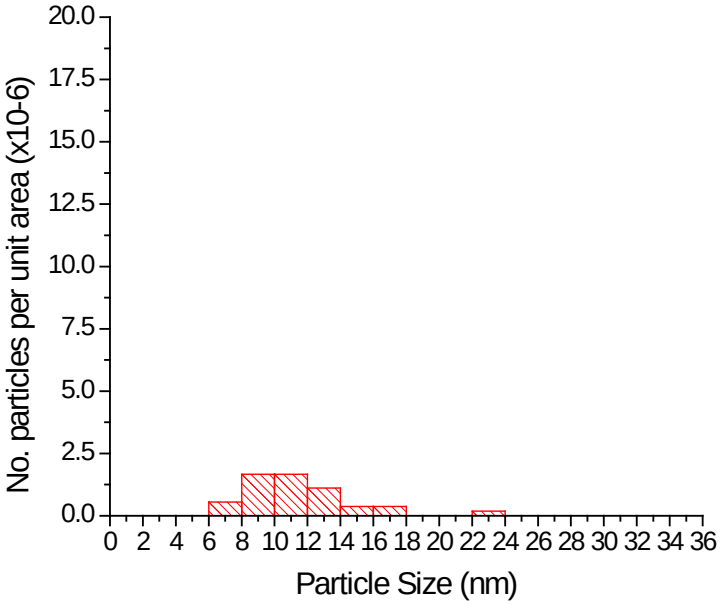

b)

Figure 4.30: Histograms displaying the number of particles per unit area as a function of size distribution for Nb-Ti, solution treatment conditions 100K/min, where a) 950°C, b) 900°C and c) 850°C.

(Continued over page)

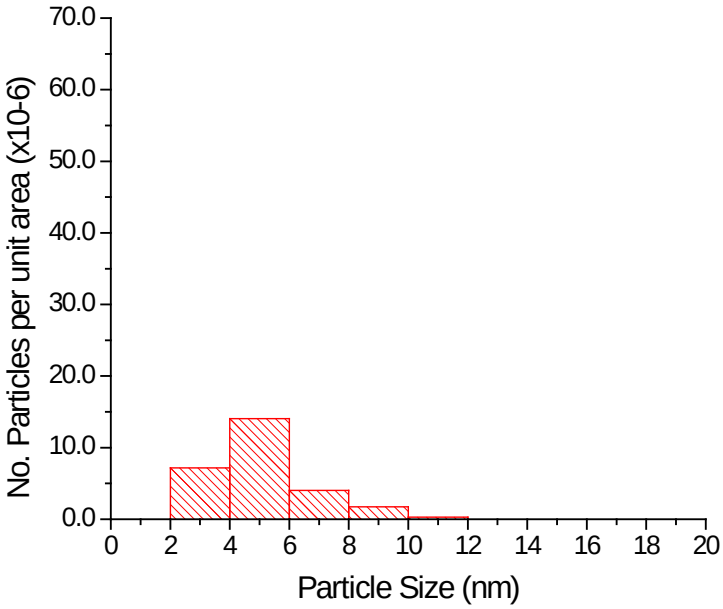
No. Particles per unit area (x10-6)
70.0
60.0
50.0
40.0
30.0
20.0
10.0
0.0
0
2
4
6
8
10
12
14
16
18
20
Particle Size (nm)

c)

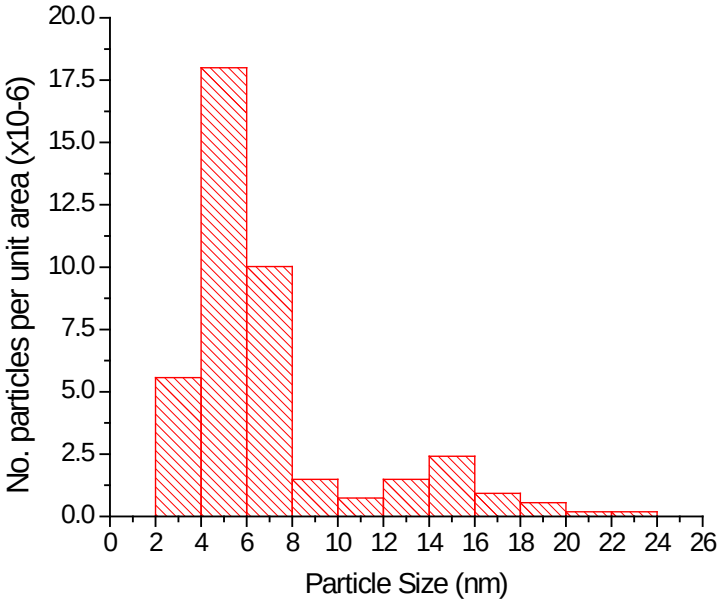

a)

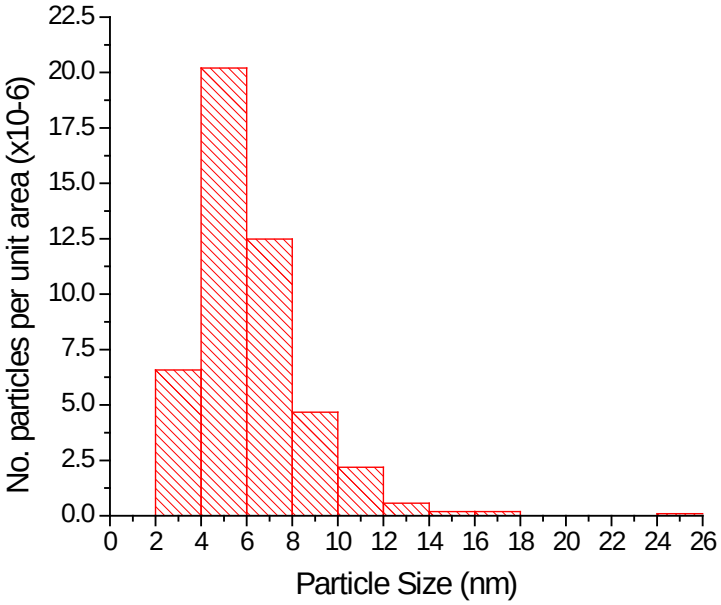

b)

Figure 4.31: Histograms displaying the number of particles per unit area as a function of size distribution for Nb-Ti, solution treatment conditions 200K/min, where a) 950°C, b) 900°C and c) 850°C.

(Continued over page)

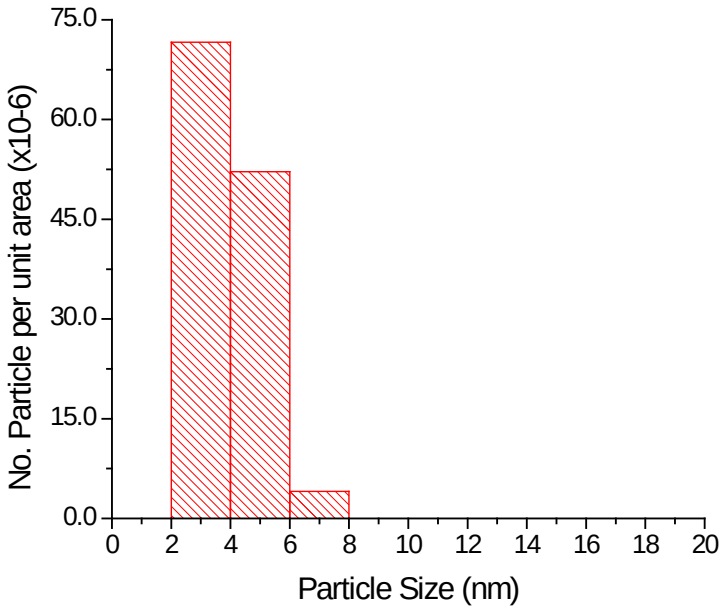

c)

4.7.6 Influence of Particle Size on Hot Ductility

Hot ductility (%RA) as a function of average particle size is graphed in Figure 4.32 for direct cast specimens. The average particle size, measured as equivalent diameter, from Nb and Nb-Ti specimens (>850°C) was included in the graph. Although there is some scatter, from Figure 4.32, it can be seen that RA drops sharply when the particle size falls below 15nm. The influence of microalloyed precipitates found in the two-phase (γ + α) region, 800-750°C, on RA is also included in Figure 4.32. There was no apparent relationship between particle size and RA for microalloyed precipitates found in the two-phase region. This is understandable because ductility is controlled by the formation of ferrite at prior austenite boundaries in the two-phase region.

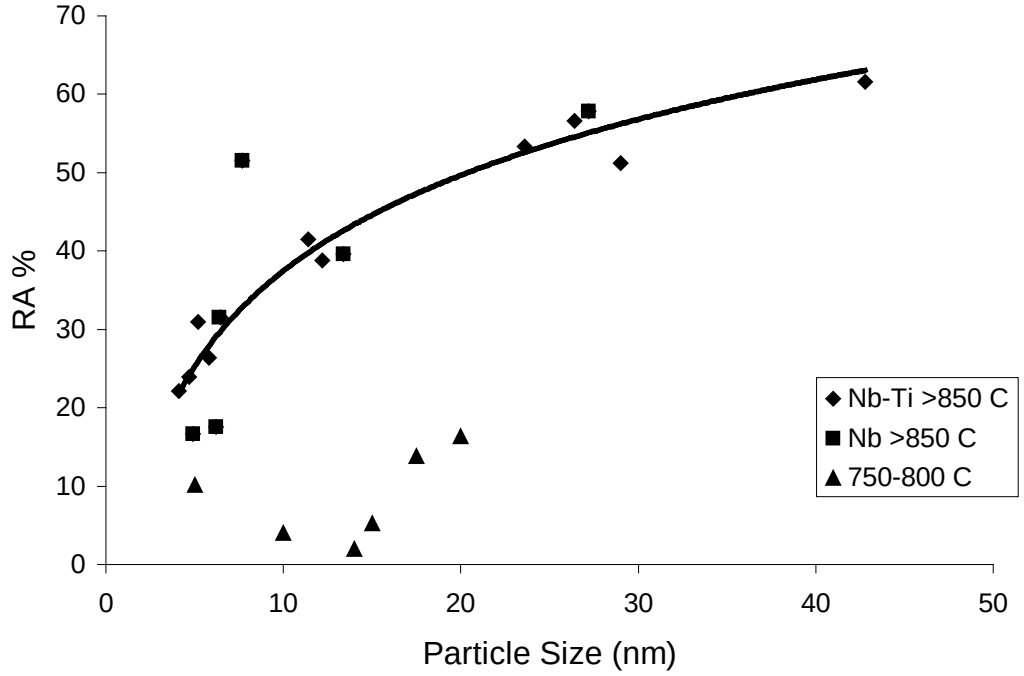

Figure 4.32: Reduction of area (RA) as a function of average particle size (nm) for precipitates in Nb and Nb-Ti specimens in the single-phase austenite region for direct cast specimens. Included in the figure is the influence of precipitation in the two-phase region, 750-800°C, on RA.

4.7.7 Influence of Interparticle Spacing on Hot Ductility

The influence of interparticle spacing on RA is graphed in Figure 4.33 for the Nb-Ti steel under direct cast conditions. Measurement of the interparticle spacing was discussed in Section 3.6. Although there is some scatter, Figure 4.33 shows that RA decreases with decreasing interparticle spacing. The interparticle spacing for all microalloyed steels at 900 and 950°C, under direct cast conditions, is shown in Table 4.7. The interparticle spacing was much larger at 950°C than it was at 900°C for all three steels. Niobium steels had a much larger interparticle spacing compared to the Ti, and Nb-Ti steels.

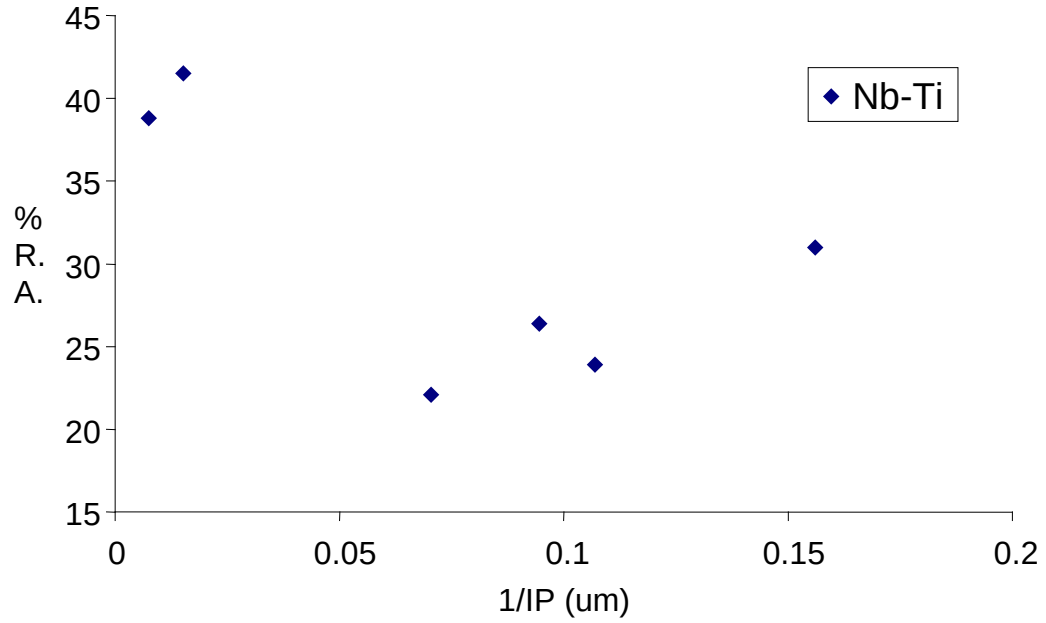

Figure 4.33: Reduction of area as a function of interparticle spacing (1/IP) for the Nb-Ti steel, under direct cast conditions.

Table 4.7: Interparticle spacing for the microalloyed steels at 900°C and 950°C, for direct cast conditions.

Steel	Interparticle Spacing (μm)	
	900°C	950°C
Nb	181.82	2000
Ti	19.38	69.44
Nb-Ti	8.49	108.44

4.8 Dilatometry and Transformation Temperatures

Dilatometry was used to determine the transformation temperatures of the Nb and Nb-Ti steels for the cooling rates of 100K/min and 200K/min. In addition to this, the Ar_3 and Ae_3 temperatures were calculated using Thermo-Calc software and also using equations, based on composition, for Ar_3 and Ae_3. Equation (4.1) was used to calculate Ar_3 and Equation (4.2) was used to calculate Ae_3 [98]. Table 4.8 summarizes the transformation temperature results.

$$Ar_3 = 911 - 310C - 80Mn - 20Cu - 15Cr - 55Ni - 80Mo \text{ (wt\%)} \quad (4.1)$$

$$Ae_3 = (911 - 29Mn + 70Si - 10Cr) - (418 - 32Mn + 86Si + Cr)C + 232C^2 \text{ (wt\%)} \quad (4.2)$$

Table 4.8: Summary of Transformation Temperatures.

Method	Transf'n	Al (°C)	Nb (°C)	Ti (°C)	Nb-Ti (°C)
Dilatometry	Ar_3- 100K		764*		754
	Ar_3- 200K		742*		721
	Ar_1- 100K		623		667
	Ar_1- 200K		617		652
Thermo-Calc	Ar_3	765.2	763.9	731.9	726.4
	Ae_3	830.6	823.7	826.3	827.8
Eq'n(4.1)	Ar_3	807.9	802.9	769.7	761.5
Eq'n(4.2)	Ae_3	841.0	834.0	832.5	834.5

* Shallow curve, temperature taken from bottom of curve.

The Ar_3 temperature was lower for the Nb-Ti steel compared to the Nb steel for both cooling rates. The Nb-Ti steel has a lower Ar_3 temperature, mainly due to the higher Mn content; a higher Mn content lowers the Ar_3 temperature. Increasing the cooling rate to 200K/min lowered Ar_3 by 33°C for Nb-Ti and 22°C for Nb steel. Dilatometry was unavailable for the C-Mn-Al and Ti steels.

From Table 4.8, it is evident that the C-Mn-Al and the Nb steel have higher Ar_3 transformation temperatures compared to the Ti and Nb-Ti steels. The Ae_3 temperatures are similar for all steels, as calculated by Equation 4.2.

4.9 Young's Modulus and Yield Stress

Results for the Young's modulus (YM), calculated theoretically (see Section 3.8 in Experimental), are shown in Table 4.9. There was little variation in the YM across all four steels due to their similar compositions and melting points. Young's modulus decreases steadily with increasing temperature.

Table 4.9: Young's modulus values for all steels determined theoretically.

Temperature	Young's Modulus (MPa)			
(°C)	C-Mn-Al	Nb	Nb-ti	Ti
700	142056.5	142200.9	141924	141890.8
750	136563	136718.1	136420.6	136384.9
800	131069.4	131235.2	130917.2	130879.1
850	125575.8	125752.4	125413.8	125373.2
900	120082.2	120269.5	119910.4	119867.3
950	114588.7	114786.7	114406.9	114361.4
975	111841.9	112045.3	111655.2	111608.5
985	110743.2	110948.7	110554.6	110507.3
1000	109095.1	109303.8	108903.5	108855.5
1015	107447	107659	107252.5	107203.8
1025	106348.3	106562.4	106151.8	106102.6
1050	103601.5	103821	103400.1	103349.6
1100	98107.95	98338.14	97896.7	97843.76

Yield stress as a function of test temperature for the Nb-Ti steel for both thermomechanical conditions and cooling rates are shown in Figure 4.34.

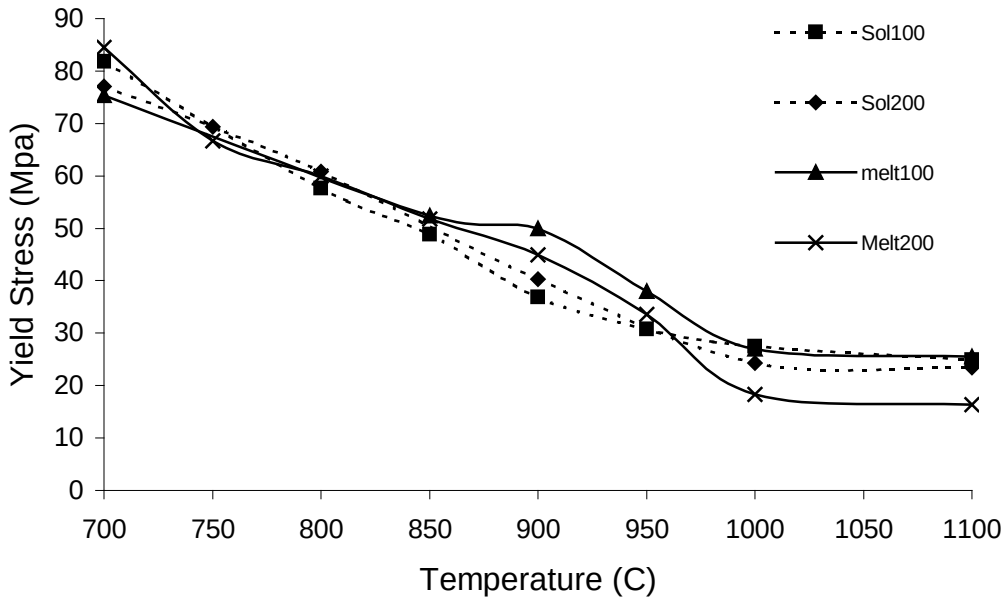

Figure 4.34: Yield stress as a function of test temperature for the Nb-Ti steel for all thermomechanical conditions.

Chapter 5:

Discussion

5.0 Discussion

The origins of low ductility and the relationships between hot tensile tests and transverse cracking during continuous casting were discussed in the literature review. In this section, variables pertinent to the thin slab casting (TSC) process, such as, alloying additions, cooling rate and thermal history, are reviewed.

There are still casting problems for difficult grades of steel, particularly for microalloyed steels containing Nb and\or Ti with carbon contents in the peritectic range. There has been little work done on the influence of TSC on the hot ductility of microalloyed steels, where higher cooling rates of approximately 200K/min (close to the surface) are observed. Accordingly, the influence of higher cooling rates on hot ductility will be discussed.

For C-Mn-Al and C-Mn-Al-Nb steel, variations in the ductility results between solution treatment and direct cast conditions have been reported in the literature. The differences between solution treatment and direct cast tests, with respect to hot ductility, will be assessed.

Complex cooling patterns during continuous casting have been shown to influence hot ductility results. In particular, conflicting results on the benefits from additions of Ti to Nb-bearing steels have been related to the influence of the complex thermal history during continuous casting. The thermal history experienced by the top surface of a continuously cast slab broadly consists of a sharp drop in temperature after exiting the mould, reheating to some maximum, before cooling slowly down to the unbending temperature. Temperature oscillations are introduced at the slab surface from the alternate impingement of water sprays and contact with the guide rolls. Due to the difficulties in simulating the complex cooling patterns of continuous cast slabs, research in this area has seldom been done. Generally, only simple cooling patterns have been investigated. The influence of complex cooling patterns on the hot ductility of Nb-Ti steels will be discussed.

5.1 Influence of Precipitation on Hot Ductility

As was discussed in the literature review, the influence of precipitation on hot ductility depends on: particle size, volume fraction and location. A fine particle size generally leads to low ductility, especially in microalloyed steels [47]. Increasing the volume fraction of fine particles will lower the ductility even further. Initiation of cavities can occur at grain boundary particles and this will enhance the failure process. Therefore, the location of particles is important.

5.1.1 Influence of Precipitate Size on Reduction of Area (RA)

The influence of precipitate size on reduction of area for the microalloyed steels is shown in Figure 5.1. In Figure 5.1, only precipitation occurring in single-phase austenite, >850°C, was included in the curve. Even though there is some scatter, the graph indicates that the precipitate size must be below 15nm to have a strong influence on the ductility (<40% RA). This result correlates closely to similar results by Comineli [73], shown in Figure 2.11, Chapter 2, which also indicated that precipitates below 15nm would be detrimental to ductility.

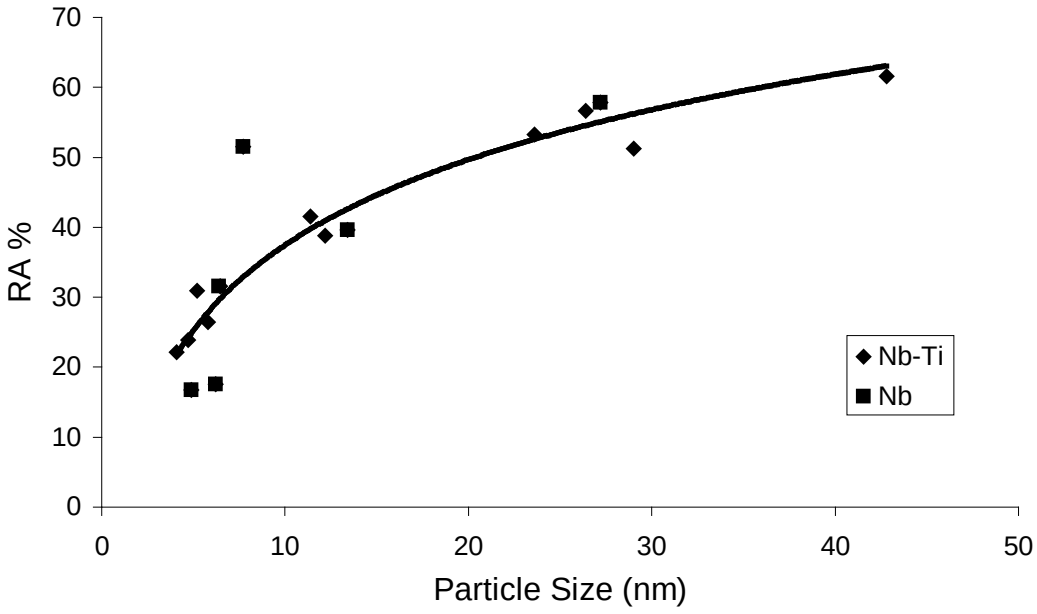

Figure 5.1: Reduction of area as a function of average particle size (nm) for precipitation (at a test temperature of ≥ 850°C) in Nb and Nb-Ti specimens.

Finer precipitation can affect hot ductility in a number of ways; two mechanisms of most interest are the influence of precipitates on grain boundary sliding and the degree of precipitation strengthening. The role of precipitation on grain boundary sliding has previously been discussed in Sections 2.4.3 and 2.5.2, in the literature review. In essence, finer precipitates are more effective in pinning grain boundaries, allowing time for cracks or voids to nucleate and grow before the grain boundary can move away and isolate the crack. The finer the particles, the more detrimental the particles are to ductility, as was the case in Figure 5.1.

The interaction between dislocations and precipitates will be a significant factor in determining strength and ductility. It is important to distinguish if dislocations cut (shear) the particles or if dislocations are by-passing (looping) the particles. The shape of the stress-strain curve will depend on whether particle shearing or non-shearing occurs. For coherent particles, glide dislocations pass through and cut the particles and the stress-strain curve will have a similar shape to that of a pure metal, apart from a higher yield stress. When the particle is hard and incoherent, dislocations can only by-pass the particle and rapid work hardening will occur due to the high rate of increase in the dislocation density [113, 119].

If particles are cut, then there will be planar slip leading to a relatively large dislocation pile-up along the slip band. This will lead to high stresses and could lower ductility due to the initiation of microcracks [114]. As carbides/nitrides are very hard and incoherent, the precipitates would be expected to resist shearing even at very fine sizes. Thus, particle cutting would not be expected. Inspection of the stress-strain curves, Figures 4.8 and 4.9, Chapter 4, show stress-strain curves with high rates of work hardening, which confirms that dislocation by-passing was the dominant operating mechanism. There was no evidence to indicate that particle cutting contributed to the low hot ductility observed for the microalloyed steels.

5.1.2 Influence of Volume Fraction of Precipitation

Increasing the volume fraction of fine particles normally results in decreasing ductility. Unfortunately, volume fraction is difficult to measure from carbon extraction replicas due to the extensive number of TEM micrographs required to give a true indication of the volume fraction. Segregation on a coarse scale makes accurate volume fraction determination difficult. While the true volume fraction was not precisely measured, an indication of the volume fraction can be obtained from the TEM results. Particle size distributions were counted from the same number of TEM micrographs that were randomly taken over a number of different replicas. From this, the particle size distribution measured as the average number of particles per unit area (density) was calculated.

An alternative method involved measuring the average interparticle spacing to obtain a measure of the volume fraction. Here, it was assumed that a decrease in interparticle spacing would indicate a higher volume fraction of precipitates given the same thermomechanical history and alloying additions. The influence of interparticle spacing on RA for the Nb-Ti steel under direct cast conditions is shown in Figure 4.33, Chapter 4. Although the trend was poor, Figure 4.33 showed decreasing RA with decreasing interparticle spacing.

5.1.3 Influence of Location of Precipitation

The location of precipitates, such as at grain boundaries, can influence hot ductility as they are preferential sites for void initiation. Grain boundary precipitates can affect hot ductility in a number of ways. At higher temperatures, grain boundary particles can initiate cavities during grain boundary sliding, while at lower temperatures, grain boundary particles enhance microvoid coalescence within the ferrite films surrounding the austenite grain boundaries. Coarser particles, approximately >50nm, arranged in rows indicate the former position of austenite grain boundaries [120]. An example of such precipitation is shown in Figure 5.2 (Nb-Ti steel, direct cast 975°C, 200K/min).

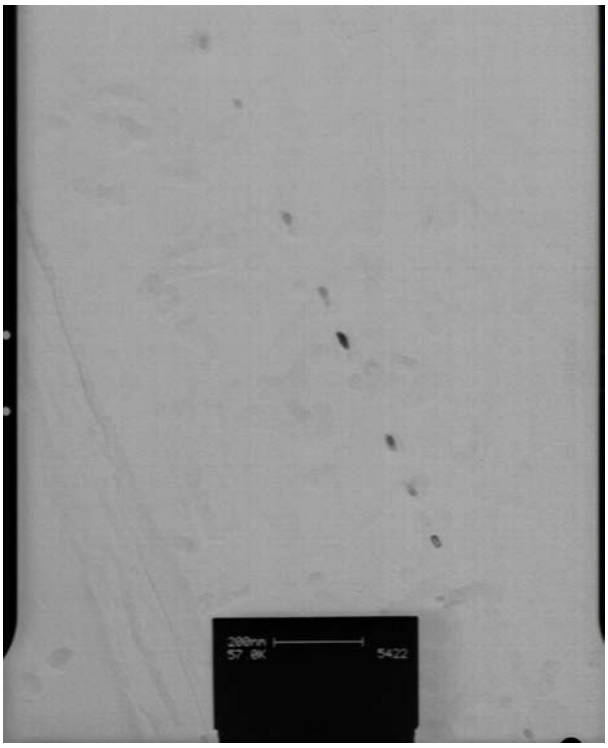

Figure 5.2: Precipitation arranged in a row, probably indicating the former position of an austenite grain boundary. (Nb-Ti steel, direct cast 975°C, 200K/min).

The formation of precipitate free zones (PFZ) are known to form in Nb microalloyed steels and will reduce hot ductility [47]. In this case, it is the absence of precipitates in regions surrounding austenite grain boundaries that cause ductility to deteriorate due to stress concentrating in this softer region. No evidence of PFZ was found in TEM analyses so this mechanism for reducing ductility could not be substantiated. Due to the small area viewed using a TEM, PFZ's may be present but were not detected.

5.2 Influence of Alloying Additions

The C-Mn-Al steel was used as the base composition to enable comparisons to be made from the additions of microalloying elements. The microalloying additions were Nb, Ti and Nb-Ti. The hot ductility behaviour of C-Mn-Al specimens will be discussed first, followed by the influence of the microalloying additions on the C-Mn-Al steel.

5.2.1 Base Composition- C-Mn-Al

For C-Mn-Al steel, hot ductility troughs were deep and narrow for all test conditions, as can be seen from Figure 4.1. The ductility troughs were between 750°C and 850°C and the minimum ductility was at 800°C for both thermomechanical conditions. Metallographic inspection of tensile specimens revealed the presence of thin films of ferrite at prior austenite grain boundaries at 800°C but not at 850°C. The ductility trough was consistent with the model described in Section 2.4.1, Chapter 2 namely; ductility was controlled by the formation of grain boundary ferrite.

Inspection of fracture surfaces at 800°C, using an SEM, showed characteristics of intergranular failure, with fine dimples covering the surface. Dimpled fracture structures are typical of failure via microvoid coalescence at precipitates and/or inclusions in ferrite films [47, 49, 77, 78]. We can conclude that transformation controlled intergranular failure due to microvoid coalescence at ferrite films was responsible for the ductility trough. Transformation controlled refers to the failure mechanism being related to the formation of ferrite in austenite. The formation of thin films of ferrite at austenite grain boundaries allows strain to concentrate in the softer ferrite film and failure ultimately occurs by microvoid coalescence in the ferrite layer. The ductility trough begins when thin ferrite films first form at prior austenite grain boundaries. The trough finishes once the temperature is sufficiently low to allow an adequate volume fraction of matrix ferrite to alleviate the stress concentration and ductility recovers. The ductility trough is accordingly referred to as transformation controlled [47].

Above the minimum ductility temperature (800°C), significant voiding, characteristic of good ductility, was observed in SEM samples. An example of a specimen with good ductility, displaying large, elongated voids can be seen in Figure 4.15h, Chapter 4. Once cracks become isolated (for example, by grain boundary migration), they are distorted into elongated voids during deformation, until final failure occurs by necking between these voids [47].

The reduction of area values for direct casting conditions were approximately 20% lower than those for solution treatment conditions across the entire test temperature

range. An increase in grain size for the direct cast specimens is considered to be the major reason for this decrease in hot ductility. The grain size for solution treatment conditions was between 500-600μm, while for direct cast conditions the grain size was over 1000μm. Previous work [71, 72] showed that once the grain size was over 400μm, there would be little further influence from grain size on hot ductility. However, the strain rate of 7.5 x 10^{-4} s^{-1} for this research was approximately an order of magnitude lower than that used for the majority of hot ductility research. Failure due to grain boundary sliding becomes increasingly active at lower strain rates and for this reason the influence of grain size on ductility was much more pronounced. When failure was due to ferrite films, decreasing the grain size would improve ductility because it is more difficult for intergranular cracks to propagate through triple points and a shorter crack length reduces the stress concentration [47, 70]. The influence of grain size on hot ductility was discussed in more detail in Section 2.5.1, in the literature review.

The effect of an increased grain size for the direct cast specimens was also seen in the stress-strain curves for the C-Mn-Al steel, as shown in Figure 5.2. When comparing stress-strain curves for solution treatment and direct cast conditions at the same temperature, the direct cast curves showed an increase in tensile strength. This increase in strength is related to the equi-cohesive temperature, which is defined as the temperature at which grains and grain boundaries have equal strength [121]. Transgranular failure will occur when the grains (slip planes) are weaker than the grain boundaries, while for intergranular fracture (as in this case) the grain boundary is the weaker component [122]. Above the equi-cohesive temperature, material with larger grain sizes will have a higher strength than a fine-grained material because the amount of grain boundary area decreases with increasing grain size.

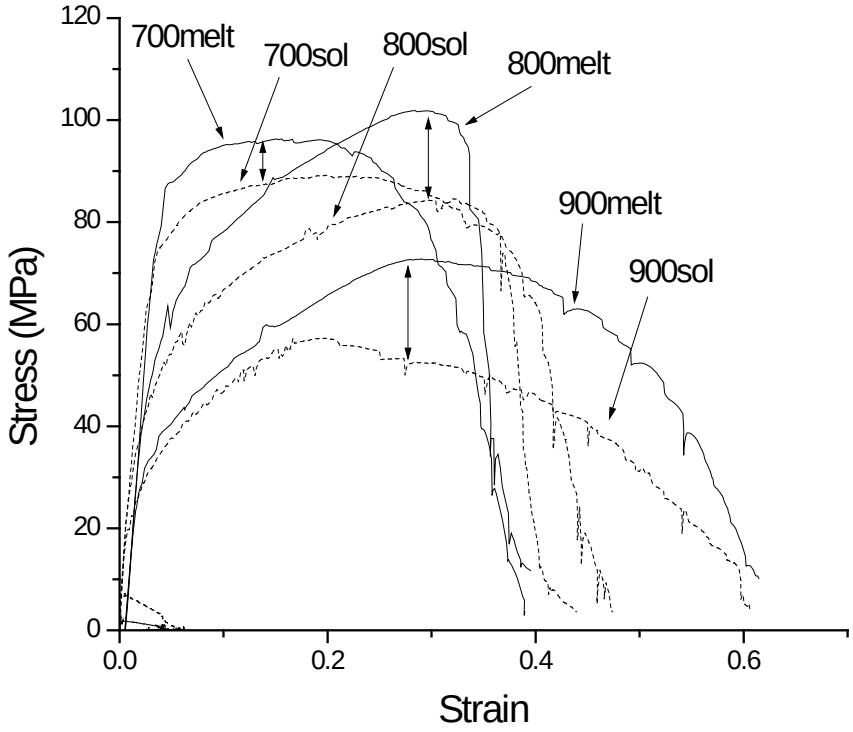

Figure 5.2: Differences in the stress-strain curves between solution treatment and direct cast conditions for C-Mn-Al specimens at 700, 800 and 900ºC, where the arrows indicate the differences in stress of the curves at the same temperature.

There is a significant difference between direct cast and reheated microstructures (excluding grain size), which may also contribute to the observed difference in hot ductility between solution treatment and direct cast conditions. Results for secondary dendrite arm spacings (SDAS) (Figures 4.12a-c) showed a marked difference in the dendritic structure between the two-thermomechanical conditions. Direct cast specimens had a much finer SDAS pattern compared to solution treatment specimens due to the relatively rapid solidification of the direct cast specimens in the Gleeble machine. Solution treatment specimens retained the solidification structure from continuous casting, where the solidification rate was substantially slower. However, it is difficult to ascertain what influence, if any, the dendritic structure may have on hot ductility.

5.2.2 Influence of Niobium (Nb)

Comparing Figure 4.1 (Al Steel) with Figure 4.2 (Nb Steel), it can be seen that addition of Nb to the C-Mn-Al steel significantly widens the ductility trough, for both solution treatment and direct cast conditions. The minimum ductility position was comparable between the two steels and was at approximately 800°C for both thermomechanical conditions. Thin films of ferrite were detected at prior austenite grain boundaries at the temperature for minimum ductility for both thermomechanical treatments for the Nb steel. Similar to C-Mn-Al specimens, the formation of thin ferrite films was responsible for promoting intergranular failure at 800°C. However, unlike the C-Mn-Al steel, ductility continued to be poor above the minimum ductility temperature. The addition of Nb had a marked influence on the width but not the depth of ductility troughs.

Grain boundary sliding in austenite is the accepted mechanism of intergranular failure in Nb steels after the disappearance of ferrite films at the prior austenite grain boundaries [47, 72, 78, 81, 87]. Observations of fracture surfaces with an SEM showed that intergranular decohesion occurred and the fracture faces were flat and smooth, characteristic of failure via grain boundary sliding [47, 49, 77, 78]. An example of smooth featureless facets is shown in Figure 4.15e, in Section 4.

Niobium enhances grain boundary sliding in several ways; fine matrix precipitation strengthens the matrix and concentrates stress into the softer grain boundary regions (PFZ), fine grain boundary precipitates can pin grain boundaries inhibiting sliding, while coarser grain boundary precipitates encourages voiding and the extension of cracks formed by grain boundary sliding [47]. In the present examination, fine Nb(C,N) precipitates contributed to failure via grain boundary sliding but PFZ were not observed. It was believed that PFZ did not form due to the relatively low Nb addition. Ductility was inferior in the Nb alloy and this suggests that even low Nb levels, corresponding to a low volume fraction of precipitation, can still be detrimental to hot ductility.

Weiss and Jonas [86] determined PTT diagrams for the precipitation of Nb(C,N) in austenite for undeformed conditions, 5% prestrain (strain-induced) and for dynamic

precipitation. The PTT diagram was shown in Figure 2.13, Chapter 2. The temperature for the maximum rate of precipitation of Nb(C,N) in undeformed austenite was approximately 950°C, while for a 5% prestrain the maximum rate was closer to 900°C and about one order of magnitude faster than that of static precipitation. For dynamic precipitation, the maximum rate was close to 900°C and one order of magnitude faster compared to static precipitation with 5% prestrain (two orders of magnitude faster than static precipitation in undeformed austenite).

As can be seen from Figure 4.2, ductility began to fall rapidly below 950°C, which is in the vicinity of the predicted onset of both static and strain-induced Nb(C,N) precipitation. Fine precipitation was found between 950°C and 850°C, for direct cast specimens using carbon extraction replicas, which were identified as Nb-bearing. Figure 4.21 shows a typical example of fine Nb(C,N) precipitation. Under solution treatment conditions, virtually no precipitates were found at 950°C, where ductility was high (>70%), but fine precipitates (4-8nm) were found at 900 and 850°C, where ductility was low (<40%). This suggests that Nb was more readily available for precipitation at higher temperature under direct cast conditions than for solution treatment conditions. This was most likely due to segregation of Nb during direct casting.

From Figure 4.2, it is clear that ductility was lower for as-cast conditions compared to solution treatment conditions. A difference in grain size, as well as the difference in the dendritic structure, may again account for this behaviour, as was discussed in the previous section. The austenite grain size for all steels was shown in Table 4.2. The grain size was approximately 100μm larger under direct cast conditions for the Nb steel.

There were very few precipitates found at 800°C and below for either thermomechanical condition, where the difference in ductility was the greatest. At higher temperatures (>900°C), precipitation strongly influenced ductility; offsetting any effect from the difference in microstructure and ductility was much closer for both conditions. However, due to the effect of significantly different microstructures (segregation effects, precipitate characteristics and grain size) between solution treatment and direct cast specimens, it was difficult to determine what degree of

influence changes in precipitation behaviour had on ductility. Segregation, during direct casting, will affect precipitation of Nb, Al and S in the Nb Steel. Segregation of Nb to austenite grain boundaries during solidification and cooling may result in an increase in grain boundary precipitation, which is more detrimental to ductility. On the other hand, if coarse Nb(C,N) eutectics are formed at high temperatures close to the interdendritic regions, then there will be less Nb available to precipitate in a fine form at lower temperatures [47]. Increased grain boundary precipitation can promote voiding during grain boundary sliding, can pin grain boundaries and prevent dynamic recrystallisation. Consequently, one could expect direct cast conditions to be of greater detriment to hot ductility.

There have been several researchers [47, 69, 78, 88] who have found improved ductility under as-cast conditions, compared to solution treatment conditions, for Nb microalloyed steels. This discrepancy between previous research and the results of this current research can be readily explained by the influence of solidification on Nb precipitation. Previous findings [47, 48, 78, 80] concluded that, intense segregation of Nb under direct cast conditions promoted the formation of coarse Nb(C,N) precipitates at interdendritic boundaries. Niobium was tied-up in the interdendritic precipitation and consequently, there was a reduced amount of Nb available for precipitation as strain-induced Nb(C,N) during further processing. Hot ductility improved under direct cast conditions due to a reduction of fine, detrimental Nb(C,N) precipitation.

The results from the current research revealed no evidence of coarse Nb(C,N) precipitation at the interdendritic boundaries, only fine (5-25nm) Nb(C,N) were observed. Hence, ductility was low in the present case for direct cast conditions due to precipitation of fine Nb(C,N). The precipitation behaviour was similar for both test conditions in this research and this was reflected in the similarities of hot ductility. Other authors [79, 89] have also found reduced ductility for in-situ melting tests compared to reheated tests for C-Mn-Al-Nb steels, where coarse, interdendritic Nb(C,N) precipitation was absent.

5.2.3 Influence of Titanium (Ti)

Comparing Figure 4.1 (Al Steel) with Figure 4.3 (Ti Steel), it can be seen that the addition of Ti to the C-Mn-Al steel significantly widens the ductility trough, for both solution treatment and direct cast conditions. As was observed for the Nb Steel, grain boundary sliding in austenite was responsible for widening the ductility trough. Failure due to grain boundary sliding was enhanced due to the precipitation of fine TiN particles. For the Ti steel the minimum ductility temperature was 750°C for solution treatment conditions and was 800°C for direct cast conditions. Thin films of ferrite were detected at prior austenite grain boundaries at the temperature for minimum ductility, similar to that found for C-Mn-Al specimens.

Under solution treatment conditions, ferrite films were found at 800°C and 750°C but the ductility was lower at 750°C. The ferrite films were very narrow and discontinuous at 800°C, while at 750°C; ferrite had fully delineated the prior austenite grain boundaries. It would be expected to be more difficult for cracks to link together in a discontinuous film of ferrite because the boundaries of the discontinuous films would inhibit the propagation of cracks. This accounted for the improved ductility at 800°C.

Unlike the Nb steel, the addition of Ti resulted in a significant difference in ductility between direct cast and solution treatment conditions. Ductility remained above (or equal to) 40% RA for the solution treatment curves, while for as-cast conditions, ductility fell below 40% RA, between 750°C and 950°C (see Figure 4.3). The solution treatment temperature of 1330°C was insufficient for the dissolution of TiN due to the low solubility of TiN in austenite [47]. Undissolved TiN restricts abnormal grain growth of austenite at 1330°C and finer austenite grains will be retained at this temperature. Therefore, grain refinement was predominately responsible for the significantly higher ductility under solution treatment conditions. Hot ductility generally improves as grain size decreases for the reasons listed in Section 2.5.1. The average austenite grain size was approximately 144μm for solution treatment specimens, while the grain size was over 400μm for direct cast specimens.

EDXS analysis of particles revealed that fine Nb-bearing precipitates were found in preference to fine Ti precipitates at 950 to 875°C for 100K/min and 850 to 800°C for 200K/min. Niobium was not added to this steel and the chemical analysis (atomic emission spectroscopy) did not detect Niobium. This means that the average Nb level in the Ti steel was <0.003%. However, Nb levels as low as 0.002% has been known to influence steel properties though precipitation [123]. Niobium pick-up during processing was the expected source of trace levels of Niobium. It is not fully understood why Nb would precipitate in preference to Ti, considering the Ti level was 0.018% and Nb was below 0.003%. It is believed that segregation of Nb during direct casting may be responsible for the occurrence of Nb precipitation at segregated regions. This is supported by the absence of Nb precipitation under solution treatment conditions. Niobium and Titanium would compete for the available nitrogen but because precipitation of Nb(C,N) occurs very rapidly around 950°C, it is assumed that Nb(C,N) precipitated in preference to TiN at the above-mentioned temperatures. Although it is conceivable that niobium may have precipitated as NbC, not Nb(C,N), particularly if there was a small amount of free nitrogen.

5.2.3.1 Influence of Dynamic Recrystallisation on the Ti Steel Under Solution Treatment Conditions

The hot ductility curves for the Ti steel under solution treatment conditions, displayed a distinct transition point, where ductility improved sharply with increasing temperature. It is believed that the occurrence of dynamic recrystallisation was responsible. At 900°C a wide variation in RA was recorded across four tests, two specimens had (relatively) low ductility, 55.8% and 61.8% and two specimens had high ductility, 82% and 86.7% (See Appendix A). Metallographic investigation of these specimens indicated that dynamic recrystallisation had occurred in the two high RA samples but not for the two low RA samples. Evidence of dynamic recrystallisation was observed in the stress-strain curves as well as from the refinement of grain size of the respective samples. The stress-strain curves are shown in Figure 5.3, where arrows indicate fluctuations for the two high RA specimens. Also included in Figure 5.3 is a stress-strain curve from a specimen tested at 950°C, note the lower tensile strength but similar total elongation, to the high

RA curves. Stress fluctuations in stress-strain data are a manifestation of dynamic recrystallisation [74, 81, 105].

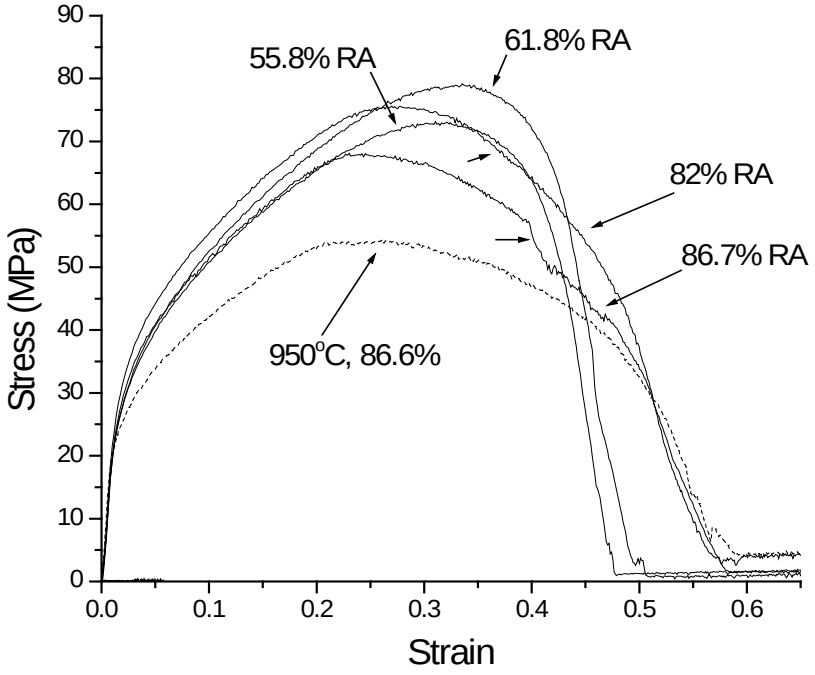

Figure 5.3: Stress-strain curves for Ti specimens under solution treatment conditions at 900°C, where two curves, corresponding to specimens with high ductility, displayed evidence of dynamic recrystallisation (marked with arrows).

It was difficult to measure the austenite grain size, as the fully martensitic structure of the quenched steel was difficult to etch to reveal the prior austenite grain boundaries. However, grain size was more readily distinguished at the edge of the hot zone due to ferrite delineation, as can be seen from Figures 5.4a and 5.4b. Figure 5.4a clearly shows a steadily increasing grain size across the ‘cold’ to ‘hot’ transition zone for the low RA samples, while in Figure 5.4b, the continuation of fine grains in the hot zone indicated that dynamic recrystallisation has refined the grain size in the specimens with high reduction of area.

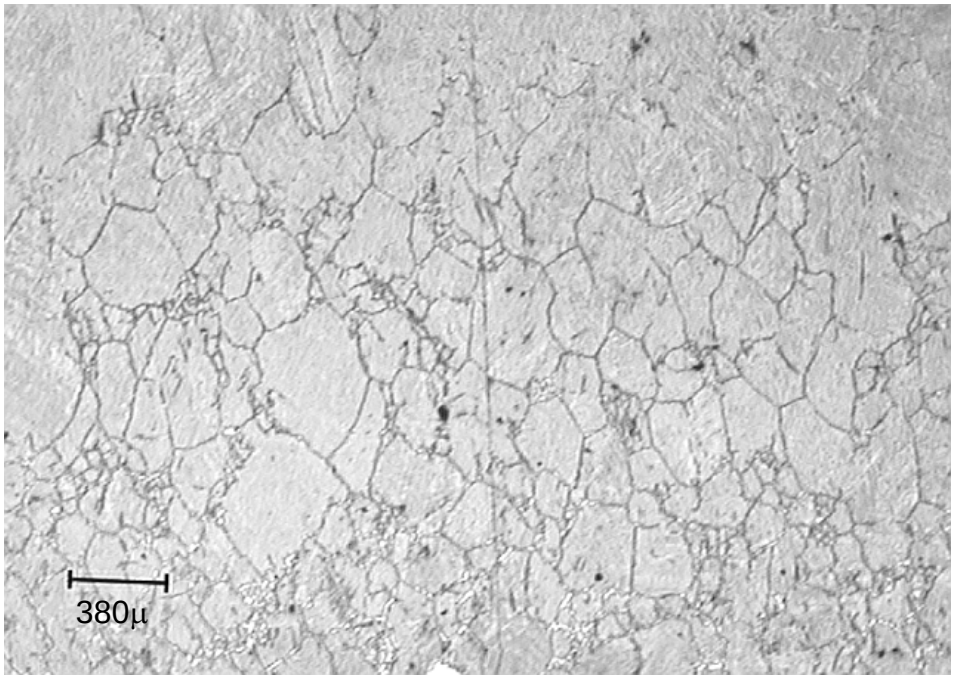

Figure 5.4a: Grain delineation at the edge of the ‘hot zone’ in a Ti specimen tested at 900°C, 100K/min, with low hot ductility. Note the large grain size.

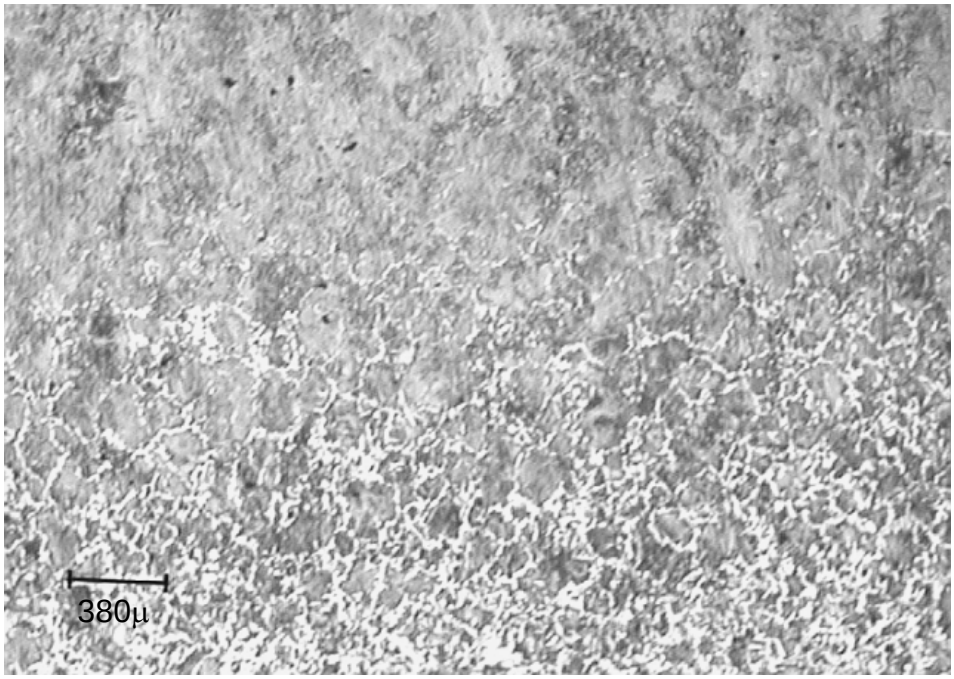

Figure 5.4b: Grain delineation at the edge of the ‘hot zone’ in a Ti specimen tested at 900°C, 100K/min, with high hot ductility. Note the fine grain size.

The reasons why dynamic recrystallisation occurred in some specimens at 900°C but not others is unclear but it is suggested that 900°C is approximately a transition point for dynamic recrystallisation to occur. Any minor variation in the necking behaviour, temperature fluctuations (especially in the necked region), degree of strain hardening or precipitation, could trigger dynamic recrystallisation. Due to the nature of the heating method for Gleeble tensile testing (resistance heating), once necking occurs, the temperature can fluctuate in the necked region due to the decrease in cross-sectional area and arcing between voids or cracks. Any increase in temperature will increase the likelihood of dynamic recrystallisation occurring. The similarity of the initial portion of the stress-strain curves indicates that all four tests were at the same temperature. Dynamic recrystallisation will also depend on the degree of strain hardening [114] and precipitation [74, 81, 105].

It was not expected that precipitation would have an influence on dynamic recrystallisation. Grain boundary precipitation can inhibit dynamic recrystallisation by pinning austenite boundaries [105]. Finer precipitates are more effective in pinning grain boundaries. Inspection of TEM data for precipitation at 900°C under solution treatment conditions for the Ti steel showed that relatively coarse precipitates, >100nm were dominant and a sparse amount of fine, 6-12nm precipitates were randomly dispersed in the matrix. It may be concluded that precipitation at 900°C would have little influence on dynamic recrystallisation due to the lack of fine particles.

Generally, dynamic recrystallisation occurs when the dislocation density reaches high levels and the rate of strain hardening is high [114]. Necking occurs when the increase in strength due to strain hardening fails to compensate for the decrease in cross-sectional area and plastic instability begins. The formation of the neck introduces a complex triaxial state of stress, which increases the tendency for fine cracks or cavities to grow and coalesce into a central crack [114]. Mintz et al. [105] concluded from previous experiments that dynamic recrystallisation must be sufficiently advanced in order to isolate cracks and to delay fracture. The isolation of cracks is required to prevent cracks from joining together and causing failure via coalescence. Based on the argument presented by Mintz [105], it is conceivable that in the low ductility specimens

at 900°C, fracture was sufficiently advanced before the strain was sufficient for dynamic recrystallisation to occur.

5.2.4 Influence of Niobium-Titanium (Nb-Ti)

Comparing Figure 4.1 (Al Steel) with Figure 4.4 (Nb-Ti Steel), it can be seen that the addition of Nb and Ti to the C-Mn-Al steel again led to a significant widening of the hot ductility trough. The trough was extended to higher temperatures due to precipitation of NbTi(C,N) enhancing intergranular failure via grain boundary sliding in austenite.

The minimum ductility value was shifted to lower temperatures (750°C), compared to that for the C-Mn-Al steel. The shift to lower temperatures was due to the Nb-Ti steel having a lower Ar_3 temperature, 761°C compared to 808°C (calculated from Equation 4.1, Chapter 4). The Ar_3 temperature controls the formation of ferrite and ductility will improve once there is a significant volume fraction of ferrite formed in the matrix. The higher Mn level in the Nb-Ti steel, 1.23%Mn compared to 0.63%Mn for the C-Mn-Al steel, was largely responsible for the reduced Ar_3 temperature. Metallographic work at 800°C and 750°C detected thin films of ferrite at the prior austenite boundaries under both thermomechanical conditions. Intergranular failure occurred along these ferrite films via the microvoid coalescence mechanism, as described in Figure 2.8, Chapter 2.

Under solution treatment conditions, there was a sharp drop in ductility between 800°C and 750°C. Lower ductility was observed at 750°C due to the formation of thin films of ferrite at prior austenite grain boundaries, which was not present at 800°C. A similar situation was observed in the Ti steel but ferrite was observed at 800°C in the Ti steel. The higher transformation temperature of the Ti steel accounts for the observed formation of ferrite in the Ti Steel but not in the Nb-Ti steel.

The interparticle spacing of NbTi(C,N) particles was calculated for temperatures between 850°C and 950°C under direct cast conditions and was graphed in Figure 5.5. The interparticle spacing steadily decreased as the temperature fell from 950°C to 850°C. Included in Figure 5.5 are the corresponding RA values in the same temperature

range, which was graphed on the secondary Y-axis. Figure 5.5 indicates that RA values decrease with decreasing interparticle spacing. The ductility change does not progressively decrease with decreasing interparticle spacing, which indicates that interparticle spacing was not the only influence on ductility.

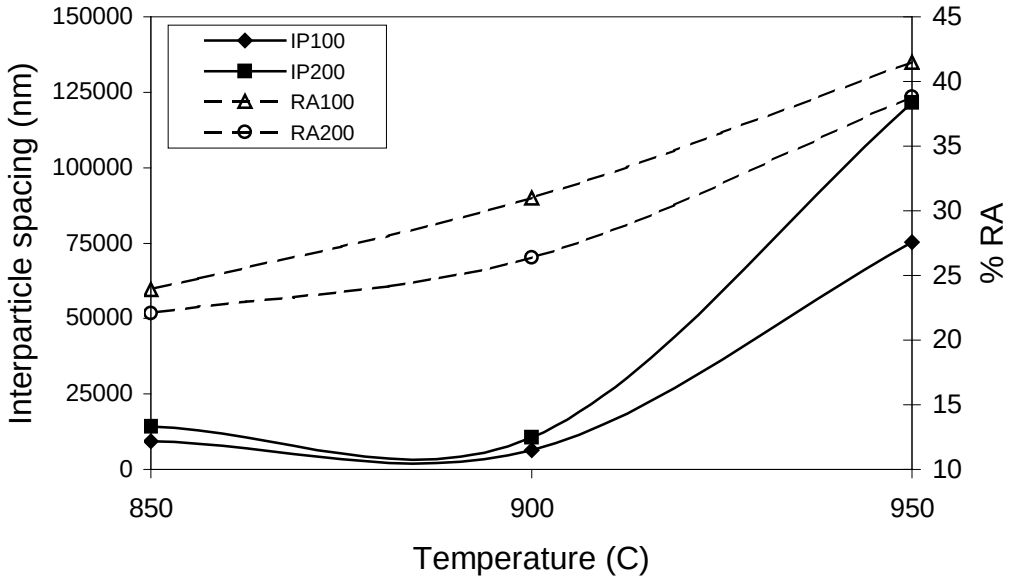

Figure 5.5: Interparticle spacing as a function of temperature with the corresponding RA values plotted on the secondary Y-axis. Values were obtained from the Nb-Ti steel under direct casting conditions.

The Nb-Ti steel showed a substantial difference in ductility between solution treatment and direct cast conditions (Figure 4.4). Ductility was generally above 40% RA for solution treatment conditions, while for direct cast conditions, ductility was below 40% between 700°C and 950°C for 100K/min and between 700°C and 1000°C for 200K/min. A significant decrease in the grain size was once again the overriding factor contributing to this substantial difference in hot ductility. The beneficial effects of finer grain size on hot ductility were discussed in Section 2.5.1, Chapter 2.

5.2.5 Comparisons of Hot Ductility Under Solution Treatment Conditions

Figure 4.6 combines the solution treatment curves for all steels for both cooling rates. The C-Mn-Al steel had excellent ductility at 850°C and above. From Figure 4.6, it is clear that the addition of microalloying elements, Nb, Ti or Nb-Ti, (to C-Mn-Al steels)

significantly widens the ductility trough under solution treatment conditions. Ductility did not reach 60% RA until 930°C for Nb steel, 880°C for Ti steel and for the Nb-Ti alloy, 800°C for 100K/min and 930°C for 200K/min. An RA value of 60% can be regarded as being good ductility. The widening of the ductility troughs was due to microalloying precipitates encouraging failure via grain boundary sliding in single-phase austenite. Fine microalloying precipitates can pin austenite grain boundaries and allow cracks to form, mainly at triple points, due to grain boundary sliding. The pinning of the austenite grain boundaries allows time for cracks to develop and coalesce, until ultimately, failure occurs.

At temperatures of most interest for unbending in the thin slab casting process, >900°C, Ti steel had the best ductility, followed by Nb-Ti steel, while the Nb steel had the lowest ductility. This suggested that the addition of Nb lowered the ductility of the Ti steel under solution treatment conditions. This was most likely due to the higher total microalloying content of the Nb-Ti steel.

The Nb steel was the only alloy that had a significant portion of its ductility tough below 40% RA. The Nb steel had a much larger grain size compared to the two Ti-bearing steels; therefore the influence of grain size on ductility was largely responsible for the above order for the microalloyed steels. This highlights the limitations of solution treatment tests for accessing the likelihood of steels developing transverse cracks during continuous casting, particularly for Ti-bearing steels. According to the results carried out under solution treatment conditions, one would not expect transverse cracking for the two Ti containing steels and a low probability of cracking for the Nb steel, except if the unbending temperature dropped below 900°C. As will be discussed in the following section, the direct cast results revealed different conclusions.

5.2.6 Comparisons of Hot Ductility Under Direct Cast Conditions (as-cast)

The RA curves as a function of temperature for direct casting conditions were shown in Figure 4.7. Under direct cast conditions, the microalloyed steels showed significantly inferior ductility to that of the C-Mn-Al steel. Of the microalloyed steels, Nb steel had

the best ductility at temperatures above 900°C, followed by the Ti steel and then the Nb-Ti steel. The influence of grain size, as seen under solution treatment conditions, was no longer a significant factor for the hot ductility results of the microalloyed steels. It is believed that precipitation was now predominately responsible for the order of hot ductility.

The precise volume fraction was not measured from the carbon extraction replicas, as explained earlier, but qualitative comparisons can be made from the TEM results. The interparticle values shown in Table 4.7 imply that the Nb-Ti steel had a larger volume fraction of fine precipitates compared to the Ti steel and Nb steel. It can be seen from the histograms in Appendix B that there was a significantly higher particle density for the Nb-Ti steel, taken from the same number of fields of view, than that for the Nb or Ti steels. It is likely that an increased volume fraction in precipitation was responsible for the Nb-Ti steel displaying the lowest ductility. Addition of Nb and Ti together can accelerate precipitation and it is reasonable to assume that a higher volume fraction of precipitates, over that for singular addition of either Nb or Ti, would result. Addition of Nb and Ti together can accelerate precipitation because complex precipitates have a much larger driving force for precipitation than for binary precipitates [124, 125]. The addition of Nb and Ti together will have a synergistic effect and the combined soluble level of Nb and Ti would determine the driving force for precipitation of NbTi(C,N).

Figure 4.7 indicated, by the lower ductility of the Nb-Ti steel, that Ti additions to Nb steels could increase transverse cracking susceptibility. It was previously suggested that an increase in the volume fraction of fine precipitation due to the addition of Ti to the Nb steel was responsible for the lower ductility. This result is in agreement with other work [63, 90, 92, 93]. However, commercial experience has found that small additions of Ti (~0.01%) to Nb steels have been beneficial for preventing transverse cracking during continuous casting [48, 63, 90, 92-94]. This discrepancy between laboratory tests and commercial experience implies that direct cast laboratory tests still fail to accurately simulate conditions during continuous casting.

Mintz [48, 94, 126] has suggested that laboratory tests do not show the true behaviour of Ti due to the absence of complex cooling patterns experienced by continuously cast

slabs prior to straightening. Briefly, a continuously cast slab experiences a sharp drop in temperature on exit of the mould, then reheats to some maximum before cooling slowly down to the unbending temperature. Temperature fluctuations occur during cooling due to the alternate impingement of water sprays and contact with guide rolls. Mintz [48, 94, 126] believed that the complex thermal pattern encourages precipitation of Ti and the precipitation behaviour of Ti will strongly affect hot ductility. Due to the high stability of TiN in austenite, precipitates would be expected to remain stable once nucleated, for example, during a drop in temperature. During any increases in temperature, particles would coarsen. The complex thermal history during continuous casting could promote the coarsening of Ti precipitates, which would be beneficial to transverse cracking.

For the present investigation, fine NbTi(C,N) precipitates were observed in direct cast specimens without temperature cycling and inferior ductility for the Nb-Ti steel was observed. The influence of simulating the thermal history during casting on RA of Nb-Ti steel will be discussed in Section 5.4.3.

5.3 Influence of Cooling Rate

In general, it has been found that increasing the cooling rate leads to lower ductility for both C-Mn-Al steels and microalloyed steels [49, 69, 82, 90, 91, 93]. The lower ductility was ascribed to either a refinement of the inclusion size (MnS), refinement of AlN or refinement of microalloying precipitates. Evaluating the influence of cooling rate is important in regard to thin slab casting, where the cooling rates near the surface of the strand are much higher than those for conventional casting.

5.3.1 C-Mn-Al

Increasing the cooling rate widened the trough by approximately 50°C for direct cast specimens. Apart from this, the cooling rate had no other influence on hot ductility. Previous work on C-Mn-Al steels [91] has shown that faster cooling rates result in finer sulphides and/or AlN particles situated at the austenite boundaries and this can be

detrimental to ductility. Finer sulphides or AlN are more effective at pinning the austenite grain boundaries and reduce ductility by enhancing grain boundary sliding. In the present examination, TEM work failed to pick-up any fine sulphides or AlN but it is difficult to extract these particles using carbon extraction replicas. However, it was not expected that AlN particles would be present, as AlN is known to be sluggish to precipitate, at similar concentrations of Al and N [47, 48, 81]. The MnS inclusions are normally present in steels and a refinement of MnS inclusions was the expected reason for lowering the ductility at 850°C at 200K/min. The influence of MnS on hot ductility was discussed in Section 2.6.2, Chapter 2.

For a given volume fraction, finer MnS inclusions situated at boundaries would have a closer interparticle spacing. This would make it easier for cracks to link-up, promoting failure due to microvoid coalescence in austenite. Unfortunately, the MnS distribution was not determined. However, inspection of the longitudinal fracture surfaces at 850°C revealed evidence of microvoid coalescence at 200K/min (Figure 5.5a) but only discrete voids at 100K/min (Figure 5.5b). It is believed that a finer MnS distribution was responsible for the decrease in ductility at the higher cooling rate. Further work is required to substantiate this finding.

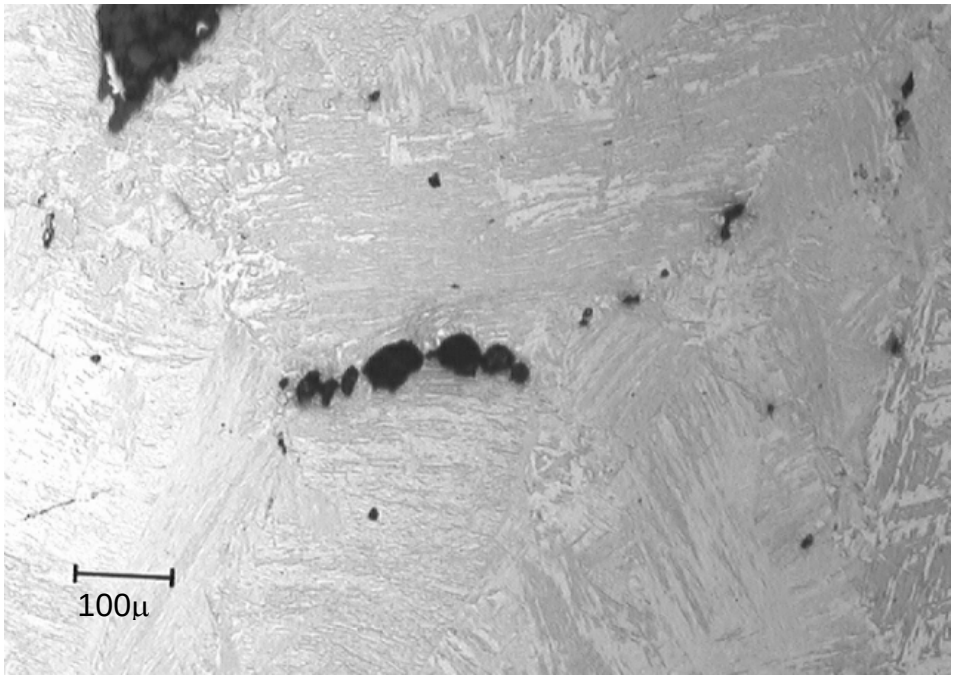

Figure 5.5a: Microvoid coalescence, typical of a C-Mn-Al specimen tested at 850°C at 200K/min (100x).

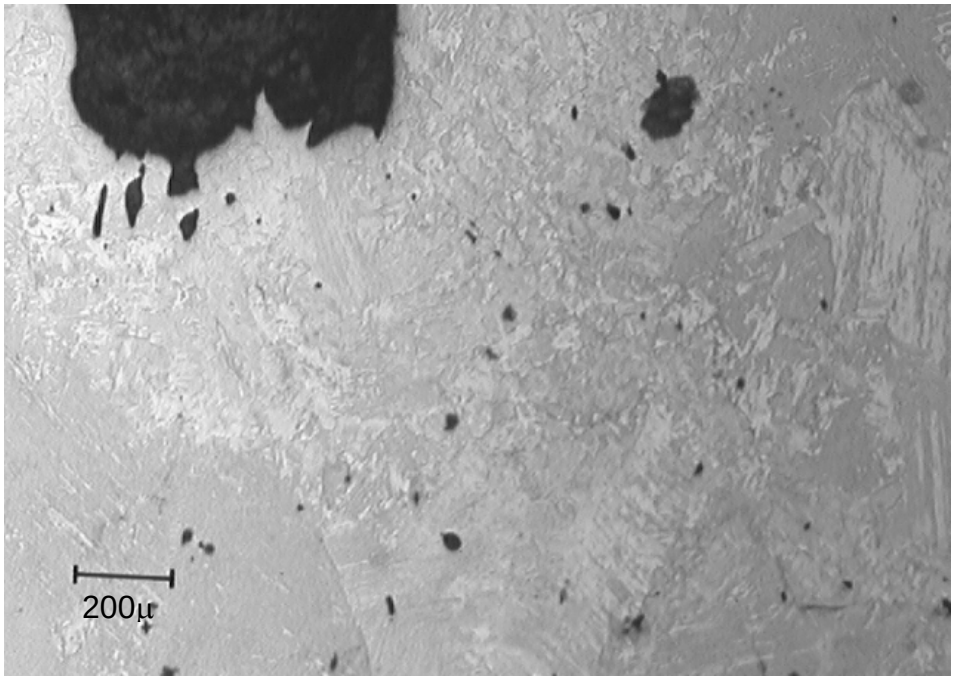

Figure 5.5b: Discrete voids, typical of a C-Mn-Al specimen tested at 850°C at 100K/min (50x).

5.3.2 C-Mn-Al-Nb

There was little influence from the cooling rate on ductility for the Nb steel under either test condition. This was reflected in the similar precipitation behaviour for the two cooling rates, for each of the thermomechanical conditions. There was a slight lowering of the ductility between 1000°C and 900°C for the higher cooling rate under direct casting conditions. Average precipitate sizes were slightly finer at 950°C and 900°C for the higher cooling rate, 7.7nm and 6.4nm respectively, compared to 27.2nm and 13.4nm for the slower cooling rate. Although the difference in ductility was only ~5% RA, which was also the error in testing, the difference in ductility was consistent from 1000°C to 900°C. This implies that increasing the cooling rate did influence ductility between 1000°C and 900°C.

5.3.3 C-Mn-Al-Ti

Increasing the cooling rate had no influence on the Ti steel when tested under solution treatment conditions. Under direct cast conditions the cooling rate had a few minor influences on hot ductility. A sharper drop at 950°C for the 200K/min cooling rate was the most notable change. TEM data showed fine, 10-20nm Ti precipitates at 950°C at 200K/min, while 15-20nm Nb precipitates were found at 100K/min. This small decrease in precipitate sizes may be sufficient to reduce ductility. The influence of precipitate size on RA was discussed in Section 5.1.1, where the RA as a function of particle size was plotted in Figure 5.1. In Figure 5.1, it was noted that RA decreased steadily once precipitate size fell below approximately 20nm, indicating that a small decrease in particle size, in the above size range, will reduce RA.

For C-Mn-Al-Ti steels, it has been reported [91] that a much slower cooling rate (25K/min) was generally required for any significant improvement in ductility to be achieved. A slow cooling rate of 25K/min was required to allow enough time for TiN particles and inclusions to coarsen sufficiently in order to reduce the impact of these particles on hot ductility. The present findings agree with this, as there was only a minor

influence on ductility from decreasing the cooling rate from 200K/min to 100K/min. TiN particles were sufficiently fine at 100K/min to cause poor ductility and increasing the cooling rate to 200K/min created little further refinement in particle size.

5.3.4 C-Mn-Al-Nb-Ti

Increasing the cooling rate had a marked influence on ductility for the Nb-Ti steel under solution treatment conditions. Ductility was approximately 10-15% lower at 200K/min than ductility at 100K/min (although both curves follow a similar trend). Stress-strain curves, Figure 5.6, show a decrease in the total elongation (hence lower ductility) at a cooling rate 200K/min, compared to 100K/min, at respective temperatures. The cooling rate had little influence on grain size, as the average grain size was approximately 144μm for both cooling rates. The influence of the cooling rate on precipitation was the most likely explanation for this difference in hot ductility, as has been found previously for C-Mn-Al-Nb-Ti steels [93].

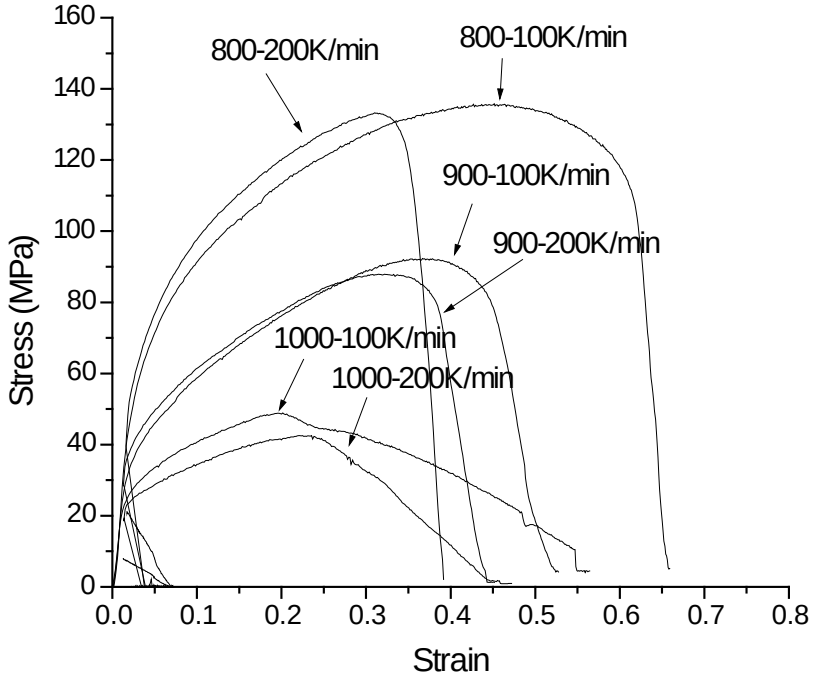

Figure 5.6: Stress-strain curves for the Nb-Ti steel showing the changes in the stress-strain behaviour between 100K/min and 200K/min at 800°C, 900°C and 1000°C.

Particle size histograms for Nb-Ti specimens (solution treatment) at 950-850°C for cooling rates 100K/min and 200K/min were displayed in Figures 4.30a-c and 4.31a-c. The mean precipitate sizes between 950-850°C were smaller for the higher cooling rate. The respective mean precipitate sizes at 950, 900 and 850°C are 16.0, 11.4 and 5.1nm for 100K/min and for 200K/min, 7.4, 6.3 and 4.0nm. These differences in precipitate size are small but all are sufficiently fine to substantially reduce ductility. Inspection of the histograms, however, reveals that at 200K/min there was a significantly higher density of fine precipitates. This indicates that there was an increase in the volume fraction of fine precipitates at 200K/min. It was the volume fraction of precipitates, not just a difference in size, which was responsible for the reduced ductility found at 200K/min under solution treatment conditions.

Given the same amount of alloying additions, if the increased cooling rate promoted a higher volume fraction of fine precipitates, then the interparticle spacing must decrease. The interparticle spacing was measured between 850°C and 950°C for both cooling rates and is graphed in Figure 5.7. It is evident from Figure 5.7 that the interparticle spacing was consistently finer at the higher cooling rate between 850°C and 950°C. There was also a small decrease in interparticle spacing with decreasing temperature, which coincides with the hot ductility curves, where a gradual decrease in RA was recorded in this temperature range.

Increasing the cooling rate usually leads to lower hot ductility by refining the particle size. In this case, it has been concluded that an increase in the density (volume fraction) of fine particles was the main factor for lowering ductility. Observations using a TEM revealed that there was an increased tendency for precipitates to arrange in clusters at the higher cooling rate. An example of such clustering is displayed in Figure 5.8. It is believed that the faster cooling rate allowed the microalloying elements to remain in solution for longer, resulting in a greater fraction of NbTi(C,N) to precipitate at lower temperatures. The longer an element remains in solution (supersaturation), the higher the driving force for precipitation. Consequently, an increased amount of fine NbTi(C,N) precipitated in clusters. Further work would be required to substantiate this theory; establishing a precipitation-time temperature curve for this steel would be beneficial.

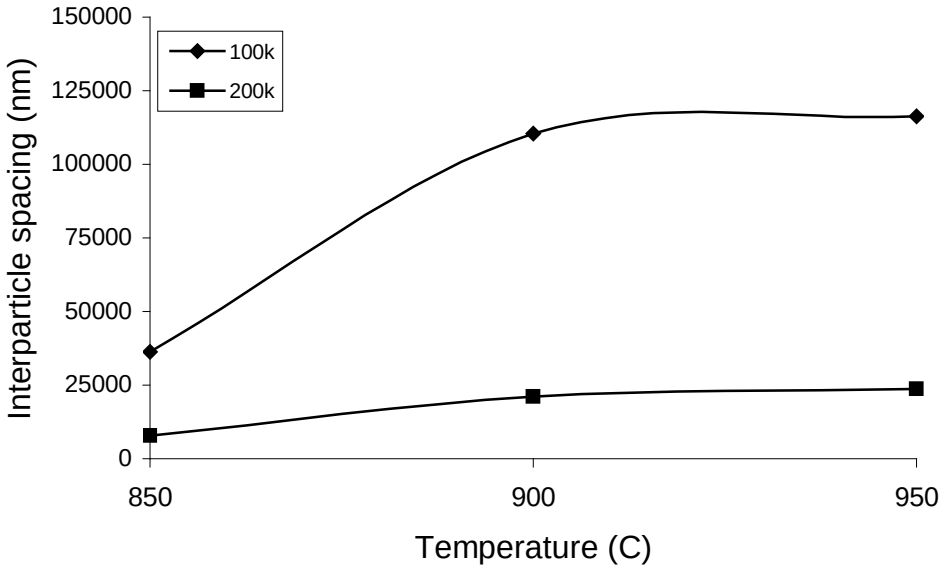

Figure 5.7: Interparticle spacing as a function of temperature for the cooling rates of 100K/min and 200K/min for the Nb-Ti steel under solution treatment conditions.

Figure 5.8: Typical example of clustering seen in Nb-Ti specimens (900°C) tested under solution treatment conditions, 200K/min.

The cooling rate had a minor influence on hot ductility under direct cast conditions. The most noticeable difference, and most significant, was that ductility began to drop at a temperature about 15-20°C higher for the faster cooling rate. This result is significant because the greater the width of the trough (to a higher temperature) the more difficult it will be to carryout straightening above the region of embrittlement. At 1015°C, RA was above 60% for both cooling rates, by 1000°C, RA was still 60% for 100K/min but dropped to 53% for 200K/min. The average precipitate size at 1000°C was 42.8nm at 100K/min and 23.6nm at 200K/min. At 950°C, the mean precipitate sizes were similar, approximately 12nm, and there was no further influence of the cooling rate on hot ductility below 950°C. The higher cooling rate would restrict the time available for coarsening of precipitates and this resulted in lower ductility.

5.4 Influence of Temperature

In general, as the test temperature increased, particles became coarser and there was a corresponding improvement in ductility. In the case of C-Mn-Al specimens, ductility improved once the temperature was high enough to prevent the formation of ferrite at prior austenite grain boundaries. In the case of the microalloyed steels, the improvement in ductility with increasing temperature was related to the behaviour of precipitates. The influence of precipitate size on RA was previously shown in Figure 5.1.

It has been often observed that the ductility trough for C-Mn-Al steels stretches from the Ae_3 to 20-30K below the Ar_3 (undeformed) temperatures [47, 48, 65, 66]. The Ae_3 temperature was calculated, using formulae (4.2) (based on composition), to be 841°C and the Ar_3 temperature, using formulae (4.1) was calculated to be 807°C, as shown in Table 4.8, Chapter 4. The Ar_3 temperature was calculated for undeformed conditions for ease of comparison with other alloys. Deformation generally raises Ar_3 by increasing the number of nucleation sites for ferrite nucleation. The position of the ductility trough and the Ae_3 and Ar_3 temperatures show good agreement. The sharp recovery of ductility at approximately the Ae_3 temperature, for the C-Mn-Al steel, supports the observation that ductility was controlled by the formation of ferrite at prior austenite grain boundaries.

For the microalloyed steels, the recovery of ductility at the low end of the temperature trough coincided with the Ar_3 temperatures, which are detailed in Table 4.8, for the respective steels. The Ti steel and the Nb-Ti steel have a higher Mn level than that for the Nb steel, consequently, the Ar_3 temperature was lower for the Ti steels and the ductility troughs were shifted to lower temperatures. However, the Ae_3 temperature did not mark the high temperature, good ductility end of the trough for the microalloyed steels, as was seen for the C-Mn-Al steel. The trough was extended to higher temperatures as a result of the transition from failure in the ferrite films to failure via grain boundary sliding in single-phase austenite. Grain boundary sliding is generally absent in C-Mn-Al steels with low levels of Al and N [47], as was the case in the present examination.

The high temperature, good ductility end of the ductility trough for the microalloyed steels was largely controlled by precipitation. As temperature increases, precipitation becomes coarser and ductility improved. Therefore, the higher the temperature at straightening, the less likely slabs will develop transverse cracking. For thin slab casting with hot direct rolling, the straightening temperatures are generally high and this will be beneficial in preventing transverse cracking.

In laboratory hot tensile tests, if dynamic recrystallisation occurs, then excellent ductility will be observed. Dynamic recrystallisation moves the boundaries away from cracks and failure is delayed in this way. In Figure 4.10, Dynamic recrystallisation was evident at 1000°C in the stress-strain curves of the microalloyed steels under solution treatment but not direct cast conditions. The occurrence of dynamic recrystallisation in the solution treatment tests was probably due to the finer grain size promoting dynamic recrystallisation. In Figure 4.11, dynamic recrystallisation was evident at 1100°C in the stress-strain curves of all steels and high ductility was observed. It is important to acknowledge that dynamic recrystallisation will not occur during continuous casting due to the low strain and the coarse grain size [48, 65, 66, 70]. Therefore, care must be taken when evaluating the susceptibility of steel to transverse cracking if dynamic recrystallisation is present in the tensile tests.

5.4.1 Influence of Cyclic Thermal Oscillations on Hot Ductility of Nb-Ti Steels

The influence of simulating the thermal history experienced by the surface of a strand under thin slab casting conditions on hot ductility of Nb-Ti steel was investigated. As discussed in the literature review, the beneficial influence of Ti additions observed in production is probably related to the thermal history of the slab, prior to straightening. The main argument was that thermal fluctuations encourage precipitation of Ti-based precipitates at an early stage of continuous casting, allowing more time for precipitates to coarsen and lessening their impact on hot ductility.

Results for RA values at a test temperature of 900°C are shown in Figure 4.5. The relative positions of the cyclic thermal history tests to the hot ductility curves for Nb-Ti can been seen in Figure 4.4. It is clear from these two figures that introducing cyclic thermal oscillations improved ductility over specimens tested without a complex thermal history. Decreasing the average cooling rate from 200K/min (Cycle 1) to 100K/min (Cycle 3) improved ductility, where the amplitude of oscillations for both cycles was ±50°C. At an average cooling rate of 200K/min, increasing the amplitude of oscillations from ±50°C (Cycle 1) to ±100°C (Cycle 2), marginally decreased ductility.

A careful examination of the particle distributions (histograms), for the different thermal histories, was carried out to understand the precipitation behaviour and the resultant hot ductility. It is important to note that the particle analysis was carried out on quenched samples and were not subjected to deformation as for the hot ductility specimens. Histograms for the relevant particle distributions are shown in Section 4.6.5, Figures 4.28a-c. The average precipitate sizes in Cycles 1-3 were, 30.8nm, 12.3nm and 21.6nm, respectively. For the equivalent Nb-Ti specimens tested at 900°C, without thermal oscillations, the average precipitate sizes were 5.2nm and 5.8nm, for the cooling rates of 100K/min and 200K/min, respectively. Large precipitates (>40nm), which were absent under direct cast conditions, were also found when thermal oscillations were introduced. In general, the coarser particle distribution resulted in improved hot ductility for the specimens subjected to the cyclic thermal oscillations.

In Cycle 1, there was a wide variation in the particle size, which included fine (<15nm), medium (20-40nm) and large (>40nm) particles. The wide distribution in the particle sizes is probably related to the large variations in temperature of the thermal history. When comparing to the TEM results for direct casting, without oscillations, fine particles corresponded to those found at 900°C, medium particles to those found at 1000°C and large particles represent those found at 1100°C.

Cycle 1 and Cycle 3 had the same amplitude of oscillations, ±50°C, but Cycle 3 had a slower average cooling rate of 100K/min. Cycle 1 and Cycle 3 had similar distributions, except Cycle 1 had a larger proportion of coarser precipitates, between 40 and 100nm (at the expense of finer precipitates as indicated by the lower particle density), which where absent in Cycle 3. The slower cooling rate of Cycle 3 may have allowed more time for precipitation of finer particles when reheating from 900°C to 1100°C, prior to the thermal oscillations. Assuming similar volume fractions, there would be less Nb and Ti in solution to precipitate as coarser particles (40-80nm) at higher temperatures, on reheating.

Increasing the amplitude of the temperature oscillation from ±50°C to ±100°C, at an average cooling rate of 200K/min, resulted in slightly lower ductility and a finer precipitate distribution. One would expect coarser particles and improved ductility when increasing the amplitude of the oscillations. Similar work by Mintz [59] on Nb-bearing steels, found that increasing the amplitude of the temperature cycles, improved ductility by coarsening Nb precipitates. It was observed that Cycle 2 had a higher density of fine particles, <10nm, than what was seen in Cycles 1 and 3. The increase in the density of fine particles suggested that a second wave of fine precipitates nucleated during the temperature oscillations. Increasing the amplitude of oscillations to ±100°C, resulted in an initial drop in temperature of 990°C, compared to 1040°C for ±50°C. It is believed that this initial drop to 990°C was sufficiently low to nucleate a second wave of fine NbTi(C,N). This also explains why there were fewer coarser particles for Cycle 2, as the majority of Nb and Ti had already come out of solution prior to the upward heating cycle of the oscillations. Larger precipitates, >80nm, were also found for Cycle 2, which were expected to have precipitated around 1100°C, on reheating.

It is clear that the particle distribution was significantly coarser when complex thermal histories were introduced. Hot ductility was improved in the tensile tests when the thermal history of a continuously cast strand under thin slab casting conditions was more closely simulated, as opposed to directly cooling to the test temperature from the melt. The reason for this improvement in ductility was concluded to be due to the cyclic thermal histories encouraging coarser particle distributions. The cyclic thermal histories were based on plant data for the cooling history of the wide face of a continuously cast strand under thin slab casting conditions, the details of which are included in the experimental section.

To gain a better understanding of the evolution of NbTi(C,N) in the cyclic temperature oscillation tests, a specimen was quenched at T_{min} (900°C) and at T_{max} (1100°C), after reheating. For the specimen quenched at T_{min}, only a few fine (<10nm) NbTi(C,N) were detected. The particle distribution was detailed in Figure 4.29a. This indicated that NbTi(C,N) only requires a short time at temperatures around 900°C to begin to form. At 1100°C (T_{max}), precipitation was more extensive, fine (<15nm) NbTi(C,N) were detected in rows, coarser (15 to 40nm) NbTi(C,N) were randomly dispersed and a few larger TiN particles were present. The particle distribution was displayed in Figure 4.29b.

The above results indicate that NbTi(C,N) will readily precipitate during the reheating stage after the initial temperature drop, for the given thermomechanical conditions. There would be time for precipitation during the reheating stage as the rate of reheating was much slower than the cooling rate to the minimum temperature. This substantiates the earlier assumption that the lower cooling rate in Cycle 3 allowed a greater amount of time for fine particles to precipitate.

Comparing Figure 4.28a (Cycle 1) to Figure 4.29b (quenched at 1100°C), it was observed that there was a lower percentage of precipitates below 10nm for Cycle 1. This implies that fine precipitates, which were observed after quenching from 1100°C, coarsened during the cyclic temperature oscillations.

It can be concluded from the cyclic thermal oscillation results that NbTi(C,N) will precipitate during the reheating stage after the initial temperature drop and will coarsen during the temperature oscillations on cooling. Decreasing the average cooling rate during reheating and temperature cycling will allow more time for precipitates to coarsen. Increasing the time prior to straightening should be beneficial for reducing the occurrence of transverse cracking during continuous casting due to the beneficial effects of coarser particles. From a practical standpoint, increasing the time to straightening would require decreasing the casting speed. There is generally little opportunity to vary the casting speed [47] and decreasing the casting speed would also reduce productivity.

5.5 Limitations of Solution Treatment and Direct Cast Laboratory Hot Tensile Tests

Comparisons between solution treatment and direct cast conditions and the respective limitations of each test will be dealt with in more detail in this section. It is important in physical simulations to obtain as realistic conditions as possible, with the aim to produce accurate, meaningful results. When translating laboratory results to the problem of transverse cracking, an understanding of the limitations of laboratory tests is essential to prevent misinterpretation of results.

Previous research has generally shown that solution treatment tests are misleading and have significant limitations when testing alloys containing Ti and S due to the low solubility of sulphides and TiN at solution treatment temperatures (1300-1400°C) [47, 48, 64, 69, 78]. Undissolved TiN particles restrict grain growth at the solution treatment temperature and a substantially finer austenite grain size will have an overriding influence on hot ductility. Undissolved TiN particles also reduce the amount of Ti and N in solution available for subsequent precipitation during testing. Results of this present work plainly agree with these findings with regards to Ti steels. Undissolved MnS limits the amount of Mn and S available for precipitation at lower temperature. Precipitation of fine MnS at lower temperature will have a strong influence on hot ductility, particularly in the absence of microalloying elements.

However, it is generally believed that solution treatment conditions are adequate to determine the ductility of C-Mn-Al and C-Mn-Al-Nb steels because Nb and Al are taken into solution at the typical solution treatment temperatures (1200-1350°C) and will be available for precipitation [47, 48, 64]. Solution treatment conditions also produce large austenite grain sizes for C-Mn-Al and C-Mn-Al-Nb steels, similar to those for as-cast conditions. For this reason, the influence of grain size and precipitation on hot ductility would be expected to be similar for solution treatment tests and direct cast tests. However, this research has shown that a difference in grain size between solution treatment and direct cast tests can influence the ductility of C-Mn-Al and C-Mn-Al-Nb steels, particularly at low strain rates. While solution treatment tests can predict similar results to direct cast tests, current results suggest that the true ductility behaviour of C-Mn-Al and C-Mn-Al-Nb steels is not shown unless direct cast conditions are used for testing.

For C-Mn-Al steels, it has been found by a number of researchers [48, 69, 76, 82, 83] that segregation has a significant influence of on the precipitation behaviour of AlN and consequently, the hot ductility. It has been reported that the solubility product of [Al] x [N] had to approach 2 x 10^{-4} for precipitation to occur in samples with 1.4% Mn for solution treatment tests. However, precipitation of AlN has been noted to occur for direct cast conditions in C-Mn-Al steels with low Al/N ([Al] x [N] = 1 x 10^{-4}) levels, presumably due to segregation [48, 69, 76, 82, 83]. Turkdogan [51] has calculated that Al concentration at grain boundaries can increase by a factor of 6 due to segregation. Thus, for C-Mn-Al steels that have low Al levels, precipitation may not occur under solution treatment conditions but may occur under direct cast conditions.

For C-Mn-Al-Nb steels, the influence of direct cast conditions can yield variable results, depending on the precipitation behaviour, as was discussed in Section 5.2.2. Improved hot ductility was found under direct casting conditions if coarse Nb(C,N) precipitates at interdendritic boundaries were observed [47, 48, 78, 80]. On the other hand, lower hot ductility was found for direct cast tests for C-Mn-Al-Nb steels when eutectic Nb(C,N) was absent [79, 89]. In the absence of coarse, interdendritic Nb(C,N) precipitation, as was the case in the present examination, precipitation of fine Nb(C,N) is unrestricted and lower ductility under direct casting conditions would be expected. Coarse Nb(C,N)

eutectics are not present at the surface of continuously cast slabs so care must be taken with interpreting laboratory tensile results if eutectic Nb(C,N) were found to have precipitated [78, 85].

Solution treatment tests also fail to show the true extent of the detrimental affects of S on hot ductility. This effect is due to the low amount of S that can redissolve at 1330°C. Significant residual levels of S are commonly found in C-Mn-Al and Nb bearing steels and the influence of S on hot ductility of as-cast steels will only be revealed under direct cast conditions. Abushosha [78] found that increasing the S level caused a lower ductility for C-Mn-Al steels and C-Mn-Al-Nb steels under direct cast conditions.

5.5.1 Influence of Segregation and Homogenisation Time

Direct cast conditions allow segregation effects and the relationship between segregated, interdendritic regions and the formation of the austenite boundaries to influence hot ductility results. The influence of segregation can deteriorate ductility by increasing grain boundary precipitation and consequently, enhancing failure via grain boundary sliding [47]. The effect of precipitation on hot ductility not only depends on size and volume fraction, but also location [79, 89]. The inherent differences between direct cast and solution treatment procedures will strongly effect the location of precipitates and hence, the thermomechanical history will effect hot ductility.

The homogenisation time (Table 4.4) was calculated for selected elements, based on the diffusion time at 1330°C and the SDAS for solution treatment (150μm) and direct cast (50μm) conditions. While only a simple calculation was performed, it was adequate to give a good indication of the mobility of the selected elements. It can be seen from Table 4.4 that Mn, Nb and Ti are extremely slow to diffuse in austenite and S, while much faster, is still slow in comparison to the time spent at high temperature during testing.

This indicates that the segregation pattern formed during continuous casting, with respect to Mn, S and microalloying elements, will vary little during the short solution

treatment time. Thus, there would be little opportunity for segregation to grain boundaries during solution treatment, where as for direct cast specimens the austenite grain boundaries will form at the segregated, interdendritic regions. Therefore, it is reasonable to assume that direct cast conditions would produce a greater number of grain boundary precipitates, which have a strong influence on hot ductility.

Chapter 6:

Conclusions & Future Work

6.0 Conclusions

1) The low ductility of the steels examined at temperatures below 850°C is due to microvoid coalescence within the thin films of ferrite, which formed surrounding prior austenite boundaries. This is consistent with earlier observations on other steels.

2) Intergranular failure above 850°C is due to crack initiation via grain boundary sliding in the austenite. Grain boundary sliding is favoured by the low strain rate (7.5×10^{-4} s^{-1}), large grain size and is enhanced by the presence of fine precipitates.

3) Microalloying additions to C-Mn-Al steel significantly widen the ductility trough due to enhanced precipitation. However, the trough depth is essentially the same for the steels investigated because the formation of thin ferrite films controlled ductility at the minimum trough position.

4) Ductility is improved when grain boundary migration is sufficient to isolate cracks formed by grain boundary sliding, leading to extensive voiding. Excellent ductility is always obtained under conditions where dynamic recrystallisation occurs.

5) Increasing the cooling rate decreases ductility by promoting a finer precipitate size.

6) For the Nb-Ti steel tested under solution treatment conditions, increasing the cooling rate strongly reduced hot ductility. The lower ductility at the higher cooling rate is most probably due to a decrease in the interparticle spacing.

7) The ductility of solution treated specimens were always higher than that of direct cast. For the Ti bearing steels, the presence of TiN particles restricted grain growth during solution treatment. Consequently, the improved ductility under

solution treatment conditions was due to the significant reduction in austenite grain size.

8) This study has confirmed the general notion that the impact of Ti and Nb on hot ductility is best assessed by determining the mechanical properties of direct cast rather than solution treated material.

9) The combination of 0.019% Nb with 0.015%Ti (Nb-Ti Steel) leads to lower ductility than for the combination of 0.022% Nb 0.018% Ti, under direct cast conditions.

10) In contrast to the findings of this study, commercial practice indicates that Ti improves hot ductility. This apparent anomaly may be due to the inability of laboratory tests to fully simulate practical experience.

11) For Nb-Ti samples, simulating the thermal history near the surface of a continuous cast strand promoted a coarser particle distribution compared to specimens that were cooled directly to the test temperature. This accounts for the improved ductility of the thermal history specimens. During the thermal history simulation, the formation of precipitates was encouraged during reheating, after the initial temperature drop. These precipitates coarsened during subsequent temperature cycling as a result of time spent at higher temperatures then the test temperature.

12) For the thermal history experiments, increasing the amplitude of the temperature oscillations between 1100°C and 900°C lowered the hot ductility slightly. This slight reduction in hot ductility was attributed to an increase in the amount of fine NbTi(C,N) particles. These particles were believed to have formed during the initial temperature drop at the beginning of the thermal oscillations.

13) Reducing the average cooling rate during the thermal history experiments improved hot ductility by allowing increased time for fine particles to coarsen during Ostwald ripening.

14) The presence of coarser precipitation (>20nm) generally gives rise to better ductility.

6.1 Recommendations and Suggestions for Future Work

1) The present results suggested that the low strain rate was a significant factor in contributing to the observed difference in hot ductility between solution treatment and direct cast conditions. The present work should be repeated to investigate the influence of higher strain rates.

2) The addition of both Nb and Ti led to lower hot ductility under direct cast conditions. It is suggested that further work using a wider range of Nb, Ti and N additions is required to improve the knowledge of the hot ductility behaviour of Nb-Ti microalloyed steels.

3) Further work needs to be carried out to investigate the influence of commercial thermal histories on Nb and Nb-Ti steels by implementing more detailed laboratory studies. The influence of variations in the minimum temperature drop, reheating temperature and thermal oscillations on precipitation evolution should be determined.

4) Quantitative electron microscopic analysis of microalloying precipitation under different thermomechanical processing conditions may be conducted to acquire more detail on the influence of volume fraction and interparticle spacing on hot ductility.

5) Experimental data on the kinetics of NbTi(C,N) precipitation is lacking at the present time. Experiments to determine the precipitation behaviour of NbTi(C,N) under various hot ductility conditions would be very useful in predicting the behaviour of Nb-Ti steels.

6) Further work is required to determine the influence of segregation on precipitation and hence, hot ductility. In particular, establishing the role of segregation on the formation of grain boundary precipitation.

7) Raising the deformation temperature leads to coarser precipitates and hence, improved ductility. Therefore, it is recommended that the straightening temperature be kept as high as possible for microalloyed steels for conventional and thin slab casting.

6.2 Publications

1) K.R. Carpenter, B.A. Parker, C.R. Killmore and P.A. Manohar, “Hot Ductility of Nb-Ti Microalloyed Steel”, THERMEC 2000- International Conference on Processing & Manufacturing of Advanced Materials, Processing, Fabrication, Properties, Applications, Las Vegas, U.S.A, 4-8 December 2000

2) K.R. Carpenter, B.A. Parker and C.R Killmore, “Hot Ductility of Nb, Ti and Nb-Ti Microalloyed C-Mn-Al Steels”, Thermomechanical processing: Microstructure, Modelling and Control, IMMPETUS, University of Sheffield, UK, 23-26 June, 2002.

3) K.R. Carpenter, B.A. Parker, P.A. Manohar and C.R. Killmore, “The Hot Ductility of Nb, Ti, Nb-Ti microalloyed steels and the influence of thermal history on the Nb-Ti steel”, Yet to be published, in the Ironmaker and Steelmaker.

Chapter 7:

References

7.0 References

1. Editor, Nucor's second thin slab CSP plant, Steel Times, 1991(10): p. 560-561.

2. Priestner, R., Microstructural change during the hot working of as-cast austenite, Materials Science Forum, 1998. 284-286: p. 95-104.

3. Doring, K. and H. Wiesinger, Continuous casting and rolling of thin slabs, Metallurgical Plant and Technology International, 1990. 5: p. 16-29.

4. Nilles, P., Quality aspects in near net shape casting, Metallurgical Plant and Technology International, 1994(3): p. 46-56.

5. Pleschiutschnigg, F., I. von Hagen, H. Hoppmann, and G. Gosio, The I.S.P. process, its potential and first operating results, Metallurgical Plant and Technology International, 1993. 4: p. 44-68.

6. Korchynsky, M., New steels for new mills, Scandinavian Journal of Metallurgy, 1999. 28: p. 40-45.

7. Muojekwu, C.A., D.Q. Jin, I.V. Samarasekera, and J.K. Brimacombe, Thermomechanical history of steel strip during hot rolling- A comparison of conventional cold-charge rolling and hot-direct rolling of thin slabs. In 37th MWSP CONF. PROC., ISS, 1996: p. 617-633.

8. Lubensky, P.J., S.L. Wigman, and D.J. Johnson. High strength steel processing via direct charging using thin slab technology, In Microalloying '95 Conference Proceedings. 1995: p. 225-233.

9. Brimacombe, J.K. and I.V. Samarasekera. The challenges of thin slab casting, In Proc. Int. Symposium on Near-Net-Shape Casting in the Minimills. 1995. Vancouver, British Columbia, Canada. p. 33.53.

10. Korchynsky, M. High strength low alloy steels produced by thin slab casting, In THERMEC' 97: International Conference on Thermomechanical Processing of Steels & Other Materials. 1997. Wollongong, Australia. p. 2,247-2,253.

11. Kaspar, R. and O. Pawelski. Thermomechanical treatment of direct-charged thin slabs, In METEC Congress, VDEVI. 1994. Dusseldorf, Germany. p. 390-365.

12. Kaspar, R. and N. Zentara, Optimization of process parameters of direct charging of near-net shape cast steel products, La Revue de Metallurgie-CIT, 1997(4): p. 533-540.

13. Streubel, H., Thin-slab casting with liquid core reduction, Metallurgical Plant and Technology International, 1999. 22(3): p. 62-66.

14. Coassin, G. and U. Meroni, Flexible thin slab conticaster, Metallurgical Plant and Technology International, 1994. 3: p. 110-120.

15. Ritt, A., Casting better with better surface quality, Iron Age New Steel, 1997. 13(4): p. 66-70.

16. Borsi, R. and M. Rotti, Direct thin slab rolling at Algoma, Iron and Steel Engineer, 1998(5): p. 62-64.

17. Kothe, D., B. Kruger, F. Pieschiutschnigg, M. Spangenberg, and C. Ceasar, ISP-Thin slab casting and rolling concept for economical processing of quality products, Iron and Steel Engineer, 1997(6): p. 31-41.

18. Pleschiutschnigg, F., First minimill with I.S.P. technology in comparison with other hot-strip production lines, Metallurgical Plant and Technology International, 1992. 2: p. 66-82.

19. Yost, C., Thin-slab casting and rolling- A new technology to benefit the US steel industry, Steel Times International, 1998(7): p. 28-48.

20. Rohde, W. and G. Flemming, Current state, capabilities and Further development of the CSP technology, Metallurgical Plant and Technology International, 1995. 18(4): p. 82-98.

21. Essadiqi, E., L.E. Collins, M.T. Shehata, and I.K. Chiang. Thin slab casting simulation of 1020 C steel with liquid core reduction, In Second Canada-Japan Symposium on Modern Steelmaking and Casting Techniques ed. J.J. Jonas, J.D. Boyd and N. Sano, 1994: 33rd Annual Conference of Metallurgists of CIM. p.251-264.

22. Yamanaka, A., S. Kumakura, K. Okamura, T. Kanazawa, T. Murakami, M. Oka, I. Takeuchi, and T. Watanabe, Thin slab casting with liquid core reduction, Ironmaking and Steelmaking, 1999. 26(6): p. 457-462.

23. Muojekwu, C.A., D.Q. Jin, V.H. Hernandez, I.V. Samarasekera, and J.K. Brimacombe. Hot-direct rolling, runout table cooling and mechanical properties of steel strips produced from thin slabs, In 38th MWSP CONF. PROC. 1997: ISS. Vol. XXXIV: p. 351-366.

24. Leroy, V. and J.C. Herman. The microstructure and properties of steels processed by thin slab casting, In Microalloying '95 Conference Proceedings. 1995. p. 213-222.

25. Kunishige, K. and N. Nagao, Strengthening and toughening of Hot-direct-rolled steels by addition of a small amount of Titanium, ISIJ International, 1989. 29(11): p. 940-946.

26. Flemming, G., F. Hofmann, W. Rohde, and D. Rosenthal, The CSP plant technology and its adaptation to an expanded production programme, Metallurgical Plant and Technology International, 1993. 2: p. 84-96.

27. Rodhe, W., The CSP (Compact Strip Production) casting and rolling technology, SEAISI Quarterly, 1990(1): p. 38-47.

28. Flemming, G. and K.E. Hensger. CSP for HSLA hot strip, In 40th MWSP CONF. PROC. 1998: ISS. p. 775-786.

29. Hendricks, C., W. Rasim, H. Janssen, H. Schnitzer, E. Sowka, and P. Tesè, The casting rolling plant of Thyssen Krupp Stahl, Steel Times, 1999. 227(8): p. 306-308.

30. Davis, R.F. and K.L. Kain. Making MINIGRATED steel products at ACME STEEL, In 39th MWSP CONF. PROC. 1998: ISS. Vol XXXV: p. 893-903.

31. Schloemann-Siemag, A round-up of CSP thin slab, Steel times, 1998. 5: p. 175-178.

32. Editor, ISP- Thin slab challenge to Nucor, Steel Times, 1993(10): p. 417-419.

33. Gottardi, R., L. Nannini, and A.D. Martegani, Net and near net shape continuous casting: Developments in thin slab casting, Steel Times, 1992(11): p. 524-525.

34. Gottardi, R., L. Nannini, and A.D. Martegani, Net and near net shape continuous casting- New developments in mini-mills, Metallurgical Plant and Technology International, 1992. 3: p. 46-50.

35. Donini, E.A., R. Borsi, and A. Carboni, Flexible thin-slab rolling: Matching the requirements of integrated producers, Iron and Steel Engineer, 1997(6): p. 39-44.

36. Vazzoler, N. and S. Buoro, High speed casting of peritectic steels in the Danieli thin slab caster, Steel Times, 1998(5): p. 172-173.

37. Ritt, A., Thin slabs from BOF steel in Canada, New Steel, 1998. 14(2): p. 20-25.

38. Wilson, A. and J. Pietryka, TSP, a new method of thin slab casting and rolling, Metallurgical Plant and Technology International, 1994. 3: p. 122-130.

39. Gretz, R.D., The rolling technique of the TSP Process: A low-cost method of slab casting and rolling, SEAISI Quarterly, 1995(4): p. 51-56.

40. Editor, Continuous thin slab casting and rolling technology in producing quality strip, Industrial Heating, 1993. 12: p. 40-43.

41. O'Malley, R.J. Casting technologies supporting the development of direct hot charged carbon and stainless steel production at Armco's Mansfield Operations, In 39th MWSP CONF. PROC. 1998. Vol XXXV: p. 849-860.

42. Flick, A., J. Watzinger, O. Silbermann, and J. Fuchshuber, Operational results of the Conroll plant at Armco, Steel Times, 1998(5): p. 174,178,181.

43. Kanazawa, T., Y. Minamimura, S. Kumakura, Y. Tozaki, K. Abe, K. Tsujita, and T. Shiozaki, Quality strip production with a high speed medium thick slab caster, La Revue de Métallurgie-CIT, 1998(11): p. 1429-1434.

44. Dunholter, D.A., Design and start-up of the North Star BHP Steel mini mill, Iron and Steel Engineer, 1997(12): p. 49-52.

45. Berry, B., What medium-slab casting can do?, New Steel, 1997. 13(11): p. 46-53.

46. Mizumo, M., K. Tsujita, T. Kanazawa, and Y. Minamimura, Quality strip production process at Trico Steel, Steel Times, 1998(5): p. 169-170.

47. Mintz, B., S. Yue, and J.J. Jonas, Hot ductility of steels and its relationship to the problem of transverse cracking during continuous casting, International Materials Review, 1991. 36(5): p. 187-217.

48. Mintz, B., The influence of composition on the hot ductility of steels and to the problem of transverse cracking, ISIJ International, 1999. 39(9): p. 833-855.

49. Maehara, Y., K. Yasumoto, H. Tomono, T. Nagamichi, and Y. Ohmori, Overview: Surface cracking mechanism of continuously cast low carbon low alloy steel slabs, Materials Science and Technology, 1990. 6(9): p. 793-806.

50. Irving, W.R., Continuous casting of steel. 1993, London: The Institute of Materials.

51. Turkdogan, E.T., Causes and effects of nitride and carbonitride precipitation in HSLA steels in relation to continuous casting, AIME Steelmaking Conference proceedings, 1987. 70: p. 399-409.

52. Harada, S., S. Tanaka, H. Misumi, S. Mizoguch, and H. Horiguch, A formation mechanism of transverse cracks on CC slab surface, ISIJ International, 1990. 30(4): p. 310-316.

53. Irving, W.R., A. Perkins, and Gray, Effect of steel chemistry and operating parameters on surface defects in continuously cast slabs, Ironmaking and Steelmaking, 1984. 1(3): p. 146-151.

54. Brimacombe, J.K. and K. Sorimachi, Crack formation in the continuous casting of steel, Metallurgical Transactions B, 1977. 8B(9): p. 489-505.

55. Lait, J.E. and J.K. Brimacombe, Solidification during the continuous casting of steel, ISS Transactions, 1982. 1: p. 1-12.

56. Suzuki, M., H. Hayashi, H. Shibata, T. Emi, and I. Lee, Simulation of transverse crack formation on continuously cast peritectic medium carbon steel slabs, Steel Research, 1999. 70(10): p. 412-419.

57. Maehara, Y., K. Yasumoto, Y. Sugitani, and K. Gunji, Effect of carbon on hot ductility of as-cast low alloy steels, Transactions ISIJ, 1985. 25: p. 1045-1092.

58. Suzuki, M., C.H. Yu, H. Shibata, and T. Emi, Recovery of hot ductility by improving thermal pattern of continuously cast low carbon and ultra low carbon steel slabs for hot direct rolling, ISIJ International, 1997. 37(9): p. 862-871.

59. Mintz, B., J.M. Stewart, and D.N. Crowther, The influence of cyclic temperature oscillations on precipitation and hot ductility of a C-Mn-Nb-Al steel, ISIJ Transactions, 1987. 27: p. 959-964.

60. El-wazri, A.M., F. Hassani, S. Yue, and E. Es-sadiqi, Influence of physical simulation on the hot ductility behaviour of a microalloyed steel in the continuous casting process, I&SM, 1998(1): p. 37-41.

61. El-wazri, A.M., F. Hassani, S. Yue, E. Es-sadiqi, L.E. Collins, and K. Iqbal, The effect of thermal history on the hot ductility of microalloyed steels, ISIJ International, 1999. 39(3): p. 253-262.

62. Akhlaghi, S., F. Hassani, and S. Yue. Effect of thermomechanical history on the hot ductility of a Nb-Ti microalloyed steel, In 40th MWSP CONF. PROC. 1998: ISS. p. 699-705.

63. Abushosha, R., R. Vipond, and B. Mintz, Influence of Titanium on hot ductility of as cast steels, Materials Science and Technology, 1991. 7(7): p. 613-621.

64. Mintz, B. and R. Abushosha, Effectiveness of hot tensile tests in simulating straightening in continuous casting, Materials Science and Technology, 1992. 8(2): p. 171-177.

65. Cowley, A., R. Abushosha, and B. Mintz, Influence of Ar_3 and Ae_3 temperatures on hot ductility of steels, Materials Science and Technology, 1998. 14(11): p. 1145-1153.

66. Mintz, B., Importance of Ar_3 temperature in controlling ductility and width of hot ductility trough in steels, and its relationship to transverse cracking, Materials Science and Technology, 1996. 12(2): p. 132-138.

67. Lewis, J., J.J. Jonas, and B. Mintz, The formation of deformation induced ferrite during mechanical testing, ISIJ International, 1998. 38(3): p. 300-309.

68. Mintz, B., J. Lewis, and J.J. Jonas, Importance of deformation induced ferrite and factors which control its formation, Materials Science and Technology, 1997. 13(4): p. 379-388.

69. Abushosha, R., S. Ayyad, and B. Mintz, Influence of cooling rate and MnS inclusions on hot ductility of steels, Materials Science and Technology, 1998. 14(3): p. 227-235.

70. Mintz, B., R. Abushosha, and A. Cowley, Preliminary analysis of hot ductility curve in simple C-Mn steels, Materials Science and Technology, 1998. 14(3): p. 222-226.

71. Crowther, D.N. and B. Mintz, Influence of grain size on hot ductility of plain C-Mn steels, Materials Science and Technology, 1986. 2(9): p. 951-955.

72. Crowther, D.N. and B. Mintz, Influence of grain size and precipitation on hot ductility of microalloyed steels, Materials Science and Technology, 1986. 2(11): p. 1099-1105.

73. Comineli, O., The Influence of cooling rate and microalloying addition of Ti and Nb on the hot ductility of HSLA steels, Thesis, In Dept. Mechanical Engineering and Aeronautics. 1998, City University: London.

74. Mintz, B., R. Abushosha, and M. Shaker, Influence of deformation ferrite, grain boundary sliding and dynamic recrystallisation on hot ductility of 0.1-0.75%C steels, Materials Science and Technology, 1993. 9(10): p. 907-914.

75. Crowther, D.N. and B. Mintz, Influence of carbon on hot ductility of steels, Materials Science and Technology, 1986. 2(7): p. 671-676.

76. Mintz, B., R. Abushosha, O.G. Comineli, and M.A. Loyola de Oliveira. The influence of sulphides on the hot ductility of steels, In THERMEC' 97: International Conference on Thermomechanical Processing of Steels & Other Materials. 1997. Wollongong, Australia. p. 867-873.

77. Maehara, Y. and T. Nagamichi, Effect of sulphur on hot ductility of niobium containing low carbon steels during low strain rate deformation, Materials Science and Technology, 1991. 7(10): p. 915-921.

78. Abushosha, R., R. Vipond, and B. Mintz, Influence of sulphur and niobium on hot ductility of as cast steels, Materials Science and Technology, 1991. 7(12): p. 1101-1107.

79. Revaux, T., P. Deprez, J. Bricout, and J. Oudin, In situ solidified hot tensile test and hot ductility of some plain carbon steels and microalloyed steels, ISIJ International, 1994. 34(6): p. 528-535.

80. Mintz, B., Z. Mohamed, and R. Abu-shosha, Influence of calcium on hot ductility of steels, Materials Science and Technology, 1989. 5(7): p. 682-688.

81. Crowther, D.N., Z. Mohamed, and B. Mintz, The relative influence of dynamic and static precipitation on the hot ductility of microalloyed steels, Metallurgical Transactions A, 1987. 18A(11): p. 1929-1939.

82. Abushosha, R., S. Ayyad, and B. Mintz, Influence of cooling rate on hot ductility of C-Mn-Al and C-Mn-Nb-Al steels, Materials Science and Technology, 1998. 14(4): p. 346-351.

83. Cardoso, G.I., B. Mintz, and S. Yue, Hot ductility of aluminium and titanium containing steels with and without cyclic temperature oscillations, Ironmaking and Steelmaking, 1995. 22(5): p. 365-377.

84. Mintz, B. and J.M. Arrowsmith, Hot-ductility behaviour of C-Mn-Nb-Al steels and its relationship to propagation during the straightening of continuously cast strand, Metals Technology, 1979. 6: p. 24-31.

85. Mintz, B., J.R. Wilcox, and D.N. Crowther, Hot ductility of directly cast C-Mn-Nb-Al steel, Materials Science and Technology, 1986. 2(6): p. 589-594.

86. Weiss, I. and J.J. Jonas, Interaction between recrystallisation and precipitation during the high temperature deformation of HSLA steels, Metallurgical Transactions A, 1979. 10A(7): p. 831-840.

87. Ouchi, C. and K. Matsumoto, Hot ductility in Nb-bearing high-strength low-alloy steels, Transactions ISIJ, 1982. 22: p. 181-189.

88. Mintz, B. and R. Abushosha, The hot ductility of V, Nb/V and Nb containing steels, Materials Science Forum, 1998. 284-286: p. 461-468.

89. Deprez, P., J.P. Bricout, and J. Oudin, Tensile test on in situ solidified notched specimens: effects of temperature history and strain rate on the hot ductility of Nb and Nb-V microalloyed steels, Materials Science and Engineering, 1993. A168: p. 17-22.

90. Mintz, B. and D.N. Crowther, The influence of small additions of Ti on the hot ductility of steels, In Titanium technology in microalloyed steels, ed. T.N. Baker. 1997, London: The Institute of Materials. p. 98-113.

91. Abushosha, R., O. Comineli, and B. Mintz, Influence of Ti on hot ductility of C-Mn-Al steels, Materials Science and Technology, 1999. 15(3): p. 278-286.

92. Luo, H., L.P. Karjalainen, D. Porter, H. Limatainen, and Y. Zhang, The influence of Ti on the hot ductility of Nb-bearing steels in simulated continuous casting process, ISIJ International, 2002. 42(3): p. 273-282.

93. Comineli, O., R. Abushosha, and B. Mintz, Influence of titanium and nitrogen on hot ductility of C-Mn-Nb-Al steels, Materials Science and Technology, 1999. 15(9): p. 1058-1068.

94. Mintz, B., Influence of nitrogen on hot ductility of steels and its relationship to problem of transverse cracking, Iron & Steelmaking, 2000. 27(5): p. 343-347.

95. Suzuki, K., S. Miyagawa, Y. Saito, and K. Shiotani, Effect of Microalloyed nitride forming elements on precipitation of carbonitride and high temperature ductility of continuously cast low carbon Nb containing steel slab, ISIJ International, 1995. 35(1): p. 34-41.

96. Mintz, B., R. Abushosha, and D.N. Crowther, Influence of small additions of copper and nickel on hot ductility of steels, Materials Science and Technology, 1995. 11(5): p. 474-481.

97. Manohar, P.A. and M. Ferry. The development of a technique for the determination of hot ductility of as-cast steel, In Proceedings of Materials 98, The Biennial Conf. of the Institute of Materials engineering Australasia, Ltd. ed. M. Ferry, 1998. p. 131-138.

98. Karjalainen, L.P., H. Kinnunen, and D. Porter, Hot ductility of certain microalloyed steels under simulated continuous casting conditions, Materials Science Forum, 1998. 284-286: p. 477-484.

99. Crowther, D.N., M.J.W. Green, and P.S. Mitchell, The influence of composition on the hot cracking susceptibility during casting of microalloyed steels processed to simulate thin slab casting conditions, Materials Science Forum, 1998. 284-286: p. 469-476.

100. Mintz, B. and Z. Mohamed, Influence of test direction on hot ductility of austenite, Materials Science and Technology, 1988. 4(3): p. 895-902.

101. Morrison, W.B., R.C. Cochrane, and P.S. Mitchell, The influence of precipitation mode and dislocation substructure on the properties of Vanadium-treated steels, ISIJ International, 1993. 32(10): p. 1095-1103.

102. Lankford JR., W.T., Some considerations of strength and ductility in the continuous-casting process, Metallurgical Transactions, 1972. 3(6): p. 1331-1357.

103. El-wazri, A.M., F. Hassani, S. Yue, E. Es-sadiqi, L.E. Collins, and K. Iqbal, Effects of reheat conditions on the hot ductility of Nb-Ti and Ti-B microalloyed steels, Canadian Metallurgical Quarterly, 2000. 39(1): p. 55-64.

104. Akhlaghi, S. and S. Yue, Effect of thermal processing on the hot ductility of a Nb-Ti microalloyed steel, ISIJ International, 2001. 41(11): p. 1350-1356.

105. Mintz, B., R. Abushosha, and J.J. Jonas, Influence of dynamic recrystallisation on the tensile ductility of steels in the temperature range 700 to 1150°C, ISIJ International, 1992. 32(2): p. 241-249.

106. Suzuki, H., S. Nishimura, and S. Yamaguchi, Characteristics of hot ductility in steels subjected to melting and solidification, Transactions ISIJ, 1982. 22: p. 48-56.

107. Zhang, L. and D.C. Guo, A general etchant for revealing prior-austenite grain boundaries in steels, Materials Characterization, 1993. 30: p. 299-302.

108. Won, Y.M. and B. Thomas, Simple model of microsegregation during solidification of steels, Metallurgical and Materials Transactions A, 2001. 32A(7): p. 1755-1767.

109. Weisgerber, B., M. Hecht, and K. Harste, Investigations of the solidification structure of the continuously cast slabs, Steel Research, 1999. 70(10): p. 403-411.

110. Martin, J.W., R.D. Doherty, and B. Cantor, Stability of microstructure in metallic systems, 2nd ed. 1997, Cambridge: Cambridge University Press.

111. Ashby, M.F. and R. Ebeling, On the determination of number, size, spacing and volume fraction of spherical second-phase particles from extraction replicas, Transactions of the Metallurgical Society of AIME, 1966. 236(10): p. 1396-1404.

112. Stumpf, W.E. and C.M. Sellars, Measurement of particle density and volume fraction from extraction replicas, Metallography, 1968. 1: p. 25-34.

113. Martin, J.W., Precipitation Hardening. 1968, London: Pergamon Press Ltd.

114. Dieter, G.E., Mechanical Metallurgy, SI Metric Edition. 1988, London: McGraw-Hill Book Company.

115. Frost, H.J. and M.F. Ashby, Deformation-Mechanism maps, The plasticity and creep of metals and ceramics. 1982, Oxford: Pergamon Press.

116. Ashby, M.F. and D.R.H. Jones, Engineering materials 1, An introduction to their properties and applications. 1980, Oxford: Pergamon Press.

117. Brandes, E.A. and G.B. Brook, eds. Smithells Metals Reference Book, 7th ed. 1992, Butterworth & Heinemann: Oxford.

118. Craven, A.J., K. He, A.J. Garvies, and T.N. Baker, Complex heterogeneous precipitation in titanium-niobium microalloyed Al-killed HSLA steels- I. (Ti,Nb)(C,N) particles, Acta Materialia, 2000. 48: p. 3857-3868.

119. Nicholson, R.B., G. Thomas, and J. Nutting, The interaction of dislocations and precipitates, Acta Metallurgica, 1960. 8: p. 172-176.

120. Kneissl, A.C., G. Posch, C.I. Garcia, and A.J. DeArdo. Precipitation and recrystallization during TMP of complex microalloyed HSLA steels, In International Symposium on Low-Carbon Steels for the 90's, ed. Asfahani, R. and Tither, G., 1993: TMS. p. 113-119.

121. Jeffries, Z., AIME, 1919. 60: p. 474-576.

122. Rosenhain, W. and D. Ewen, Journal of Institute of Metals, 1913. 10: p. 119.

123. Killmore, C.R., Private Communication, BHP Steel, Port Kembla. 2002.

124. Zou, H. and J.S. Kirkaldy, Carbonitride precipitate growth in titanium/niobium microalloyed steels, Metallurgical Transactions A, 1991. 22A(6): p. 1511-1524.

125. Okaguchi, S. and T. Hashimoto, Computer model for prediction of carbonitride precipitation during hot working in Nb-Ti bearing HSLA steels, ISIJ International, 1992. 32(3): p. 283-290.

126. Mintz, B., R. Abushosha, O. Comineli, and S. Ayyad. The hot tensile test as a means of accessing the susceptibility of steel to cracking during continuous casting, In Proceedings of 7th International Symposium on Physical Simulation of Casting, Hot Rolling and Welding, ed. Mintz B., 1997: National Research Institute of Japan. P. 449-467.

Appendix A:

Abnormal Data Points and Experimental Scatter

Appendix A: Interpreting abnormal data points and experimental scatter

Displayed below in Figure A is a plot of %RA verses temperature for the Nb-Ti microalloyed steel, showing the experimental scatter. Two abnormal data points were observed at 985°C (33.5% RA) and at 1000°C (32.8% RA), and are marked as an 'x'.

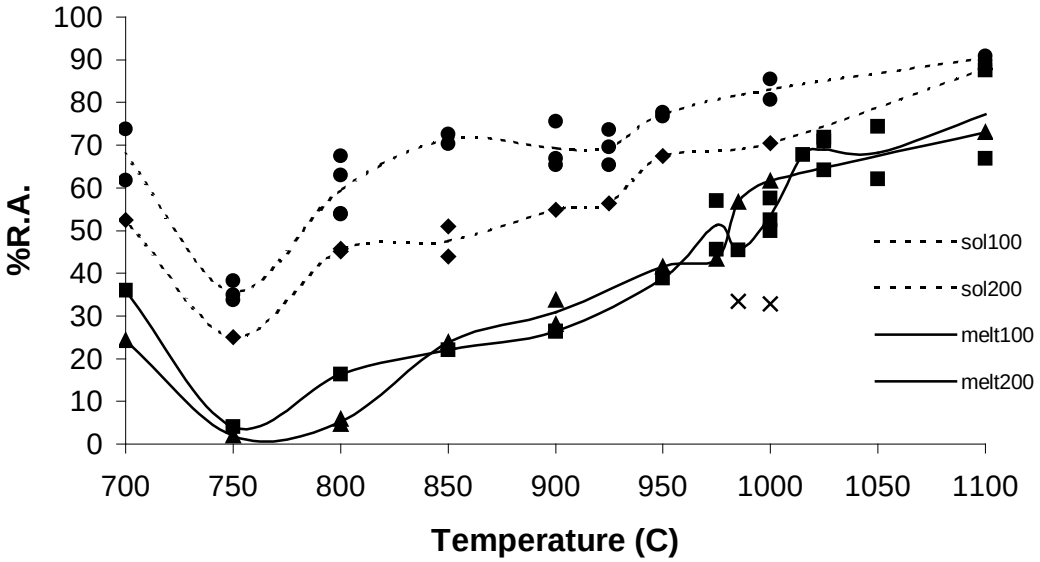

Figure A: Hot ductility curves for the Nb-Ti steel showing experimental scatter and two abnormal data points.

The two abnormal points were analyzed to understand why they displayed considerably lower ductility than what would be expected at that temperature. The first step is to check the time – temperature plot to access if there were any spikes in the temperature, which may indicate that the T/C detached and reattached during melting. Concerns were raised that the actual temperature of the specimens were lower than what the T/C indicated even if there was no noticeable indication of T/C failure, or the fracture occurred outside the "hot zone", which would also be at a lower temperature. If the actual temperature of testing was lower, than the abnormal points would fall on the ductility line, as the observed ductility is of similar ductility to that found at lower temperatures. The T/C position with respect to the fracture position, close to the midpoint of the sample, indicated that the fracture was indeed with-in the hot zone.

The stress-strain data for the abnormal points are compared to stress-strain curves of typical specimens, as displayed in Figure B. From Figure B, the initial portion of all stress-strain curves are closely matched, indicating that all samples were at a similar temperature. It can be seen from Figure B that the 'abnormal' test curves failed prematurely, well before the maximum strength was reached. The cause of the premature failure is difficult to ascertain. It is suggested that a detrimental defect was introduced during the melting and solidification procedure. A crack could easily occur when the specimen is at the nil strength temperature and this would readily lead to low ductility in subsequent testing.

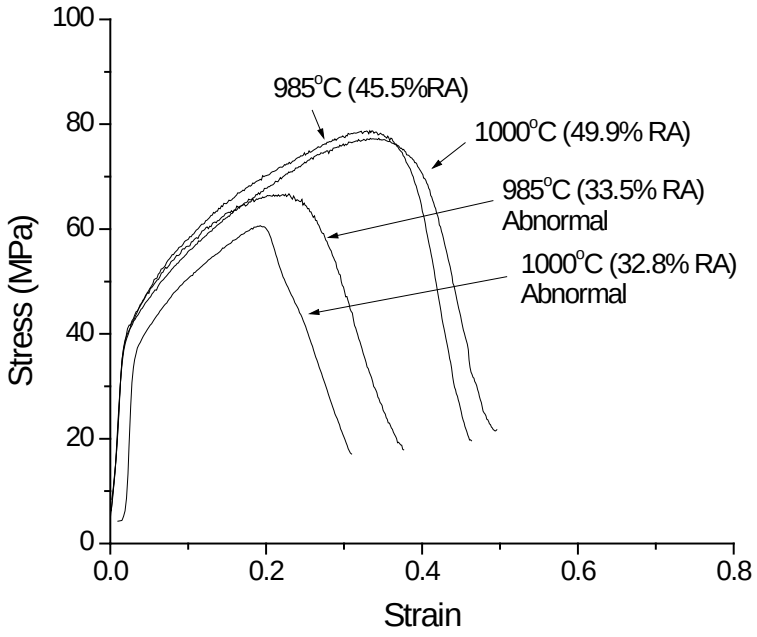

Figure B: Stress-strain curves for 1000°C and 985°C, Nb-Ti steel 200K/min direct cast conditions, for normal and abnormal tensile tests.

Experimental scatter at 900ºC for the Ti steel tested under Solution treatment conditions

In Figure C, the experimental scatter for the Ti steel under solution treatment conditions is shown. It can be seen that at 900°C a wide variation in RA was recorded, two specimens had (relatively) low ductility, 55.8% and 61.8% and two specimens had high ductility, 82% and 86.7%.

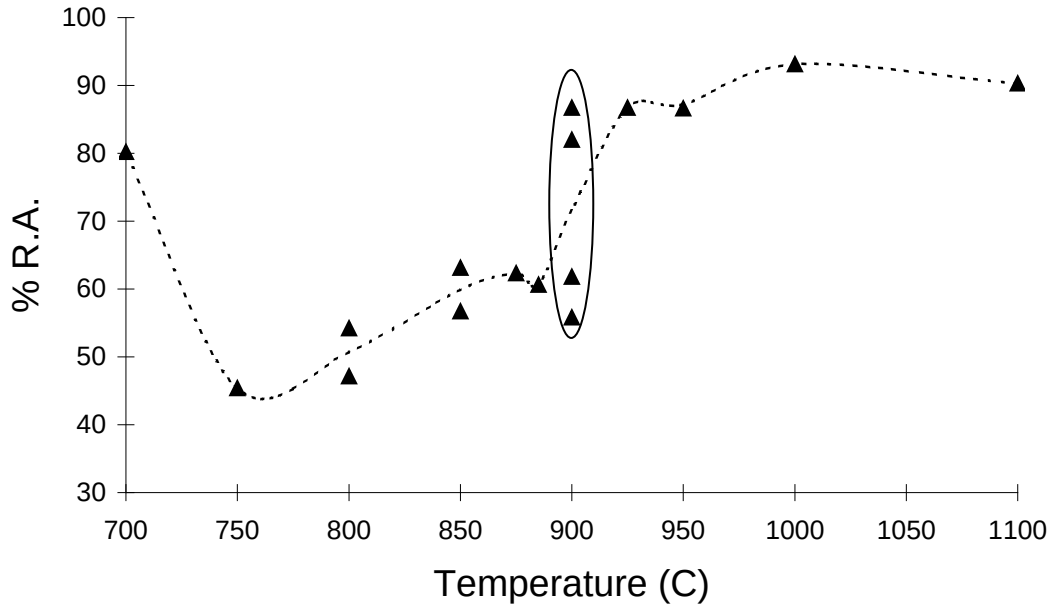

Figure C: A wide variation in the reduction of area points were observed at 900ºC (circled) for the Ti steel tested under solution treatment conditions at 100K/min.

Appendix B:

Histograms- Particle Size Distributions

Appendix B: Histograms- Particle Size Distribution

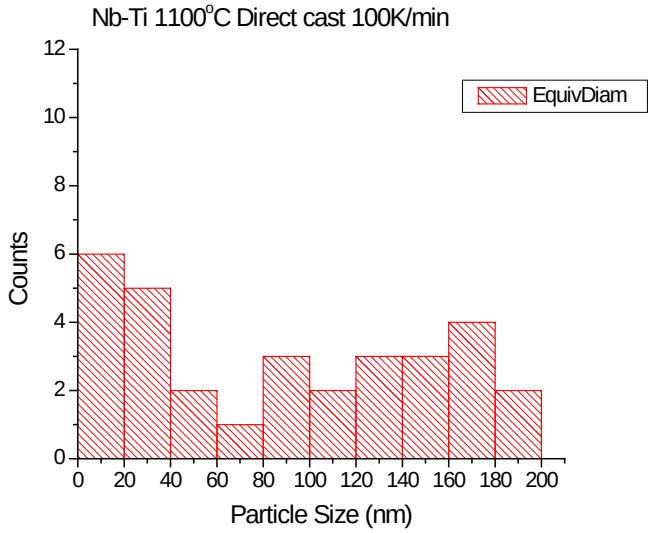

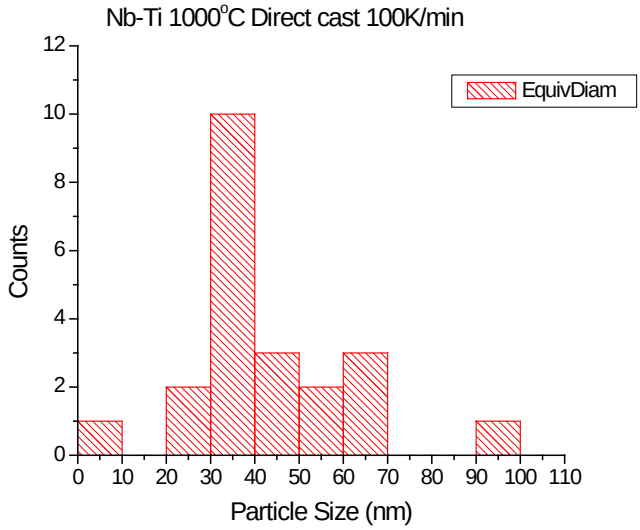

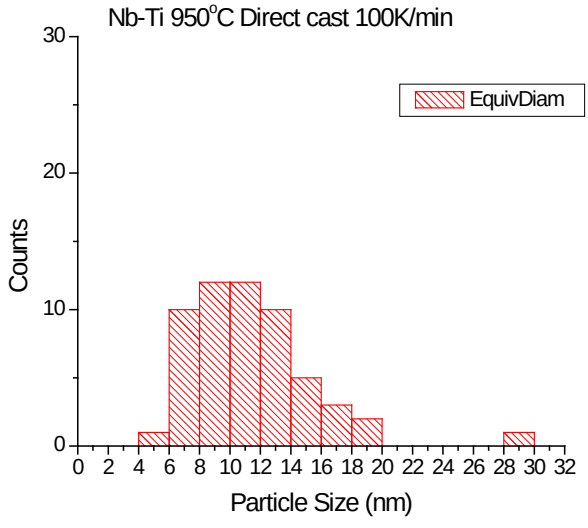

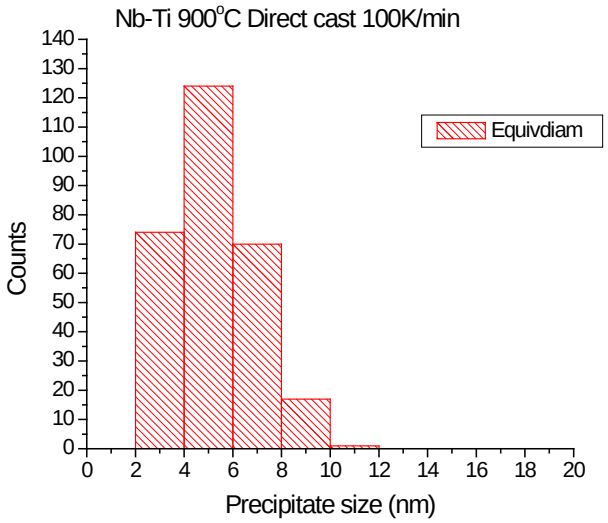
Nb-Ti 900°C Direct cast 100K/min
Equivdiam
Counts
Precipitate size (nm)
0
10
20
30
40
50
60
70
80
90
100
110
120
130
140
0
2
4
6
8
10
12
14
16
18
20

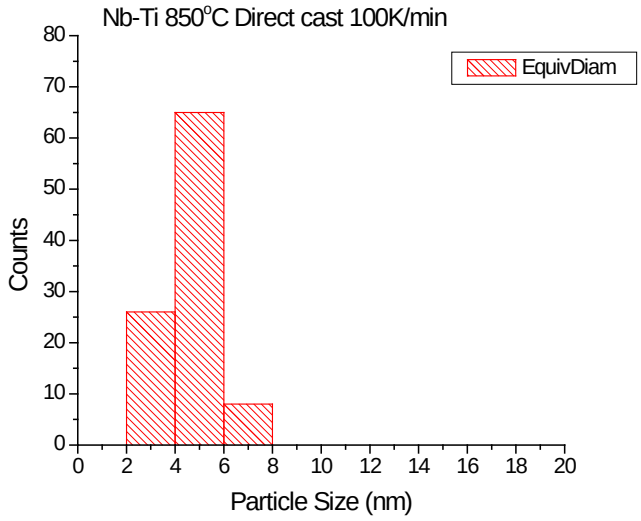
Nb-Ti 850°C Direct cast 100K/min
EquivDiam
Counts
Particle Size (nm)
0
10
20
30
40
50
60
70
80
0
2
4
6
8
10
12
14
16
18
20

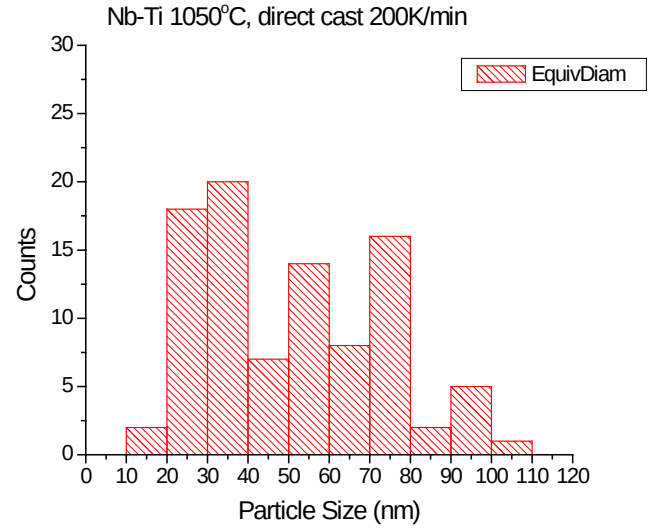
Nb-Ti 1050°C, direct cast 200K/min
EquivDiam
Counts
Particle Size (nm)
0
5
10
15
20
25
30
0 10 20 30 40 50 60 70 80 90 100 110 120

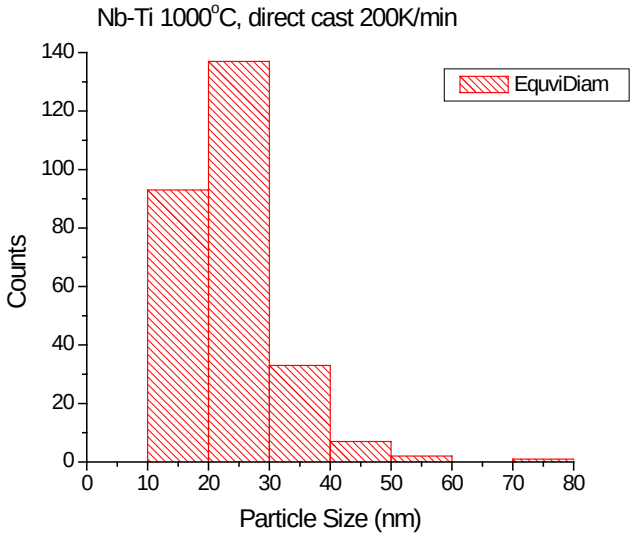
Nb-Ti 1000°C, direct cast 200K/min
EquviDiam
Counts
Particle Size (nm)
0
20
40
60
80
100
120
140
0 10 20 30 40 50 60 70 80

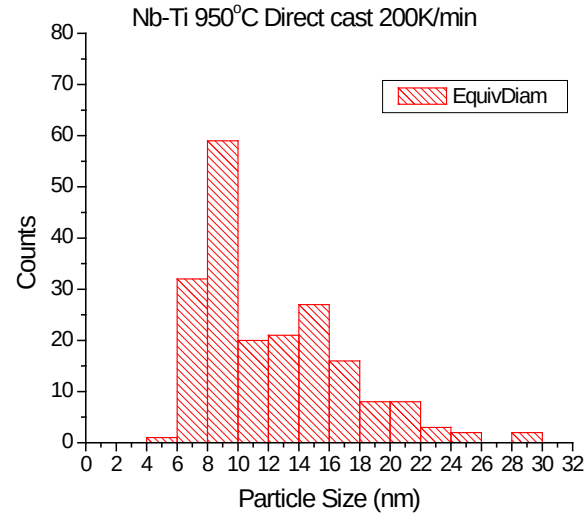
Nb-Ti 950°C Direct cast 200K/min
EquivDiam
Counts
Particle Size (nm)
0
10
20
30
40
50
60
70
80
0 2 4 6 8 10 12 14 16 18 20 22 24 26 28 30 32

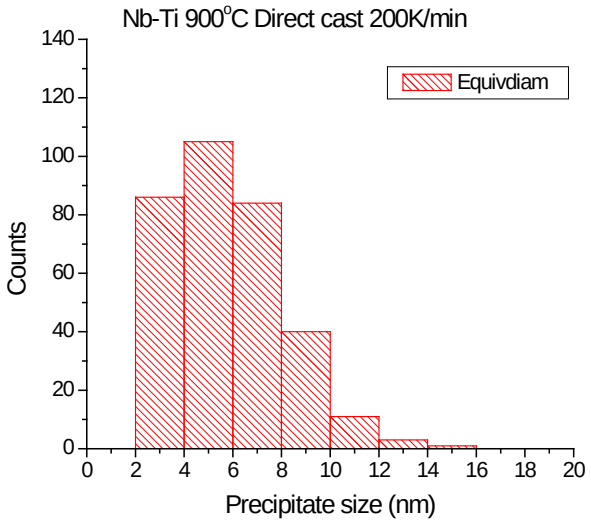
Nb-Ti 900°C Direct cast 200K/min
Equivdiam
Counts
Precipitate size (nm)
0
20
40
60
80
100
120
140
0
2
4
6
8
10
12
14
16
18
20

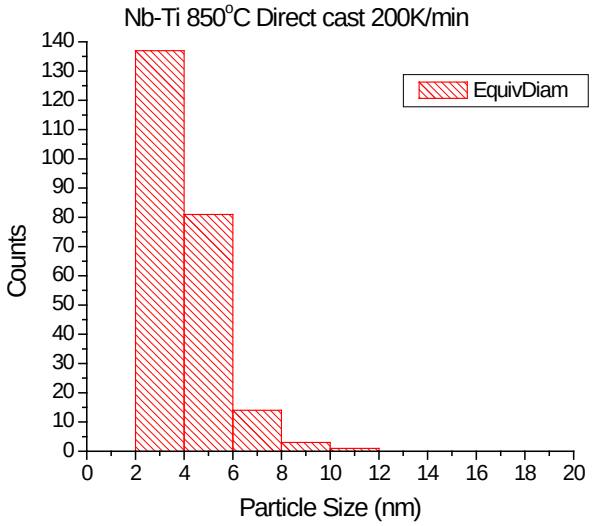
Nb-Ti 850°C Direct cast 200K/min
EquivDiam
Counts
Particle Size (nm)
0
10
20
30
40
50
60
70
80
90
100
110
120
130
140
0
2
4
6
8
10
12
14
16
18
20

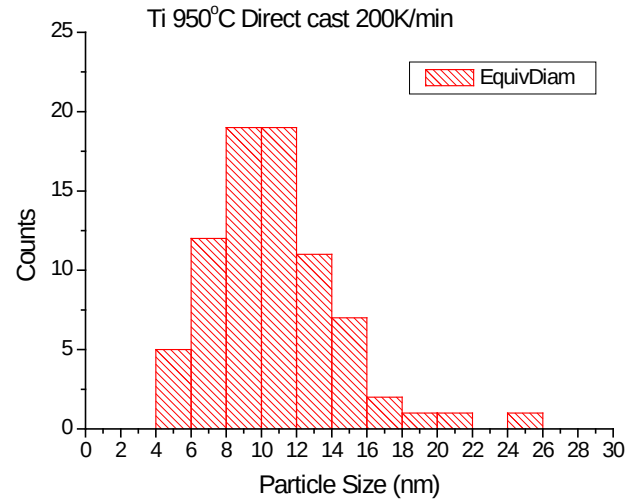
Ti 950°C Direct cast 200K/min
EquivDiam
Counts
Particle Size (nm)
0
5
10
15
20
25
0 2 4 6 8 10 12 14 16 18 20 22 24 26 28 30

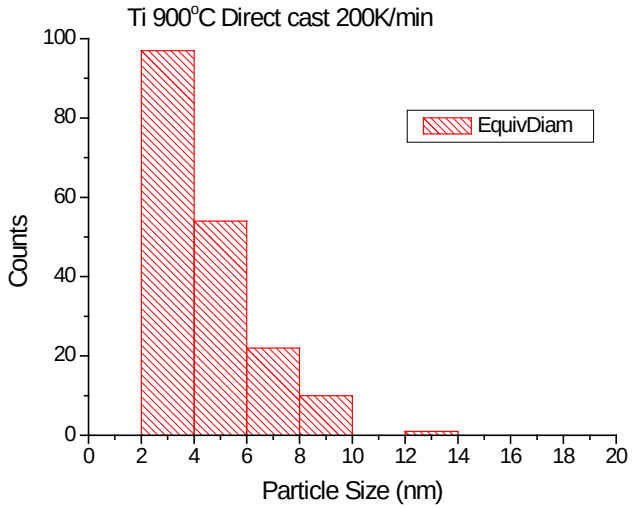
Ti 900°C Direct cast 200K/min
EquivDiam
Counts
Particle Size (nm)
0
20
40
60
80
100
0 2 4 6 8 10 12 14 16 18 20

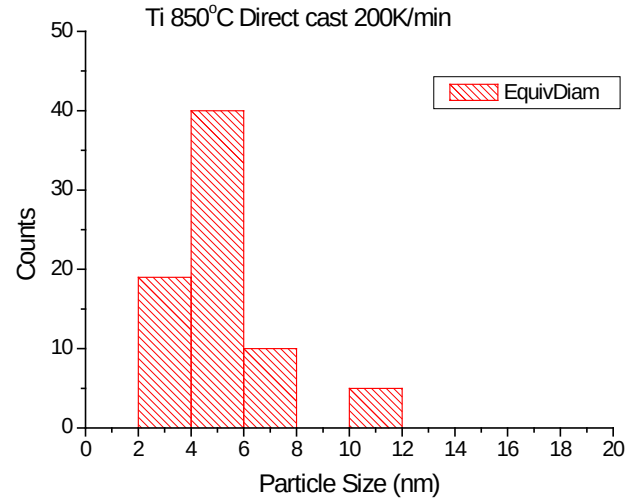
Ti 850°C Direct cast 200K/min
EquivDiam
Counts
Particle Size (nm)
0
10
20
30
40
50
0 2 4 6 8 10 12 14 16 18 20

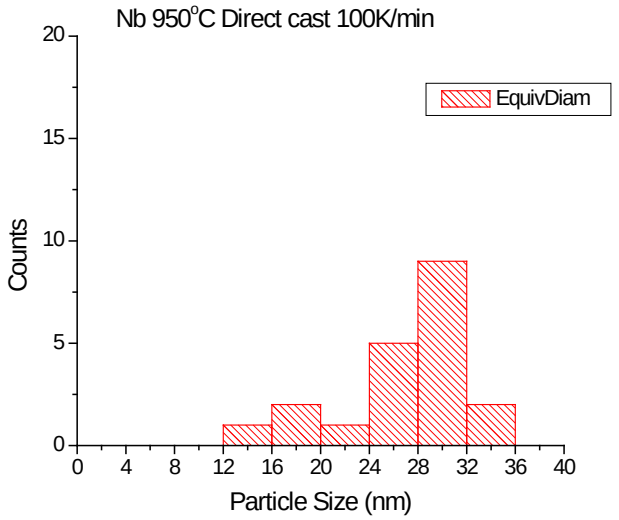
Nb 950°C Direct cast 100K/min
EquivDiam
Counts
Particle Size (nm)
0
5
10
15
20
0 4 8 12 16 20 24 28 32 36 40

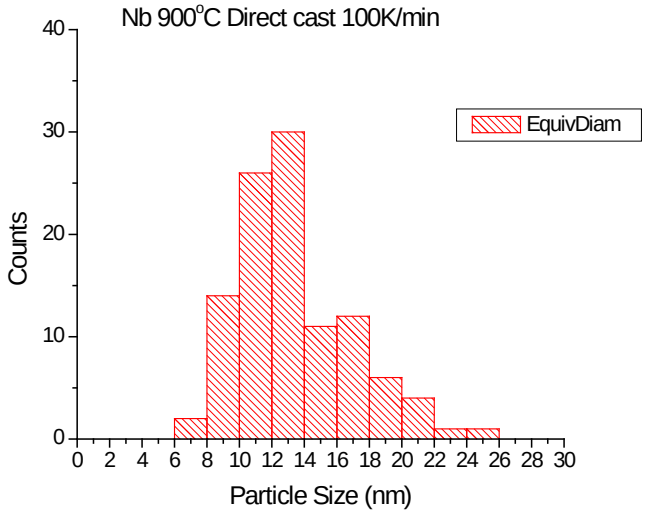
Nb 900°C Direct cast 100K/min
EquivDiam
Counts
Particle Size (nm)
0
10
20
30
40
0 2 4 6 8 10 12 14 16 18 20 22 24 26 28 30

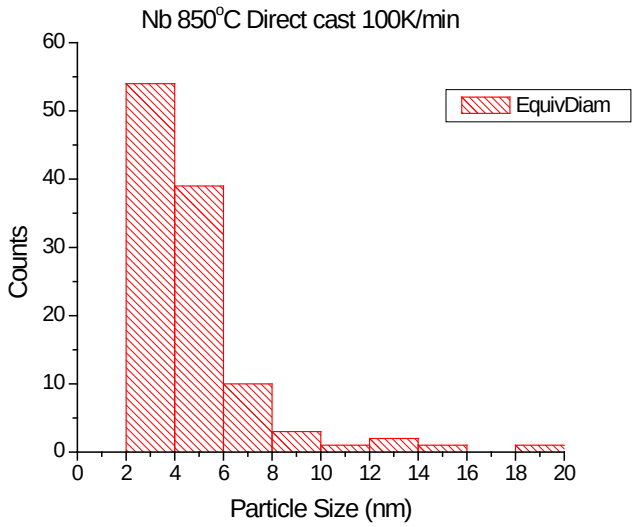
Nb 850°C Direct cast 100K/min
EquivDiam
Counts
Particle Size (nm)
0
10
20
30
40
50
60
0 2 4 6 8 10 12 14 16 18 20

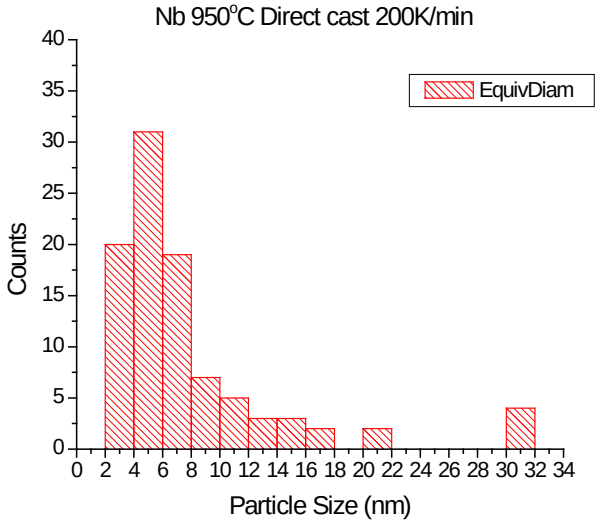
Nb 950°C Direct cast 200K/min
EquivDiam
Counts
Particle Size (nm)
0 2 4 6 8 10 12 14 16 18 20 22 24 26 28 30 32 34
0 5 10 15 20 25 30 35 40

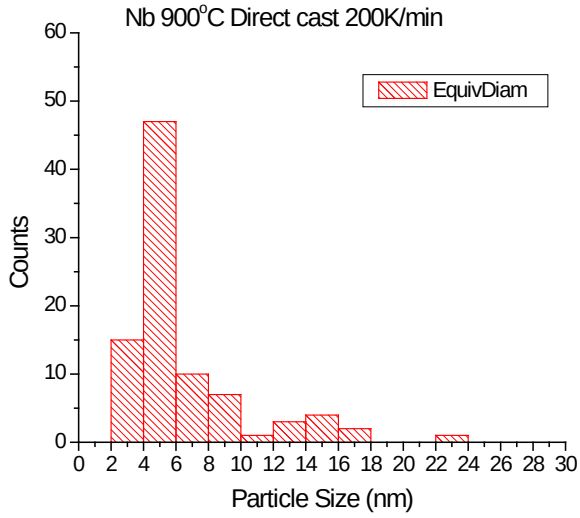
Nb 900°C Direct cast 200K/min
EquivDiam
Counts
Particle Size (nm)
0 2 4 6 8 10 12 14 16 18 20 22 24 26 28 30
0 10 20 30 40 50 60

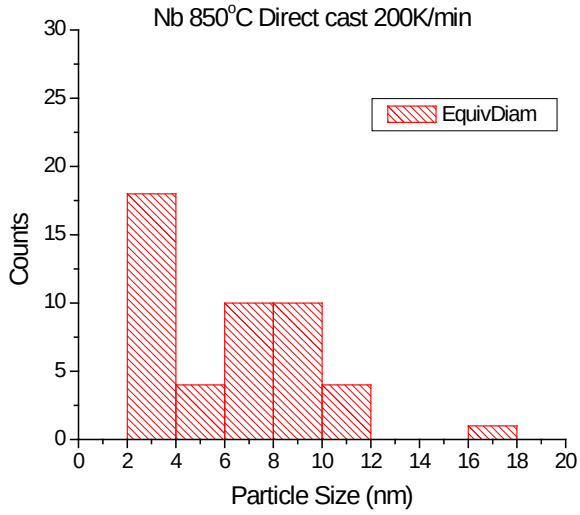
Nb 850°C Direct cast 200K/min
EquivDiam
Counts
Particle Size (nm)
0 2 4 6 8 10 12 14 16 18 20
0 5 10 15 20 25 30